Molecular Recognition Using Nanotube-Adsorbed Polymer Complexes

by
Jingqing Zhang

Bachelor of Science in Chemical Engineering
Tsinghua University, 2007

Master of Science in Chemical Engineering Practice
Massachusetts Institute of Technology, 2012

SUBMITTED TO THE DEPARTMENT OF CHEMICAL ENGINEERING IN PARTIAL FULFILLMENT OF THE REQUIREMENTS FOR THE DEGREE OF DOCTOR OF PHILOSOPHY IN CHEMICAL ENGINEERING
AT THE
MASSACHUSETTS INSTITUTE OF TECHNOLOGY

December 2012
[FEBRUARY 2013]

Signature of Author:

Department of Chemical Engineering
December 13, 2012

Certified by:

Michael S. Strano
Charles and Hilda Roddey Professor of Chemical Engineering
Thesis Supervisor

Accepted by:

Patrick S. Doyle
Professor of Chemical Engineering
Chairman, Committee for Graduate Students

Molecular Recognition Using Nanotube-adsorbed Polymer Complexes

by
Jingqing Zhang

Submitted to the Department of Chemical Engineering
on Dec 13, 2012, in Partial Fulfillment of the
Requirements for the Degree of
Doctor of Philosophy

Abstract

We first reported the selective detection of single nitric oxide (NO) molecules using a specific DNA sequence of $d(AT)_{15}$ oligonucleotides, adsorbed to an array of near infrared fluorescent semiconducting single-walled carbon nanotubes (AT_{15}-SWCNT). While SWNT suspended with eight other variant DNA sequences show fluorescence quenching or enhancement from analytes such as dopamine, NADH, L-ascorbic acid, and riboflavin, $d(AT)_{15}$ imparts SWNT with a distinct selectivity toward NO. In contrast, the electrostatically neutral polyvinyl alcohol, enables no response to nitric oxide, but exhibits fluorescent enhancement to other molecules in the tested library. For AT_{15}-SWCNT, a stepwise fluorescence decrease is observed when the nanotubes are exposed to NO, reporting the dynamics of single-molecule NO adsorption via SWCNT exciton quenching. We describe these quenching traces using a *birth-and-death* Markov model, and the maximum likelihood estimator of adsorption and desorption rates of NO is derived. Applying the method to simulated traces indicates that the resulting error in estimation is less than 5% under our experimental conditions, allowing for calibration using a series of NO concentrations. As expected, the adsorption rate is found to be linearly proportional to NO concentration, and the intrinsic single-SWCNT-site NO adsorption rate constant is 0.001 s^{-1} μM NO^{-1}. The ability to detect nitric oxide quantitatively at the single-molecule level may find applications in new cellular assays for the study of nitric oxide carcinogenesis and chemical signaling, as well as medical diagnostics for inflammation.

Further, we also explored the concept of creating molecular recognition sites using polymer-SWCNT complexes. Molecular recognition is central to the design of therapeutics, chemical catalysis and sensor platforms, with the most common mechanisms involving biological structures such as antibodies[1] and aptamers[2, 3]. The key to this molecular recognition is a folded and constrained heteropolymer pinned, via intra-molecular forces, into a unique three-dimensional orientation that creates a binding pocket or interface to recognize a specific molecule. An alternate approach to constraining a polymer in three-dimensional space involves adsorbing it onto a cylindrical nanotube surface[4-7]. To date, however, the molecular recognition potential of these structured, nanotube-associated complexes has been unexplored. In this work, we demonstrate three distinct examples in which synthetic polymers create unique and

highly selective molecular recognition sites once adsorbed onto a single-walled carbon nanotube (SWCNT) surface. The phenomenon is shown to be generic, with new recognition complexes demonstrated for riboflavin, L-thyroxine, and estradiol, predicted using a 2D thermodynamic model of surface interactions. The dissociation constants are continuously tunable by perturbing the chemical structure of the heteropolymer. The complexes can be used as new types of sensors based on modulation of SWCNT photoemission, as demonstrated using a complex for real time spatio-temporal detection of riboflavin in murine macrophages.

Cardiac biomarkers troponin I and T are recognized as standard indicators for acute myocardial infarction (AMI, or heart attack), a condition that comprises 10% of U.S. emergency room visits [8]. There is significant interest in a rapid, point-of-cae (POC) device for troponin detection[9]. In this work we demonstrate a rapid, quantitative, and label-free assay specific for cardiac troponin T detection, using fluorescent single-walled carbon nanotubes (SWCNTs). Chitosan-wrapped carbon nanotubes are crosslinked to form a thin gel that is further functionalized with nitrilotriacetic acid (NTA) moieties. Upon chelation of Ni^{2+}, the Ni^{2+}-NTA group binds to a hexa-histidine-modified troponin antibody, which specifically recognizes the target protein, troponin T. As the troponin T binds to the antibody, the local environment of the sensor changes, allowing for the detection through changes in SWCNT bandgap fluorescence intensity. In this work, we have developed the first near-infrared SWCNT sensor array for specific cTnT detection. Detection can be completed within 3 minutes, and the sensor responds linearly to the cTnT concentrations, with the experimental detection limit of 100 ng/ml (2.5 nM). This platform may provide a promising new tool for POC AMI detection in the future. Moreover, the work presented two useful methods of characterizing two commonly used functional groups, amines and carboxylic acids in soft gels, and this will be useful for other researchers studying hydrogel chemistry. In addition, we synthesized and characterized chitosan-gels both with and without NTA groups, and we compared fluorescence responses upon the addition of four different divalent cations, including Ni^{2+}, Co^{2+}, Mg^{2+}, and Mn^{2+}. We proposed a model based Flory-Huggins theory, without any fitted parameters, that is able to describe the fluorescence increase as the Ni^{2+} concentration increases. The model suggests that the strong binding of Ni^{2+} onto NTA groups decreases the number of mobile ions in the gel, resulting in a reduction in the ionic chemical potential inside the gel. As a result, the gel de-swells, leading to a local SWCNT concentration increase and an increase in the SWCNT fluorescence signal.

Thesis Supervisor: Michael S. Strano
Charles and Hilda Roddey Professor of Chemical Engineering

Acknowledgements

This thesis would not have been possible without the support from my thesis advisor, Professor Michael S. Strano. His enthusiasm for research, broad range of knowledge, and deep insight on the scientific challenges have guided and influenced me every day on my way toward the completion of my PhD. I am also very grateful that he has always ensured that I work on projects that interest me, and has always supported the exploration of multiple directions in my thesis. Beyond a research advisor, Professor Strano is an excellent mentor, guiding me through difficult times in research and having spent many hours with me discussing my future career path.

I also thank my committee members, Professor William M. Deen, Professor Robert S. Langer, Professor Steven R. Tannenbaum, and Professor Gerald N. Wogan. I am very fortunate to be advised by such a multidisciplinary team of intellectual giants, and each of them is the leader in their field. They have always advised me with my best interest in mind – ensuring my thesis is taking the right direction and providing many useful recommendations in the scientific development of my thesis. In addition to my yearly committee meetings, Professor Deen has always been an excellent mentor to me, providing support and guidance for my thesis, and I know I can always turn to him whenever I have any questions regarding modeling. Professor Langer has always ensured that I bear the "big picture" in mind, and has provided very valuable career advice. Professor Tannenbaum is very insightful, and some of the key suggestions he made became an indispensable part of my thesis. Professor Wogan is a wonderful mentor to me, and has been very supportive of each little progress I was making toward the competition of my PhD. I cannot be more thankful for having them on my committee.

I thank the entire Strano group for the tight collaboration and friendship. In particular, I thank Geraldine Paulus and Ardemis Boghossian for being so supportive and providing such close friendship for the past 5 years. I also want to thank Arde and Zachary Ulissi for forming a collaborative and productive team with me, and we co-authored many papers together. I also want to thank Dr. Paul Barone, Dr. Daniel Heller, and Dr. Hong Jin for their training me on several of the lab instruments early in my PhD, and giving me graduate school guidance. Without them, I do not know how I would have started in the

Strano lab. I want to thank Andrew Hilmer, Dr. Jong-Ho Kim, and Dr. Steven Blake for early training in organic chemistry, and spending many hours with me answering my chemistry-related questions. I want to thank Nigel Reuel and Dr. Sebastian Kruss for forming a very good subgroup, tackling all hydrogel-related engineering issues, and the support and scientific suggestions they have provided in the past several years. I also thank Steven Shimizu, Dr. Joel Abrahamson, Fatih Sen, Selda Sen, Dr. Tom McNicholas and Dr. Bin Mu for many helpful research discussions and friendship.

I thank the collaborators I have outside the Strano lab, including Shangchao Lin from Professor Blankschtein lab, and Professor Blankschtein. Their modeling results significantly enhanced my understanding of some of my experimental results, and I thank them for spending countless hours solving the model together with me, and for all the helpful discussions we had in the past. I thank Dr. Robert Croy, Dr. Deyu Li, from Professor John Essigmann's lab, and Professor Essigmann for training me on radiolabeling measurements and the helpful discussions we had to improve the quality of my work. I thank Laura Trudel from Wogan lab for training me on cell work, and Dr. Nicole Iverson from Essigmann and Wogan lab for answering many biology-related questions.

I thank the stellar undergraduates who have worked with me in the past, including Alina Rwei, Allison Hinckley, Mia Shandell, Zeke Schmois, and Flor De La Cruz. They have made my research progress so much easier and provided a lot of fun to our office life.

I thank my dearest Chinese friends including Dahua Lin, Fei Liang, Jing Chen, Maokai Lin, Yaodong Zhang and Jie Sun for their support and friendship. I especially want to thank Dahua for answering many of my programming-related questions, and we have co-authored many papers together. I thank Darin Bellisario, Sarah Miller, Geraldine Paulus, Dirk Gevers, Steven Shimizu, Jennifer Shimizu, Ardemis Boghossian, and Francois Le Floch-Yin for becoming such close friends over the past years and having enlightened my life outside the Strano lab. I am fortunate to be friends with a group of very supportive, understanding and talented individuals, and I cannot imagine finishing my PhD without them.

I am forever grateful for the love, support from my parents, Zhiyuan Di and Xiaoqun Zhang. Although neither of them have any science background, they have been very supportive of me pursuing my dreams.

Contents

List of Figures

List of Tables

1 Introduction of Carbon Nanotube Fluorescence

1.1 Carbon nanotube Fluorescence and Optical Sensing Mechanism

Single-walled carbon nanotubes (SWCNTs) are cylindrical graphene layers with nanometer-sized diameters. Since the discovery of SWCNT's band gap fluorescence in 2002[10], fluorescence-based imaging and sensing have becoming an emerging field. Figure 1.1 gives the 1D tight binding model on the van Hove singularity of SWCNT's 1D electronic states, where E_{ii} denotes the optical transition energy between i-th valence and conduction bands. Fluorescence is explained as a process where absorption at E_{22} is followed by fluorescence at E_{11}, which usually is in the near-infrared[10].

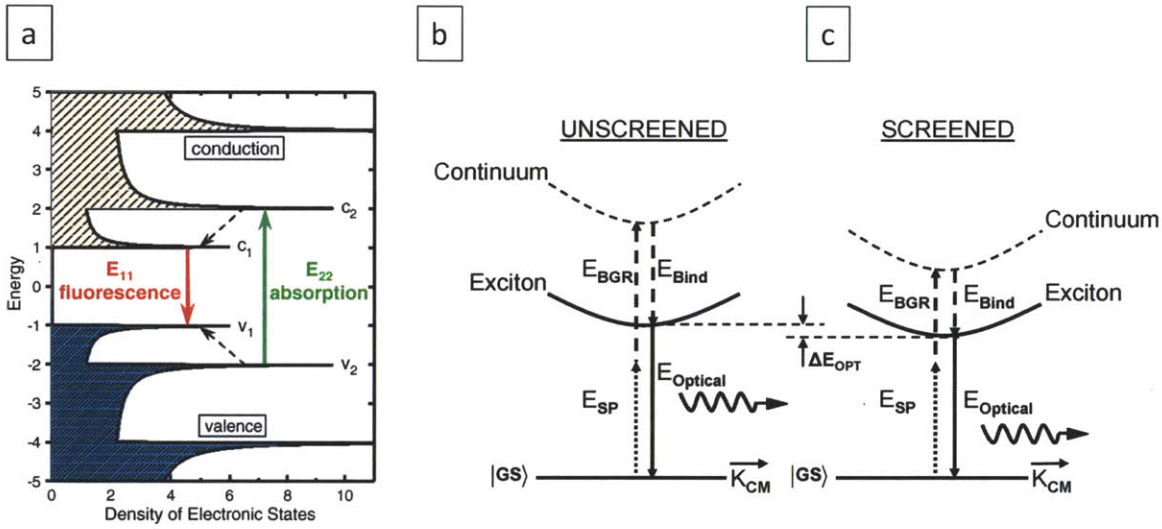

Figure 1.1 Schematic density of electronic states for a single nanotube structure. (a) Solid arrows depict the optical excitation and emission transitions of interest; dashed arrows denote nonradiative relaxation of the electron (in the conduction band) and hole (in the valence band) before emission. (Figure adopted from reference [10], Reprinted with permission from AAAS). (b) and (c) Energy diagrams of the effect of the band gap renormalization and exciton binding energies on the optical transition energy in (b) unscreened and (c) screened environments. (Figures adopted with permission from [11]. Copyright 2007 American Chemical Society)

Although the 1D tight binding model picture is easy to understand, it does not fully reveal the SWCNT photophysics. Semiconducting SWCNTs are excitonic in nature[12, 13]. An exciton is a photo-excited electron-hole pair bound by a Coulomb interaction, and the associated energy, strong exciton binding energy, or E_{Bind}, is more significant in

SWCNT than in other materials, because of the semiconducting property of SWCNT and its 1D structure[14, 15]. Instead of measuring the single particle bandgap, SWCNT fluorescence experiment measures the optical transition energy, or $E_{Optical}$, which is largely tuned by E_{Bind}. As shown in the schematic of Figure 1.1b and Figure 1.1c, $E_{Optical}$ is determined by a combination of single particle band gap, E_{SP}, electron-electron interaction energy, E_{BGR}, and the strong exciton binding energy, E_{Bind}, or, $E_{Opt} = E_{SP} + E_{BGR} - E_{Bind}$. Different local environment affects the dielectric constants, modulating both E_{BGR} and E_{Bind}, varying $E_{Optical}$, which provides one mechanism for SWCNT sensing.

In addition to the aforementioned mechanism through the change in the local dielectric constant, another typical fluorescence modulation mechanism is through a mechanism where redox active molecules either donate or withdraw either ground-state or excited state electrons, enhancing or quenching SWCNT fluorescence[16, 17]. Detailed review can be found in the reference [18].

1.2 Advantages of SWCNT for Optical Sensing in Biological Systems

SWCNT are cylindrical graphene layers with nanometer-sized diameters that emit stable near-infrared (NIR) light with no reported photobleaching threshold[19-21], which allows for prolonged imaging in living cells and tissues[21-25]. Moreover, their one-dimensional electronic structure results in great sensitivity to analytes of interest. Previous work in our laboratory has demonstrated that a synthesized diaminophenyl functionalized dextran polymer enables rapid and direct response of SWCNT to NO[25]. Recently, single-molecule adsorption on the SWCNT sidewall has been resolved through quenching of excitons [26-31], enabling a new generation of optical sensors capable of the ultimate detection limit: single molecules. The recorded fluorescence modulation, supplemented with proper calibration, provides a means for evaluating the concentration

of the quencher molecule, even at low concentrations[24, 25, 29, 30, 32]. Furthermore, compared with small molecule fluorescent probes, non-diffusive SWCNTs allow otherwise impossible quantification of molecules with precise spatial resolution at the nanometer scale. This type of platform has recently demonstrated its capability of studying reactive oxygen species signaling at the single cell level[30].

SWCNT fluorescence exhibits the three essential figures of merit (FOM) necessary for the development of biologically applicable fluorescence-based sensors: quantum yield, photo-stability, and tissue transparency in the SWCNT emission range[23]. The first figure of merit, quantum yield, ϕ, is the number of photons emitted per incident photon absorbed upon excitation [33-36], or

$$\phi = \frac{\text{\# Photons Emitted}}{\text{\# Photons Absorbed}} \quad (1.1)$$

However, since absorption is strongly dependent on wavelength[37], quantum yield will vary according to incident excitation wavelength. Since SWCNT emission contains quantitative information on the immediate environment of the nanotube, measureable quantities are required for the development of sensor applications that rely on analyte binding in the vicinity of the nanotube.

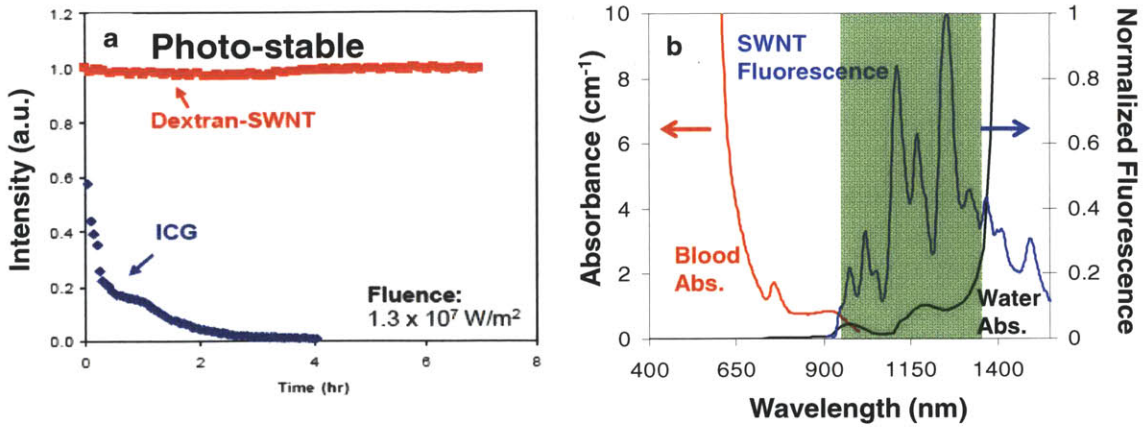

Figure 1.2 Demonstration of SWCNT photo-stability and tissue transparency. (a) Most fluorophores, such as indocyanine green (ICG) undergo rapid photobleaching upon continuous illumination (blue). SWCNT-based emission (red) remain photo-stable even under high fluence (1.3 x 107 W/m^2). (b) SWCNT fluoresces (blue) primarily in the near-infrared regime (820 – 1600 nm^{-1}). Blood (red) and water (black) absorbance primarily occurs in the visible and infrared regimes, respectively. The gap in tissue absorbance, which occurs in the near-infrared regime, ensures minimal tissue interference with SWCNT fluorescence emission. (Adapted from Wray and co-workers [37] with permission from Elsevier).

The second figure of merit, photo-stability, is essential for real-time monitoring of SWCNT fluorescence over extended periods of time. Most organic [38] and nanoparticle [39] fluorophores undergo photobleaching upon continuous illumination (Figure 1.2a). However, even under high fluence ($1.3x10^7$ W/m^2), SWCNTs demonstrate continual stability in their fluorescence emission[21, 37]. The ability to maintain constant fluorescence emission under continuous illumination not only ensures reproducibility in fluorescence measurements, but also alludes to the development of sensors with indefinite lifetimes. A quantitative comparison of the photo-stability and resulting lifetimes of various fluorescing molecules and of SWCNTs is compared assuming a time-dependent signal intensity [23]:

$$I_s = I_0 \phi e^{-2\mu d - k\tau} \quad (1.2)$$

where I_s is the emission florescence intensity, I_0 is the incident excitation intensity, d is the distance in which the sensor is implanted from the surface of the tissue with an absorption coefficient of μ, k is the pseudo-first-order photobleaching rate constant and τ is the exposure lifetime. The results of this rate constant comparison are summarized in Table 1.1, which indicates that SWCNTs are the only fluorophores to date that do not photo-bleach over extended periods of time.

Table 1.1 Comparison of Photobleaching Tendency of Common Organic and Nanoparticle Fluorophores (Table adapted with permission from Reference [23]. Copyright 2005 American Chemical Society)

	Photo-bleaching rate constant	Fluence	Nominal Sensor Lifetime
	hr^{-1}	mW/cm^2	
IR-Dye 78-CA[39]	250.92	600	3.2 s
Cy5[39]	20.52	600	39.1 s
Indocyanine Green[38]	0.0412	28	5.4 h
Type II NIR QD[39]	0.0827	600	2.7 h
SWCNT[21, 23]	0	1.0×10^6	∞

Though the third figure of merit, tissue transparency within the SWCNT emission range, is not necessarily required for the development of a stable and accurate sensor, it is essential for any optical sensor operating *in vivo*. This FOM refers to the condition in which living tissue absorption does not interfere with the excitation and emission wavelengths of SWCNT-based sensors emission [37-41]. It is important to note that though tissue such as blood and skin do absorb light over a limited range of wavelengths, these wavelengths do not overlap with the nanotube excitation and emission wavelengths necessary for optical sensing. As shown in Figure 1.2b, blood absorbance occurs in the

visible range, whereas water absorbance occurs in the infrared. SWCNTs fluoresce in the near-infrared window where there is minimal blood and water absorbance, and is therefore suitable for *in vivo* applications. Assuming a maximum *in vivo* sensing error of 20%, the maximum working lifetime of the sensing device can be approximated as

$$\tau = -\frac{\ln(0.8)}{k} \quad (3)$$

based on the aforementioned photobleaching rate constants, sensor lifetimes can be approximated taking into account the effects of tissue absorption on quantum yield. A comparison of these values as conducted by Barone and co-workers[23] is summarized in

Table 1.2 Comparison of commonly utilized visible and near-Infrared organic and nanoparticle fluorescent probes based on quantum yield (Q. Y.) and absorbance in human whole blood (μ)[23, 37]. (Table adapted with permission from Reference [23]. Copyright 2005 American Chemical Society)

Standards	Q. Y.	Conditions for Q. Y. measurement	excitation	μ (cm^{-1})	μ (cm^{-1})	FOM[a]
	%		nm	oxy	Deoxy	
Cy5	27	PBS	620	2	60	3.20×10^{-28}
Fluorescein	95	0.1 M NaOH, 22°C	496	150	120	5.23×10^{-118}
Rhodamine 6G	95	water	488	200	105	3.30×10^{-133}
Rhodamine B	31	water	514	110	190	1.60×10^{-131}
Indocyanine Green	0.266	water (0.15 g/l)	820	0.96	0.77	4.72×10^{-4}
Indocyanine Green	1.14	blood (0.08 g/l)	830	1.01	0.7788	1.91×10^{-3}
Type II NIR QD	13	PBS	840	1.05	0.778	2.09×10^{-2}
SWCNT	0.1	PBS	1042	0.889	0.12	3.65×10^{-4}

[a] Based on a 1-cm implanted sensor device, an average μ is utilized.

In addition to demonstrating the three necessary FOMs, functionalized SWCNTs in particular also possess many properties that render them ideal as sensor platforms for biological systems, particularly when queried by optical means. For instance, some non-

covalently functionalized polymer-SWNT constructs have proven amenable to biodistribution studies without acute toxicity in mouse models[42, 43]. Although SWCNTs have been shown to inhibit human HEK293 cell growth via apoptosis and decreasing cellular adhesion capabilities[44], recent studies reveal that SWCNT toxicity decreases with increasing sidewall functionalization, with functionalized nanotubes demonstrating substantially less cytotoxic tendencies relative to surfactant-suspended nanotubes[45]. Unlike non-functionalized SWCNTs, SWCNTs that are properly functionalized with chelating molecules such as diethylentriaminepentaacetic (DTPA) demonstrate no retention within the reticuloendothelial organs and are excreted as intact nanotubes[46]. Further studies suggest that functionalized nanotubes do not affect the functional activity of B and T lymphocytes and macrophages upon uptake *in vitro*, thus preserving the functionality of primary immune cells[47]. In addition to demonstrating enhanced biocompatibility and diminished cytotoxicicty, functionalization also imparts SWCNTs with analyte-specific interactions. It has been demonstrated in many examples that the selectivity of SWCNTs for molecules of interest could be imparted from different non-covalently functionalized wrapping molecules, such as proteins or enzymes[24, 48], DNA oligonucleotides[22, 48-50], peptides[51, 52], and synthetic polymers[53]. Thus, the purpose of SWCNT functionalization is two-fold: to enhance biocompatibility and to impart analyte-specific sensing capabilities.

2 Selective Fluorescence Sensor for Nitric Oxide Detection

Some of the work, text and figures presented in this chapter is reprinted or adapted with permission from reference [32].

2.1 Significance of Nitric Oxide Detection

Nitric oxide (NO) is an important cellular signaling molecule[54-56], critical for maintaining vascular physiology[57-60] and regulating immune defense[54, 61]. In addition, its paradoxical roles in carcinogenesis remain unclear, with experimental results suggest both pro- and anti- cancer effects[62-66]. It has been established that there are two fundamental factors complicating the biological effects of NO *in vivo*: its concentration and its location of production[62, 64, 66, 67]. Accurate detection of NO is essential to understanding its diverse biological roles. Difficulties arise mainly due to its rapid diffusivity, and high reactivity with endogenous molecules, including oxygen, exposed thiols, other free radicals, and heme proteins[68-74]. The resultant short life-time and its cellular reaction byproducts affect the accuracy of detection in many cases. Chemical approaches to the detection of nitric oxide or its reaction products have been a constant focus of research in recent years, most of which are on designing and synthesizing organic fluorophores[70, 75-97] or quantum dots[98, 99] that modulate fluorescence upon exposure to NO. Our laboratory has previously demonstrated that single-walled carbon nanotube (SWCNT) wrapped in a diaminophenyl dextran is capable of detecting NO within live murine macrophages[25]. In the present work, we develop an alternate construct based on a specific DNA oligonucleotide that allows selective

detection of NO at the single molecule level, for the first time. This forms a basis for studying NO generation in cellular signaling networks, as we have previously demonstrated for the case of H_2O_2 signaling, initiated by epidermal growth factor receptor (EGFR)[29, 30].

The most extensively used method of NO quantification, the Greiss assay, is robust but indirect, as it only measures the oxidation product of NO, or NO_2^-. Alternatively, NO selective electrodes, electron paramagnetic resonance and chemiluminescence assays may quantify NO directly with high sensitivity, but often lack spatial resolution[69, 70, 76]. Fluorescence-based probes combined with microscopy are particularly useful for resolving spatial and temporal aspects of NO production[70, 75-77]. Many techniques rely on the reaction of a diamino-aromatics with either N_2O_3[78, 79] or NO^+ [80-83], leading to the formation of a highly fluorescent product. A promising recent approach uses a 5-amino-1-naphthonitrile derivative with NO^+ to form a diazo ring that fluoresces in red [84]. Although lacking direct reactivity with NO, these methods represent the state-of-the-art, and are widely applied[75]. In addition, recent work on fluorescent nitric oxide cheletropic traps (FNOCT)[85, 86], and metal-based probes[87-97] that react directly with NO, are also promising approaches. Organic fluorophores are highly sensitive and robust, but also tend to photobleach, limiting their useful lifetime, and often preventing quantitative analysis[21].

Single-walled carbon nanotubes (SWNT) are used ubiquitously as chemical sensors of various types, with fluorescent sensing emerging as a particularly advantageous modality. SWNT are cylindrical graphene layers with nanometer-sized diameters that emit stable near-infrared (NIR) light with no reported photobleaching threshold[19-21],

which allows for prolonged imaging in living cells and tissues[21-25]. Moreover, their one-dimensional electronic structure results in great sensitivity to analytes of interest. Previous work in our laboratory has demonstrated that a synthesized diaminophenyl functionalized dextran polymer enables rapid and direct response of SWNT to NO[25]. Recently, single-molecule adsorption on the SWNT sidewall has been resolved through quenching of excitons [26-31], enabling a new generation of optical sensors capable of the ultimate detection limit: single molecules. The recorded fluorescence modulation, supplemented with proper calibration, provides a means for evaluating the concentration of the quencher molecule, even at low concentrations[24, 25, 29, 30]. Furthermore, compared with small molecule fluorescent probes, non-diffusive SWNTs allow otherwise impossible quantification of molecules with precise spatial resolution at the nanometer scale. This type of platform has recently demonstrated its capability of studying reactive oxygen species signaling at the single cell level[30].

Here we report the first fluorescence-based SWNT sensing array made of single-stranded $d(AT)_{15}$ DNA oligonucleotide-wrapped SWNT (AT_{15}-SWCNT). This 30-base oligomer imparts SWNT with the capability of directly, and selectively, quantifying NO concentrations. We find that the AT_{15}-SWNT complex is unique in its high selectivity toward NO when compared with a library of other DNA sequences and polymers. Each single AT_{15}-SWNT on the array exhibits an intense fluorescence signal at near-infrared wavelengths (900-1400 nm), and records the dynamics of single molecule NO adsorption and desorption on the SWNT through a quantized change in intensity. We develop a generic algorithm based on a *birth-and-death* Markov process to determine the local NO concentration from each SWNT on the array. While we find the experimental, ensemble

detection limit for NO to be 300 nM for the entire array, the ability to detect NO generation locally with nanometer precision enables new enzymatic and cellular assays. This analysis is a significant improvement over approaches reported previously[29] in that information from a single fluorescence intensity trace (a single sensor) can inform the local concentration of the analyte.

2.2 Materials and Experiments

2.2.1 DNA Oligonucleotide, Polymer Nanotube Suspension

SWNTs were suspended with both $d(AT)_{15}$ and $d(GT)_{15}$ oligonucleotides using methods similar to the one published previously[22]. Briefly, HiPCO SWNTs purchased from Unidym were suspended with a 30-base (dAdT) or (dGdT) sequence of ssDNA (Integrated DNA Technologies) in a 2:1 SWNT:DNA mass ratio in 0.1 M NaCl in distilled water. Samples were sonicated with a 3 mm probe tip (Cole-parmer) for 10 minutes at a power of 10 watts, followed by benchtop centrifugation for 180 minutes (Eppendorf Centrifuge 5415D) at 16,100 RCF. Afterwards, the supernatant was collected and the pellet discarded.

For suspension with other polymer materials, SWNTs were first suspended in a 2 wt % sodium cholate (SC) aqueous solution using previously published methods[19, 24]. Briefly, 1 mg/ml Unidym SWNTs were added to 40 ml 2 wt % SC in NanoPure H_2O and were sonicated with a 6 mm probe tip at 40 % amplitude (~12W) for 1 hr in an ice bath. The resulting dark black solution was ultracentrifuged in a SW32 Ti rotor (Beckman Coulter) at 153,700 RCF (max) for 4 hrs to remove unsuspended SWNT aggregates and catalyst particles. The desired polymer for SWNT suspension was then dissolved, at 1

wt %, in the SC-SWNT and the mixture was placed in a 12 – 14 kD MWCO dialysis bag and dialyzed against 2l of 1x Tris buffer (20 mM, pH 7.3) for 24 hours to remove free SC and allow the polymer to self-assemble on the nanotube surface. The dialysis buffer was changed after 4 hrs to ensure SC removal. The resulting suspensions were clear to the eye and were free of SWNT aggregates, indicating successful suspension[100].

2.2.2 NO Solution

NO solution is obtained using a method similar to the one reported previously[25]. Briefly, 3 ml of phosphate buffer saline (PBS, 1x) was contained in a 5 ml round bottom flask and sealed with a septum with two needles inserted providing an inlet and an outlet respectively. After Argon gas (Airgas) was purged for 2 hours to remove dissolved oxygen in the buffer, nitric oxide gas (99.99%, Electronicfluorocarbons) was introduced for 20 min at an outlet pressure of 2 psi. The concentration of NO was measured using horseradish peroxidase assay[81, 101]. Series dilution of NO solution was achieved by mixing concentrated NO solution with PBS buffer (Argon pre-purged for 2 hours) in a pear-shaped flask (Argon pre-purged for 20 minutes). The syringe apparatus was purged with Argon before usage.

2.2.3 Atomic Force Microscopy (AFM) Imaging

In this work, two different types of surface were used for AFM imaging for different purposes. In order to verify that SWNT suspension yields individual SWNT and to estimate the height of the wrapping on the SWNT surface, AT_{15}-SWNT was deposited on an oxygen plasma pre-wetted silicon dioxide surface. In this case, free DNA was removed from AT_{15}-SWNT suspension using spin column (Microspin^{TM}S-400HR

columns, GE Healthcare), and the suspension was diluted to 7.5 mg/l concentration measured using UV-Vis-NIR scanning spectrophotometer (UV-3101 PC Shimadzu). The concentration of SWNT was determined using absorbance at 632 nm with ε = 0.036 $(mg/l)^{-1}cm^{-1}$. Oxygen plasma (Harrick Plasma) was applied to enhance the hydrophilicity of the silicon dioxide surface, assisting DNA-SWNT adsorption on the surface. The sample was then spin-coated to the silicon dioxide surface (LaureII Technology Corporation, model WS-650MZ-23NPP/LITE) for 1 min with ramp speed of 500 RPM and final speed of 2500 RPM. The resultant AFM images are shown in Figure 2.1 and Figure 2.2.

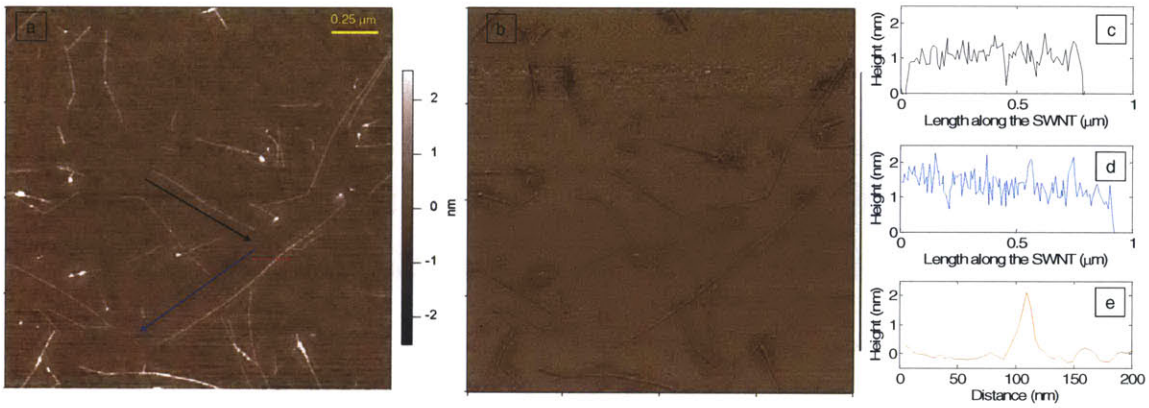

Figure 2.1 Atomic Force Microscopy (AFM) image of AT_{15}-SWNT, along with section and height analysis. (**a-b**) Typical AFM (tapping mode) images (height, **a**; phase, **b**) of AT_{15}-SWNT deposited on an oxygen plasma pre-wetted, silicon dioxide surface. (**c-e**) Height profile of the AT_{15}-SWNT along the length of the nanotube with arrows in the original AFM image (**a**) indicating the direction of the profiling (black arrow, **c**; blue arrow, **d**). The bands reach about 0.5 - 1 nm from the surface of the SWNT. (**e**) Height profile from left to right along the dotted red line in image (**a**).

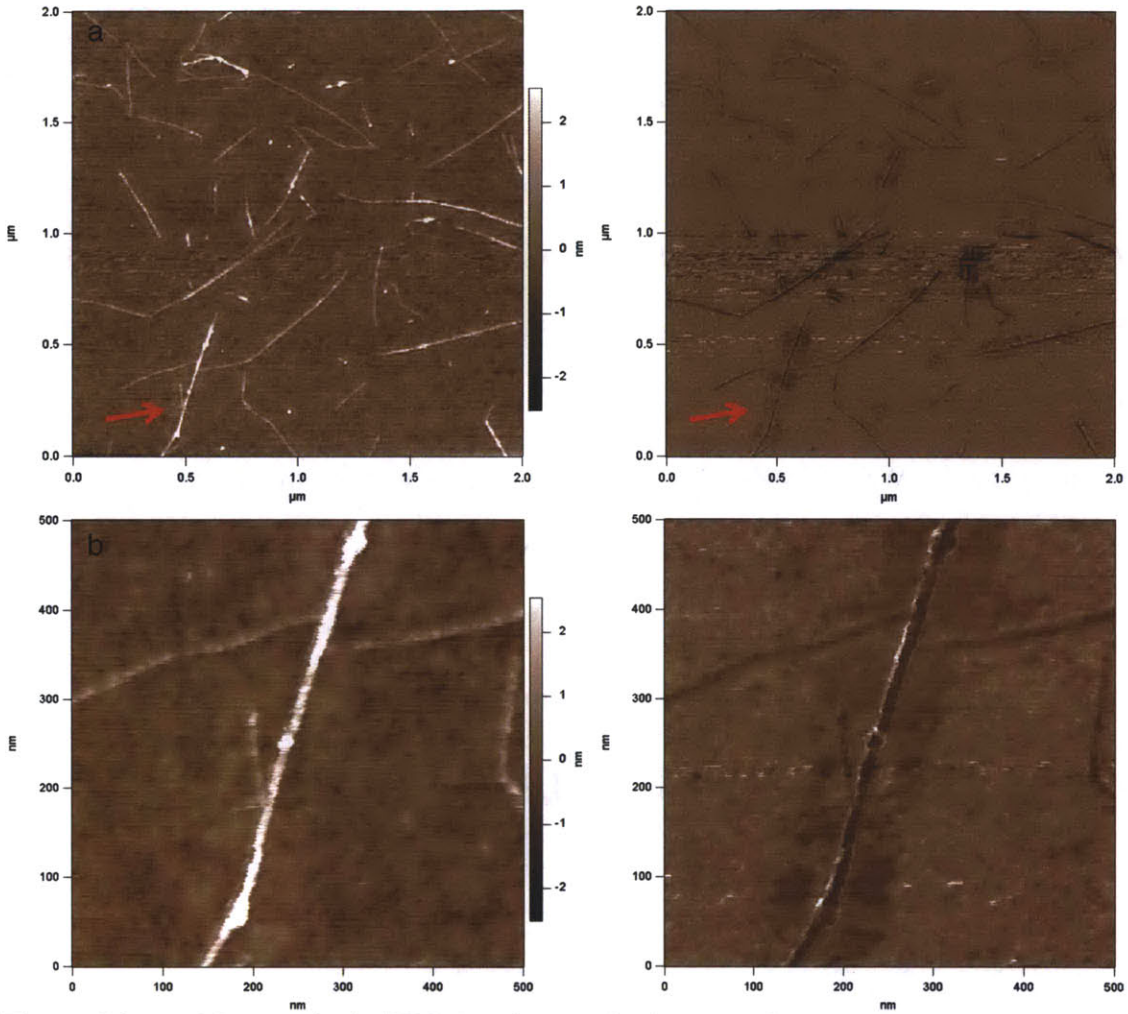

Figure 2.2 More typical AFM (tapping mode) images of AT_{15}-SWNT deposited on the oxygen plasma pre-wetted silicon dioxide surface. (**a**) Height (left) and phase (right) image of another scanning position on the same sample with scan size of 2 μm. (**b**) Height (left) and phase (right) image of the SWNT indicated by the red arrow in b) with scan size of 0.5 μm.

In order to verify that SWNT is individually deposited on a solid substrate, AFM images (Figure 2.3) were taken with SWNT samples that were deposited on silicon dioxide surface pre-treated with 3-aminopropyltriethoxysilane (APTES). For sample preparation, the same procedure was used as in the sample required for fluorescence detection, except that the silicon dioxide surface was used for depositing instead of the

glass slide, in order to obtain a smoother surface for AFM imaging. All the AFM images were taken using Asylum Tapping/AC mode soft tips (AC240TS).

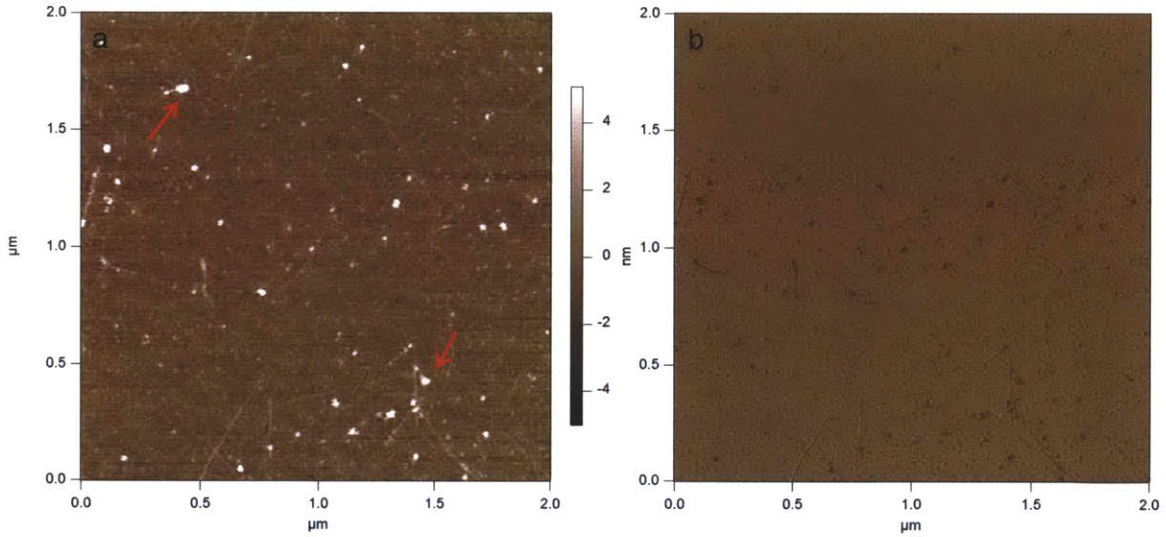

Figure 2.3 Height (**a**) and phase (**b**) AFM images (tapping mode) of AT_{15}-SWNT deposited on APTES pre-treated silicon dioxide surface. White dots indicated by red arrows were insoluble APTES from the sample.

2.2.4 Measurement of SWNT Photoluminescence (PL); Setup for High Throughput Screening Assay

All polymer wrapped SWNT solutions were diluted to a final SWNT concentration of 2 mg/l. The following analytes were initially dissolved in DMSO, including ATP, cAMP, creatinine, D-aspartic acid, glycine, L-citrulline, L-histidine, quinine and sodium pyruvate; all other analytes dissolved in 1x Tris. Analyte solutions were added to the SWNT, such that the final DMSO concentration was 1 vol %, the mixture was incubated for 1 hr and the resulting SWNT PL was measured with a home-built near infrared (nIR) fluorescence microscope. Fluorescence measurement upon exposure NO was measured using previously published methods[25]. The high-throughput screening setup is shown in Figure 2.4. Briefly, a Zeiss AxioVision inverted microscope was coupled to a Princeton Instruments InGaAs OMA V array detector through a PI Acton SP2500 spectrometer.

Sample excitation was from a 785 nm photodiode laser, 450 mW at the source and 150 mW at the sample.

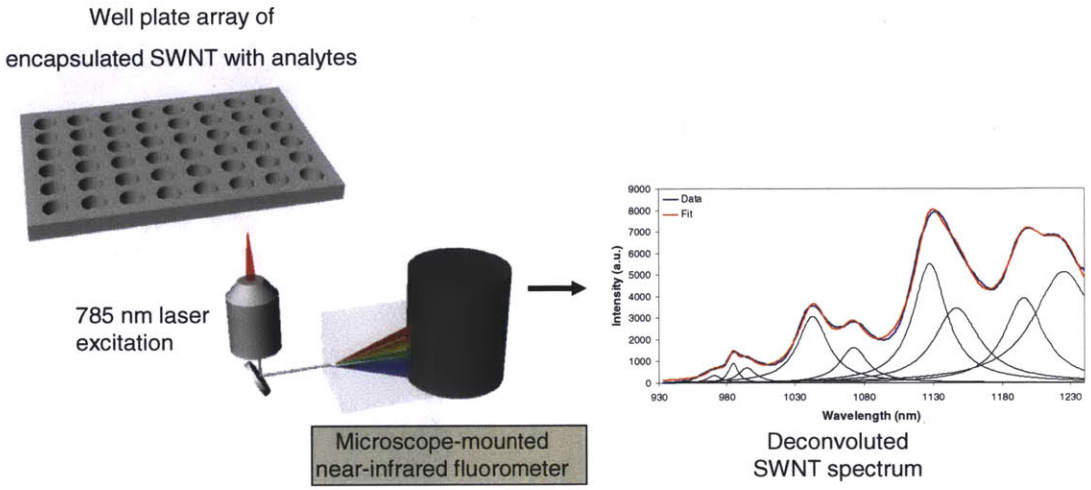

Figure 2.4 Setup for high throughput screening assay and data analysis. Polymer and DNA oligonucleotides of various sequences were used to suspend SWNTs and screened against a custom-designed analyte tray with 36 biologically relevant common molecules. SWNT PL was measured using a home-built near-infrared fluorescence microscope, excited at 785 nm. Fluorescence peak center and intensity of each nanotube species were obtained through spectral deconvolution.

2.2.5 Deconvolution of SWNT Photoluminescence Spectra

The fluorescence spectra were fitted using a sum of $N = 9$ Lorentzian lineshapes (8 nanotube peaks and 1 G-prime peak). The fluorescence intensity at any energy, E, is a sum over the contributions of all the species present in solution:

$$I(E) = \sum_{i=1}^{N} \frac{C_i}{2\pi} \frac{\Gamma_i}{\left(E - E_{0,i}\right)^2 + \Gamma_i^2/4}$$

The parameters to be estimated for the Lorentzian profile of the i^{th} entity have been outlined below.

C_i – area under the peak

Γ_i – full width at half maximum (FWHM, meV)

$E_{0,i}$ – peak center in terms of energy (meV)

Initial guesses for the peak areas were calculated from the control spectrum. The area under the i^{th} peak was expressed as a fraction of the total area under the spectrum. This fraction was determined from the intensity of the investigated peak. The initial guesses for the FWHM of different nanotubes were obtained either from 2D excitation-emission profile similar to reported[10] or scaled according to their diameters[102] to ensure a good fit. The FWHM and peak center for the G-prime peak were kept constant (11 meV and 1258.72 meV respectively) and only its peak area was floated. In all, 31 parameters were used to fit a single fluorescence spectrum. Each Γ_i ($E_{0,i}$) was constrained within a 10 meV (50 meV) window to maintain the physical validity of the fit. For responses such that the degree of quenching is over 50% the shifting response is set to zero due to the difficulty in distinguishing between actual shifting and relative intensity change of different species.

2.2.6 Screening of AT_{15}-SWNT against Other 9 Reactive Oxygen and Nitrogen species

Sodium peroxynitrite and Angeli's salt was purchased from Cayman Chemical, and other chemicals in this experiment was purchased from Sigma. Stock solution of NO_2^-, NO_3^-, H_2O_2 and ClO^- were prepared by dissolving them in water at 6 mM; $ONOO^-$ and Angeli's salt were first dissolved at 6 mM in solutions of 0.3 M of NaOH and 0.01 M NaOH respectively. O_2^- was prepared following procedure in the literature. [103] Briefly, an excess amount of KO_2 was added to DMSO, and the mixture was vortexed followed by centrifugation to remove the pellet. The resultant supernatant yields a stock solution

of 3.6 mM O_2^-. Analyte solutions were added to the SWNT (2 mg/l in 50 mM PBS, pH = 7,.4), such that the final concentration was 60 μM. The response was monitored for 10 min after addition. Hydroxyl radical was generated using Fenton's reaction, where H_2O_2 and $FeSO_4$ (60/0.6, 300/3 and 1000/10 μM as final concentration) were added into the SWNT solution, and the reaction was monitored for 10 min and after 12 hours after addition of the reagents. Rose bengal was used to generate singlet oxygen using a similar procedure as described previously[30, 104]. Briefly, the solution of AT_{15}-SWNT (2 mg/l) was exposed to 60 μM of rose bengal, and excited at 560 nm to generate singlet oxygen. The SWNT fluorescence response was recorded by quickly switching the excitation source at the end of every minute to a 785 nm laser (same as described in Section 2.4) for 3 seconds. Repeating this cycle, the response was monitored for 10 minutes, at the end which, the 560 nm-excitation source was turned off, and three additional spectra excited using 785 nm were taken every minute.

2.2.7 Microscopy and Data Collection for Single Molecule NO Detection

AT_{15}-SWNTs were deposited onto a petri dish pre-treated with APTES (Figure 2.5) substrate, and three times of washing removed suspended SWNT as well as free DNA in the sample. The electrostatic interaction between AT_{15}-SWNT and APTES is enough to keep the construct stable at physiological pH. The microscopy technique is similar to that reported in the literature[29] (Figure 2.5). Briefly, samples were excited by a 658 nm laser (LDM-OPT-A6-13, Newport Corp) at 33.8 mW. The fluorescence of AT_{15}-SWNT was imaged and monitored in real time through a 100x TIRF objective for hours using an inverted microscope (Carl Zeiss, Axiovert 200), with a 2D InGaAs array (Princeton

Instruments OMA 2D) attached. Movies were acquired at 0.2 s/frame using the WinSpec data acquisition program (Princeton Instruments). Before the actual experiment, a control movie (same movie length as the experiment movie) was taken to ensure a stable baseline. In the experiment, nitric oxide in PBS (1x, pH 7.4) buffer was injected through a fine hole, allowing minimal exposure to air.

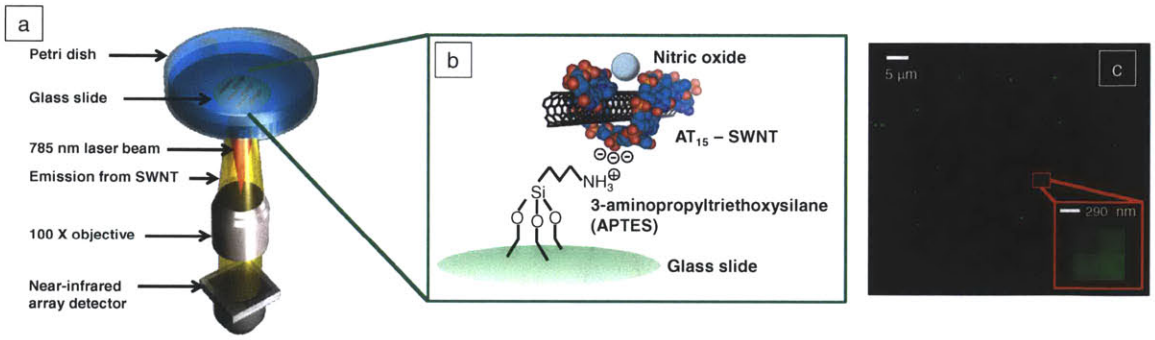

Figure 2.5 Fluorescence-based SWNT array capable of detecting NO. (**a**) Schematic of the microscope setup. A 658 nm laser beam (red) excites at the SWNT array deposited on the glass-bottomed petri dish. The emission light (yellow) is collected by a near-infrared array detector through a 100x TIRF objective mounted on a inverted microscope. (**b**) Schematic of the SWNT array: individual AT_{15}-SWNT complexes are deposited on the petri dish, which is pre-treated by 3-aminopropyltriethoxysilane (APTES), through electrostatic interaction. (**c**) A representative near-infrared fluorescence image of the individual AT_{15}-SWNT deposited on the glass bottomed petri dish. The inset shows a near-infrared fluorescence image of a 2x2 pixel, diffraction-limited spot representing the fluorescence of an individual SWNT on the glass slide. The laser power at the sample is 33.8 mW.

2.3 Results and Discussions

2.3.1 Nitric Oxide Selective PL Quenching of $d(AT)_{15}$ DNA-wrapped SWNT

Individual suspension of SWNT encapsulated in $d(AT)_{15}$ DNA (AT_{15}-SWNT) is confirmed by AFM (Figure 2.1 and 2.2). As depicted in the molecular model of Figure 2.6a and 2.6b, it is generally accepted that the nucleobases of the DNA stack on the sidewall of the SWNT, while the sugar-phosphate backbone extends away from the surface. This is consistent with both experimental evidence including AFM[105, 106] and optical absorption data[107], as well as molecular dynamics simulations[6, 108-111]

reported to date. Through $\pi-\pi$ stacking of the bases on the sidewall of the SWNT, the phosphate backbone of the DNA is exposed to water, allowing SWNT to remain colloidally stable.

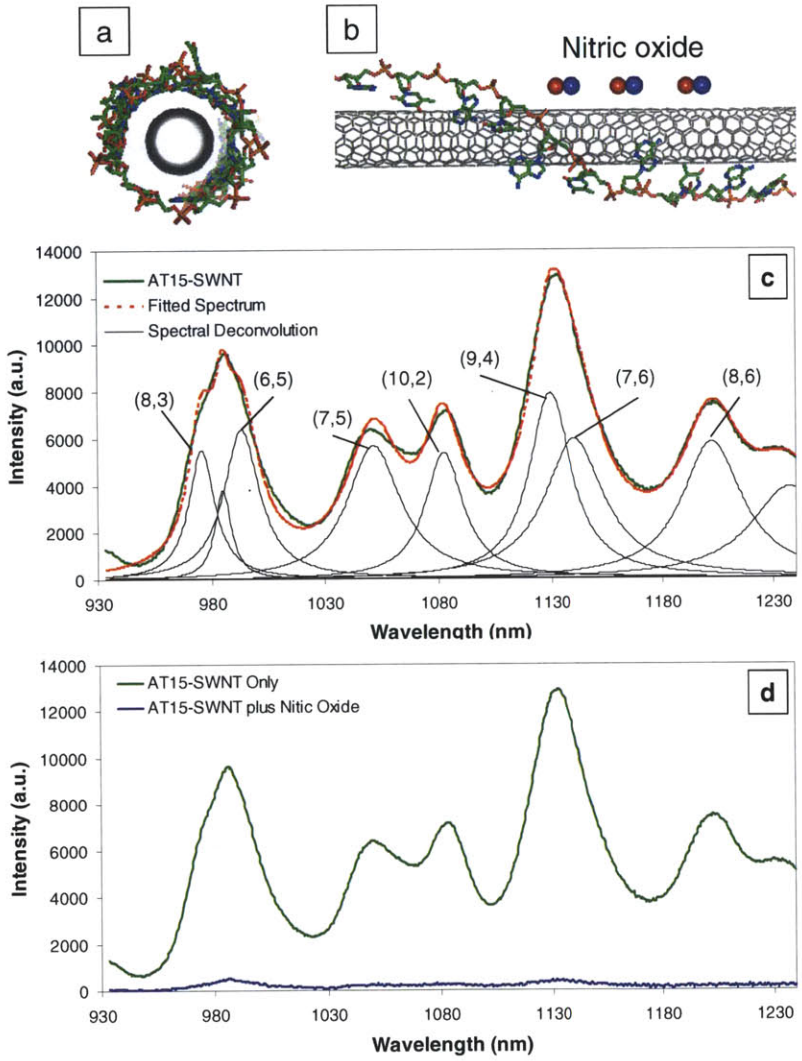

Figure 2.6 The optical response of $d(AT)_{15}$ DNA oligonucleotide wrapped SWNT (AT_{15}-SWNT) upon exposure to NO. (**a**) and (**b**) Front and side schematic views of one of the several binding structures of AT_{15}-SWNT simulated from a HyperChem simulation package. Bases of the DNA stack on the sidewall of the SWNT, and the sugar-phosphate backbone extends away from the surface. (**c**) The nIR fluorescence spectrum (solid green) of AT_{15}-SWNT recorded with a 50x objective upon 785 nm laser excitation (150 mW at the sample). The spectral deconvolution reveals 7 nanotube species and a Raman peak (solid black), with the sum of these contributions (dotted red) matching the profile of the actual data. (**d**) Complete quenching (solid blue) of AT_{15}-SWNT fluorescence is observed when the SWNT sample is exposed to NO (60 μM, in 1x PBS).

We utilized a custom-designed near-infrared SWNT fluorescence imaging microscope and spectrometer to characterize emission (Figure 2.4). Upon 785 nm laser

excitation, near-infrared (nIR) emission of AT_{15}-SWNT can be captured by a 1D InGaAs spectrometer (Figure 2.6c,d). In order to determine the SWNT species present in the SWNT suspension, a 2D excitation-emission profile was taken as described previously[10] (Figure 2.7). By using this plot to identify the emission peak center of each SWNT species, the corresponding 1D fluorescence spectrum can be deconvoluted into individual species contributions (Figure 2.6c).

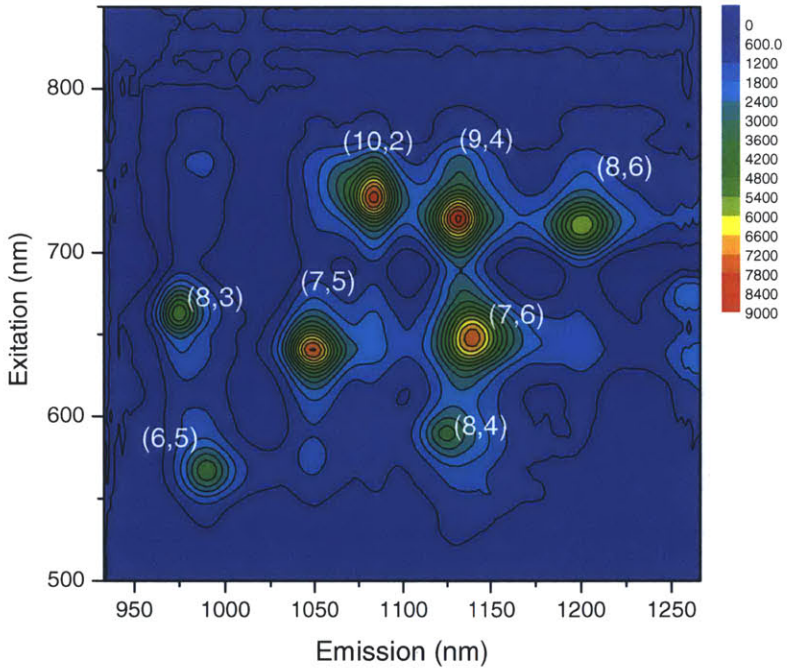

Figure 2.7 Contour plot of fluorescence intensity versus excitation and emission wavelengths for AT15-SWNT and nanotube assignment.

Table 2.1 Concentration of analytes listed in the high-throughput screening assay.

Analyte	Concentration mM	Analyte	Concentration mM
17-α-Estradiol	0.10	L-Ascorbic acid	0.50
2,4-Dinitrophenol	0.48	L-Citrulline	0.11
Acetylcholine chloride	0.54	L-Histidine	0.10
α-Tocopherol	0.51	L-Thyroxine	0.10
Adenosine	0.51	Melatonin	0.49
ATP	0.11	NADH	0.51
cAMP	0.10	Nitric oxide	0.06
Creatinine	0.10	Quinine	0.01
Cytidine	0.48	Riboflavin	0.10
D-Aspartic acid	0.02	Salicylic acid	0.49
D-Fructose	10.80	Serotonin	0.11
D-Galactose	5.00	Sodium azide	0.51
D-Glucose	10.90	Sodium pyruvate	0.50
D-Mannose	10.30	Sucrose	0.10
Dopamine	0.49	Thymidine	0.52
Glycine	0.50	Tryptophan	0.25
Guanosine	0.51	Tyramine	0.49
Histamine	0.51	Urea	0.49

We find that the DNA sequence in AT_{15}-SWNT is unique in its ability to allow selective quenching from primarily NO when compared with a large panel of potentially interfering species. Upon exposure to nitric oxide (60 μM, in 1x PBS), the fluorescence of all observed SWNT species is completely quenched (Figure 2.6d). We designed an automated, high-throughput screening assay whereby fluorescence modulation of DNA oligonucleotides, peptides, and other synthesized polymer-encapsulated SWNT is monitored upon exposure to 36 biological molecules (Table 2.1). These molecules serve to fingerprint and probe differences in the response of distinct polymer-SWNT complexes. We conclude from this screening that NO exclusively quenches this complex, with essentially no response from other analyte species in the library (Figure 2.8). This is in marked contrast to what is seen for an electrostatically neutral polymer, polyvinyl alcohol (PVA-SWNT), whose fluorescence is not affected by NO (Figure 2.8d). Note

that this is in spite of the fact that concentrations of the majority of library species (~500 μM) are higher than that of NO (60 μM) in the screening, while others are constrained by their solubility. Removing free DNA from the SWCNT suspension has little effect on the selectivity (Figure 2.9). We conclude that the wrapping polymer is responsible for the observed selectivity. For instance, $d(GT)_{15}$ differs from $d(AT)_{15}$ by a replacement of one base type, but its response is very different, with quenching from dopamine, histamine, L-ascorbic acid, melatonin, NADH and riboflavin (Figure 2.8b). Other $d(AT)_{15}$ variants including $d(AAAAT)_6$, $d(AAATT)_6$, $d(AAT)_{10}$, $d(ATT)_{10}$, $d(AAAT)_7$, $d(AATTT)_6$, $d(AATT)_7$ show response profiles similar to $d(AAT)_{10}$ (Figure 2.8c), where additional molecules besides NO also greatly modulate SWNT fluorescence. Fluorescence spectra of SWNT suspended in those DNA strands are shown in Figure 2.10. Of all AT variants studied, AT_{15}-SWCNT appears to be the only DNA-SWCNT complex that shows a selective response toward NO over riboflavin (Figure 2.8e). In fact, such a selective response of SWNT imparted by an adsorbed DNA molecule has been reported previously. For instance, it has been shown that certain DNA sequences attached to SWNT can recognize specific odor molecules through a change in electronic resistance[112-114]. Moreover, while PVA-SWNT shows a quenching response to dopamine, similar to a typical DNA response profile, its fluorescence is enhanced when exposed to reducing agents including NADH, L-ascorbic acid and melatonin, which is in contrast to the DNA-SWNT response profile.

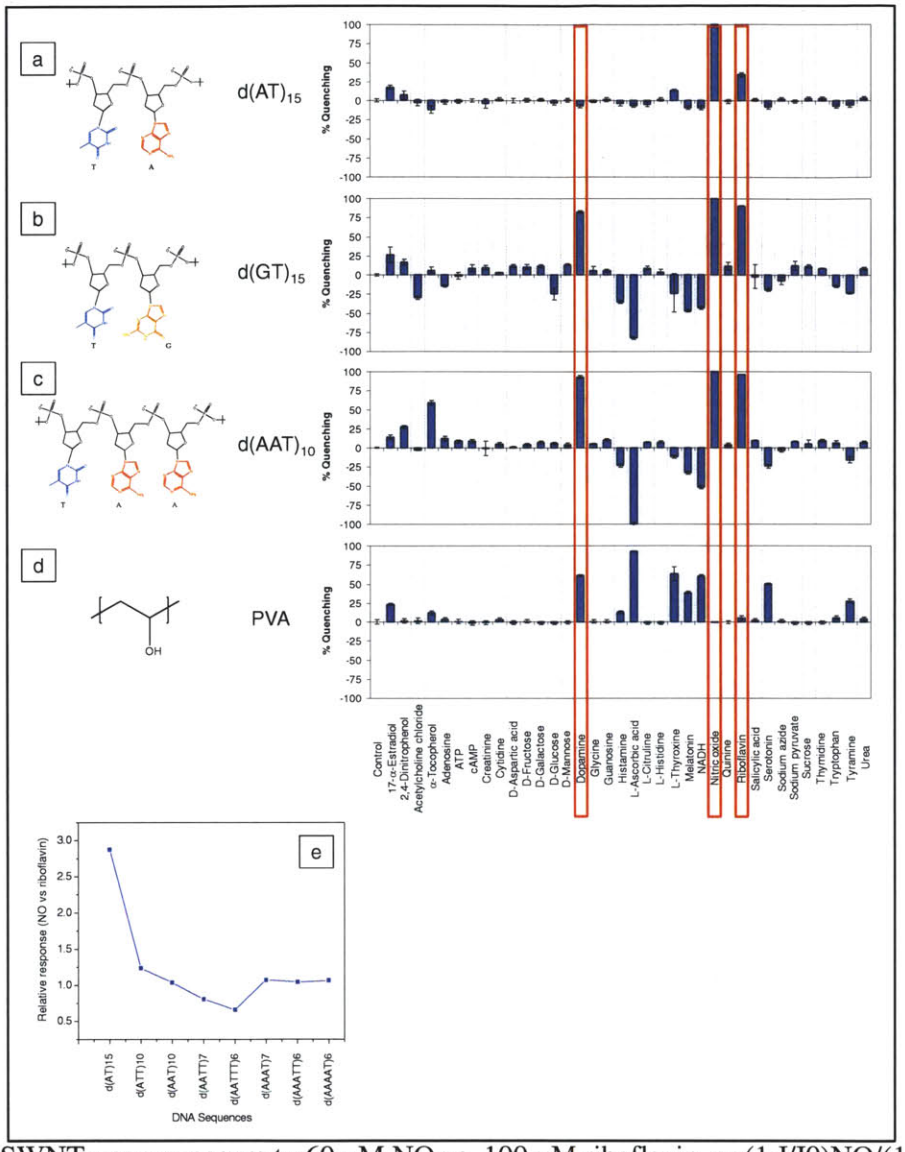

Figure 2.8 Selective NO response of AT15-SWCNT and high throughput screening of polymer-SWCNT complexes. Bar charts represent the percentage of quenching (1-I/I0) of the (7,5) nanotube species when wrapped in four different polymers: d(AT)15 DNA (a), d(GT)15 DNA (b), d(AAT)10 DNA (c), and polyvinyl alcohol (PVA, d) upon exposure to the 36 analytes. Red boxes highlight the responses of the four types of polymer-SWNT complexes to dopamine, riboflavin and NO. (e) Relative quenching response of DNA encapsulated (7,5) SWNT upon exposure to 60 μM NO vs. 100 μM riboflavin, or (1-I/I0)NO/(1-I/I0)riboflavin.

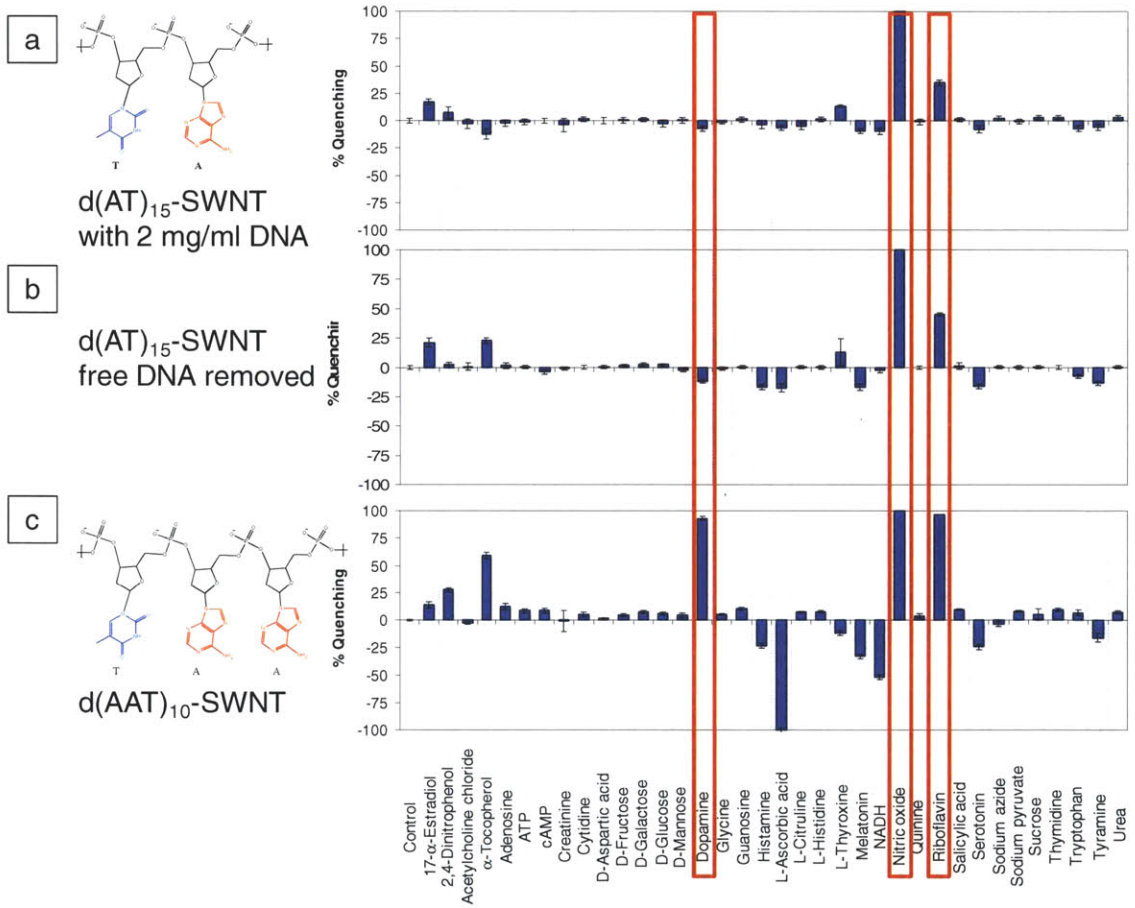

Figure 2.9 Comparison of selectivity of AT_{15}-SWNT containing and without free DNA. Bar charts represent the percentage of quenching ($1-I/I_0$) of the (7,5) nanotube species when wrapped in: AT_{15}-SWCNT containing free DNA (**b**), AT_{15}-SWCNT without free DNA (**c**) and AAT_{10}-SWCNT (**c**) upon exposure to the 36 analytes. Red boxes highlight the responses of the polymer-SWNT complexes to dopamine, riboflavin and NO.

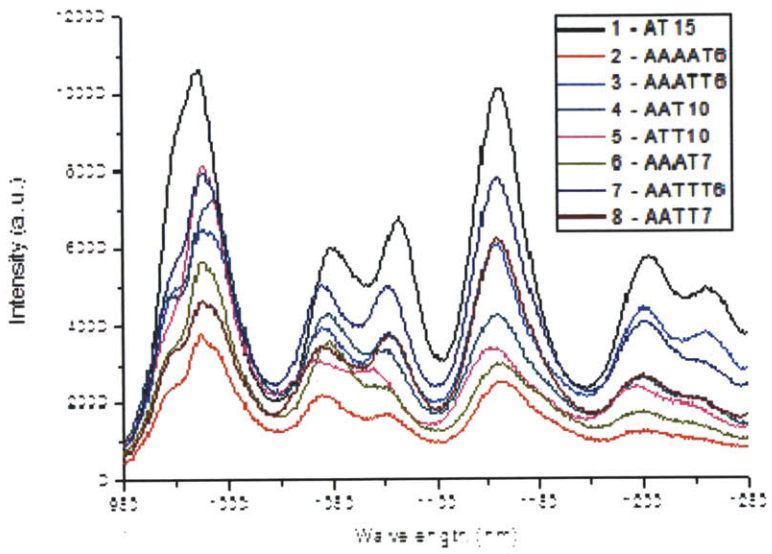

Figure 2.10 Fluorescence intensity comparison among SWNT (2mg/l) suspended in 8 DNA sequences. Laser power is 150 mW at the sample.

We attribute the selectivity of $d(AT)_{15}$-SWCNT to potentially three distinct components: redox selectivity, non-radiative energy loss, and steric hindrance. Addressing the first, we note that most of the responses shown in Figure 2.8 are the results of interaction between redox-active molecules and polymer-SWCNT complexes. For instance, the LUMO levels of NO (-0.5 V)[115] and riboflavin (-0.318 V)[116] are close to the conduction bands of the SWNT species utilized in this work[117]. Therefore, it is plausible that they cause fluorescence decrease through excited-state electron quenching[17]. Moreover, the fluorescence enhancements caused by reducing agents including NADH, L-ascorbic acid and melatonin on DNA-SWCNT are likely because NADH reduces the DNA wrapping whose LUMO band is below the Fermi level of semiconducting SWNTs[118], resulting in a recovery of photoluminescence that is pre-quenched by DNA[17]. More specifically, HOMO electrons of NADH can compete with SWNT excited state electrons for the vacancies at the LUMO level of DNA, inhibiting

SWNT excitons from quenching (Figure 2.11a). We also noticed that DNA-SWCNT fluorescence enhancement after NADH addition is weakened as the energy gap between conduction band of SWNT and LUMO of DNA molecule decreases, or generally as the diameter of the SWNT increases (Figure 2.11e), supporting the fluorescence enhancing mechanism we proposed. In contrast, the mechanism of PVA-SWNT fluorescence quenching caused by reducing agents has not been extensively studied, although others have reported similar observations[119]. We hypothesize that NADH and other reducing agents donate electrons directly to the conduction bands of PVA-SWNT, and extra electrons in the conduction bands can then quench excitons through a non-radiative Auger recombination[120, 121] (Figure 2.11b). An attempt to assign the absolute values of oxidation potential measured of NADH (0.282 V)[122], melatonin (0.95 V)[123] and L-ascorbic acid (0.74 V)[124] in the SWNT potential scale[16, 119, 125, 126] results in the potential levels of those molecules lying below the conduction bands and above the valence bands of SWNT, and we therefore expect to see an increase in electron density in the SWNT valence bands upon addition of those analytes. However, upon exposure to the analytes, experimentally measured absorption spectra of both PVA-SWCNT and DNA-SWCNT remain invariant (Figure 2.12). This inconsistency may reflect the fact that reported oxidation potentials are measured through voltammetry where complete electron transfer and the formation of new adducts are involved, whereas electron transfer between SWCNT and the cited molecules appears reversible, suggesting a weaker, electron-sharing mechanism between the SWCNT surface and the adsorbates. Hence, we only considered the relative oxidation potentials of those molecules, and constructed a

potential plot that summarizes redox level of the SWNT, encapsulating polymer, and the interfering molecules (Figure 2.11c).

Redox potentials cannot alone account for selectivity, however. Counter-intuitively, dopamine appears to quench all polymer-SWNT complexes except AT_{15}-SWNT, although its HOMO level is between NADH and L-ascorbic acid. We consider that dopamine may behave as a defect site on the SWNT, which form an non-radiative energy 'sink' of excitons, causing fluorescence quenching[127]. Because the size of dopamine (Figure 2.11d) is small compared to the anticipated gaps in the DNA adsorbed phase, and the aromatic ring structure can π- π stack on the SWNT surface, this hypothesis is plausible. A polymer that prohibits direct adsorption of dopamine to the SWNT surface, for example, can eliminate this response.

a PL enhancing mechanism:
Reducing agents reverse excited state quenching caused by wrapping molecule, increasing transitions from excitons to photons.

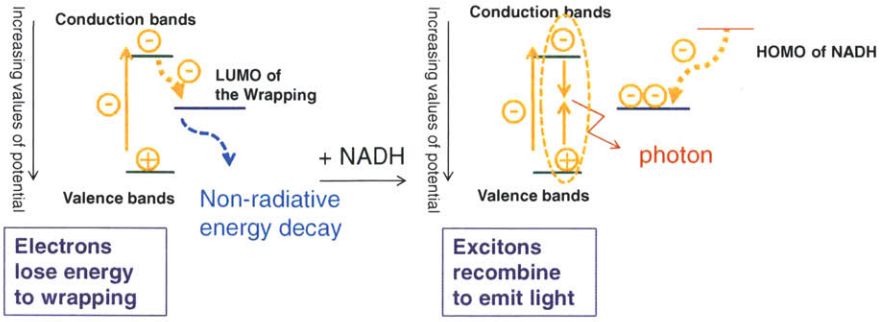

b PL quenching mechanism:
Reducing agents fill electrons in conduction bands, quench excitons through nonradiative recombination.

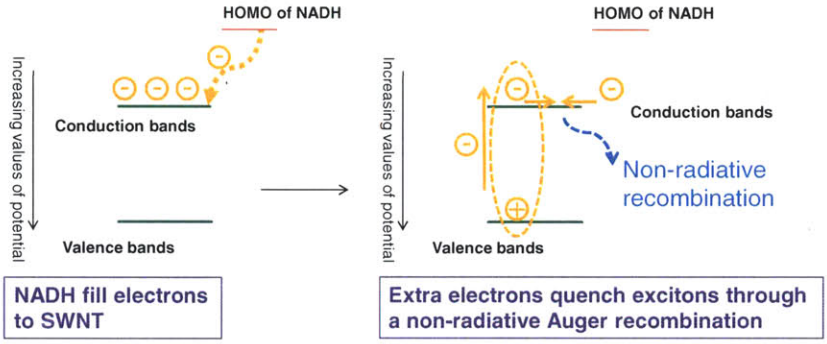

c Redox levels of reducing molecules and SWNT

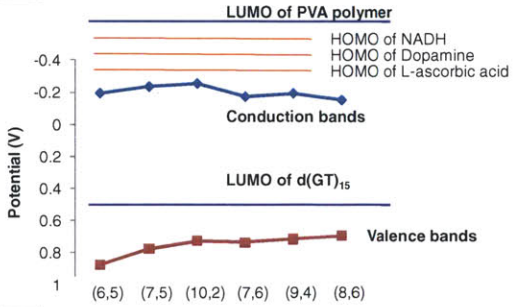

d

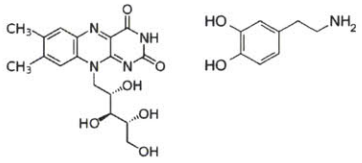

e

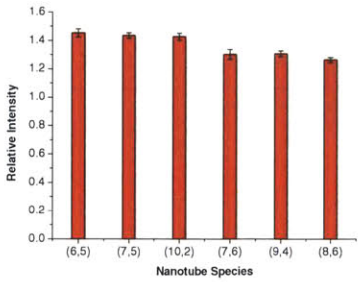

Figure 2.11 Illustration of the contribution of redox interactions to the selectivity of the polymer-SWNT complexes. (a) A plausible mechanism for SWNT fluorescence enhancement. In this process, polymers adsorbed on the SWNT surface initially act as exciton quenchers, since excited electrons decay to the LUMO level of the polymer wrapping. When NADH is added to the solution, it donates electrons to the polymer LUMO level, thereby preventing exciton decay. This results in a subsequent enhancement of the SWNT photoluminescence. (b) A plausible quenching mechanism. NADH and other reducing agents donate electrons directly to the conduction bands of polymer-SWNT, and extra electrons in the conduction bands quench excitons through a non-radiative Auger recombination. (c) Potential levels of SWNT, wrapping polymers, and redox-active molecules. Potentials of SWNT conduction and valence bands are obtained from reference [16, 119, 125, 126], and DNA doping levels are estimated from reference [118]. The HOMO levels of NADH, dopamine, l-ascorbic acid are plotted relative to the potential of the SWNT. (d) Molecular structure of riboflavin and dopamine. (e) Relative intensity (I/I0) of GT15-SWNT exposed to NADH compared to the control where no analytes were added, as a function of SWNT species.

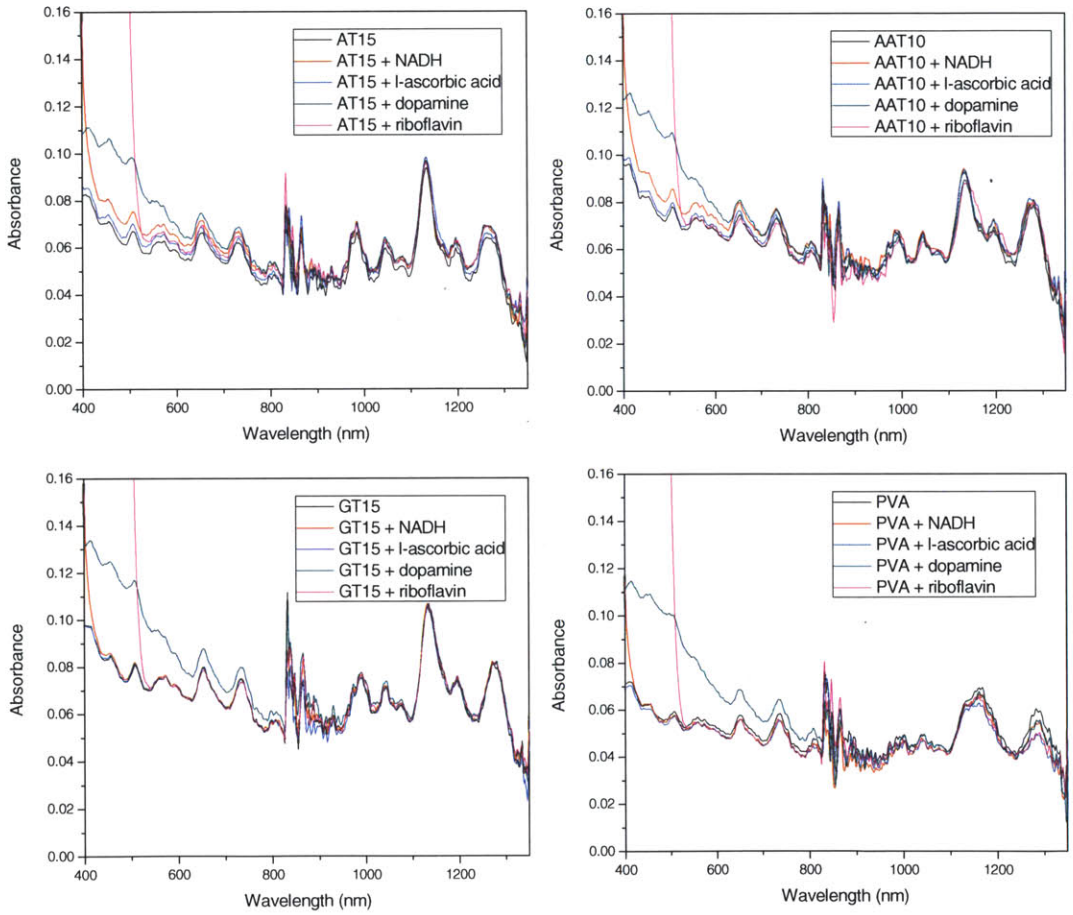

Figure 2.12 Absorption spectra of AT_{15}, GT_{15}, AAT_{10} and PVA suspended SNWT upon 1 hour exposure to NADH, L-ascorbic acid, dopamine, and riboflavin. Concentration of SWNT is maintained at 2 mg/l in the buffer. Noise at 380 nm results from fast scanning which is the only solution in order to synchronize all measurements after 1 hour exposing the SWNT solution to the analytes. Absorption of dopamine, riboflavin and NADH at low wavelength cause the sloping base line at 400-500 nm (riboflavin and NADH) and 400 - 800 nm (dopamine).

All redox related responses discussed above appear to be attenuated in the case of AT_{15}-SWNT. We suspect that the sequence adopts a conformation on the nanotube surface that results in steric exclusion of most analytes except nitric oxide. This can be the case if $d(AT)_{15}$ forms closely spaced bands along the circumference of the tube, thereby blocking the adsorption of molecules greater in size than NO. Sequence-dependent variability in DNA adsorption configuration is not unusual, and is likely to be one of the factors involved in utilizing DNA sequences to separate carbon nanotube by chirality[7, 105]. In our work, AFM micrographs of AT_{15}-SWNT (Figure 2.1) suggest AT_{15} wraps SWNT uniformly with heights between 0.5-1 nm above the surface of SWNT, although we were unable to resolve regular helical patterns that have been observed previously for other sequences[105, 106]. Currently, we are not able to prove directly that $d(AT)_{15}$ forms more closely spaced bands on SWNT compared to other AT variants or DNA sequences. However, the concept of a sequence or structure induced steric selectivity is also indirectly supported by the fact that AT_{15}-SWNT and PVA-SWNT show deviations from the typical quenching pattern observed with other sequences. In particular, dopamine and riboflavin fail to cause quenching in the cases of AT_{15}-SWNT and PVA-SWNT, respectively. The relative sizes of these molecules (approximately 9x9x3 Å for dopamine and 10x12x4 Å for riboflavin, Figure 2.11d) mean that a void in the adsorbed phase of at least 1 nm needs to form in order to have direct energy transfer

from the SWNT to the molecule. The unadsorbed portion of the wrapping molecule then interacts with the adsorbed phase creating the binding site, and both of these factors can allow for steric selectivity.

The case of NO adsorption on PVA-SWNT is unusual. Because of its small size, NO tends to quench nearly every complex we have tested to date. However, for PVA-SWNT, there is no response. It is possible that NO reacts directly with the PVA itself, via exposed hydroxyl groups, for example. However, this would not itself explain the lack of response, since quenching would be apparent as soon as these sites were saturated. Another possibility may involve a subsequent pore blocking due to the formation of organo-nitrite after reaction with NO[128]. This potential mechanism is a topic for future work. Regardless of mechanism, the obvious selectivity demonstrated in this case, and the above examples, clearly indicate that the polymer adsorbed phase on SWNT strongly influences the apparent selectivity of the complex, and this has significant implications for all sensor applications of carbon nanotubes.

2.3.2 Selectivity of AT_{15}-SWNT Against Other Reactive Oxygen and Nitrogen species

To examine the biological relevance of this platform, the responses of AT_{15}-SWNT were screened against nine reactive oxygen (ROS) and nitrogen species (RNS). Once exposed to 60 μM of each analyte, the SWNT show little or no response to NO_2^-, NO_3^-, HNO, H_2O_2, OH·(hydroxyl radical), O_2^- (superoxide), and ClO^-, but quenching to peroxynitrite ($ONOO^-$) and singlet oxygen ($^1O_2$) (Figure 2.13). However, interference from peroxynitrite and singlet oxygen with the sensor is expected to be minimal, if any,

for the applications that we wish to pursue. The reported half-life of NO in a biological system is in the order of seconds [129, 130], and the main contribution of its short-lived lifetime is its reactivity with haemoglobin. While 0.5 μM NO in aqueous solution has a half-life of 10-15 sec when equilibrated with room air[131], at a much lower concentration (0.01 - 1 μM, biologically relevant concentration), its half-life is much longer (500 sec)[132]. In contrast, the lifetime of singlet oxygen in water without any interference is only 4 μs [133-135], which is over 1000 times shorter-lived than NO. In our single-molecule detection scheme, the transitions are recorded at 0.2 sec/frame. Adsorbed singlet oxygens, if any, are more likely to be decomposed before the quenching transition is recorded.

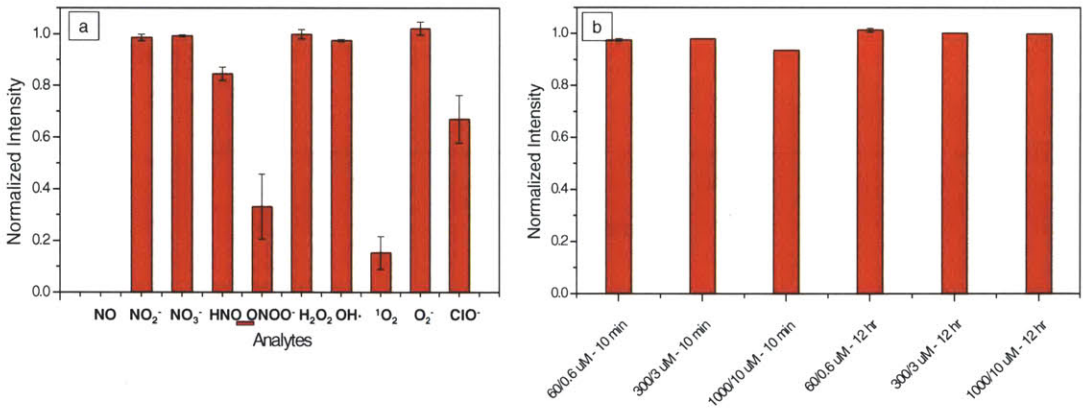

Figure 2.13 Fluorescence response of AT_{15}-SWNT to a panel of reactive oxygen and nitrogen species. (**a**) Fluorescence intensity (I/I_0, intensity/initial intensity) of (7,5) species of AT_{15}-SWNT measured 10 minutes after addition of 60 μM of each analyte. SWNT is at 2 mg/l in PBS (pH = 7.4, 50 mM). (**b**) AT_{15}-SWNT response to hydroxyl radical. Fluorescence intensity (I/I_0, intensity/initial intensity) of (7,5) species of AT_{15}-SWNT measured 10 minutes and 12 hours after addition of $H_2O_2/FeSO_4$ (Concentration of each reaagent is indicated in the x-axis). SWNT is at 2 mg/l in PBS (50 mM).

Peroxynitrite self-decomposes at physiological pH, with a half-life of 2 sec [136]. In the presence of dissolved CO_2, the half-life is significantly decreased [137, 138]. In

addition to its shorter life time compared to NO, our sensor exhibits a much more sensitive response to NO than to peroxynitrite. The response time for NO is $t_{1/2}$ = 1.1 sec, but 28 sec to peroxynitrite (Figure 2.14), which is also much longer than the half-life of peroxynitrite. Therefore, it is highly unlikely that a trace amount of peroxynitrite in a biological system would interfere with NO detection.

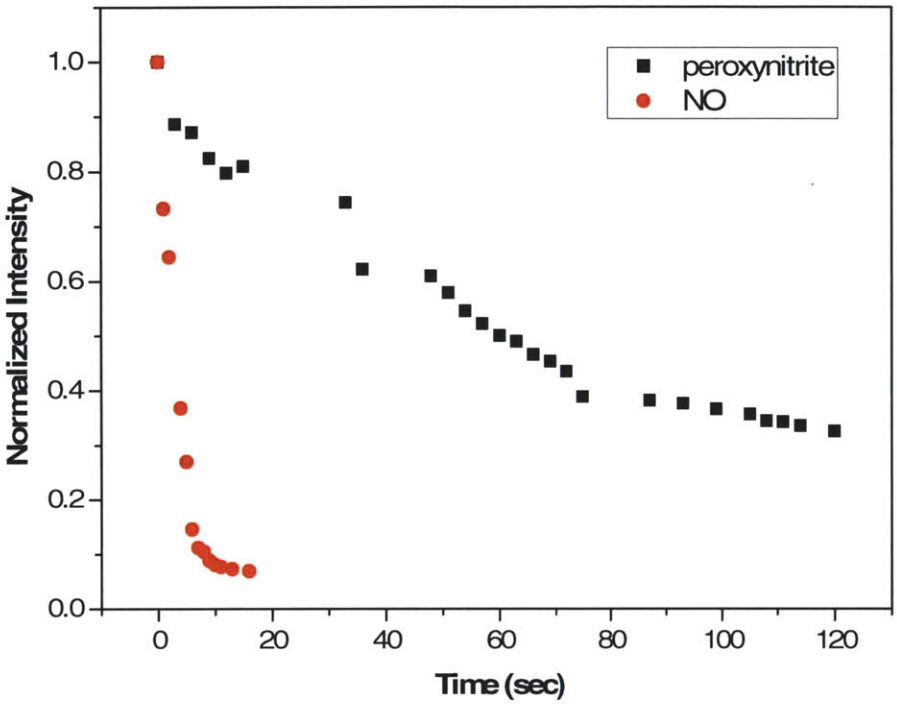

Figure 2.14 Comparison of response time of AT_{15}-SWNT to NO (red circle) and peroxynitrite (black square). Fitted using a first-order kinetics (exponential decay) results in a sensor response time of $t_{1/2}$ = 1.1 sec for NO and 28 sec for peroxynitrite.

2.3.3 Arrays of SWNT Reporting Single Molecule Adsorption of NO

A NO sensing SWNT array was realized by depositing individual AT_{15}-SWNT on APTES-treated, glass-bottomed, petri dish through electrostatic interactions (Figure 2.5). This tethering appears to enhance the efficiency of SWNT deposition, and also keeps the complex immobilized on the glass slide during multiple rinsing steps. Upon 658 nm laser excitation, the SWNT on the array emits stable near-infrared light, which is collected in real-time by a near-infrared two-dimensional array detector at a frame rate of 0.2 s/frame. In the fluorescence image (Figure 2.5c), each individual AT_{15}-SWNT is shown as a

diffraction-limited fluorescent spot of approximately 2x2 pixel size, with each pixel representing an area of 290x290 nm^2. The AFM micrographs (Figure 2.3) confirm that AT_{15}-SWNT is individually deposited on the substrate. Once the array is exposed to NO, stepwise photoluminescence quenching of each SWNT in the array is observed over time (Figure 2.15, red). In order to obtain meaningful results, the dark current is first obtained by averaging the camera signal over a 20x20 pixel area that does not contain SWNT, and then subtracting it from each trace. Mechanistically, as the NO adsorbs on the accessible area of the SWNT, excitons that form within the exciton excursion radius of the NO adsorption site (one exciton diffusion length) are quenched. Therefore, even sparse adsorption of NO on the SWNT causes a stepwise decrease in the SWNT fluorescence. We have reported similar observations for H_2O_2[29, 30] and $Fe(CN)_6^{3-}$ [29], while others have investigated H^+ [26], and diazonium salts[26-28]. Each observed quenching step reports a single molecule NO adsorption event, and each fluorescence enhancing step reflects a single desorption event. Consider a single SWNT being divided into N segments, each of which is approximately the size of the exciton-diffusion length [26-28]. At any instance, we have the reaction,

$$\mathrm{NO} + \theta \underset{k_d}{\overset{k_a}{\rightleftarrows}} \theta^* \qquad (1)$$

where k_a and k_d are defined as the single-site adsorption and desorption rates of NO on SWNT respectively. θ and θ^* refer to empty and NO-occupied sites, respectively. Mass action of reaction (1) reveals:

$$\begin{aligned} &\frac{d\theta}{dt} = -(k_a[\mathrm{NO}])\theta + k_d(\theta^*) \\ &\theta + \theta^* = N \end{aligned} \qquad (2)$$

where N is the total number of sites on the SWNT. At the NO concentration range we are testing, it is valid to assume that NO adsorption on the SWNT does not change its bulk concentration, therefore, k_a and [NO] can be grouped into one variable, k_a', and it satisfies,

$$k_a' = k_a[\mathrm{NO}] \quad (3)$$

Although both k_a' and k_d will affect the fluorescence response, we are more interested in k_a' because it provides a direct measure of NO concentration. The concentration of NO determines both the degree of quenching of the fluorescence over the observation time, as well as the rate. The representative traces in Figure 2.15d indicate that within 600 s, around 40%, 60%, 100% and 100% of quenching were observed at steady state when the sensor was exposed to 0.16 μM, 0.78 μM, 3.9 μM, and 19.4 μM of NO, respectively. In addition, 100% quenching of the SWNT occurs much faster in the case of 25 μM exposure than that of the 5 μM exposure, as expected. Moreover, only at low concentration were desorption steps even observed which indicates that k_a' becomes diminished as concentration of NO decreases, as expected from equations (2) and (3). These observations motivate the adoption of a generic analysis capable of extracting the local NO concentration directly from the transient quenching response.

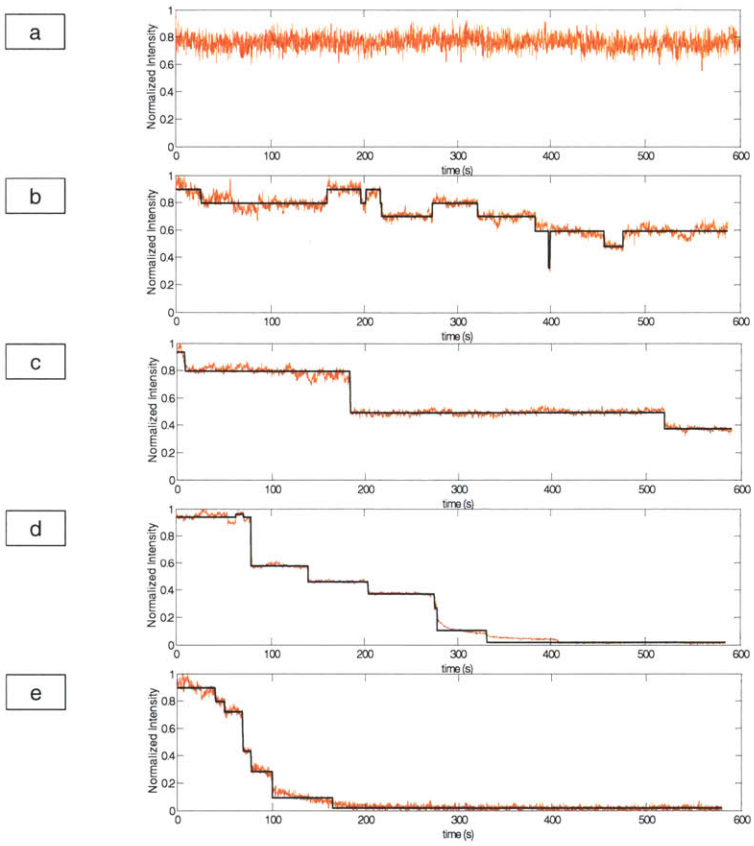

Figure 2.15 Representative fluorescence time-trace (red) of a diffraction-limited spot (2x2 pixels) after being exposed to NO (t = 0 s) at five different concentrations (**a**, 0 μM, **b**, 0.16 μM, **c**, 0.78 μM, **d**, 3.9 μM, **e**, 19.4 μM) and fitted traces (Chi-squared error-minimizing step-finding algorithm, black). Each trace is normalized by the difference between the starting intensity and the dark-current intensity, and the latter is obtained through averaging intensity over a 20x20 pixel spot that does not contain any SWNT.

2.3.4 Stochastic Analysis Using the Maximum Likelihood Estimation (MLE) for a Birth-and-Death Process

Previously, we investigated H_2O_2 as a quenching molecule over a film of collagen-wrapped SWNT with an observation time of 3000s[29]. Briefly, we first used *Hidden Markov Modeling* (HMM)[29, 139] to distinguish actual stepwise transitions from noise in the fluorescence time-traces. Then, we converted transitions from all the traces (usually 100 traces) into an average transition probability matrix which can be used to estimate k_a' and k_d. One limitation of this method is that it requires sufficient transitions between two adjacent intensity states to obtain an accurate transition matrix. As a consequence, HMM usually requires a relatively large number of transitions to provide accurate parameter estimates. For example, in Figure 2.15c and 2.15d we observe that

only one transition occurs between two adjacent states during our observation time of 600s, and computing a transition probability matrix through each trace would be insufficient. For the same reason, over 100 traces were needed per film in order to narrow the standard deviation in estimating the rate constant shown in our previous work[29]. Our interest in using these arrays as nanoscale sensors motivates the development of analysis methods that use as few resulting traces as necessary. This will increase both the temporal and spatial resolution.

In order to determine NO concentration at each SWNT, we adapt a new stochastic analysis method based on an alternative Markov model, the *birth-and-death* process, which we show leads to better accuracy in determining k_a' and k_d. In a *birth-and-death* Markov model, a population, X_t, undergoes diminutions and additions over a period of observation, t, similar to the fluorescence modulation observed for each nanotube in our experiments. Again, suppose that a single SWNT can be divided into N segments, each of which is in the size of the exciton-diffusion length. The fast moving excitons in a single segment can be completely quenched once a single NO molecule adsorbs anywhere on that segment. Therefore, a single SWNT can be simply visualized as a 1D array that contains N reactive sites. In the view of the *birth-and-death* Markov process, a single SWNT is a population with a maximum population size of N. The exact length of exciton-diffusion does not affect the analysis. An adsorption event results in a fluorescence decrease (quenching) and reduces the unoccupied site population by one. A desorption event therefore is the reverse. How the population size changes over time is of interest, because it directly relates to the observed fluorescence response in time. It is clear that the population size at the next time interval ($t+h$) is affected by the current

population size, X_t, as well as the probability of adsorption or desorption occurring on any individual in the population. Similarly, the number of empty sites on a single SWNT in the next moment is dependent upon the current number of empty sites on the SWNT combined with the single-site adsorption and desorption rates. This process can be described using a typical state transition-rate diagram as shown in Figure 2.16, or alternatively in a probability form (equation (4)), either of which is another representation of the mass action equation (2).

$$P(X_{t+h} = j \mid X_t = i) = \begin{cases} (N-i)k_d h + o(h) & (j = i+1), \\ 1-(N-i)k_d h - ik_a' h + o(h) & (j = i), \\ ik_a' h + o(h) & (j = i-1), \\ o(h) & (\text{otherwise}). \end{cases} \quad (4)$$

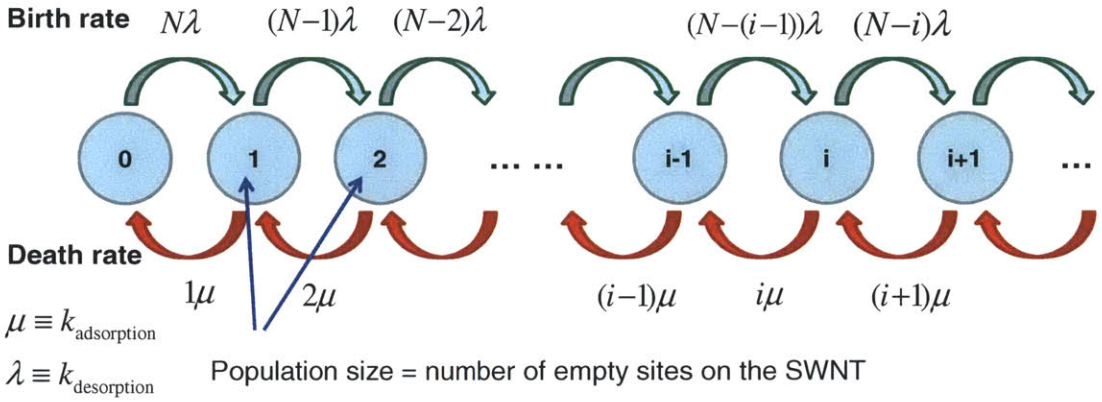

Figure 2.16 State transition-rate diagram of the *birth-and-death* process. The numbers in the circle indicate the states, or the population sizes of the *birth-and-death* process at any instant, t; and in the case of single-molecule adsorption, these numbers also indicate the number of empty sites on a single SWNT. Green arrows represent possible birth transitions between states with a birth rate of $(N-i)\lambda$ for a population size of i, and red arrows represent possible death transitions between states with a death rate of $i\mu$ for the same population size.

More specifically, the probability of a desorption event (the number of empty sites changes from i to i+1) occurring in the next small time interval is proportional $(N-i)k_d$, and the probability of an adsorption event (the number of empty sites changes from i to i-

1) is proportional to ik_a'. Note that k_a' is proportional to the concentration of quencher; while k_a, which reflects the very nature of the interaction between NO molecule and SWNT, is a constant. Therefore, an accurate estimation of k_a' provides a proper calibration of the concentration of the quencher. This process mentioned above is not a typical linear *birth-and-death* process that is well described in literature where both k_a' and k_d are proportional to population size, i. However, applying the theory of the maximum likelihood estimation (MLE)[31, 140] to this process allows one to estimate the only two process parameters k_a' and k_d from the observation on the change of site population in a single SWNT. Detailed derivation of the maximum likelihood estimator is available in the Section 2.4. The MLE estimator for this process, $\vec{\theta}_{max}$ is a two dimensional vector,

$$\vec{\theta}_{\max} = (\hat{k}_{a,M}', \hat{k}_{d,M}) = (\frac{D_t}{S_t}, \frac{B_t}{N \cdot t - S_t}) \quad (5)$$

where D_t and B_t are the number of deaths (adsorption) and births (desorption) in the time interval [0, t], respectively. We use $\hat{k}_{a,M}'$ and $\hat{k}_{d,M}$ to denote MLE estimator for k_a' and k_d. And B_t + D_t equals the total number of transition events. The parameter S_t is defined as $\int_o^t X_u \mathrm{d}u$, which evaluates the total time lived by the population in the time interval [0, t].

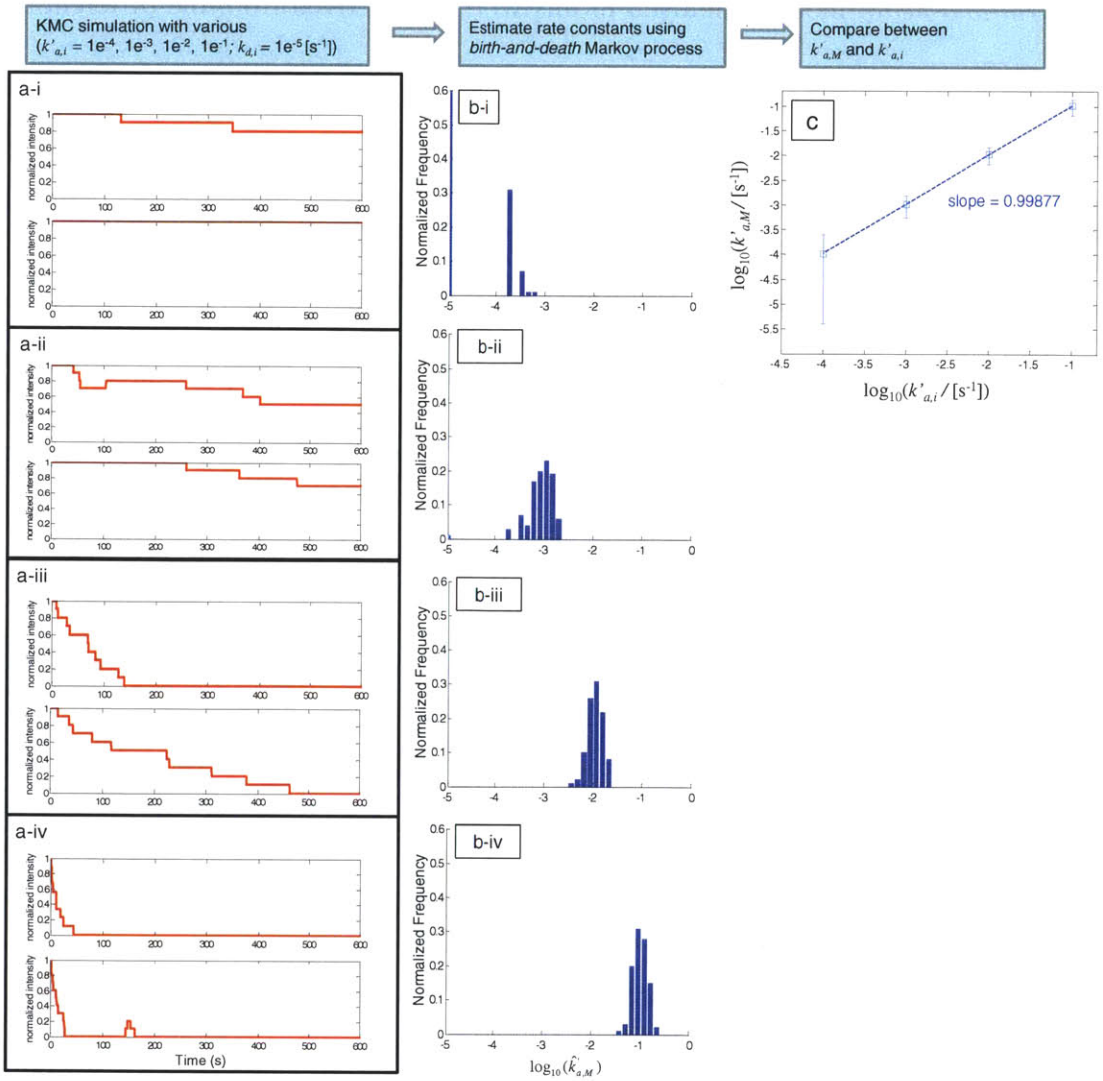

Figure 2.17 Kinetic Monte Carlo (KMC) simulation of stochastic quenching on a single SWNT, and the rate constant estimation obtained using the MLE of the *birth-and-death* Markov process. (**a**) Representative KMC simulated traces with inputted adsorption rate constants ($k'_{a,i}$) of 0.0001 (**a-i**), 0.001 (**a-ii**), 0.01 (**a-iii**) and 0.1 (**a-iv**) s^{-1}, and a desorption rate constant ($k_{d,i}$) of 0.00001 s^{-1}. The maximum number of states, N, used in the simulation is 10. Both simulation time and observation time are 600 s. (**b**) Histogram of $\hat{k}'_{a,M}$ in a $\log_{10}$ scale corresponding to the four simulated conditions in (**a**). Rate constants smaller than 0.00001 s^{-1} are included in the bin whose rate constant is 0.00001 s^{-1} for better visualization. Each histogram is generated from 100 traces. $\hat{k}'_{a,M}$ of multiple traces is a S_t-weighted average of $\hat{k}'_{a,M}$ from single traces. (**c**) The $\hat{k}'_{a,M}$ value, evaluated from 100 traces, as a function of $k'_{a,i}$ (square, S_t-weighted average of $\hat{k}'_{a,M}$; error bar, standard deviation of $\hat{k}'_{a,M}$ from each trace). Linear fitting yields a slope of 1, indicating a good agreement between the MLE estimated rates and the input rates.

The *birth-and-death* model employed in this work was derived from the differential equation (2), therefore it correctly reflects the chemistry of the underlying process; whereas the HMM is just an approximation relying on several non-physical assumptions. In addition, the time that the underlying process stays at each particular state before the subsequent transition is a random variable whose distribution is obviously state-dependent. While being neglected by HMM, this dependency is explicitly captured by the *birth-and-death* process.

2.3.5 Validation of the stochastic analysis on Kinetic Monte Carlo (KMC) simulation

The robustness of the stochastic analysis was tested through applying the *birth-and-death* MLE method to KMC simulated time-traces using various sets of input rates (denoted as $k'_{a,i}$ and $k_{d,i}$), and different N values. An example simulates 100 traces at four different values of $k'_{a,i}$ (0.0001, 0.001, 0.01 and 0.1 sec^{-1}) but the same $k_{d,i}$ of 0.00001 sec^{-1}, with N = 10 and an observation time of 600 sec. These parameters were chosen such that the simulation produces traces that behave similarly to experimental observations in Figure 2.15, in order to provide guidance of the accuracy of this stochastic analysis method in our experimental operating condition. As expected, even for the same input rates and N, generated time-traces exhibit different degree or rate of quenching due to the stochastic nature of the process (Figure 2.17a), resulting in a distribution of $\hat{k}'_{a,M}$ evaluated from each trace. The histogram of $\hat{k}'_{a,M}$, evaluated using 100 traces each with a 600 s observation time, is centered about $k'_{a,i}$ in each case (Figure 2.17b). For estimating $\hat{k}'_{a,M}$ from multiple traces, a S_t-weighted average of $\hat{k}'_{a,M}$ is

required (Supplementary Information). Plotting $\hat{k}'_{a,M}$ against $k'_{a,i}$ yields a slope of unity, proving that $\hat{k}'_{a,M}$ can indeed be used to calibrate $k'_{a,i}$ (Figure 2.17c). And even 10 traces with an observation time of 600 s can well recover the true $k'_{a,i}$ with a less than 5% deviation (Table 2.2). A more generalized comparison of $\hat{k}'_{a,M}$, evaluated using various N, numbers of traces and observation times, are summarized in Table 2.2, 2.3 and Figure 2.18, 2.19.

Table 2.2 Effect of observation time and number of traces on $\hat{k}'_{a,M}$ estimation.

Number of traces	10			100			1000			10000		
Observation time (s)	600	3000	30000	600	3000	30000	600	3000	30000	600	3000	30000
$k_{a,i}$ [s^{-1}]	$k'_{a,M}$ [s^{-1}]											
1.000E-01	9.85E-02	9.84E-02	9.78E-02	1.02E-01	9.94E-02	1.01E-01	1.00E-01	1.01E-01	9.90E-02	1.00E-01	1.00E-01	1.00E-01
1.000E-02	1.05E-02	1.05E-02	9.82E-03	1.05E-02	9.76E-03	1.03E-02	1.01E-02	9.95E-03	1.01E-02	9.98E-03	1.00E-02	1.00E-02
1.000E-03	9.78E-04	9.49E-04	1.02E-03	1.04E-03	1.01E-03	1.03E-03	1.00E-03	9.96E-04	9.93E-04	1.00E-03	1.00E-03	1.00E-03
1.000E-04	1.03E-04	1.03E-04	9.48E-05	1.03E-04	9.64E-05	1.00E-04	1.04E-04	1.01E-04	9.80E-05	9.85E-05	1.01E-04	9.97E-05
$k_{a,i}$ [s^{-1}]	$\sigma(k'_{a,M})$ [s^{-1}]											
1.000E-01	4.70E-02	3.60E-02	3.81E-02	3.72E-02	3.56E-02	1.77E-02	3.88E-02	3.71E-02	3.70E-02	3.87E-02	3.83E-02	3.29E-02
1.000E-02	4.49E-03	3.85E-03	2.52E-03	3.78E-03	3.68E-03	3.37E-03	4.08E-03	3.49E-03	3.51E-03	3.85E-03	3.90E-03	3.38E-03
1.000E-03	3.06E-04	1.69E-04	2.38E-04	4.92E-04	3.45E-04	3.63E-04	5.71E-04	3.92E-04	3.40E-04	5.22E-04	3.91E-04	3.39E-04
1.000E-04	1.30E-04	5.18E-05	2.88E-05	1.48E-04	5.75E-05	4.34E-05	1.43E-04	6.74E-05	3.68E-05	1.37E-04	6.76E-05	3.60E-05
$k_{a,i}$ [s^{-1}]	% error = $(k'_{a,M} - k'_{a,i})/k'_{a,i}$ x 100%											
1.000E-01	-1.46	-1.58	-2.25	2.03	-0.56	1.39	0.25	1.11	-0.99	0.28	0.29	0.01
1.000E-02	4.57	5.16	-1.76	4.71	-2.41	2.67	0.68	-0.51	0.63	-0.24	0.47	0.33
1.000E-03	-2.17	-5.12	2.02	3.69	1.07	3.34	0.30	-0.44	-0.67	0.29	0.19	0.09
1.000E-04	3.08	3.45	-5.21	3.30	-3.58	0.15	3.52	1.30	-2.00	-1.48	0.88	-0.29

** Four sets of input adsorption rates, $k'_{a,i}$, for KMC simulated traces.

† S_t-weighted average $\hat{k}'_{a,M}$. Simulation is performed at $k_{d,i}$ = 0.00001 s^{-1} and N = 10.

‡ S_t-weighted standard deviation of $\hat{k}'_{a,M}$

Table 2.3 Effect of observation time and number of traces on $\hat{k}'_{a,M}$ estimation. KMC simulated traces are generated using N = 1000. 1000 traces were generated for each sets of input rates, ($k'_{a,i}$, $k_{d,i}$) = (0.1, 0.00001), (0.01, 0.00001), (0.001, 0.00001), (0.0001, 0.00001). Units are in [s^{-1}]. For each pair of input rates, the *birth-and-death* stochastic analysis method was then used to extract an estimated value of $\hat{k}'_{a,M}$ from every trace. This same analysis was performed several times while varying observation time from 600, 3000 to 30000 s. In addition, we examined how the S_t-weighted average and standard deviation of $\hat{k}_{a,M}$ vary when only a subset of the total number of traces is used (number of traces = 1, 10, 100, 1000). These values are summarized for each observation time and set of input rates.

Number of traces	1			10			100			1000		
Observation time (s)	600	3000	30000	600	3000	30000	600	3000	30000	600	3000	30000
$k_{a,i}$ [s^{-1}]	$k'_{a,M}$ [s^{-1}]											
1.000E-01	1.04E-01	9.83E-02	9.92E-02	1.00E-01	9.99E-02	1.01E-01	1.00E-01	1.01E-01	1.00E-01	1.00E-01	1.00E-01	9.99E-02
1.000E-02	9.83E-03	1.01E-02	1.02E-02	9.85E-03	1.01E-02	1.02E-02	1.00E-02	1.00E-02	9.98E-03	1.00E-02	1.00E-02	1.00E-02
1.000E-03	1.02E-03	9.97E-04	1.03E-03	9.83E-04	9.84E-04	1.01E-03	9.98E-04	1.00E-03	9.94E-04	1.00E-03	9.99E-04	1.00E-03
1.000E-04	9.64E-05	9.88E-05	1.00E-04	1.03E-04	9.97E-05	9.95E-05	9.95E-05	9.95E-05	1.00E-04	1.00E-04	1.00E-04	9.99E-05
$k_{a,i}$ [s^{-1}]	$\sigma(k'_{a,M})$ [s^{-1}]											
1.000E-01	0.00E+00	0.00E+00	0.00E+00	3.50E-03	4.01E-03	3.66E-03	2.98E-03	3.28E-03	3.05E-03	2.99E-03	3.21E-03	2.74E-03
1.000E-02	0.00E+00	0.00E+00	0.00E+00	2.47E-04	3.88E-04	2.03E-04	3.26E-04	3.17E-04	2.92E-04	3.20E-04	3.16E-04	2.72E-04
1.000E-03	0.00E+00	0.00E+00	0.00E+00	5.65E-05	3.30E-05	2.01E-05	5.07E-05	3.24E-05	2.94E-05	4.72E-05	3.25E-05	2.74E-05
1.000E-04	0.00E+00	0.00E+00	0.00E+00	1.11E-05	6.85E-06	3.03E-06	1.30E-05	6.31E-06	3.12E-06	1.31E-05	6.22E-06	3.07E-06
$k_{a,i}$ [s^{-1}]	% error = $(k'_{a,M} - k'_{a,i})/k'_{a,i}$ x 100%											
1.000E-01	3.75	-1.66	-0.85	0.49	-0.15	0.66	0.26	0.56	0.20	0.02	0.10	-0.05
1.000E-02	-1.74	0.75	1.86	-1.46	1.44	1.60	0.31	0.33	-0.16	0.03	-0.01	-0.02
1.000E-03	1.91	-0.27	3.05	-1.72	-1.61	0.97	-0.21	0.06	-0.58	0.08	-0.11	0.09
1.000E-04	-3.62	-1.20	0.05	2.89	-0.31	-0.47	-0.54	-0.52	0.40	0.18	0.16	-0.10

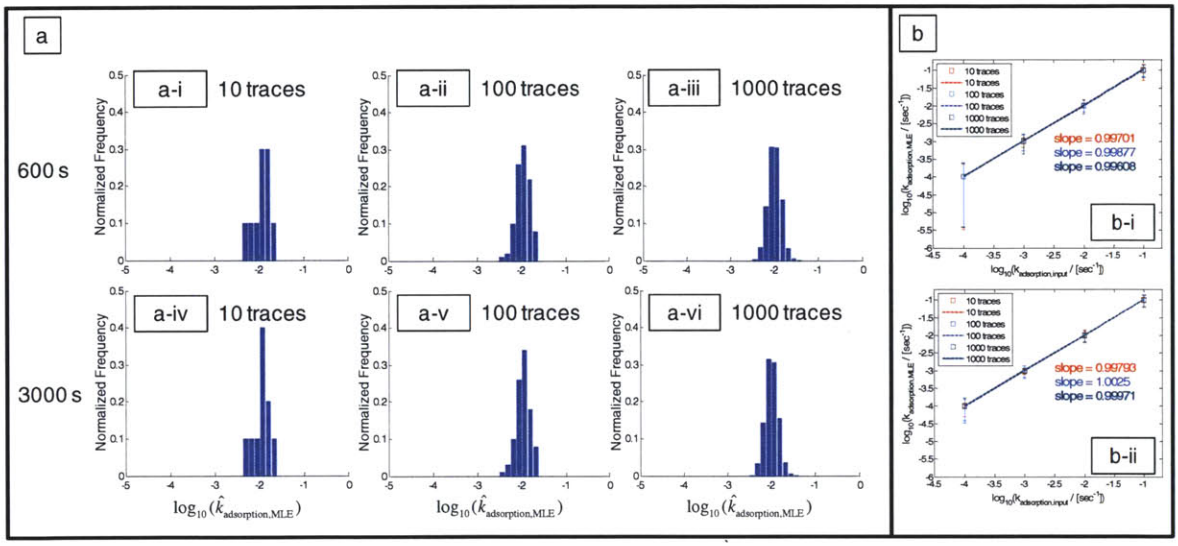

Figure 2.18 Effect of observation time and number of traces on estimation for KMC traces (N = 10). (**a**) An example to study the effect of observation time and number of traces on the $\hat{k}'_{a,M}$ estimation. Histogram of $\hat{k}'_{a,M}$ estimated from 10 (**a-i, a-iv**), 100 (**a-ii, a-v**), 1000 (**a-iii, a-vi**) KMC traces using 600 s (top) and 3000 s (bottom) as observation time. Input values are $k'_{a,i}$ = 0.01 s^{-1}, $k_{d,i}$ = 0.00001 s^{-1}, and N = 10. (**b**) The $\hat{k}'_{a,M}$ and standard deviation of the distribution as a function of $k'_{a,i}$ of the KMC in a $\log_{10}$-$\log_{10}$ scale, and fitted with a linear trend with slope indicated in the figure (square, $\hat{k}'_{a,M}$ of multiple traces; error bar, standard deviation). Each panel represents the $\hat{k}'_{a,M}$ obtained with a different observation time (b-i, 600 s; b-ii, 3000 s).

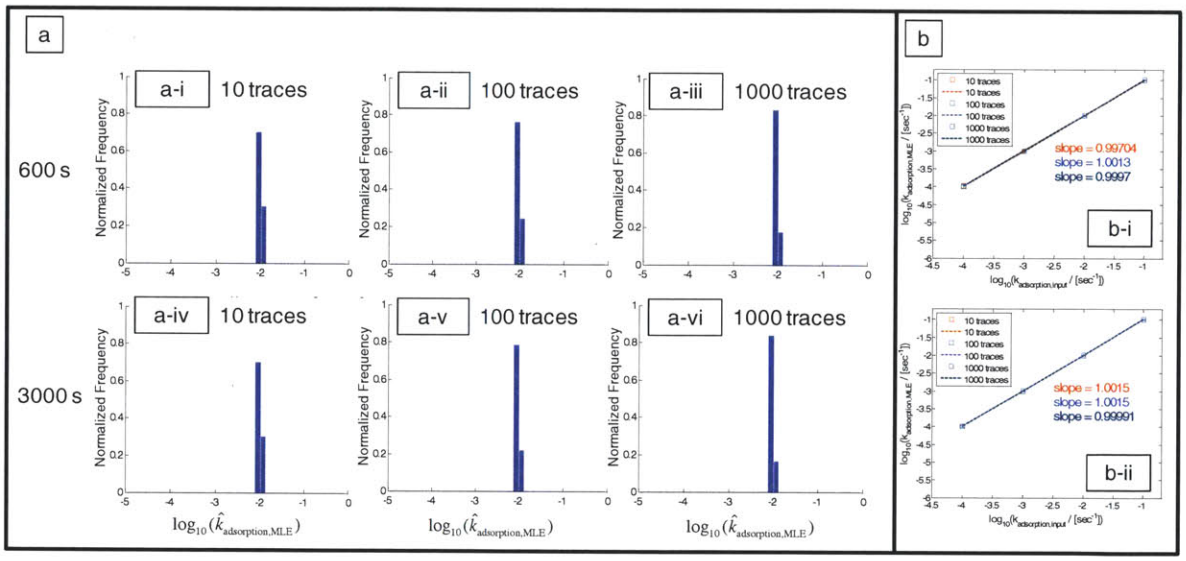

Figure 2.19 Effect of observation time and number of traces on estimation for KMC traces (N = 1000). (**a**) An example to study the effect of observation time and number of traces on the $\hat{k}'_{a,M}$ estimation. Histogram of $\hat{k}'_{a,M}$ estimated from 10 (**a-i, a-iv**), 100 (**a-ii, a-v**), 1000 (**a-iii, a-vi**) KMC traces using 600 s (top) and 3000 s (bottom) as observation time. Input values are $k'_{a,i}$ = 0.01 s^{-1}, $k_{d,i}$ = 0.00001 s^{-1}, and N = 1000. (**b**) The $\hat{k}'_{a,M}$ and standard deviation of the distribution as a function of $k'_{a,i}$ of the KMC in a $\log_{10}$-$\log_{10}$ scale, and fitted with a linear trend with slope indicated in the figure (square, $\hat{k}'_{a,M}$ of multiple traces; error bar, standard deviation). Each panel represents the $\hat{k}'_{a,M}$ value obtained with a different observation time (b-i, 600 s; b-ii, 3000 s).

While the parity between the obtained $\hat{k}'_{a,M}$ and $k'_{a,i}$ reveals the accuracy of this MLE method, the standard deviation of the distribution (or the width of the histogram) reflects the stochastic nature of the process, whereby for the same set of inputs, simulated traces always exhibit slightly different quenching rates. Similarly, in an actual experiment where a small number of quenching molecules is added, each sensor produces slightly different time-traces due to the probability distribution of the quencher molecule adsorbed on each sensor, and we will also expect a distribution of the sensor responses.

The standard deviation of the distribution decreases as the observation time increases, which eventually approaches a lower limit that is due solely to stochasticism. Large sets of simulation results suggest that the number of traces does not affect the standard deviation of the distribution, and this lower limit is always about 30% of $k_{a,i}^{'}$ (Table 2.2). The speed in which the standard deviation of the distribution converges to its limiting value is input rate-dependent. It turns out that for high $k_{a,i}^{'}$ (0.1 s^{-1} , 0.01 s^{-1}), the standard deviation easily reaches its lower bound even using 600 s observation of 10 traces; however, for low $k_{a,i}^{'}$ (0.0001 s^{-1}), to reach this lower bound it requires an increase of observation time (Table 2.2). This is because at low $k_{a,i}^{'}$, very few transitions occur within the first 600 s. Recording sufficient transitions within longer observation time will allow us to obtain a more accurate $\hat{k}_{a,M}^{'}$ for each trace, resulting in a distribution of $\hat{k}_{a,M}^{'}$ solely due to the stochastic nature. However, it is worth noting even when there may not be sufficient transitions in a single trace, the $\hat{k}_{a,M}^{'}$ from just 10 traces is still very accurate (within 5% error from the true value of $k_{a,i}^{'}$). This again shows the advantage of the MLE model whereby only two parameters require estimation, $\hat{k}_{a}^{'}$ and k_d, and therefore not many transitions are needed to provide an accurate parameter evaluation.

2.3.6 Calibration of the Sensor Platform by Exposing the SWNT Array to Aqueous NO solution; Determination of the NO Adsorption Rate Constant

Calibration of the AT15-SWNT sensor array was carried out by exposing the array to aqueous NO solution at different concentrations, ranging from 0.16 μM to 19.4 μM

(Figure 2.15). A custom-written MATLAB program automatically selects 50 brightest diffraction-limited spots with each representing a single SWNT, and extracts the fluorescence intensity in time, resulting in a set of 50 time-traces each experiment. We chose the brightest SWNTs to ensure they have fewer defects chemically and structurally [26-28], and therefore are most sensitive to the changes in the environment. Each time-trace is then subjected to another custom-written MATLAB routine based on a Chi-squared error-minimizing step-finding algorithm described in reference[141] to distinguish real transition events from noise (Figure 2.15d, black). The program results in the same fitting steps compared to HMM-based step-finding algorithm ([29, 30, 139]), but reduces the computational time by 90. [142] （Appendix A）

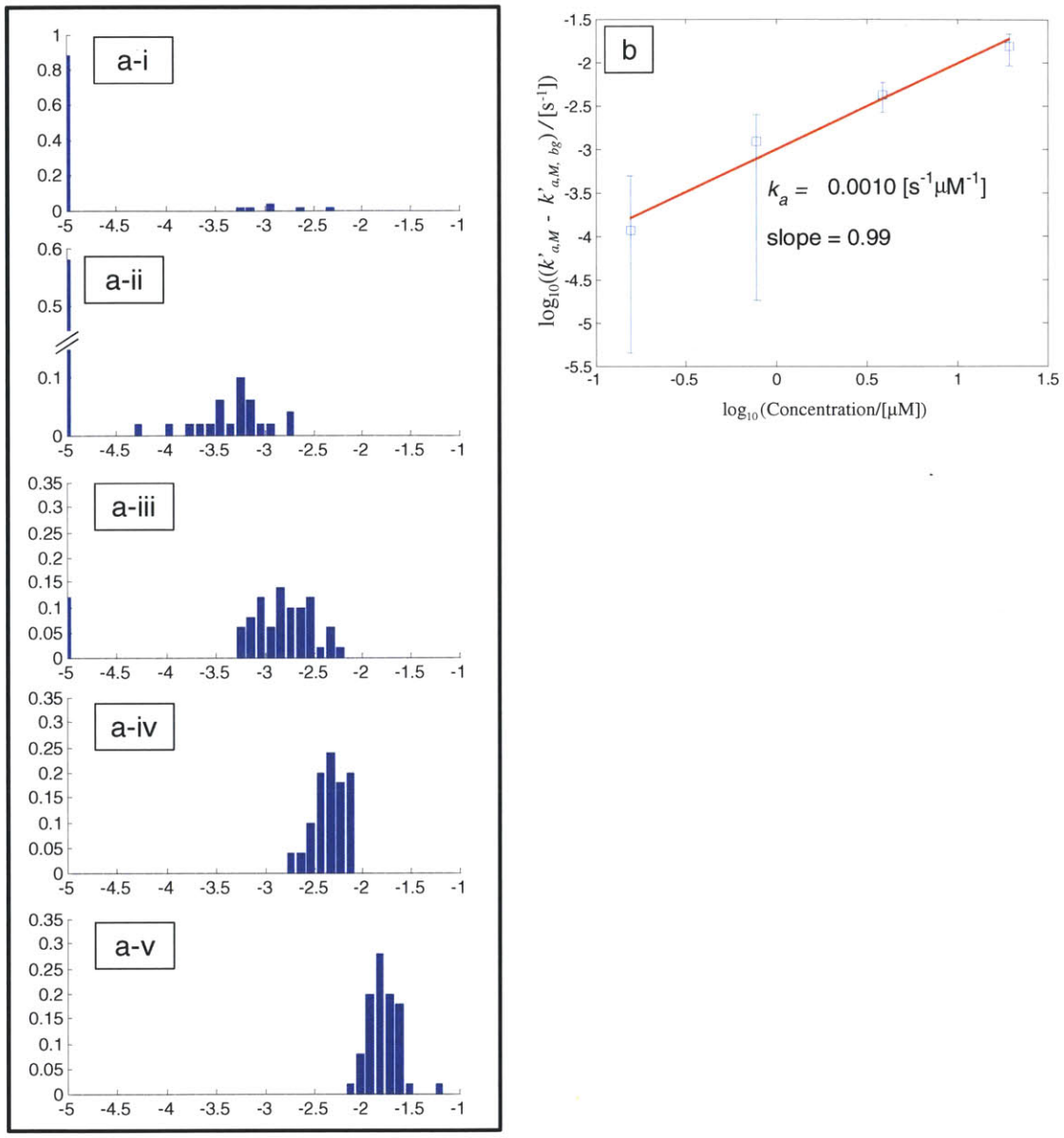

Figure 2.20 Calibration of the AT_{15}-SWNT sensor array with NO solution. (**a**) Cumulative histogram of $\hat{k}'_{a,M}$ values obtained from each SWNT in the array upon exposure to NO at five different concentrations (**a-i**, 0 μM; **a-ii**, 0.16 μM; **a-iii**, 0.78 μM; **a-iv**, 3.9 μM; **a-v**, 19.4 μM). Rate constants lower than 0.00001 s^{-1} are grouped into the smallest bin. (**b**) The effective $\hat{k}'_{a,M}$, or $(\hat{k}'_{a,M} - \hat{k}'_{a,M,bg})$, evaluated from 50 time-traces, as a function of NO concentration (square, S_t-weighted average of $\hat{k}'_{a,M}$; error bar, S_t-weighted standard deviation of $k'_{a,i}$ from each trace). The data is plotted on a $\log_{10}$-$\log_{10}$ scale for better visualization of low concentration data. Fitting the data yields a slope of 1 (red dotted line), agreeing with equation (3), $k'_a = k_a[\mathrm{NO}]$, with k_a of 0.001 s^{-1} μM NO^{-1}.

Once all the transitions are identified, we apply the birth-and-death MLE to each time-trace, and each SWNT reports a $\hat{k}'_{a,M}$. At these low concentrations (~0.2-20 μM), each sensor detects a slightly different concentration of NO, mainly due to the stochastic nature of the process, which results in a distribution of the $\hat{k}'_{a,M}$ that increases as the NO concentration increases (Figure 2.20a). Close examination yields that 8 out of 50 sensors in the control experiment, in which no NO is added, also exhibit a limited number of transitions, which may be attributed to the proton adsorption on the SWNT. MLE analysis of the control experiment yields a rate describing the background fluctuation, or $\hat{k}'_{a,M,bg}$, of 0.0001 s-1. After subtracting this contribution from the $\hat{k}'_{a,M}$ values obtained at other concentrations, the observed rate constant is linearly dependent on the NO concentration with a slope of 1 (Figure 2.20b), agreeing with equation (3). The y-intercept of the fitted line reports a k_a of 0.001 s-1 μM NO-1, which provides a good calibration of the sensor array. Considering the diffusive and highly reactive property of NO, the linear trend observed experimentally is noteworthy. We estimate the ensemble detection limit as 300 nM, or 3 times the ratio of $\hat{k}'_{a,M,bg} / k_a$, since the background fluctuations are limiting. However, the sensor is infinitely photo-stable and does not intrinsically blink, allowing immobilization of large arrays. These large arrays can act as sensors that are independently addressable, as we have shown previously for H_2O_2.[30] One advantage of such an array is that NO generation can be tracked spatially, although this is still constrained by optical diffraction limit. In addition, while the standard deviation evaluated at a relatively high concentration (3.9 and 19.4 μM) lies within the

lower limit estimated through KMC, the standard deviations are higher than expected when the NO concentration further decreases. This might be because the inhomogeneity of the SWNT starts to play a role when the concentration of the analytes becomes low, since sensors possessing more defect sites are less sensitive to small changes and do not respond at low NO local concentration.

We note that single stochastic sensors of this type do not have a conventional detection limit that may be compared with an ensemble measurement. If placed near a nanometer scale generator of NO, such as a living macrophage or immobilized NO synthase, this platform can easily detect the product. The resulting bulk concentration may be trace, but such nanometer scale sensor may potentially be used to map the concentration profile in and around the generator. We have demonstrated this for the case of a H_2O_2 selective array, and studied the H_2O_2 signaling from protein EGFR as a local generator[29, 30]. Future work will extend this approach to living systems involving NO.

2.4. Detailed Birth-and-death Markov Model Derivation and KMC Simulation

2.4.1 KMC Simulating on Single Molecule Adsorption and Desorption on SWCNT; Stochastic Analysis

KMC is implanted by using the algorithm reported by reference[143], and KMC simulated traces are generated considering N = 10, and 1000. N = 10 is chosen because there are maximum of 10 quenching steps observed experimentally, and the number is consistent with maximum number of exciton diffusion-limited segments [26-28] on the SWNT for which the average length is about 1-2 μm. N = 1000 is chosen to check the

consistency of the MLE analysis method through comparing stochastic solution with deterministic solution. For each N value, 10000 traces were generated for each sets of input rates, ($k_{a,i}^{'}$, $k_{d,i}$) = (0.1, 0.00001), (0.01, 0.00001), (0.001, 0.00001), (0.0001, 0.00001). Units are in [s^{-1}]. For each N value and set of input rates, the *birth-and-death* stochastic analysis method was then used to extract a value of $\hat{k}_{a,M}^{'}$ from every trace. This same analysis was performed several times while varying observation time from 600, 3000 to 30000 s. In addition, we examined how the mean and standard deviation of $\hat{k}_{a,M}^{'}$ vary when only a subset of the total number of traces is used (Traces = 10, 100, 1000, 10000). These values are summarized for each observation time and set of input rates, and each N.

2.4.2 Maximum Likelihood Estimator, μ and λ, based on Birth-and-death Markov Process

We would like to derive the MLE estimators, or $\hat{k}_{a,M}^{'}$ and $\hat{k}_{d,M}$ for the *birth-and-death* process represented in equation (5). Here, we use μ and λ for now instead of $k_{a,i}^{'}$ and $k_{d,i}$ to keep the mathematical expression concise. For a *birth-and-death* process, the process parameter space $\vec{\theta} = (\mu, \lambda)$ can be estimated through deriving the likelihood function, $L_t(\vec{\theta})$, and computing $\vec{\theta}_{max}$ that maximizes $L_t(\vec{\theta})$ by taking the first order derivative. And the process parameter $\vec{\theta}_{max}$ is also named as maximum likelihood estimator (MLE), and in this case is a two dimensional vector.

To discuss this in detail, let X_t be the population size at time t of the *birth-and-death* process and the maximum number of population is N. And the *Markov* process can be described

$$P(X_{t+h}=j \mid X_t=i)=\begin{cases}(N-i)\lambda h+o(h) & (j=i+1),\\ 1-(N-i)\lambda h-i\mu h+o(h) & (j=i),\\ i\mu h+o(h) & (j=i-1),\\ o(h) & (\text{otherwise}).\end{cases} \quad (6)$$

We are considering the maximum likelihood estimation of the parameters μ and λ assuming that the process has been observed continuously over some time interval. For a *Markov* jump process, the likelihood is

$$L_t(\vec{\theta})=\prod_{i=1}^{n(t)}[f(X_i \mid X_{i-1})\lambda(X_{i-1})]\exp^{-\int_0^t \lambda(X_u)\mathrm{d}u} \quad (7)\ [140]$$

where θ is the parameter space, and $n=n(t)$ is the number of jumps till time t, and we assume that X_0, or the initial population size is non-random.

Note that equation (2) is equivalent to

$$L_t(\vec{\theta})=\prod_{i=0}^{n(t)-1}[f(X_{i+1} \mid X_i)\lambda(X_i)]\exp^{-\int_0^t \lambda(X_u)\mathrm{d}u} \quad (8)$$

If we consider the *birth-and-death* process described by equation (6), then we have

$$\tau(X_i)=(N-X_i)\lambda+X_i\mu$$

$$f(X_i+d \mid X_i)=\left.\begin{cases}(N-X_i)\lambda/\tau(X_i) & (d=1),\\ i\mu/\tau(X_i) & (d=-1),\\ 0 & (\text{otherwise}).\end{cases}\right\} \quad (9)$$

Substituting in equation (3),

$$
\begin{aligned}
L_t(\theta) &= \prod_{i=0}^{n(t)-1} [g(X_{i+1} \mid X_i)] \exp^{-\int_0^t \tau(X_u)\mathrm{d}u} \\
&= \lambda^{B_t} \mu^{D_t} \prod_{i=0}^{n(t)-1} [h(X_{i+1} \mid X_i)] \exp^{-\int_0^t \tau(X_u)\mathrm{d}u} \\
&= \lambda^{B_t} \mu^{D_t} \exp^{-\int_0^t ((N-X_t)\lambda + X_t\mu)\mathrm{d}u} \prod_{i=0}^{n(t)-1} [h(X_{i+1} \mid X_i)] \\
&= \lambda^{B_t} \mu^{D_t} \exp^{-(N\lambda t + (\mu-\lambda)S_t)} \prod_{i=0}^{n(t)-1} [h(X_{i+1} \mid X_i)]
\end{aligned}
\tag{10}
$$

where

$$
g(X_i + d \mid X_i) = \begin{cases} (N - X_i)\lambda & (d = 1), \\ i\mu & (d = -1), \\ 0 & (\text{otherwise}). \end{cases}
$$

$$
h(X_i + d \mid X_i) = \begin{cases} (N - X_i) & (d = 1), \\ i & (d = -1), \\ 0 & (\text{otherwise}). \end{cases}
$$

and B_t and D_t being the number of birth and death in the time interval $[0,t]$, and $B_t + D_t = n(t)$. S_t is defined as $\int_0^t X_u \mathrm{d}u$, the total time lived by the population in the time interval $[0,t]$.

The maximum likelihood estimators (MLE) of (μ, λ) are obtained by maximizing $L_t(\theta)$

$$
\begin{aligned}
\frac{\partial[ln(L_t(\vec{\theta}))]}{\partial\lambda} &= \frac{B_t}{\lambda} + S_t - Nt = 0 \\
\frac{\partial[ln(L_t(\vec{\theta}))]}{\partial\mu} &= \frac{D_t}{\mu} - S_t = 0
\end{aligned}
\tag{11}
$$

So the MLE are $\hat{\lambda}_{MLE} = \frac{B_t}{Nt - S_t}, \hat{\mu}_{MLE} = \frac{D_t}{S_t}$.

2.4.3 Unbiased (consistent) MLE Estimator for Multiple Traces

Although central limit theorem states that sufficiently large number of independent random variables will be approximately normally distributed, a consistent estimator for multiple traces is not simply a mean of estimator of each trace, especially if the sample size is limited. In this case, a consistent MLE estimator for multiple traces is required. In fact, we can derive that the $\hat{k}_a'$ for multiple traces can be expressed by the following formula,

$$\hat{k}_a' = \frac{\sum_j D_{t,j}}{\sum_j S_{t,j}} = \frac{\sum_j (S_{t,j}\hat{k}_{a,M,j}')}{\sum_j S_{t,j}} = w_j \hat{k}_{a,M,j}'$$

where j indicates the j^{th} population, and $D_{t,j}$ and $S_{t,j}$ are the number of deaths, the total time lived by the population in the time interval [0, t] for the j^{th} population, and we define,

$$w_j \equiv \frac{S_{t,j}}{\sum_j S_{t,j}}$$

Therefore, $\hat{k}_a'$ is just a S_t-weighted average of $\hat{k}_a'$ obtained from a single population (trace).

2.4.4 Validation of the Birth-and-death MLE as a Consistent Estimator

In order to validate the consistency of the MLE estimator, we ran KMC simulation at N = 1000, and applied the same stochastic analysis to the simulated traces as these traces simulated at N = 10 (discussed in Section 2.3). The results are summarized in Table 2.2. Because as N increases, the time trace approaches to an analytical solution of equation (2)

which can be described by an exponential decay. As expected, $\hat{k}'_{a,M}$ approaches a deterministic output, and even for a single trace, the error $\hat{k}'_{a,M}$ is less than 4% off the true value. In addition, the distribution converges to a delta function (Figure 2.19), resulting in a significantly reduced standard deviation. Simulation results show that the lower limit of the standard deviation is only 3% of $k_{\text{adsorption,input}}$ (Table 2.3) at N = 1000, which is only 10% of the lower bound of the standard deviation at N = 10.

2.4.5 Contribution of Slightly Larger Standard Deviation at Low $k_{a,i}$

Close examination of the distribution of $\hat{k}'_{a,M}$ from $k'_{a,i}$ indicates that the slightly larger standard deviation comes from many zero-transition traces (Figure 2.17a-i), and the MLE estimation method breaks down when there is no transition occurs. The solution to this issue is to increase observation time. It is worth noting that for small $k'_{a,i}$, increasing the observation time is rather effective in reducing the standard deviation to its lower bound. This is probably because at high $k'_{a,i}$ including 0.1 and 0.01 s^{-1}, majority of the traces have shown completely quenching within 600 s, and prolonging observation time would not affect either D_t or S_t in equation (5) (Section 2.3), and later observation becomes ineffective. In contrast, increasing observation time can decrease the standard deviation for small $k'_{a,i}$ (0.0001 s^{-1}), because at low $k'_{a,i}$, only a few transitions occur at the first 600 s. Therefore, prolonging the observation diminishes any deviation that is due to insufficient transitions. However, because NO is rather diffusive, prolonging the experiments also means losing either spatial or temporal resolution, therefore is not

recommended in this particular case. In fact, at an $k'_{a,i}$ as low as 0.0001 s^{-1}, notice that even 10 traces consistently yield a $\hat{k}'_{a,M}$ with less than 5% error, and therefore this method is very accurate and effective. In general, this simulation - check approach also provides guidance in the experimental design, and provides a more fundamental understanding on experimental data.

2.4.6 Molecular Model on AT_{15} -SWNT Structure

Computations were performed using commercial software package, HyperChem (HyperCube, FL). $d(AT)_{15}$ oligonucleotides was obtained from the nucleic acid database, and was drawn in the vicinity to the SWNT. After geometry optimization was performed on the $d(AT)_{15}$ DNA, energy minimization using Amber force field was conducted on the AT_{15}-SWNT complex. The simulation was run for 1600 psec until the conformation reaches equilibrium.

2.5 Conclusions

In conclusion, the selective detection of single nitric oxide molecules using a specific DNA sequence $d(AT)_{15}$, adsorbed to single walled carbon nanotubes (AT_{15}-SWNT) is reported. This sequence is distinct from eight other DNA variants that show fluorescence quenching or enhancement from a library of tested analytes including dopamine, NADH, L-ascorbic acid, and riboflavin. The $d(AT)_{15}$ imparts SWNT with a distinct selectivity toward NO. Polyvinyl alcohol wrapped SWNT show no response to NO, but exhibit enhancement responses to other molecules in the tested library. The wrapping molecules have shown to significantly affect the selectivity of the SWNT complex. A NO sensing platform is developed consisting of an array of individually deposited AT_{15}-SWNT. A

stepwise fluorescence decrease is observed when the sensor is exposed to NO, reporting single-molecule NO adsorption via SWNT exciton quenching. We describe these quenching traces using a *birth-and-death* Markov model, whose maximum likelihood estimator reports the adsorption and desorption rates of NO. Applying the method to KMC simulated traces suggests a less than 5% deviation in estimation under our experimental conditions, allowing for calibration using a series of NO concentrations. The adsorption rate shows a linear dependence upon NO concentration and the intrinsic single-SWNT-site NO adsorption rate constant is 0.001 s^{-1} μM NO^{-1}. The ability to detect NO quantitatively at the single molecule level has applications for the study of nitric oxide carcinogenesis, chemical signaling, and medical diagnostics for inflammation.

3 Polymer-nanotube interfaces that selectively recognizes molecules

3.1 Introduction and Significance of Creating Molecular Recognition Sites

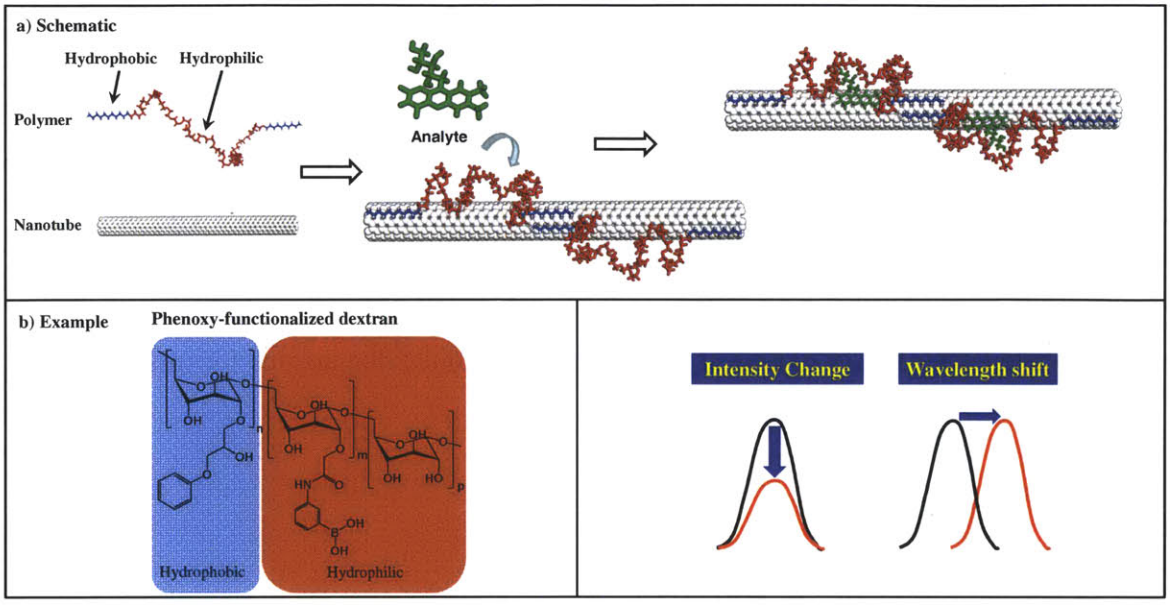

Figure 3.1 Schematic of the molecular recognition concept. (a) A polymer with an alternating hydrophobic-and-hydrophilic sequence adopts a specific conformation when adsorbed to the nanotube. The polymer is pinned in place with a footprint that creates a selective binding site for the molecule of interest, leading to either a wavelength or intensity change in SWCNT fluorescence. (b) An example of a hydrophilic-hydrophobic alternating sequence – boronic acid derivatized phenylated dextran.

Molecular recognition and signal transduction are the two the main challenges in sensor design[3, 144]. Frequently scientists and engineers borrow from nature to gain analyte specificity and sensitivity, using natural antibodies as vital components of the sensors [2, 144-147]. However, antibodies are expensive, fragile, easily lose biological activity upon external treatment, such as immobilization, and exhibit batch-dependent variation, limiting their use in widespread applications [144, 147, 148]. Moreover, certain biological molecules of interest lack a naturally existing antibody, including

toxins, drugs and explosives[149]. This has driven the search for methods to synthesize artificial antibodies from polymeric materials leading to molecularly imprinted polymers (MIP)[147, 149] and DNA-aptamers[2, 3, 147]. Given a selective binding site, the next challenge is measuring the analyte binding event[3, 144]. For fluorescence based sensors, the most common method is through Förster resonance energy transfer (FRET) between acceptor and donor fluorophores[150, 151]; however, such sensors usually require labeling[151, 152]. In addition, most fluorescence-based sensors utilize organic and/or nanoparticle fluorophores which photobleach over time, significantly limiting their capability for long-term real-time monitoring[21]. Some FRET based sensors utilize complicated mathematics to account for photobleaching kinetics[151].

The aforementioned SWCNT PL based sensors [24, 25, 49, 153] took advantage of well-known interactions between the target analyte and the polymer or protein adsorbed on the SWCNT surface. While this approach has been successful, it necessarily limits sensor design to well-known analyte-binding partner interactions and even then no signal transduction mechanism is guaranteed. As an alternative, we propose that a random polymer, with little to no affinity for the target analyte, can adopt a specific conformation when adsorbed to the nanotube via non-covalent interactions. The polymer is pinned in place such that a selective binding site is created which only recognizes the target molecule, and the binding event leads to optical signal transduction (Figure 3.1). To date, however, the potential of these structured phases to recognize external molecules has been unexplored. In this work, we explored the possibilities of constructing molecular recognition motifs based on polymer-SWCNT complexes. We also investigated the ability to tune the affinity of this type of recognition by changing both the composition of

the polymer and SWCNT parameters such as diameter. This allows us to mimic the "directed evolution" approach in the biological systems where researchers have mutated certain genes of a protein, and selected the mutants that have the highest affinity to the analytes of interest for their studies.

For studying this type of interaction, we rely on the modulation of SWCNT photoluminescence as a signal transduction mechanism for reporting the molecular recognition of these polymer-SWCNT complexes. Such nanotube based molecular recognition motifs have clear technological advantages, in that they could theoretically be engineered to recognize broad classes of molecular types. They can also be synthesized using durable and chemically resistant polymers, leading to polymer-SWCNT complexes that are stable to hydrolysis, or compatible with synthetic matrices. We also have interests in using those synthetic complexes as sensing tools, to aid research in the bio-sensing area where the nanotube based optical sensing exhibits many advantages (See Section 1.2). In this work, we focused on a few examples where the nanotube-based molecular recognition concept seems operative, with new recognition complexes demonstrated for riboflavin, l-thyroxine, and estradiol.

3.2 Materials, Polymer Synthesis, SWCNT Suspension

3.2.1 Materials

Single-walled carbon nanotubes were from the *Rice University* research reactor run 114 , *Nano-C* or *Unidym.* 1,2-distearoyl-*sn*-glycero-3-phosphoethanolamine-N-[methoxy(polyethylene glycol)-2000] (ammonium salt) (18:0 PEG2000PEG), 1,2-distearoyl-*sn*-glycero-3-phosphoethanolamine-N-[methoxy(polyethylene glycol)-5000]

(ammonium salt) （18:0 PEG5000 PE）were purchased from *Avanti Polar Lipids Inc.* DNA oligonucleotides and peptides were purchased from *Integrated DNA Technologies (IDT)* and *AnaSpec, Inc.* respectively, and used as received. NH_2-PEG5k-NH_2 has a PDI of 1.1, with MW distribution 4.5 – 5.5kDa; NH_2-PEG20k-NH_2 has a PDI of 1.1, with MW distribution 19.2 – 20.8 kDa; 4-arm NH_2-PEG has a PDI of 1.05 with MW distribution 9.5 – 10.5 kDa; 8-arm NH_2-PEG has a PDI 1.1, MW distribution is 9.5 – 10.5 kDa (Data provided by Creative PEGworks). Sodium cholate (SC), sodium dodecyl sulfate (SDS), poly (vinyl alcohol) (PVA, 87-89% hydrolyzed, 13- 23 kDa), dextran from *Leuconostoc mesenteroides* (9kD to 11kD Mw), 1,2-epoxy-3-phenoxypropane, chloroacetic acid, 3-aminophenylboronic acid, *N*-(3-dimethyl-aminopropyl)-*N*'-ethylcarbodiimide hydrochloride (EDC), *N*-hydroxysuccinimide (NHS), dimethyl sulfoxide (DMSO), 3-aminopropyltriethoxysilane (APTES) and other reaction reagents and tested analytes were purchased from *Sigma Aldrich* and used as received unless indicated otherwise. [^{3}H]-radiolabeled riboflavin was ordered from *Moravek Biochemicals and Radiochemicals.* Macrophage cell line Raw 264.7, Dulbecco's modified Eagles' medium (DMEM), and Leibovitz's L-15 medium were purchased from *American Type Culture Collection (ATCC).* Heat-inactivated fetal bovine serum (FBS) and Penicillin:Streptomycin solution containing 10,000 U/ml penicillin-G and 10 mg/ml streptomycin were purchased from *Gemini Bio-products.* 35 mm cell culturing petri dishes were purchased from *MatTek Corporation.*

3.2.2 Synthesis of PhO-Dex and BA-PhO-Dex:

Synthesis of the phenoxy functionalized dextran (**3**) was performed following Scheme 1[154]. **1** (10g) was dissolved in 90 mL 1N NaOH and pre-heated to 40 °C followed by

addition of **2** (8.3g). After completion of the reaction, **3** was precipitated by the addition of excess ethanol (EtOH) and collected via filtration. Phenoxy content was determined by measuring UV-vis absorption at 269 nm, as reported previously[154], with a Shimadzu UV-3101 PC UV-VIS-NIR scanning spectrometer.

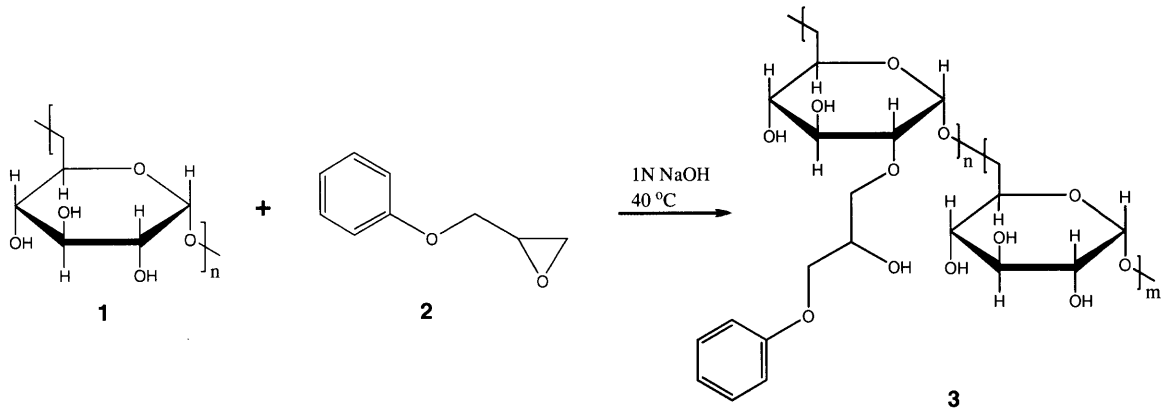

Figure 3.2 Schematic for the synthesis of phenoxy functionalized dextran, **3**.

Synthesis of boronic acid functionalized phenoxy dextran (BA-PhO-Dex, **7**) was carried out following Scheme 3.2. **3** (10 g) was first dissolved in 82.5 mL 6N NaOH and was heated to 60 °C. Chloroacetic acid (**4**, 20 g) was added and the reaction was allowed to proceed for 1.5 hrs. The carboxyl methyl phenoxy dextran (CM-PhO-Dex, **5**) was precipitated and washed with excess EtOH, collected via filtration and dried under vacuum. The degree of carboxyl functionalization on **5** was determined using acidimetric titration with phenolphthalein. **5** (1 g) was then dissolved in 30 mL H_2O, pH 5, at 25 °C with NHS (0.35 g) and EDC (0.6 g). 3-aminophenylboronic acid (0.47 g, **6**) dissolved in 5 mL DMF was added to the solution and the reaction was allowed to proceed for 12 hr. The final boronic acid functionalized phenoxy-dextran (BA-PhO-Dex, **7**) was

precipitated and washed with excess EtOH, collected via filtration and dried under vacuum. The degree of functionalization with **6** was determined based on a UV-vis absorption calibration curve at 413 nm (Figure 3.3), giving $\varepsilon = 0.0013\ mM^{-1}cm^{-1}$.

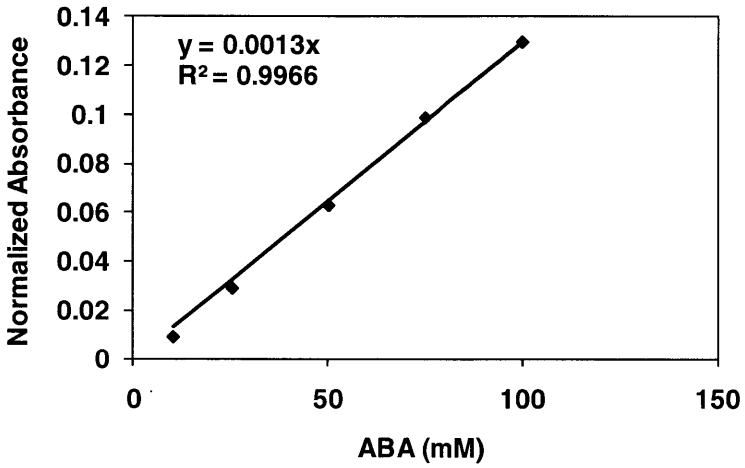

Figure 3.3 Calibration curve for determination of boronic acid composition in the synthesized BA-PhO-Dex polymer. $\varepsilon = 0.0013\ mM^{-1}cm^{-1}$. Absorption was taken at 413nm.

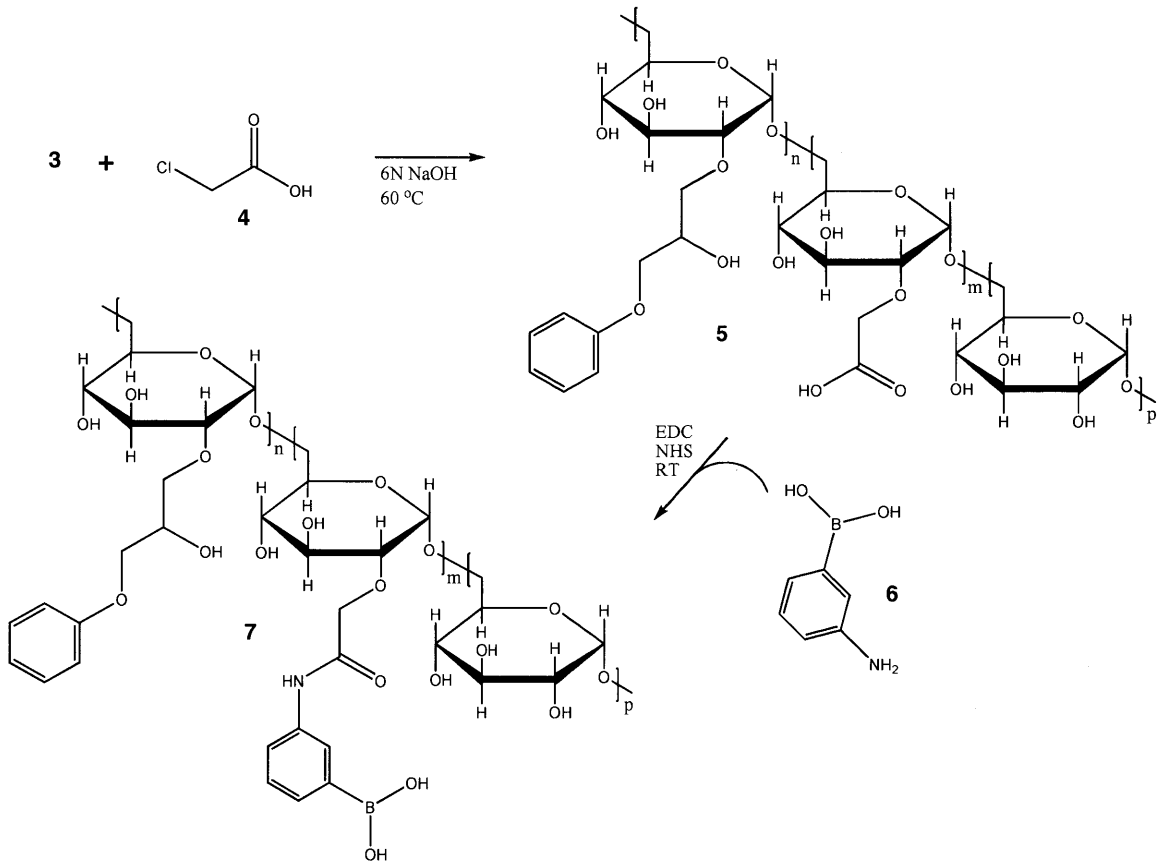

Figure 3.4 Schematic for the synthesis of boronic acid functionalized phenoxy-dextran, **7**.

3.2.3 Synthesis of RITC-PEG-RITC and FITC-PEG-FITC

Synthesis scheme of RITC-PEG-RITC and FITC-PEG-FITC is shown in Scheme 3.5. For RITC-PEG-RITC (3), amine difunctionalized poly ethylene glycol (NH_2-PEG-NH_2, 5kDa, or 20 kDa, 0.1 mol/l, 1) and rhodamine isothiocyanate (RITC, 0.22 mol/l, 2) were dissolved in mixture of 1:1 dichloromethane (CH_2Cl_2):dimethylformamide (DMF). 0.2 mol/l of N,N-diisopropylethylamine (DIEA) was then added to the reaction mixture. After three hours, the reaction product was precipitated by ether (10x in volume) and re-dissolved in DMF, and this cycle was repeated twice. And the product was precipitated by ether again, and collected using a vacuum filtration system. The purified product was characterized by UV-Vis, and FTIR.

For synthesizing FITC-PEG-FITC (**5**), the same protocol was used except that fluorescein isothiocyanate (FITC, **4**) instead rhodamine isothiocyanate (RITC, **2**) was added to the reaction mixture. The purified product was characterized by UV-Vis, and FTIR.

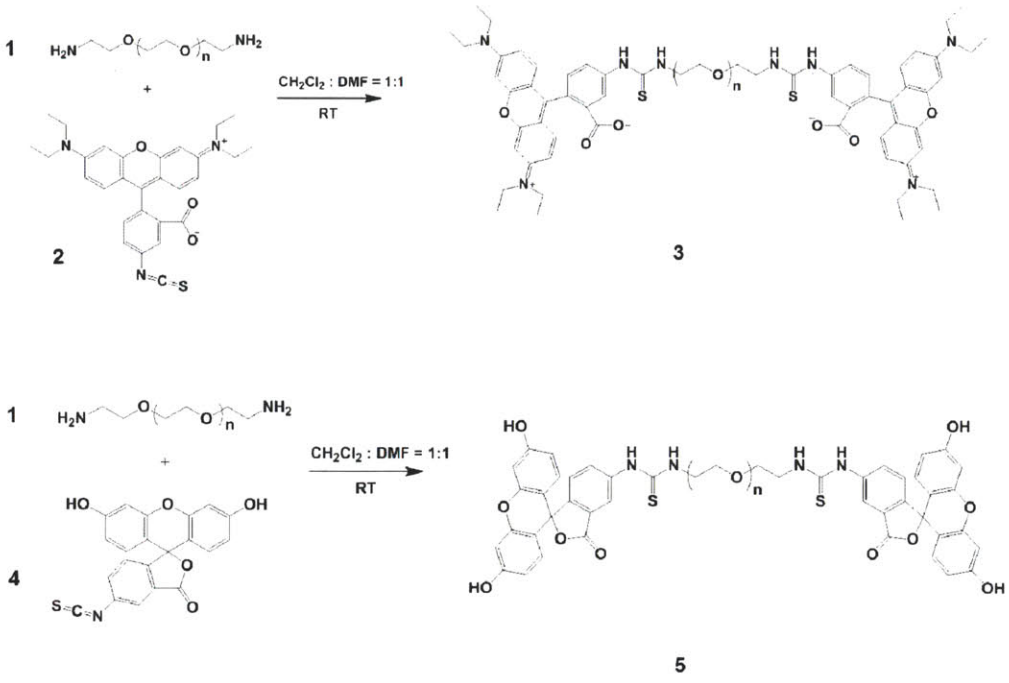

Figure 3.5 Schematic of the synthesis of RITC-PEG-RITC, **3** and FITC-PEG-FITC, **5**.

3.2.4 Synthesis of NH_2-PPEG8 (3) and Fmoc-Phe-PPEG8 (5):

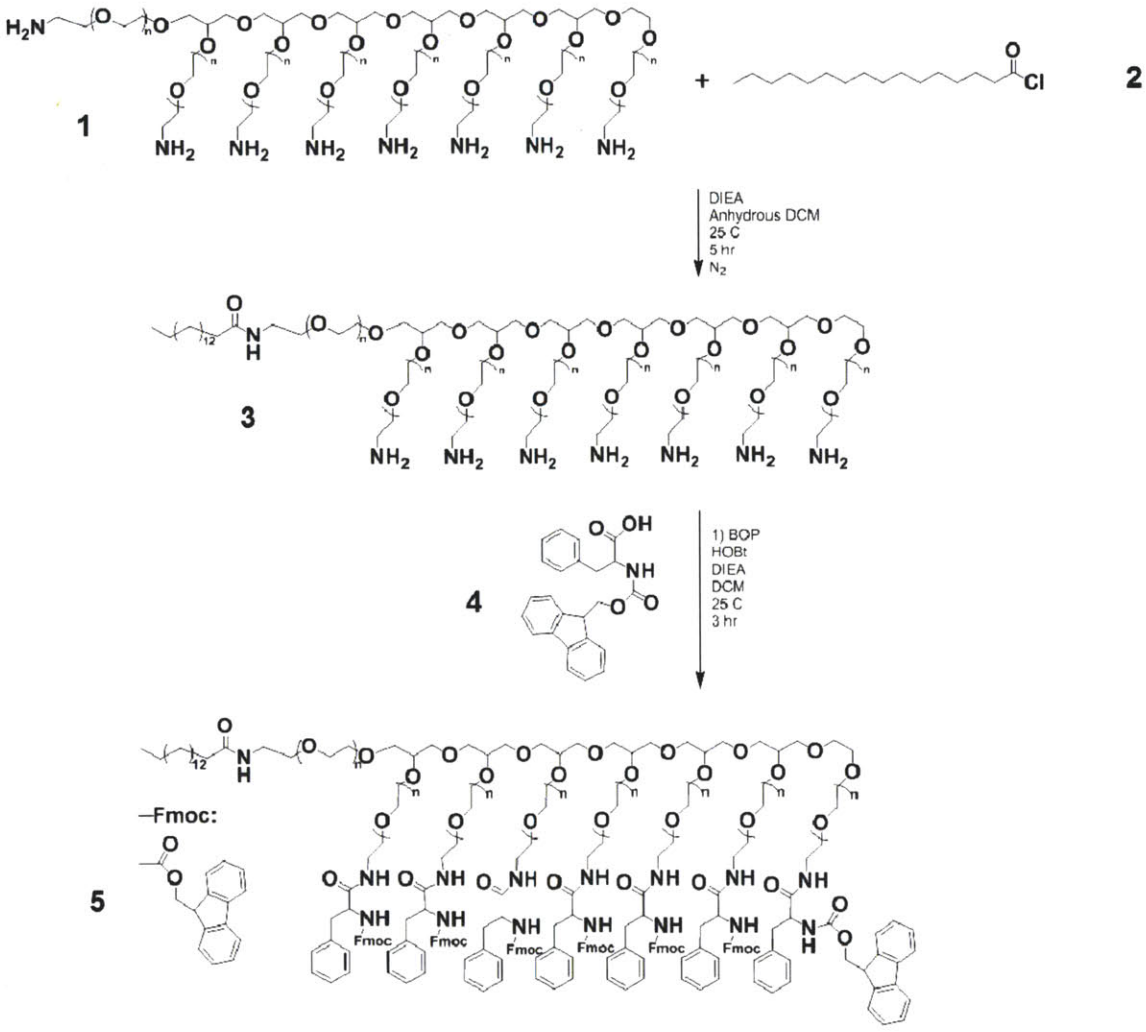

Figure 3.6 Schematic of the synthesis of Synthesis of NH_2-PPEG8 (**3**) and Fmoc-Phe-PPEG8 (**5**).

Synthesis of NH2-PPEG8 (3) and Fmoc-Phe-PPEG8 (5) were carried out following the scheme 3.6, modified from references [155, 156]. 2.4 g of 1 (10kDa) was weighed out and contained in a septum-sealed round bottom flask (RBF), and nitrogen was introduced through a schlenk line to the flask, and the air was removed through an outlet. 10 ml of anhydrous DCM was added to the flask to dissolve 1. 46 µl of DIEA was added to the flask using a microsyringe. A 20 ml vial sealed with septum was prepared, and

nitrogen was introduced for 10 min while air was removed through an outlet. 6 ml of anhydrous DCM was added to the vial, followed by 80 μl of 2 through a microsyringe. After complete mixing, the mixture in the vial was taken out using a 10 ml syringe and dropwise added to RBF for 30 min. After 6 hours of reaction under nitrogen environment, ether was added to precipitate the product, and the solvent was decanted out, and the product was re-dissolved in DCM. After three cycles of precipitation and decanting, the final precipitates were collected and dried in was dried under vacuum using the schlenk line. The product 3 was characterized using FTIR (Figure 3.7).

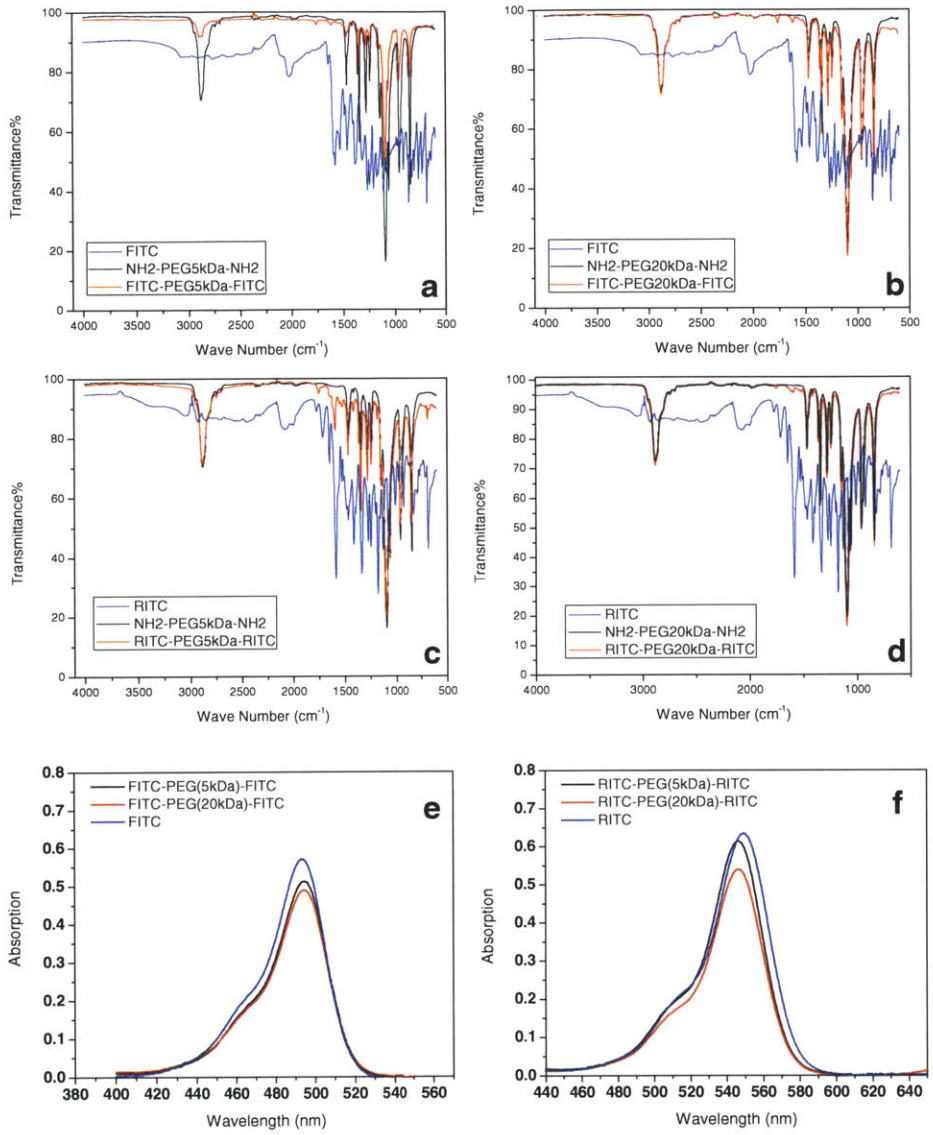

Figure 3.7 Characterization of the RITC-PEG-RITC, FITC-PEG-FITC polymers. FTIR spectra of RITC-PEG-RITC (a, 5kDa; b, 20kDa) and FITC-PEG-FITC (c, 5kDa; d, 20kDa). UV-Vis absorption spectra of FITC-PEG-FITC and FITC in 0.01 M NaOH (e), RITC and RITC-PEG-RITC in methanol (f). Both FITC and RITC were prepared in a concentration assuming that PEG is bifunctionalized. Degree of bifunctionalization of FITC-PEG (5kDa)-FITC is 90%, FITC-PEG (20kDa)-FITC 86%; degree of bifunctionalization of RITC-PEG (5kDa)-RITC is 97%, RITC-PEG (20kDa)-RITC 85%.

To synthesize 5, 0.5 g of 3, 0.199 g of Fmoc-Phe-OH (4), 0.243 g of benzotriazole-1-yl-oxy-tris-(dimethylamino)-phosphonium hexafluorophosphate (BOP reagent), 0.074 g

of 1 - hydroxybenzotriazole hydrate (HOBt) was dissolved in 7 ml of DCM. Fmoc-Phe-OH was added 1.5x7:1 mol/mol to NH2-PPEG8, and BOP, HOBt, and DIEA was added 1.6x7:1 mol/mol to NH2-PPEG8. The reaction was carried out for 3 hours at RT after the addition of 96 µl of DIEA. Ether was used to precipitate the product using the same protocol as suggested above, and the final product was dried under vacuum using the Schlenk line. The product 5 was characterized using UV-Vis (Figure 3.8).

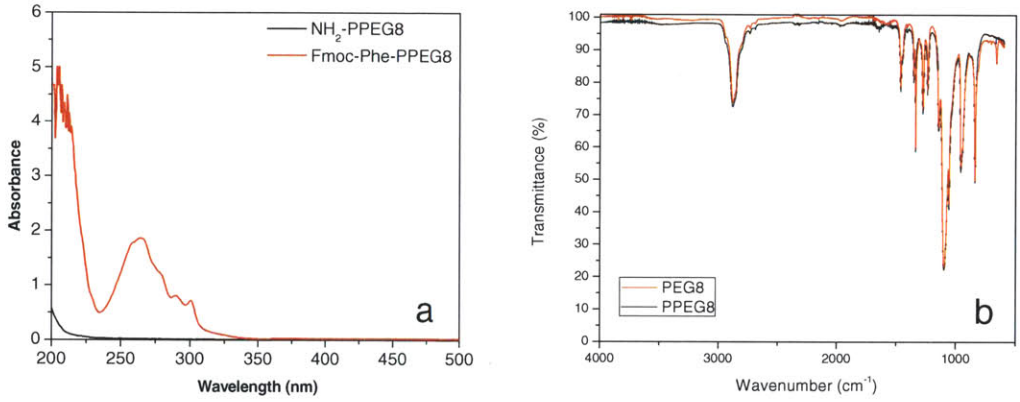

Figure 3.8 Fmoc-Phe-PPEG8, NH2-PPEG8 polymer characterization using UV absorption (a) and FTIR (b).

3.2.5 DNA Oligonucleotide, Pepetide, and Polymer Nanotube Suspension:

SWCNTs were suspended with $(GT)_{15}$ and other oligonucleotides using methods similar to those published[22]. Briefly, SWCNTs were suspended with a 30-base (dGdT) sequence of ssDNA in a 2:1 DNA:SWCNT mass ratio with typical DNA mass concentration being 1 mg/ml in 0.1 M NaCl. Both samples were sonicated with a 3 mm probe tip (Cole-parmer) for 10 min at power of 10 watts followed by twice of a 90 minute benchtop centrifugation (Eppendorf Centrifuge 5415D) at 16,100 x g afterwards the pellet discarded.

For suspension with Fmoc-Phe-PPEG8 and NH_2-PPEPG8, SWCNTs were suspended with the polymer in a 2:1 polymer:SWCNT mass ratio with polymer concentration being 2 mg/ml. Typical volume was 40 ml. Both samples were sonicated with a 6 mm probe tip (Core-parmer) for 40 min at power of 10 watts followed by twice of a 90 minute benchtop centrifugation (Eppendorf Centrifuge 5415D) at 16,100 x g afterwards the pellet discarded.

For suspension with other polymer materials, SWCNTs were first suspended in a 2 wt % sodium cholate (SC) aqueous solution using previously published methods[19, 24]. Briefly, 1 mg/mL NanoC or Unidym SWCNTs were added to 40 mL 2 wt % SC in NanoPure H_2O and were sonicated with a 6 mm probe tip at 40 % amplitude (~12W) for 1 hr in an ice bath. The resulting dark black solution was ultracentrifuged in an SW32 Ti rotor (Beckman Coulter) at 153,700 RCF (max) for 4 hrs to remove unsuspended SWCNT aggregates and catalyst particles. The desired polymer for SWCNT suspension was then dissolved, at 1 wt %, in the SC – SWCNT and the mixture was placed in a 12 – 14 kD MWCO dialysis bag and dialyzed against 2L 1X PBS buffer (50 mM, pH 7.4) for 24 hours to remove free SC and allow the polymer to self-assemble on the nanotube surface. To suspend RITC-PEG-RITC and FITC-PEG-FITC, a similar procedure was used except that the polymer was suspended at 2 wt% for RITC-PEG (5 kDa)-RITC and FITC-PEG (5 kDa)-FITC, 7.0 wt% for RITC-PEG (20 kDa)-RITC and 7.2 wt% FITC-PEG (20 kDa)-FITC to keep a consistent molar concentration of both FITC and RITC in the suspension. The dialysis buffer was changed after 4 hrs to ensure SC removal. The resulting suspensions were clear to the eye and were free of SWCNT aggregates, indicating successful suspension[100].

3.3 Instrumentation, Microscopy, and Program Automation

3.3.1 High-throughput Screening Setup

The high-throughput screening setup is similar to Section 2.24, but with improved automation by simplifying programs (Figure 3.9).

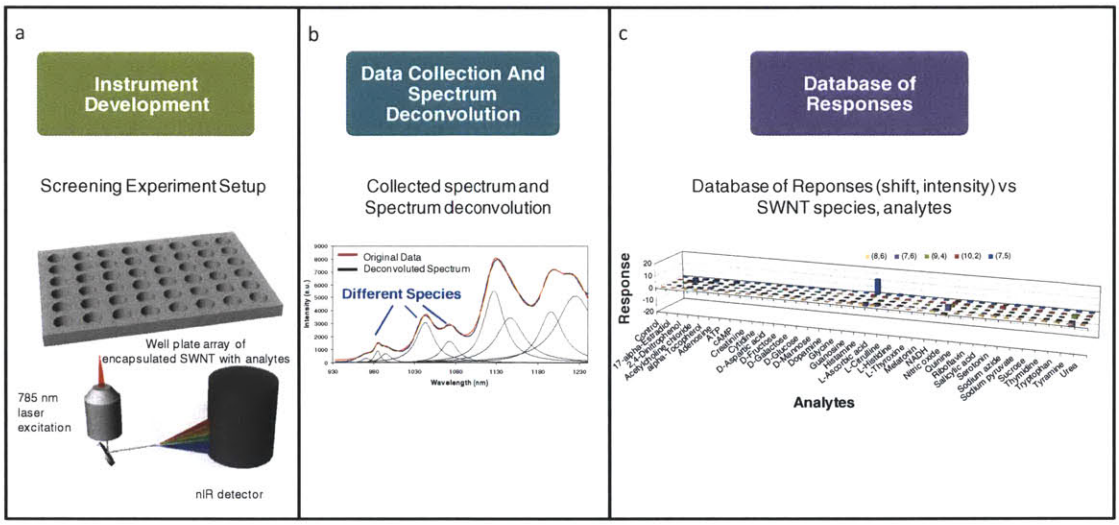

Figure 3.9 Process diagram of the high-throughput screening project. (**a**) Instrumental development involves a microscope setup where an array of wells containing differently polymer wrapped SWCNT is subjected to the screening of 36 analytes. (**b**) Data collection and spectral deconvolution: Upon laser excitation, SWCNT photoluminescence spectrum from each individual well is captured by a near infrared detector. The setup is controlled by a program so that the excitation - emission - record process is automatic. A spectral deconvolution program (Section 2.2.5) is written to resolve SWCNT photoluminescent peaks of different SWCNT chiralities. (**c**) Construction of database for responses: For each experiment, triplicates are performed on the same set of analyte per polymer-SWCNT complex), two modes of responses including intensity change and spectral shift are analyzed against analyte and SWCNT chiralities. The responses are summarized as a database for comparison across different polymer-SWCNT complexes in the future.

As an estimate of the size of the resulting data set, for each polymer wrapping there are 576 data-points from eight unique SWCNT species, two SWCNT fluorescence modalities[48] (intensity change and wavelength shift), and 36 analytes (8x2x36). Screening 10 polymer-SWCNT complexes at 30 s/analyte in triplicate with control spectra takes approximately 30 hours. Spectral deconvolution methods are the same as in

Section 2.2.5, and initial peak positions are identified through excitation-emission profile (Figure 3.10).

This data set forms a molecular "fingerprint" that characterizes, among other variables, the spatial configuration and permeability of the adsorbed phase around the nanotube, its redox state and the ability for target molecules to dynamically modulate the adsorbed phase in a switch-like fashion.

Representative spectra for RITC-PEG-RITC, FIT-PEG-FITC, PE-PEG, SC, Fmoc-Phe-PPEG8, Fmoc-Phe-PPEG4, NH_2-Phe-PPEG8, GT_{15}, BA-PhO-Dex, PhO-Dex, PVA, SDS – SWCNT are shown in Figure 3.30-3.53.

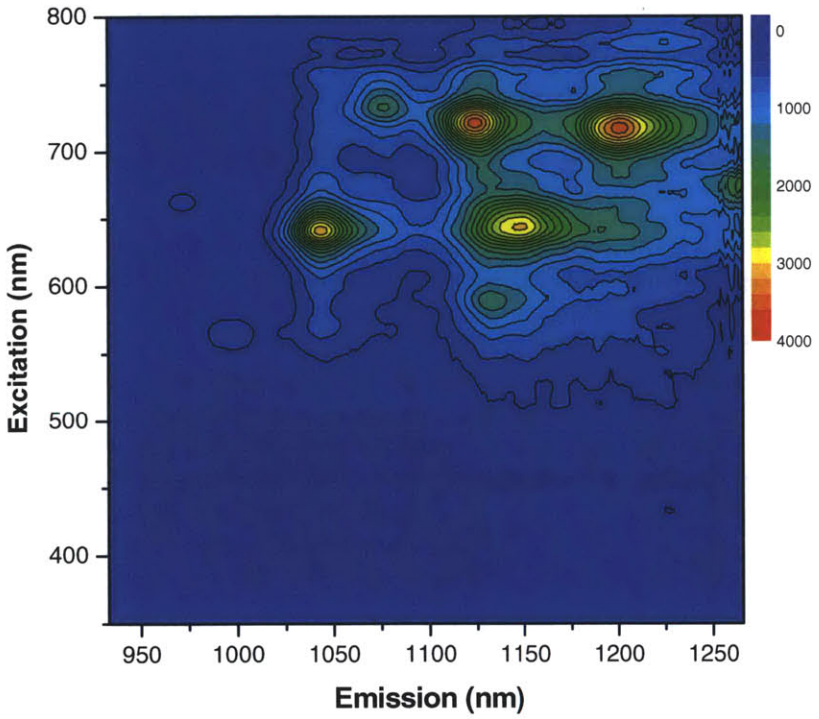

Figure 3.10 Contour plot of fluorescence intensity versus excitation and emission wavelengths for BA-PhO-Dex – SWCNT and nanotube assignment.

3.3.2 Dual-Channel Microscope and Fluorescence Detection

The recognition sites created in this work have immediate utility as fluorescent sensors of biological molecules. We have constructed a dual-channel microscope for imaging spectral shifts of nanotube fluorescence (Figure 3.11). The home-made microscope allows spectroscopic information to be elucidated by splitting the image into two channels which are adjacent in wavelength. Exposed to 658 nm laser (LDM-OPT-A6-13, Newport Corp) excitation, three SWCNT species including (8,3), (7,5) and (7,6) show bright PL. The emission light from the sample is split into two beams. The light from both beams is treated with filters to spectroscopically isolate one emission peak, and then to permit only half of the peak's emission to appear in each channel. One channel (right) on the same near infrared detector array (InGaAs OMA V array detector through a PI Acton SP2150i spectrometer) shows the long wavelength half of the peak, and the other (left) contains the short wavelength half. The filters used were designed to measure the (7,6) nanotube which has the emission maximum at 1147 nm before exposure to any analytes. The 50% cut-off/cut-on of the two edge filters used were 1100 and 1180 nm respectively to band the (7,6) emission. A 1140 nm longpass and a 1140 nm shortpass filter were placed in the emission beam before splitting to isolate the (7,6) peak.

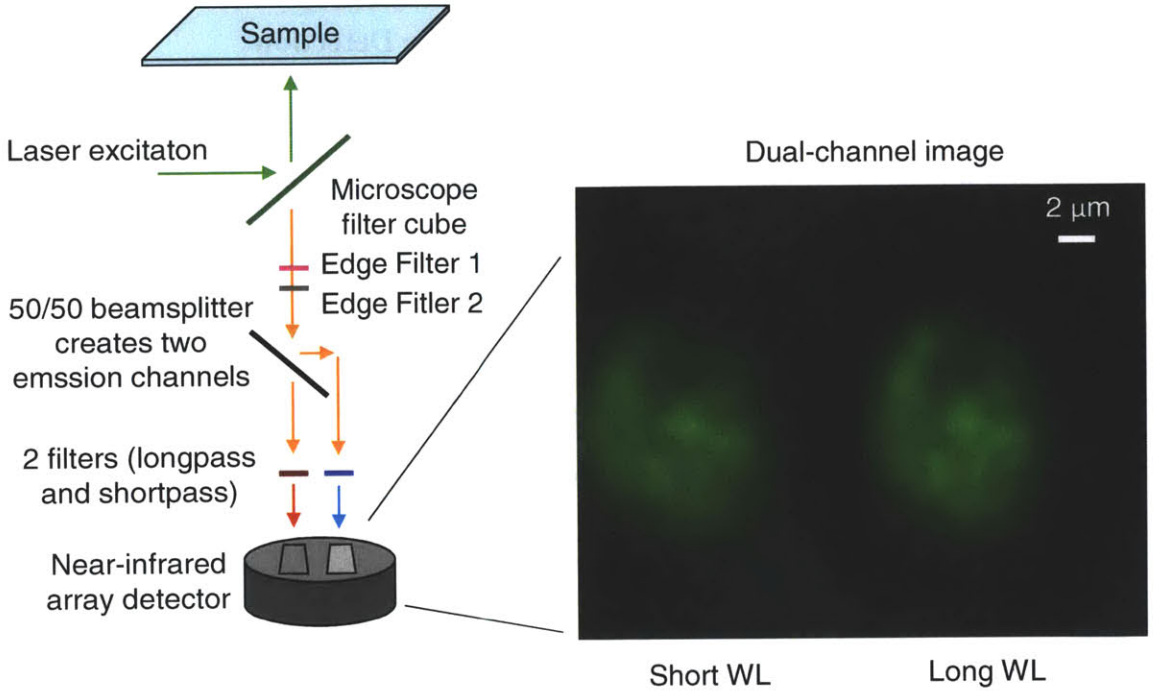

Figure 3.11 Dual channel microscope scheme. Light leaving the sample passes through a bandpass filter to spectroscopically isolate one nanotube fluorescence band. This light reaches a 50/50 beamsplitter which creates two equal beam pathways. The resulting beams pass through edgepass filters (a longpass for one and a shortpass for the other) with a 50% cut-off/cut-on at the same wavelength. The beams are captured by two different regions of a near infrared array detector.

After incubated with SWCNT for 12 hrs, the cells were ready for fluorescence imaging. This dual-channel microscope mentioned above was used to monitor in real time the change of nIR PL of BA-PhO-Dex – SWCNT inside the macrophage (Figure 3.25), in response to extracellularly-added riboflavin. Real time movies were acquired using the WinSpec data acquisition program (Princeton Instruments) for 1 hr. Visible images were acquired using an attached CCD camera (Carl Zeiss, ZxioCam MRm).

3.3.3 Dual-Channel Microscope Image Processing:

Each frame in the movie is subject de-noised by median filtration with the kernel size set to 3 x 3. The quantitative analysis is then performed as follows: total

photoluminescence quenching response is represented by normalized intensity; shifting response of the emission maximum is represented by the normalized intensity of the right (1140 – 1180 nm) channel divided by the normalized intensity of the left channel (1100 – 1140 nm). To visualize the results of analysis, a binary mask is generated by thresholding the initial frame, in which the pixels whose intensity value is above an empirically determined value is considered as within the region of interest. The values of the pixels outside this region are set to zero in the visualized results.

3.4 Polymer-SWCNT Suspension Characterization Methods

Experimentally available characterization techniques including single-particle tracking microscopy, TEM can be potential tools for imaging and characterizing the polymer adsorbed phase on the SWCNT. Another very useful technique is MD simulation, which was performed mainly in collaboration with Professor Blankschtein's group. Experimental data on molecular binding constant, polymer coverage on the SWCNT and others were generated by us and provided to our collaborator.

3.4.1 Radio-labelling and Analysis

Experimentally, we have shown that upon recognition of a molecule, the fluorescence of the polymer-SWCNT complex modulates accordingly. Adsorption isotherm and binding constants can be obtained by plotting the degree of fluorescence change (including wavelength shift and intensity change) as a function of the concentration of the molecule. However, this scheme involves two-steps for the final signal transduction. First, the molecule binds to the polymer-SWCNT complex; and then, the binding induces a signal transduction mechanism that involves fluorescence modulation. Although

providing a very sensitive detection scheme, the kinetics and the thermodynamics involved could deviate from those of the actual binding events. In order to understand this and extract the kinetics and thermodynamics of the actual binding, other experimental methods independent of the fluorescence scheme will be helpful.

The most straightforward scheme is to radiolabel the molecule of interest and quantify the radioactivity of the molecules bound on the recognition polymer-SWCNT surface, and compare it with that amount of radioactivity on a polymer-SWCNT that does not recognize the molecule. A modified scheme could be to incubate the molecules with both the recognition polymer-SWCNT and a random polymer-SWCNT separately, and compare the amount of unbound molecules through radioactivity measurement. Binding constant can be constructed by performing the experiments at different starting concentration of the molecule, and compare the value with that is from the fluorescence measurement. Either scheme would involve a method of separating the unbound molecule from the polymer-SWCNT complex. We proposed to use dialysis, spin filtration device, or size-exclusion column for separating free molecules from polymer-SWCNT complexes. One concern was that those membrane based devices may have certain non-specific interactions with even polymer-SWCNT complexes, and tried to use bovine serum albumin (BSA), triton, or other proteins or surfactants to pre-saturate those non-specific binding sites on the membrane, reducing this effect.

Specifically, adsorption isotherm of riboflavin onto the BA-PhO-Dex – SWCNT, PhO-Dex – SWCNT, as well as BA-Pho-Dex polymer was measured using ^{3}H-labeled riboflavin. The SWCNT solution used in this experiment was 2 mg/l, which was the same used in the fluorescence-based binding measurements. In both SWCNTs samples, free

polymer was removed in advance. And polymer solution was 6.7 mg/ml, which we kept the same as the polymer concentration in the BA-PhO-Dex – SWCNT sample.

The ^{3}H-labeled stock riboflavin was prepared as follows. Stock solutions of non-labelled riboflavin were first prepared in DMSO at four concentrations, including, 10 mM, 3.33 mM, 1.33 mM, and 132.8 μM. By mixing with ^{3}H-riboflavin (EtOH, 81.57 μM, 12.3 Ci /mmol) in 1:3 ^{3}H-vol/^{1}H-vol ratio, the four stock solutions contained the same amount of radioactivity, ethanol (25 vol%) and DMSO (75 vol%), but four concentrations of total riboflavin amount (7.5 mM, 2.5 mM, 1 mM, 0.12 mM).

Each prepared ^{3}H-labeled stock was added into a 350 μl 33 mg/l BA-PhO-Dex – SWCNT at 1 vol% to reach the final concentration of 75 μM, 25 μM, 10 μM, and 1.2 μM respectively, and the solution was well-mixed using pipettes. The SWCNT concentration has to be high enough to have enough riboflavin adsorb and give enough counts in the scintillation instrument. After 1 hour of waiting, from each sample, 50 μl of the mixture solution was taken out and mixed with scintillation fluid (5 ml) and used later for radioactivity counting. The remaining solution was passed through a size-exclusion column (PD MiniTrap^{TM} G-25, Exclusion limit Mr, 5000, GE HealthCare) that was prepared with BSA. In the column preparation step, 300 μl BSA (1 mg/ml) had been passed through the column at least 4 times before the column was ready for use. After the following the centrifugation protocol given by the size exclusion column, the filtrate was collected which presumably containing BA-PhO-Dex-SWCNT and the surface bound riboflavin. And the free riboflavin was assumed to be completely caught inside the column due to the size-exclusion effect. This was in fact supported by the control

experiment where a starting material of ^{3}H-labeled 7.5 mM riboflavin in PBS resulted in less than 20 counts per minute readout, which is the same as the baseline.

50 μl of the filtrate was taken and mixed with the scintillation fluid (5 ml) and then the radioactivity was measured by the scintillation counter, and the radioactivity was also converted to riboflavin concentration by measuring the radioactivity of a concentration known solution of the same type.

SWCNTs concentration of the filtrate was also needed. Even though the column was prepared with BSA in advance, there were always some residual SWCNTs that were caught inside the column. In order to eliminate the concentration-induced difference in radioactivity in the filtrate, we also performed the above experiments using not labelled riboflavin, and the absorption of the SWCNTs in the filtrate was measured using UV-Vis (λ_{632} nm = 0.036 mg/l^{-1}). This way, radio-contamination of the cuvettes was prevented.

The same protocol was used for obtaining binding isotherms for both the PhO-Dex – SWCNT and BA-PhO-Dex polymer. Experiments were performed in triplicates.

3.4.2 Single Particle Tracking (SPT) and Diffusivity Analysis:

Single particle tracking is a very commonly used method to image and track nanoparticle movement via microscopy imaging. Our laboratory and others[157-159] have previously used this technique to study both diffusional and translational diffusivity of carbon nanotubes. By keeping track of the trajectory of the particles, the mean square displacement (MSD) of the particle can be computed, and thus diffusivity can be calculated through the following equations, assuming the technique is a 2-D tracking method.

$$MSD = \left\langle r^2(t) \right\rangle = \left\langle \frac{1}{N} \sum_{i=0}^{N} (r_i(t) - r_i(0))^2 \right\rangle (1)$$

$$D = \frac{1}{4} \lim_{t \to \infty} \frac{d(MSD)}{dt} (2)$$

In this work, 10 μl SWCNT at 5-10 mg/l in water (SDS-SWCNT was imaged in 50 mM PBS buffer) was dropped in between two cover slips, and the fluorescence of the SWCNT was imaged and monitored in real time through a 100x TIRF objective for hours using an inverted microscope (Carl Zeiss, Axiovert 200), with a 2D InGaAs array (Princeton Instruments OMA 2D) attached. Movies were acquired at 0.25, 0.5 or 1 s/frame using the WinSpec data acquisition program (Princeton Instruments) for at least 1000 frames. Typically, 2-3 movies were taken per sample to account for possible variations among samples.

In order to estimate the hydrodynamic radius of the SWCNT, we estimated the average length of the SWCNT to be 550 nm by AFM (Figure 3.20), and the following equation was used where with a known diffusivity value, we solved for diameter, *D*[160-162].

$$D_0 = \frac{k_B T}{3\pi\eta L} [\ln(L/D) + 0.316 + 0.5825(D/L) + 0.050(D/L)^2]$$

The radii obtained from SPT are summarized in Table 3.1.

3.4.3 AFM

100 nm silicon wafers were pre-cleaned using acetone, followed by water, and then isopropyl alcohol. For sample preparation, 20 μl of SWCNT sample at concentrations between 10 - 20 mg/l was deposited on the substrate, and incubated at room temperature for 10 min to 1 hour. The concentration of the SWCNT and the time of incubation is

adjusted based on the density of SWCNT on the resulting film. After incubation, the sample was rinsed rigorously with DI water, and then dried under nitrogen before imaging.

AFM images were taken using Asylum MFP-3D model in tapping/AC mode with Asylum Tapping/AC mode soft tips (AC240TS). Typical scan size was 5 μm or 10 μm, adjusted based on the density of the SWCNT on the substrate. Scan rate was in between 1 - 1.5 Hz, adjusted based on the image quality, and the scan angle was always set to be 0.0°. The resultant AFM images are shown in Figure 3.19. Radii for various polymer-SWCNT constructs estimated from AFM are summarized in Table 3.1.

3.4.4 TEM

TEM images were taking using JEOL JEM 2010 high-resolution TEM with a LaB6 electron gun which can be operated between 80 – 200 kV. In a standard procedure, 1 μl of SWCNT solutions were dropped onto HC200-Cu Holey Carbon Film (Electron Microscopy Sciences), and dried in air for a few minutes. TEM images are shown in the Fig. 3.20, and the resultant diameter estimation are summarized in Table 3.1.

3.5 Cell Cultures

Raw 264.7 macrophage cells were cultured in Dulbecco's modified Eagles' medium (DMEM) containing 4.5 g/l glucose and 4 mM l-glutamine and further supplemented with 10% (v/v) heat-inactivated FBS and 1% Penicillin:Streptomycin solution. Cells were maintained at 37 °C in a humidified atmosphere with 5% carbon dioxide. Before the experiment, cells were transferred and grown in a petri dish with Leibovitz's L-15 medium and cultured at 37 °C in a humidified atmosphere. Six hours after re-plating, 0.005 μM of SWCNT was added into the culture medium, and the cells were maintained

at 37 °C in a humidified atmosphere for 12 hrs, allowing SWCNT engulfed into the cells before imaging.

3.6 Results and Discussions

To generate polymer-nanotube interfaces, candidate polymers have been synthesized in the lab. Those polymers are amphiphilic polymers such that hydrophobic domains stack on the SWCNT surface and the hydrophobic domains extend into aqueous phase, enabling entropic stabilization. In our studies, only non-ionic or weakly ionic polymers were chosen for simplicity in order to gain structural understanding. The screening is performed by parallel addition of the library of 36 analytes (Table 2.1) to the synthetic polymer-SWCNT solution contained in a 96 well plate. Excited at 785 nm, the emission spectra were deconvoluted with a custom developed spectral fitting algorithm written in MatLab that also calculated error bars. The resulting intensity and wavelength changes of each construct subjected to the addition of each analyte were recorded, with original data shown in Figures 3.30 – 3.53. This approach allowed us to identify three examples of polymer-SWCNT mediated molecular recognition.

The simplest example is the rhodamine isothiocyanate-difunctionalized poly(ethylene glycol) – SWCNT complex, or RITC-PEG-RITC – SWCNT (Figure. 3.12-i, 5 or 20 kDa), which shows fluorescence quenching exclusively to estradiol (both alpha- and beta-estradiol). To compare with this particular complex, we synthesized two additional synthetic variants, fluorescein isothiocyanate difunctionalized PEG, or FITC-PEG-FITC (Figure 2.11-ii) and distearyl phosphatidylethanolamine-PEG (PE-PEG, Figure 3.12-iii), which result in similar, non- selective response profiles. The selectivity of the response

shown by RITC-PEG-RITC – SWCNT is distinct from other schemes suing principle component analysis [163] or differential sensor responses[164] for analyte recognition, and we therefore assign it as the first demonstration of molecular recognition. In the polymer-SWCNT complex, the RITC fluorescence is quenched, providing evidence that the hydrophobic ends of the polymer are adsorbed onto the SWCNT surface (Figure 3.13). The hydrophilic PEG chain forms a loop extending into solution. This structural configuration is also corroborated by molecular dynamics (MD) simulations (performed by Dr. Shangchao Lin in Blankschtein's lab) for the three polymers (Figure 3.12a). Estradiol contains an aromatic group which can adsorb to the SWNT surface if the pendant hydroxyl groups are hydrogen-bonded to the adjacent RITC amides. The molecular weight of the PEG chain does not influence the selectivity (Figure 3.14-2.16), but the end group structure has an obvious effect (Figure 3.12a-i,ii,iii). Indeed, RITC is larger than FITC, and is zwitterionic at pH 7, resulting in electrostatic alignment and a denser packing on the SWCNT. The molecular recognition of the RITC-PEG-RITC – SWCNT to estradiol results from the strong interaction between the estradiol and RITC anchors. MD simulation at a starting coverage of 50 polymers per 20 nm of SWCNT reveals that at equilibrium, 80% of the SWCNT surface is covered by RITC anchors. Different characterization techniques have been applied here: dry-state AFM estimated a mean radius of 2.5 nm for RITC-PEG-RITC – SWCNT, consistent with 2.7 nm estimated from MD results, but smaller than 8.1 nm that is estimated from single particle tracking (SPT) experiments (Table 3.1). Under the hydrated conditions of SPT, the hydrodynamic radius can be increased. TEM images (Figure 3.20) indicate a range of radii from bare

surface (0.47 nm) to approximately twice the AFM average value (4.9 nm), reflecting variable surface coverage along the length.

Table 3.1 Tabulation of diffusivity and radius obtained from SPT, MD, AFM and TEM

Polymer - SWCNT	**Diffusivity**	**Radius**			
	$\mu m^2/s$	**nm**			
	SPT	**SPT***	**MD****	**AFM†**	**TEM††**
RITC-PEG20k-RITC – SWCNT	1.39	8.11	2.7	2.5±1.8	0.47 – 4.9
FITC-PEG20k-FITC – SWCNT	1.89	2.10	1.9	2.0±1.6	
Fmoc-PPEG8 – SWCNT	1.82	2.50	1.9	3.67±1.3	4
NH_2-PPEG8 – SWCNT	2.02	1.50	1.5	2.36±0.8	
BA-PhO-Dex – SWCNT	1.97	1.75	1.9	2.56±0.8	3.3 – 7.5
PhO-Dex – SWCNT	2.19	1.15	1.7	1.62±0.6	
SDS – SWCNT	1.81	3.12	1.2		
SC – SWCNT	2.10	1.33	1.2		

*SPT: single-particle tracking
** MD: Molecular dynamics
†AFM: Atomic force microscopy
††TEM: Transmission emission microscopy

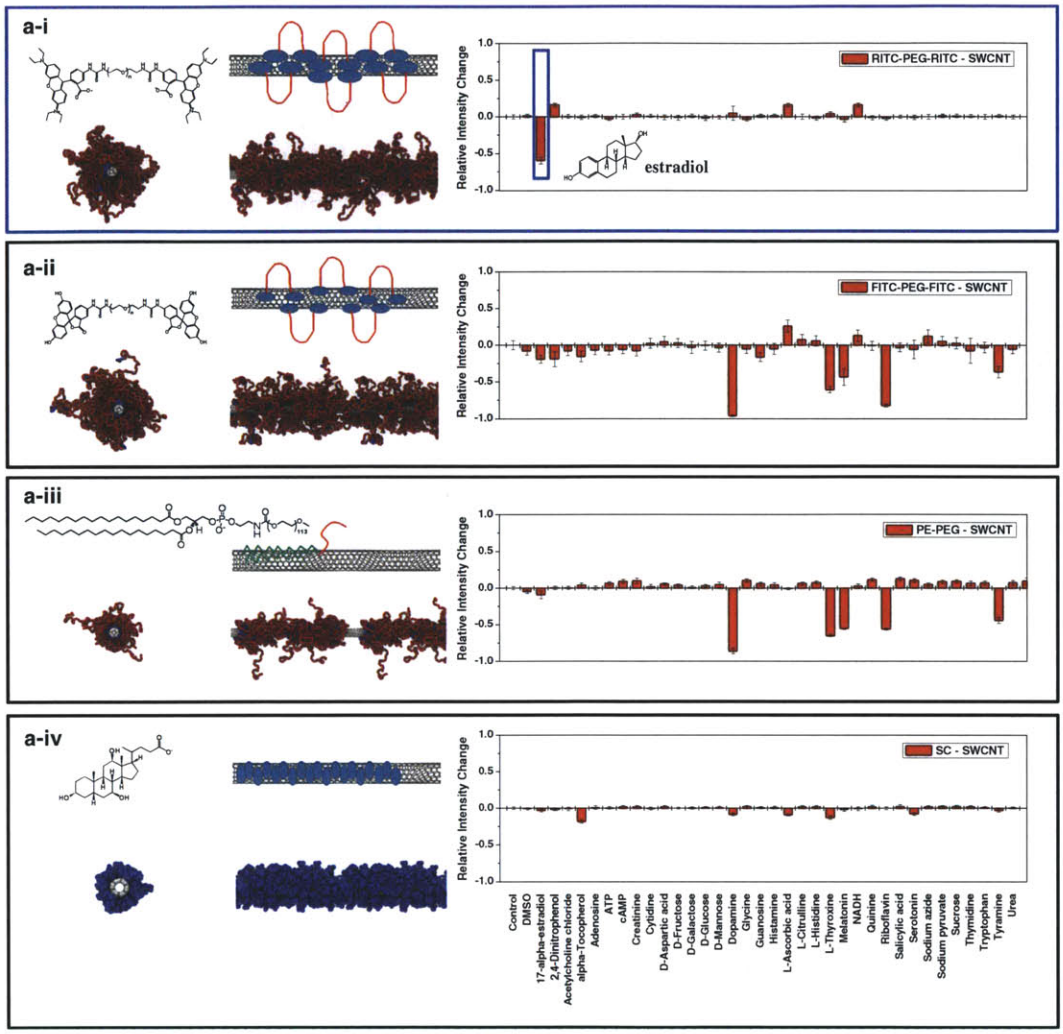

Figure 3.12 Three distinct examples of polymer-nanotube complexes that selectively recognize a molecule and their chemical analogs that do not present selectivity. (**a-i, b-i, c-i**) Three examples of nanotube antibodies including RITC-PEG-RITC – SWCNT (**a-i**), Fmoc-Phe-PPEG8 – SWCNT (**b-i**) and BA-PhO-Dex – SWCNT (**c-i**). The images on the top left of each panel is generated by performing molecular dynamics simulation either in aqueous solution or vacuum. Color codes can be referred in MD section in the supplements. A simplified molecular representation derived from either MD or chemical structure is drawn on the bottom left of each panel. Spectrum of each of the complex is shown on the top right, and RITC-PEG-RITC – SWCNT and Fmoc-Phe-PPEG8 – SWCNT show selective quenching response upon exposure to 100 μM 17-α-estradiol, and 100 μM of L-thyroxine respectively, and BA-PhO-Dex – SWCNT shows a selective shift in wavelength to 100 μM of riboflavin. (**a-ii, a-iii, a-iv, b-ii, b-iiii, b-iv**) Structure of FITC-PEG-FITC – SWCNT (a-ii), PE-PEG – SWCNT (a-iii), SC – SWCNT (a-iv), Fmoc-Phe-PPEG4 – SWCNT (b-ii), NH_2-PEG – SWCNT (b-iii), and GT_{15}-SWCNT (b-iv) and their fluorescence intensity responses to the same panel of molecules. No selective intensity response is observed among those SWCNT complexes.

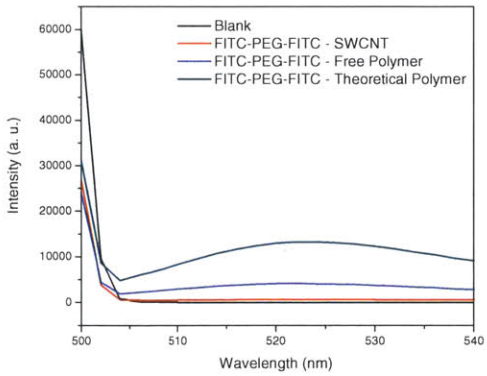

Figure 3.13 Quenched FITC fluorescence of the FITC-PEG-FITC polymer on SWCNT. The spectra were taken in a plate reader, excited at 494 nm. A FITC-PEG-FITC – SWCNT sample pass through a 100 k filter unit to remove the free polymer which shows emission (blue, λ_{max} = 523 nm), and the remaining polymer-SWCNT solution shows the same intensity as a PBS baseline, indicating the quenched state of the FITC on the SWCNT (red). Green line shows a fluorescence spectrum of a FITC-PEG-FITC, the concentration of which is prepared such that FITC ends of the polymer fully covers the SWCNT surface.

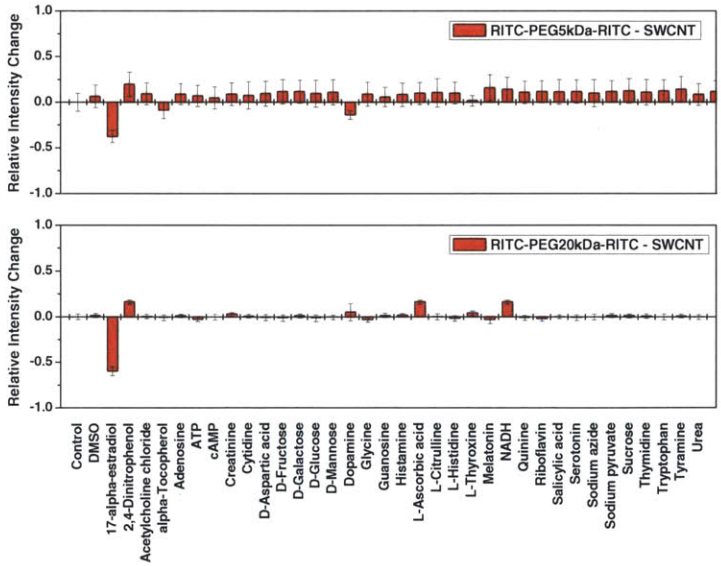

Figure 3.14 The relative fluorescence change compared to the control for RTIC-PEG5kDa-RITC (top) and RTIC-PEG20kDa-RITC (bottom) – (7,5) SWCNT after being exposed to a panel of 36 analytes.

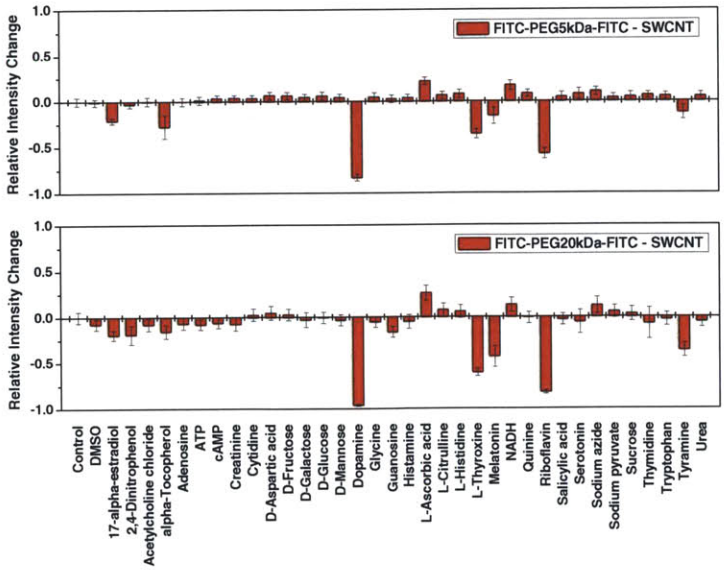

Figure 3.15 The relative fluorescence change compared to the control for FTIC-PEG5kDa-RITC (top) and FTIC-PEG20kDa-RITC (bottom) – (7,5) SWCNT after being exposed to a panel of 36 analytes.

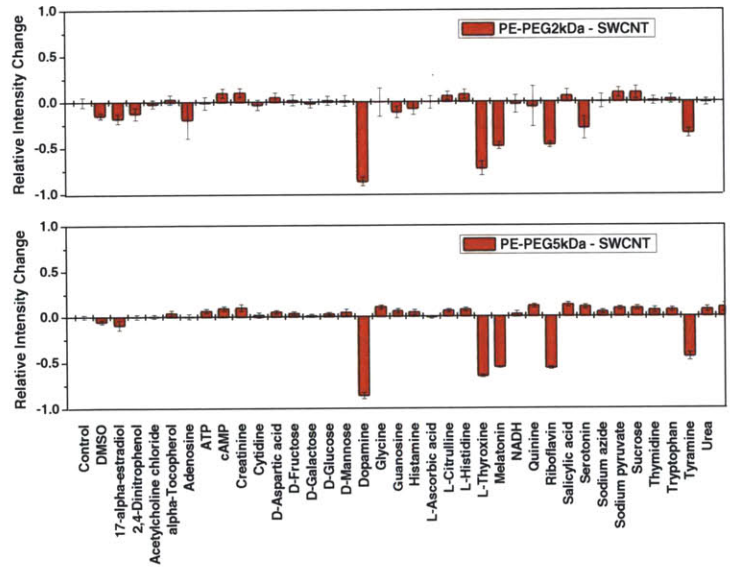

Figure 3.16 The relative fluorescence change compared to the control for PE-PEG2kDa-RITC (top) and PE-PEG5kDa-RITC (bottom) – (7,5) SWCNT after being exposed to a panel of 36 analytes.

Sodium cholate (SC) adsorbed SWCNT (Figure 3.12-iv) does not show responses to the analyte library tested, confirming the tight surface packing reported previously[165].

In contrast, $d(GT)_{15}$ DNA wrapped SWNT (Figure 3.17-iv) shows non-selective responses, suggesting a more porous interface composed of consecutive DNA helices that has also been reported previously [105]. This type of response profile that informs the accessibility of molecules to the SWCNT surface, as presented in Figure 3.12, Figure 3.17 and Figure 3.18, allows for a unique "fingerprinting" of polymer adsorbed phases in a manner inaccessible to other analytical techniques such as NMR, FTIR, and UV absorption in the field of nano-structure characterization. Structural schematics of the nanotube-complexes were deduced from a combination of polymer molecular structure and fingerprinted response profile, further supported by SPT data and MD results.

A more complex example is the PEG brush described in Figure 3.17. One brush segment is alkylated for hydrophobicity such that this segment adsorbs on the SWCNT surface, while the remaining sites can display a variety of functionalities depending upon the additional chemistry. When these sites contain Fmoc L-phenylalanine (Fmoc-Phe-PPEG8), a 7-membered brush structure recognizes L-thyroxine (Figure 3.17b-i), whereas a 3-membered analog does not (Figure 3.17b-ii). Replacing the Fmoc L-phenylalanine with amine groups results in a loss of selectivity as well (NH2-PPEG8, Figure 3.17b-iii), presumably due to the decrease in polymer hydrophobicity. For Fmoc-Phe-PPEG8 – SWNT, both the aliphatic chain and the Fmoc group adsorb on the SWCNT. Analogous to the previous example, the PEG group forms loops extending into the aqueous phase, imparting colloidal stability. Additionally, steric hindrance between PEG arms influences the packing density of Fmoc ends on the SWNT surface, providing additional control in engineering the molecular recognition site. For NH2-PPEG8 - SWCNT, only the aliphatic chain is adsorbed on the surface of the SWNT, while the amine group,

protonated at pH of 7, will extend into the aqueous phase. The less-selective response profile of NH2-PPEG8 – SWCNT suggests that there is more empty nanotube surface compared to the Fmoc-Phe-PPEG8 – SWCNT and is also consistent with the polymeric structure.

Yet another example is a 53 mol/mol boronic acid-substituted phenoxy-dextran wrapped SWCNT (BA-PhO-Dex – SWCNT, Figure 3.18a). This emission maximum of the complex red-shifts approximately 11 nm upon addition of riboflavin, but not with other diol-containing substrates that typically bind to boronic acids (Figure 3.21, Figure 3.22). The response is revered upon addition of a riboflavin binding protein (RBP), which binds to riboflavin and competes with the riboflavin - SWCNT binding (Figure 3.23). The optical modulation in this example is a wavelength red-shift instead of a fluorescence quenching shown in other examples. This type of response, attributed to solvatochromism[166] induced by a polymer/water environment dielectric change, is very rare among the systems examined to date. As an example, poly(vinyl alcohol) wrapped SWCNT (PVA – SWCNT, Figure 3.18-iii) does not show such response to the molecular library. Removal of the boronic acid to the phenoxy dextran (PhO-Dex) causes a loss of selectivity, with a response from L-thyroxine (Fig. 3.18-ii). MD simulation shows that introduction of the boronic acid group decrease the flexibility of the dextran and increases the surface coverage. Alternatively, sodium dodecyl sulfate (SDS, Fig. 3.18-iv) adsorbed SWCNT shows a non-selective response, presumably from a more loosely packed adsorbed layer predicted by other literature[167, 168], allowing for a greater molecular access to the SWCNT surface. MD simulation shows that introduction of the boronic acid group makes the dextran less flexible and increases the

surface coverage. Alternatively, sodium dodecyl sulfate (SDS, Figure 3.18c-iv) adsorbed SWCNT shows a non-selective response, presumably from a more loosely packed adsorbed layer[167, 168], allowing greater molecular access to the SWCNT surface. Comparison of radii of various polymer-SWCNT complexes using multiple characterization methods is available in Table 3.1.

The apparent dissociation constants K_d for all three selective constructs span a range in values, and are tunable by changing the chemical composition of the polymer. The response, either $\Delta I / I$ or $\Delta\lambda$, can be described by a Type I adsorption isotherm, or $\Delta\lambda = \Delta\lambda_{max} C/(C+K_d)$ (Figure 3.24a-c). We find K_d to be 25 μM for RITC-PEG-RITC – SWCNT to estradiol, 2.3 μM for Fmoc-Phe-PPEG8 – SWCNT to L-thyroxine, and 4.2 μM for BA-PhO-Dex – SWCNT to riboflavin (Figure 3.24a-c). The binding affinity and selectivity of BA-PhO-Dex – SWNT to riboflavin in a mixture of 10 different diols is unaffected, demonstrating the practical utility of the sensor in a mixture environment (Figure 3.24c). Radio-labeling, in the case of ^{3}H labeled riboflavin, reveals riboflavin partitioning into the polymer corona of the non-selective PhO-Dex – SWCNT (K_d = 344 μM, θ_{max} = 50 riboflavin per SWCNT), but the affinity is 5.3 times lower than the selective construct (K_d = 64.2 μM, θ_{max} = 36 riboflavin per SWCNT). In addition, an equal amount of unbound BA-PhO-Dex polymer as in the BA-PhO-Dex – SWCNT solution shows K_d = 72.4 μM, θ_{max} = 4.4 riboflavin per SWCNT, demonstrating minimal binding sites on just the polymer alone. It is likely that the K_d in this case appears larger than that measured from SWCNT fluorescence because some of the riboflavin is removed

as the SWCNT and riboflavin mixture passes the size-exclusion column, shifting the equilibrium.

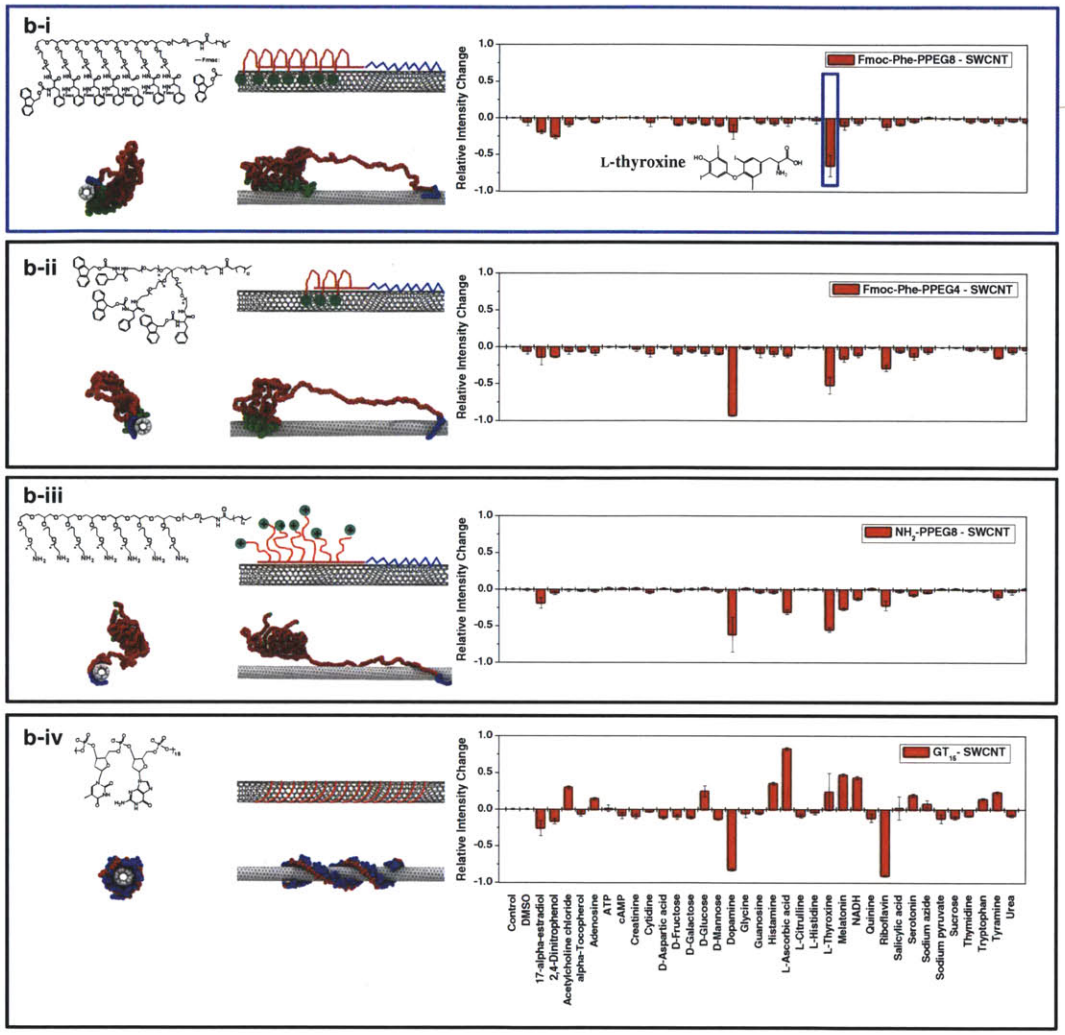

Figure 3.17 Structure of Fmoc-Phe-PPEG4 – SWCNT (b-ii), NH2-PEG – SWCNT (b-iii), and GT15-SWCNT (b-iv) and their fluorescence intensity responses to the same panel of molecules. No selective intensity response is observed among those SWCNT complexes.

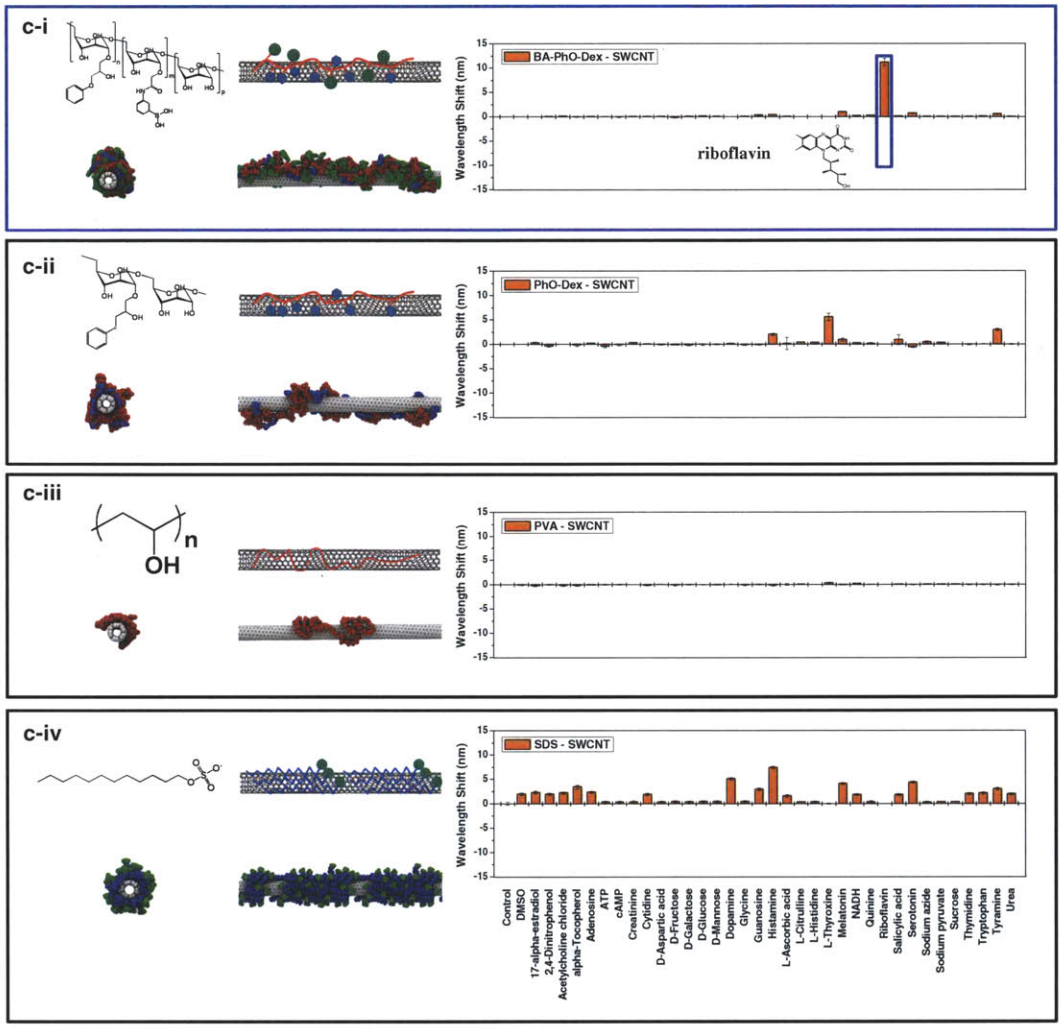

Figure 3.18 Structure of PhO-Dex – SWCNT (c-ii), PVA – SWCNT (c-iii), and SDS – SWCNT (c-iv) and the shift in emission maximum of the nanotube spectrum upon exposure to the same library of nanotubes. No selective shifting response is observed among those SWCNT complexes. For all the panels in this figure, bar chart indicates either intensity (red chart) or shift (blue chart) response of the polymer-nanotube complexes to the same panel of molecules. The polymer structure is indicated above the x-axis of the bar chart; and the molecule that the complex is selective to, if any, is indicated below the x-axis. The simplified molecular representation is deduced based on either MD results or the chemical structure of the polymer, supported by additional data such as fluorescence spectroscopy and single particle tracking.

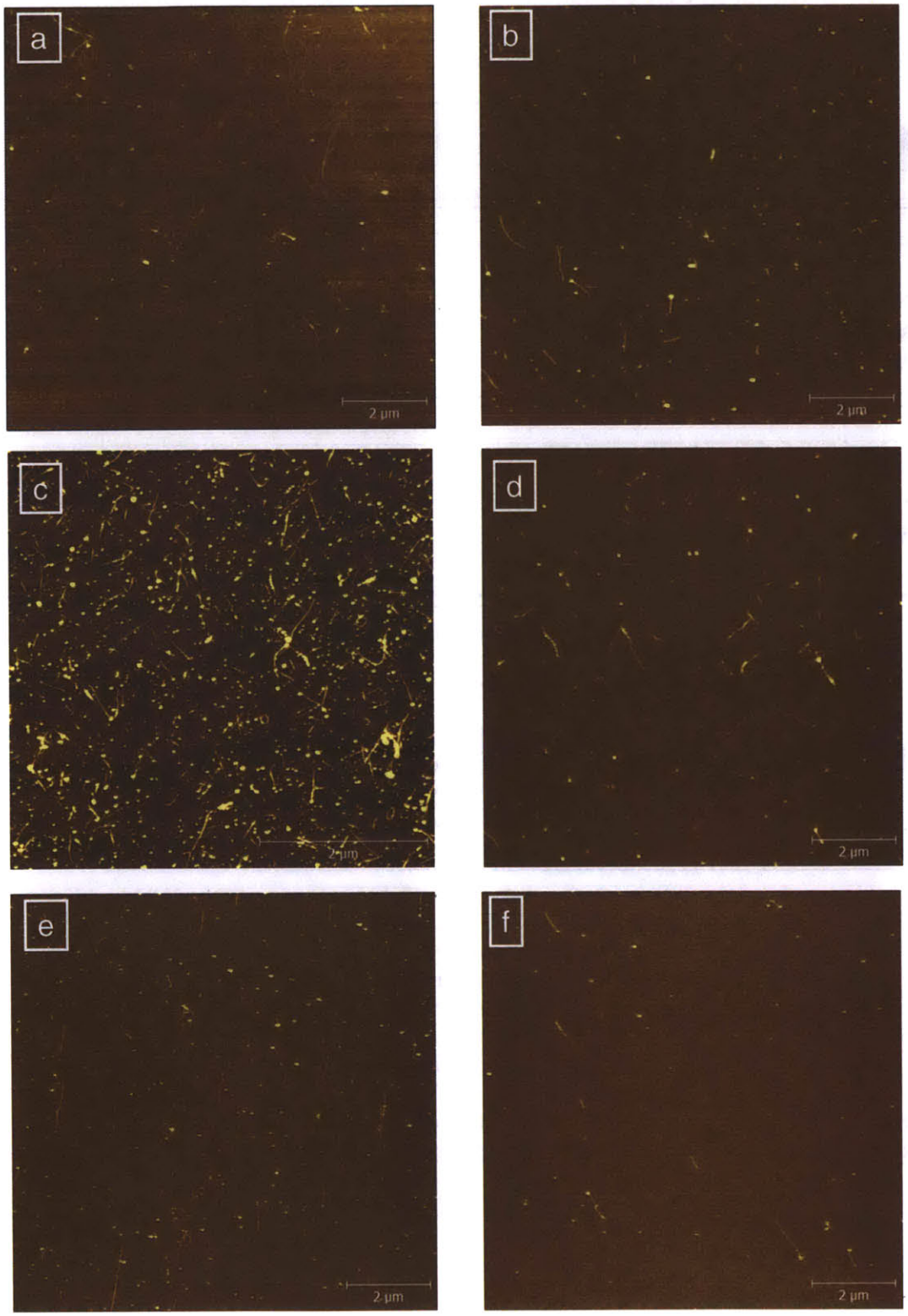
a
2 µm
b
2 µm
c
2 µm
d
2 µm
e
2 µm
f
2 µm

Figure 3.19 AFM height images of polymer-SWCNT complexes: (a) RITC-PEG-RITC – SWCNT, (b) FITC-PEG-FITC – SWCNT, (c) Fmoc-Phe-PPEG8 – SWCNT, (d) NH_2-Phe-PPEG8 – SWCNT, (e) BA-PhO-Dex – SWCNT, (f) PhO-Dex – SWCNT.

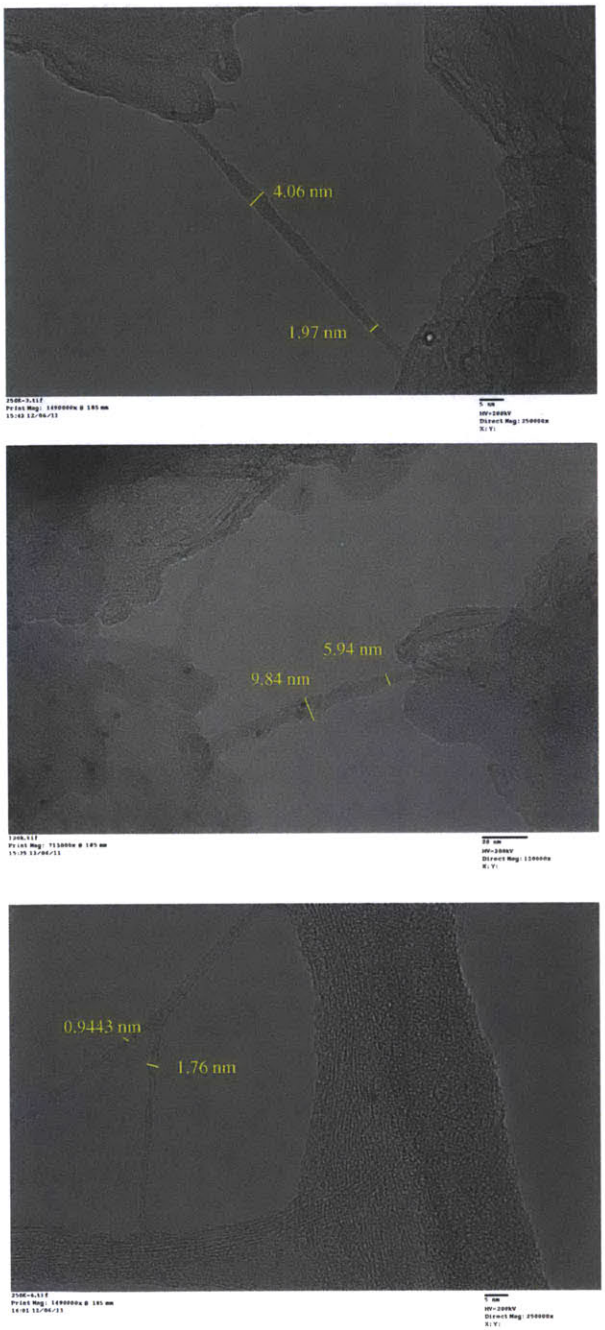

Figure 3.20a TEM images of RITC-PEG-RITC – SWCNT.

Figure 3.20b TEM images of Fmoc-Phe-PPEG8 – SWCNT.

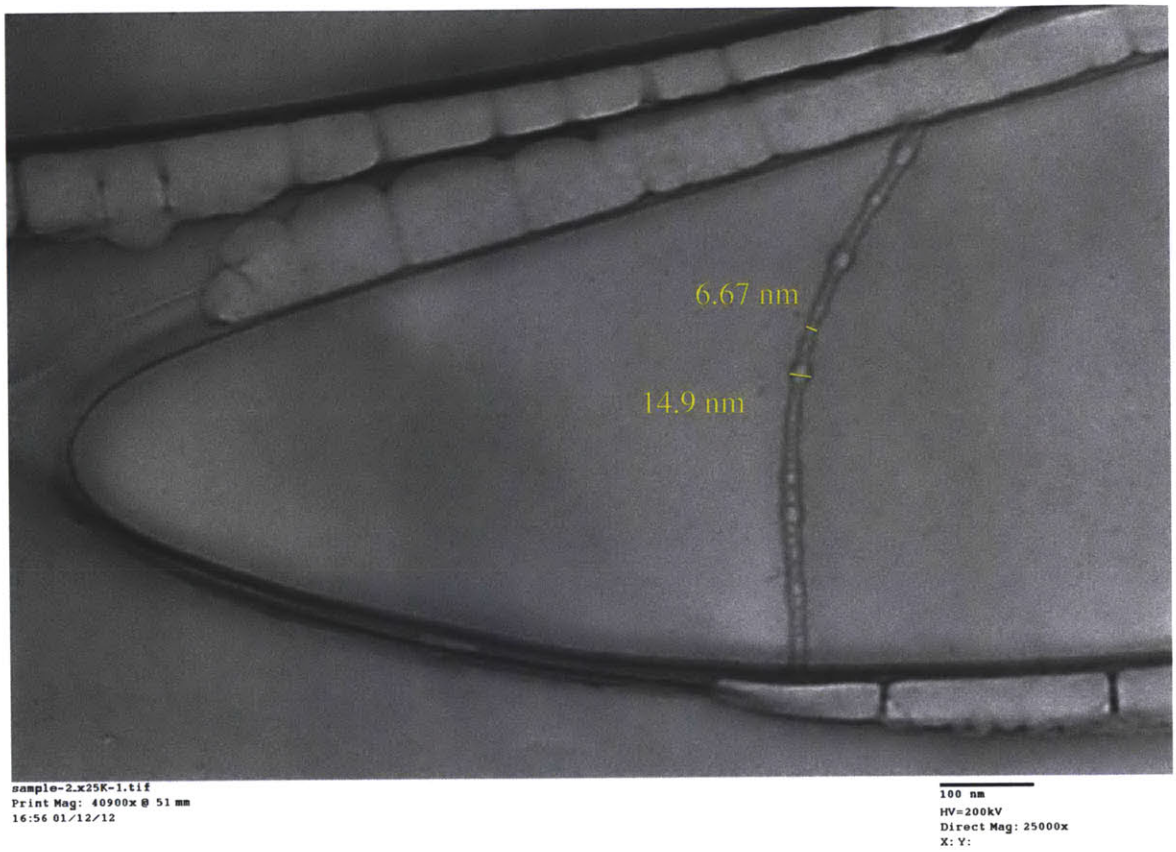

Figure 3.20c TEM images of BA-PhO-Dex – SWCNT.

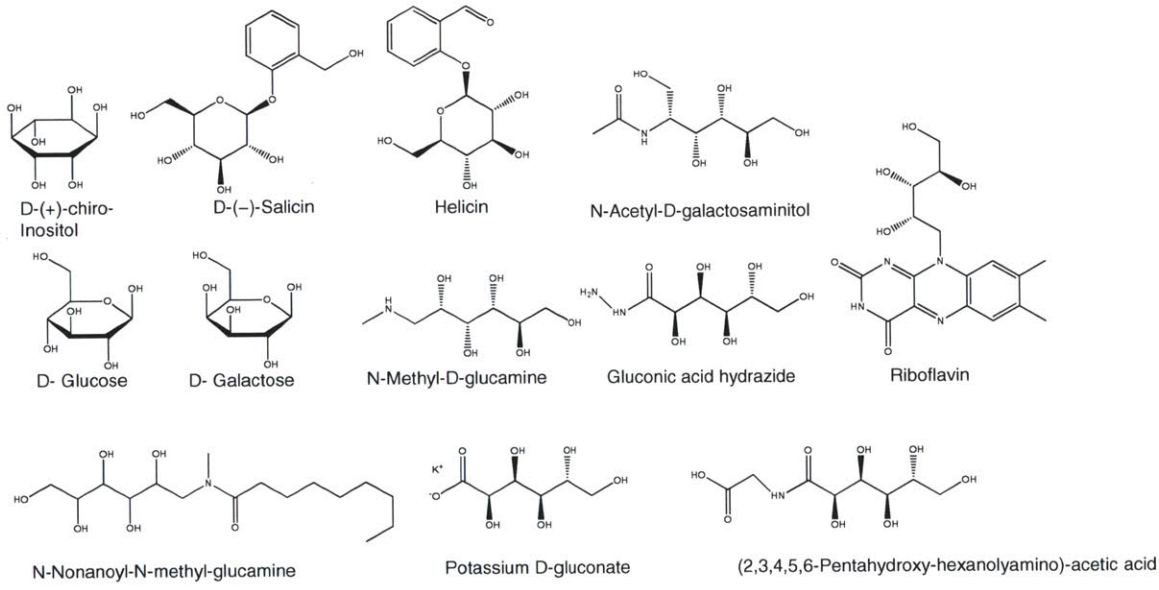

Figure 3.21 List of diol-containing molecules used in both competitive binding experiments.

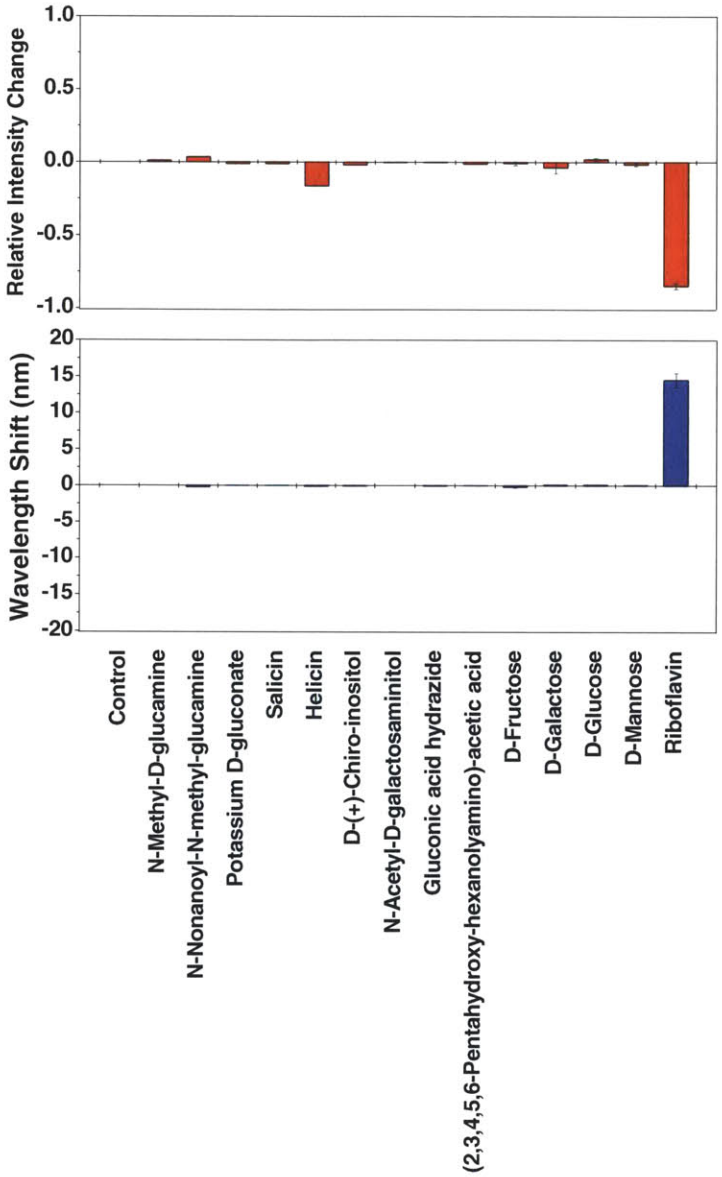

Figure 3.22 The relative fluorescence intensity change (top) and shift in emission maxima for BA-PhO-Dex –SWCNT after being exposed to a panel of diol-containing analytes. (Figure 3.21 shows the molecular structure of those molecules). Concentration of riboflavin is 100 μM, gluconic acid hydrazide is 100 μM, and others are 500 μM. The concentrations of the first two compounds are constrained by their solubility.

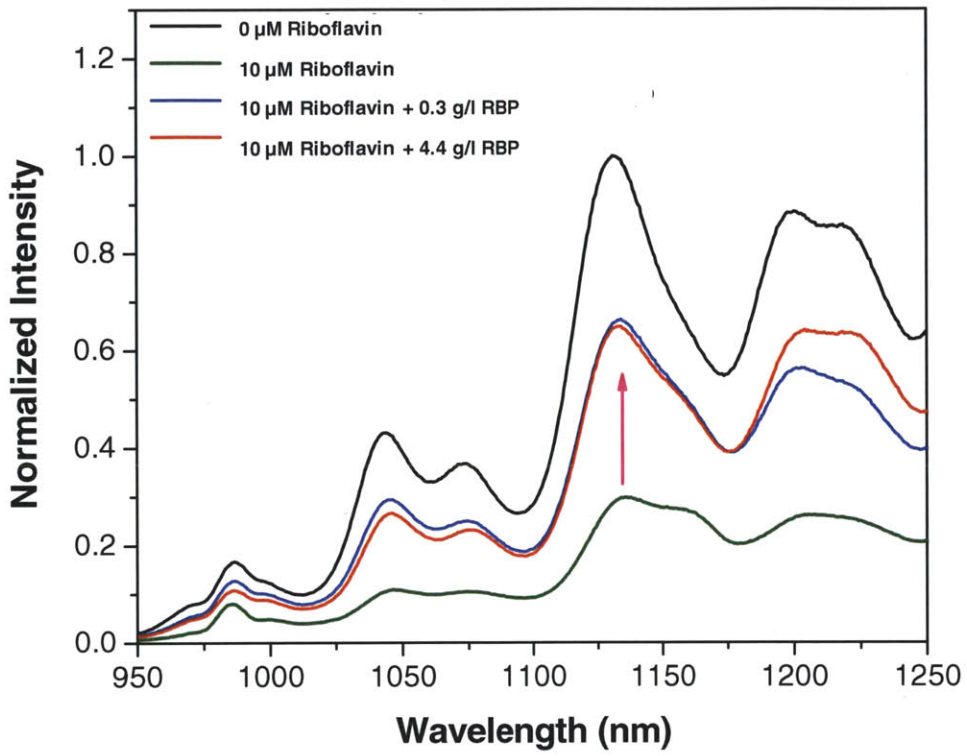

Figure 3.23 Reversible quenching of BA-PhO-Dex – SWCNT PL in response to riboflavin. Addition of 10 µM of riboflavin causes the PL of SWCNT (2 mg/l) to quench; and the addition of riboflavin binding protein (RBP) of 1:1 ratio, with 0.37 g/l RBP, reverses the quenching response. Nanotubes were excited at 150 mW with a 785 nm laser.

The structure of the BA-Pho-Dex – SWCNT allows exploration of small changes in the polymer composition. Dextran alone does not suspend SWCNTs, and the phenoxy groups create SWCNT adsorption sites via π-stacking[6, 169]. One can alter the polymer composition in a manner analogous to allosteric mutagenesis in proteins[170, 171] and examine the resulting K_d of each variant. The K_d for riboflavin decreases with increasing boronic acid:dextran ratio and decreasing phenoxy:dextran ratio (Figure 3.24e), with optimal binding occurring at a SWCNT diameter of 0.88 nm (Figure 3.24f). The K_d can be decreased 1600 fold to 1.03 µM (Table 3.2), by selecting a polymer composition

of 80 mol/mol boronic acid:dextran and the (7,6) chirality nanotube. This K_d is similar to analyte binding proteins such as glucose binding protein[172] (K_d = 0.4 μM). Hence, the binding affinity of these SWCNT complexes is comparable to some natural-occurring antibodies and bio-recognition sites. It may be possible to identify and compositionally tune a wide range of 'sensor antibodies' for various analytes with both the polymer and nanotube contributing to the recognition.

Table 3.2 Tabulation of Kd. BA-PhO-Dex – SWCNT with phenoxy:dextran ratio of 5.75 and boronic acid:dextran ratio of 53.3 was reported in Figure 3.24 c,d.

Phenoxy/Dextran (mol/mol)	Boronic Acid/Dextran (mol/mol)	K_d (μM)					
SWCNT Species		(6,5)	(7,5)	(10,2)	(9,4)	(7,6)	(8,6)
5.75	24.18	65.70	374293.52	546.45	138.89	6.57	6.39
9.93	47.49	684.93	526.32	203.67	23.28	26.98	95.06
8.75	49.66	561.80	1637.33	352.11	35.66	41.15	138.12
5.75	53.3	28.76	133.69	103.95	4.07	4.23	7.64
0	80.91	17.71	168.35	81.90	15.09	1.03	20.10

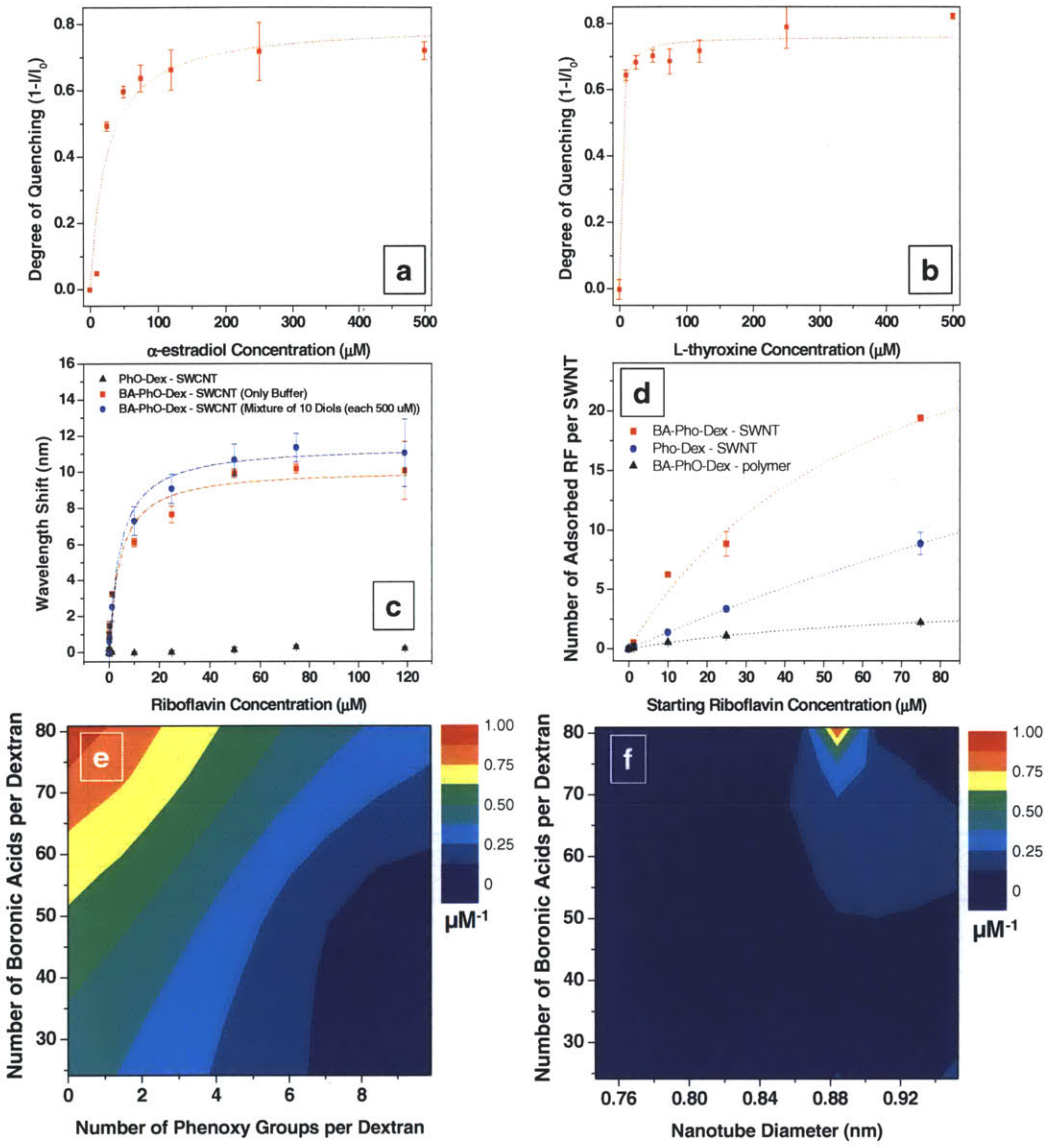

Figure 3.24 Apparent binding constants of nanotube antibodies to the molecule of interest, and the tunability of the binding constant. (**a**) Fluorescence quenching of (7,5) RITC-PEG-RITC – SWCNT as a function of estradiol concentration. Dashed lines are fits of the data to a Type I Langmuir adsorption isotherm with K_d being 25 μM, and $(\Delta I / I)_{\max}$ being 0.80. (**b**) Fluorescence quenching of (7,5) Fmoc-Phe-PPEG8 – SWCNT as a function of L-thyroxine concentration. Dashed lines are fits of the data to a Type I Langmuir adsorption isotherm, with K_d being 2.3 μM and $(\Delta I / I)_{\max}$ being 0.76. (**c**) Shift in emission maximum of (7,6) nanotube of as a function of riboflavin concentration for BA-PhO-Dex – SWCNTs (red squares) and PhO-Dex – SWCNTs (black triangles). Competitive binding curve is also taken for BA-PhO-Dex – SWCNT where each concentration of riboflavin is also mixed with 10 additional diol-containing molecules. Dashed lines are fits of the data with a Type I Langmuir adsorption isotherm with K_d

being 4.23 μM and $\Delta\lambda_{max}$ 10.2 nm with and K_d being 4.39 μM and $\Delta\lambda_{max}$ 11.5 nm without the competing analyte. PhO-Dex – SWCNTs shifting response could not be fit to a Type I isotherm. Reported data points are averages of three separate measurements and reported error bars are 2SD. (**d**) Number of adsorbed riboflavin per SWCNT as a function of starting riboflavin concentration, measured by radio-labeling experiments. Fitting the data with a Type I Langmuir isotherm reveals a K_d of 64.2, 344, 72.4 μM and $\Delta\theta_{max}$ of 36, 50, 4.4 riboflavin per SWCNT for BA-PhO-Dex – SWCNT, PhO-Dex – SWCNT, and BA-PhO-Dex – polymer, respectively. For the case of the polymer, the experiments were performed such that an equal amount of unbound BA-PhO-Dex polymer as in the BA-PhO-Dex – SWCNT solution were used. (**f**) Contour plot of $1/K_d$ of the (7,6) nanotube plotted versus polymer composition. (**e**) Contour plot of $1/K_d$ plotted as a function nanotube diameter versus the boronic acid content.

Riboflavin, or RF (Figure 3.25) is an essential vitamin for eukaryotic organisms necessary for cell survival and its transport is typically facilitated by riboflavin carrier protein (RCP)[173]. Elevated RCP levels may predict late stage (stage III or IV) breast cancer with 100% accuracy.[174] Once transported into cells, RF is then converted intracellularly to flavin mononucleotide (FMN) by riboflavin kinase (RFK, EC 2.7.1.26), and FMN can be further converted to flavin adenine dinucleotide (FAD) by FAD synthetase (PP591, EC 2.7.7.2). Also, FMN and FAD can be converted back to RF via FAD pyrophosphatase (EC 3.6.1.18), FMN phosphohydrolase (EC 3.1.3.2), or other general phosphatases.

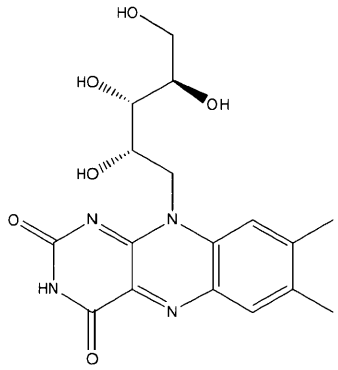

Figure 3.25 Structure of riboflavin.

With a log P value of –1.46, RF is sufficiently lipophillic to diffuse through biological membranes. Although RF can freely diffuse in and out of the cell, FAD and FMN are metabolically trapped within the cell. The high charge density of the phosphate groups prevents movement of these flavins across the membrane.

Although the isoalloxazine three-ring substructure in RF behaves as a fluorescent chromophore, the resultant fluorescent signal is difficult to distinguish from background cellular autofluorescence[175]. Therefore, researchers have been relying on a rhodamine-riboflavin (RD-RF) conjugate to follow intracellular trafficking of RF[176]. Although previous research has shown that that rhodamine-riboflavin conjugate exhibits similar ligand affinity toward the putative riboflavin transport system as [^{3}H]riboflavin, the conjugate itself is twice as big as riboflavin, which may result in a completely different internalization mechanism from riboflavin. In addition, belonging to the category of the organic dyes which photobleach upon laser excitation, this RD-RF conjugate is not suitable for long time monitoring of RF uptake. Therefore, a label-free cellular riboflavin imaging sensor which can monitor riboflavin in real-time would certainly contribute to the area of riboflavin detection.

To demonstrate the sensor utility, we incubated BA-PhO-Dex – SWCNT with Raw 264.7 macrophage cells in a riboflavin free medium overnight (Figure 3.26) [25]. Notice that the fluorescence modulation of the sensor responding to riboflavin is comparable in the buffer solution and in the medium (Figure 3.27). The home-built nIR, dual-channel imaging microscope was designed to spatially image the wavelength shifts of the (7, 6) SWCNT, λ_{max} = 1147 nm, upon riboflavin binding (Figure 3.11, left panel). The PL of the SWCNTs inside the cell can be clearly seen using the microscope (Figure 3.11, right

panel). Upon addition of riboflavin to extracellular media, the PL of SWCNTs inside the cell red-shifts systematically over time (Figure 3.26b), responding to the diffusion of riboflavin into the cell. Multiple experiments have been conducted, and the results are shown in Figure 3.28. Control experiments have also been conducted, shown in Figure 3.29. Using these results, it is possible to detect riboflavin concentration gradients inside the cell dynamically and with high resolution. It is the first riboflavin senor to date that can do real-time cellular imaging without photobleaching threshold.

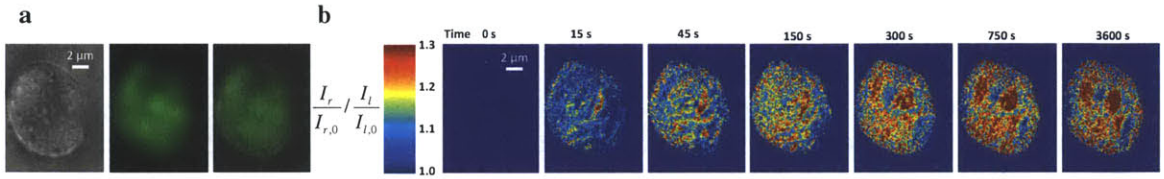

Figure 3.26 Application to spatial and temporal chemical imaging in live Raw 264.7 macrophage cells. (**a**) White light image, nIR fluorescence of BA-PhO-Dex – SWCNTs inside the macrophage before the addition of riboflavin, and the resultant overlay. (**b**) Time evolution of the fluorescence from cell-encapsulated BA-PhO-Dex – SWCNTs in response to extracellular riboflavin added at time t = 36 s. The emission maximum shifting response is represented by the normalized intensity of the right channel divided by the normalized intensity of the left channel.

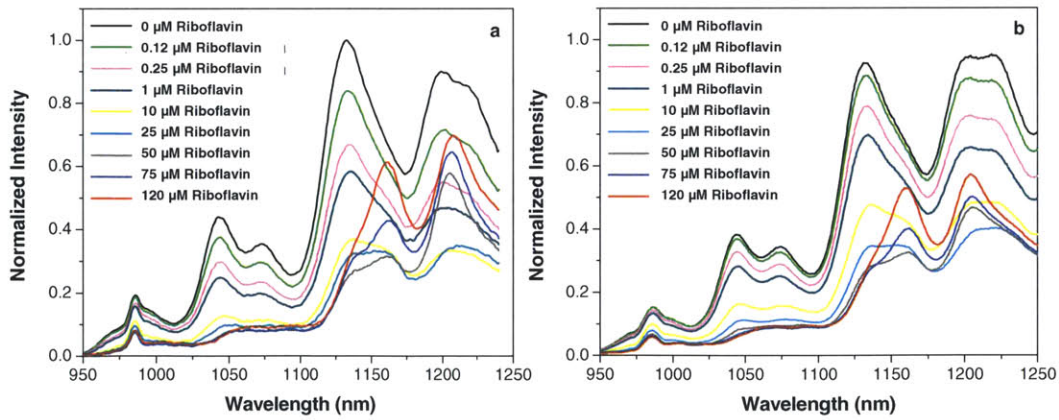

Figure 3.27 Medium stability of the BA-PhO-Dex – SWCNT sensor. Photoluminescence spectra, normalized to the initial intensity, of 53 mol/mol BA-PhO-Dex – SWCNT with 0 to 120 μM riboflavin in pH 7.4 buffer (**a**), Leibovitz's L-15 cell media (**b**). Nanotubes were excited at 150 mW with a 785 nm laser.

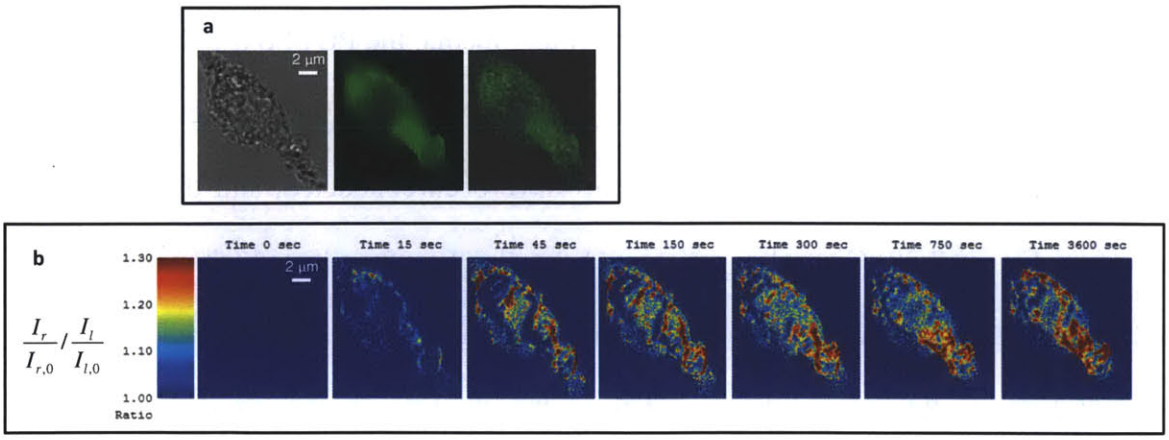

Figure 3.28 Application of the nanotube enabled molecular recognition. (**a**) White light image of a Raw 264.7 macrophage (different cell from shown in Fig. 4), nIR fluorescence of BA-PhO-Dex – SWCNTs inside the macrophage before the addition of riboflavin and the resultant overlay. (**b**) Time evolution of the fluorescence from cell-encapsulated BA-PhO-Dex – SWCNTs in response to extracellular riboflavin added at time t = 36 s. The emission maximum shifting response is represented by the normalized intensity of the right channel divided by the normalized intensity of the left channel.

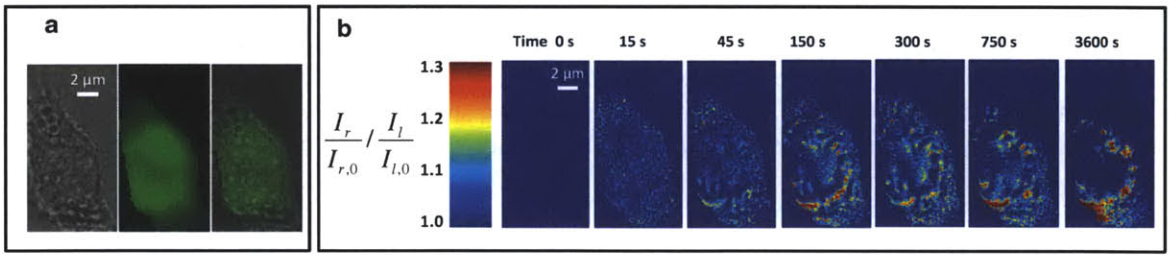

Figure 3.29 Cellular control experiments. (**a**) White light image of a Raw 264.7 macrophage, nIR fluorescence of BA-PhO-Dex – SWCNTs inside the macrophage before the addition of riboflavin and the resultant overlay. (**b**) Time evolution of the fluorescence from cell-encapsulated BA-PhO-Dex – SWCNTs in a control experiment where no extracellular riboflavin is added. The emission maximum shifting response is represented by the normalized intensity of the right channel divided by the normalized intensity of the left channel. The apparent red shift might be due to intracellular riboflavin.

In summary, such recognition constructs may be applied to future applications as new therapeutics, novel chemical catalysts and sensor platforms similar to those demonstrated in this work. The concept of molecular recognition that stems from a constrained polymer on a 3-D surface is generic. This concept can also be used in other

nanotechnology field, such as nanoparticles. The observation that binding affinity can be tuned through polymer composition modulation indicates a potentially large parameter space. Additional responses are shown in Figure 3.30 – 3.53.

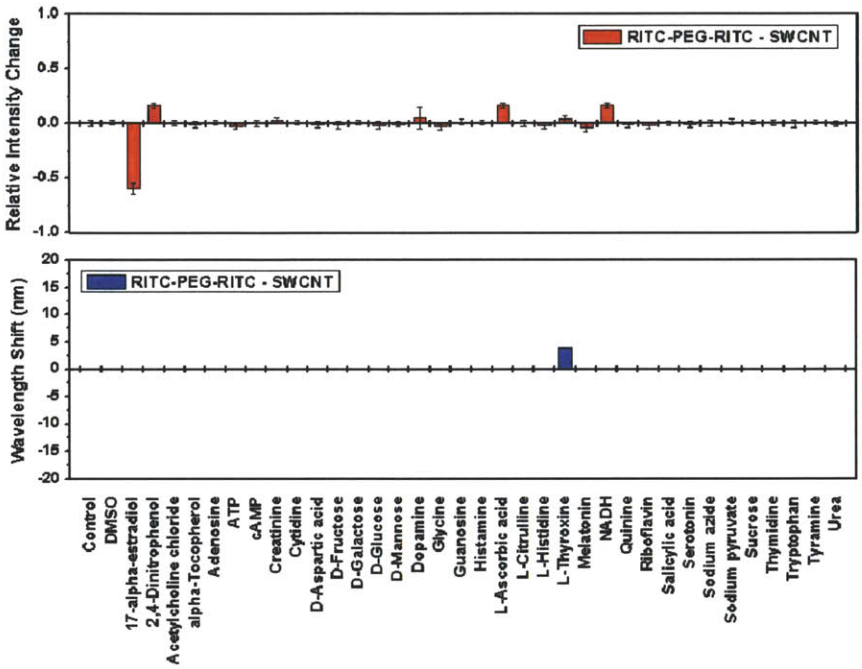

Figure 3.30 Fluorescence response of each nanotube species in RTIC-PEG20kDa-RITC – SWCNTs to 36 different analytes. Top panel: The relative fluorescence change compared to the control for RTIC-PEG20kDa-RITC – (7,5) SWCNT after being exposed to a panel of 36 analytes. Bottom panel: The shift in emission maximum of RITC-PEG20kDa-RITC – (7,5) SWCNT after exposure to each analyte. For both modes of responses, reported response is an average of three separate measurements, and reported error bars are 2SD.

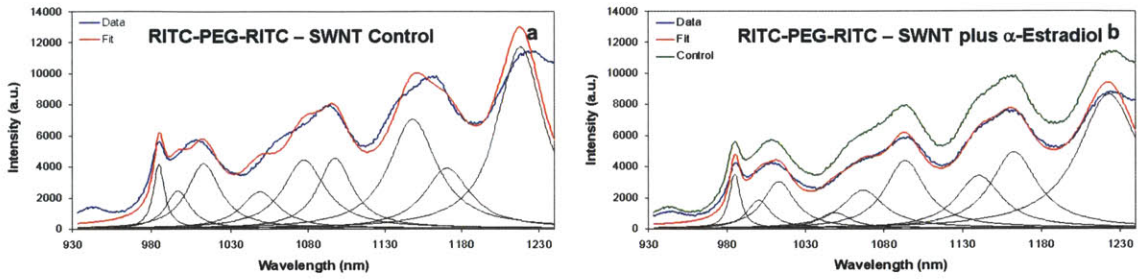

Figure 3.31 Deconvoluted spectra of fluorescence response of each nanotube species in RTIC-PEG20kDa-RITC – SWCNT to 36 different analytes. **a**, RTIC-PEG20kDa-RITC – SWCNT control deconvolution. Actual control data is shown in blue, the fitted spectrum is shown in red and the individual nanotube peaks are shown in black. **b**, RTIC-PEG20kDa-RITC – SWCNT fluorescence spectral response to 100 μM 17-α-estradiol. Actual response data is shown in blue, the fitted spectrum is shown in red, the control spectrum is shown in green and the individual nanotube peaks are shown in black.

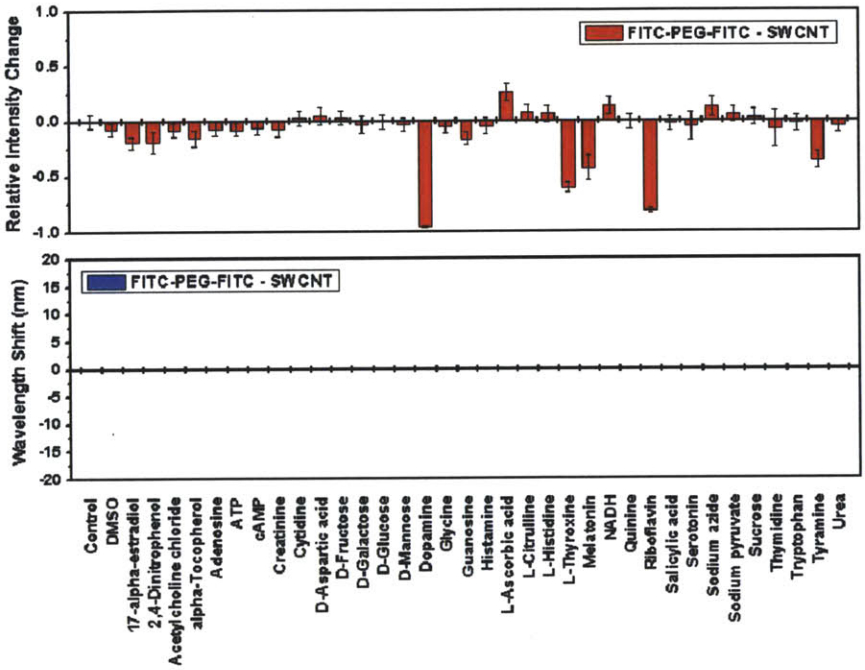

Figure 3.32 Fluorescence response of each nanotube species in FITC-PEG20kDa-FITC – SWCNTs to 36 different analytes. Top panel: The relative fluorescence change compared to the control for FITC-PEG20kDa-FITC – (7,5) SWCNT after being exposed to a panel of 36 analytes. Bottom panel: The shift in emission maximum of FTIC-PEG20kDa-FITC – (7,5) SWCNT after exposure to each analyte. For both modes of responses, reported response is an average of three separate measurements, and reported error bars are 2SD.

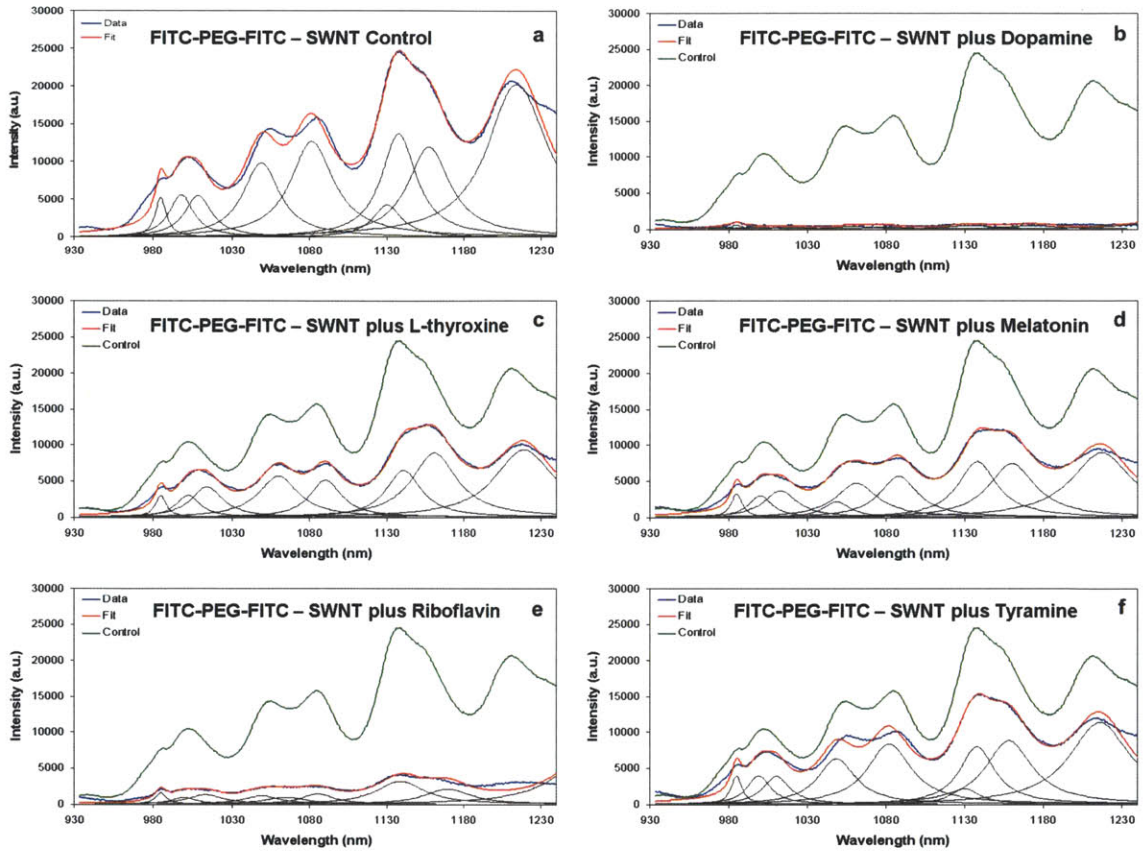

Figure 3.33 Deconvoluted spectra of fluorescence response of each nanotube species in FITC-PEG20kDa – SWCNT to 36 different analytes. **a**, FITC-PEG20kDa-FITC – SWCNT control deconvolution. Actual control data is shown in blue, the fitted spectrum is shown in red and the individual nanotube peaks are shown in black. **b-f**, FITC-PEG20kDa-FITC – SWCNT fluorescence spectral response to 490 μM dopamine (**b**), 100 μM L-thyroxine (**c**), 490 μM melatonin (**d**), 100 μM riboflavin (**e**), 490 μM tyramine (**f**). Actual response data is shown in blue, the fitted spectrum is shown in red, the control spectrum is shown in green and the individual nanotube peaks are shown in black.

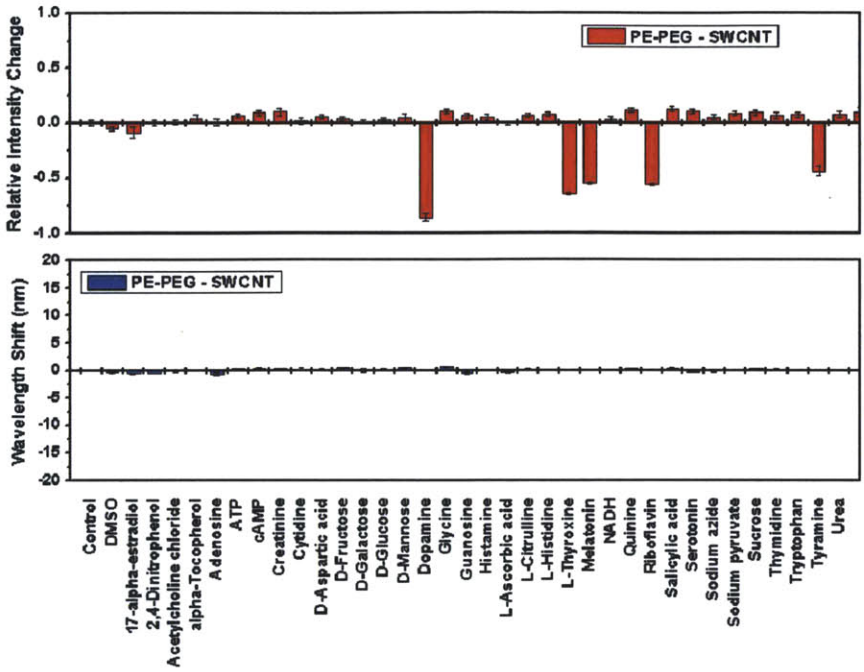

Figure 3.34 Fluorescence response of each nanotube species in PE-PEG5kDa – SWCNTs to 36 different analytes. Top panel: The relative fluorescence change compared to the control for PE-PEG5kDa – (7,5) SWCNT after being exposed to a panel of 36 analytes. Bottom panel: The shift in emission maximum of PE-PEG5kDa – (7,5) SWCNT after exposure to each analyte. For both modes of responses, reported response is an average of three separate measurements, and reported error bars are 2SD.

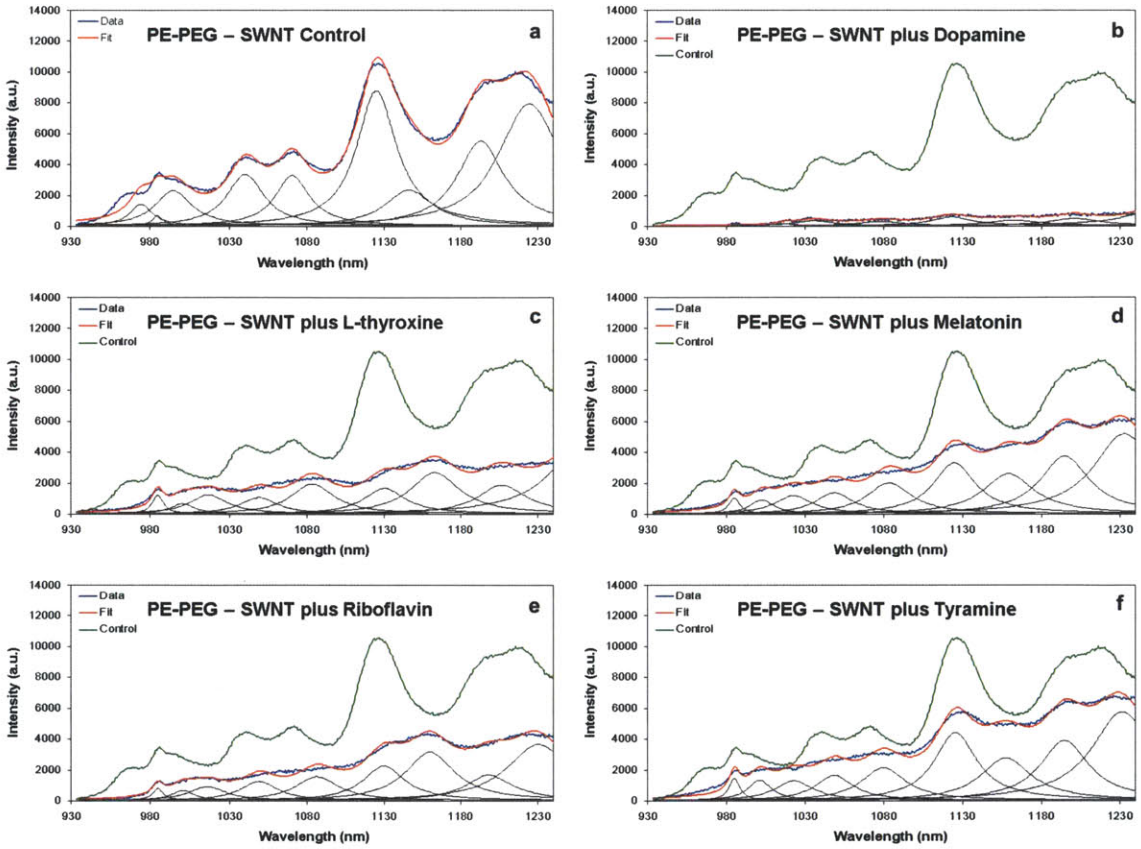

Figure 3.35 Deconvoluted spectra of fluorescence response of each nanotube species in PE-PEG5kDa – SWCNT to 36 different analytes. **a**, PE-PEG5kDa – SWCNT control deconvolution. Actual control data is shown in blue, the fitted spectrum is shown in red and the individual nanotube peaks are shown in black. **b-f**, PE-PEG5kDa – SWCNT fluorescence spectral response to 490 μM dopamine (**b**), 100 μM L-thyroxine (**c**), 490 μM melatonin (**d**), 100 μM riboflavin (**e**), 490 μM tyramine (**f**). Actual response data is shown in blue, the fitted spectrum is shown in red, the control spectrum is shown in green and the individual nanotube peaks are shown in black.

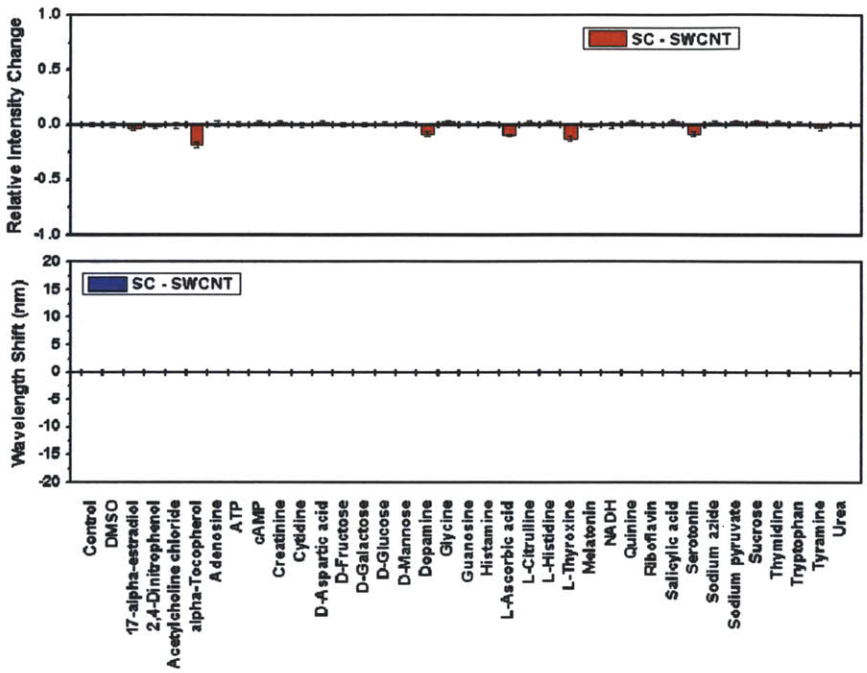

Figure 3.36 Fluorescence response of each nanotube species in SC – SWCNTs to 36 different analytes. Top panel: The relative fluorescence change compared to the control for SC – (7,5) SWCNT after being exposed to a panel of 36 analytes. Bottom panel: The shift in emission maximum of PE-PEG5kDa – (7,5) SWCNT after exposure to each analyte. For both modes of responses, reported response is an average of three separate measurements, and reported error bars are 2SD.

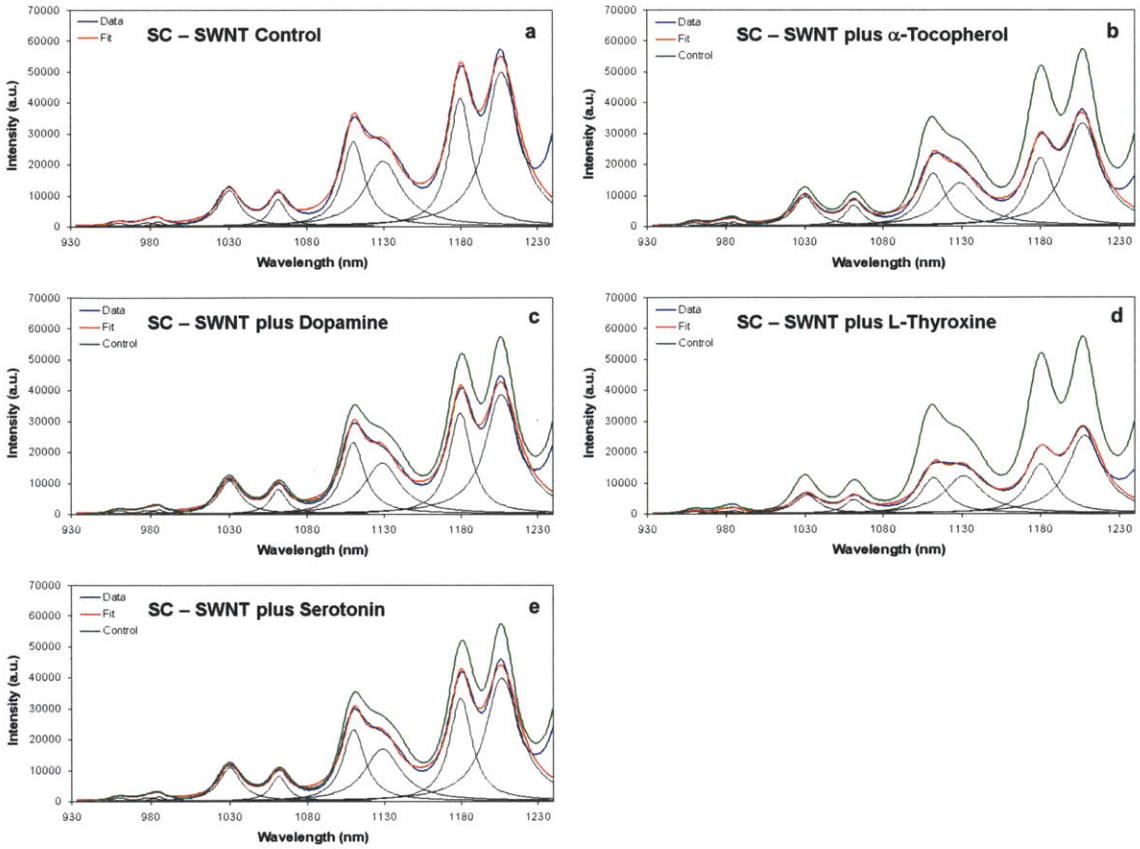

Figure 3.37 Deconvoluted spectra of fluorescence response of each nanotube species in SC – SWCNT to 36 different analytes. **a**, SC – SWCNT control deconvolution. Actual control data is shown in blue, the fitted spectrum is shown in red and the individual nanotube peaks are shown in black. **b-e**, SC – SWCNT fluorescence spectral response to 510 μM α-tocopherol (**b**), 490 μM dopamine (**c**), 100 μM L-thyroxine (**d**), 490 μM melatonin (**d**), 100 μM serotonin (**e**). Actual response data is shown in blue, the fitted spectrum is shown in red, the control spectrum is shown in green and the individual nanotube peaks are shown in black.

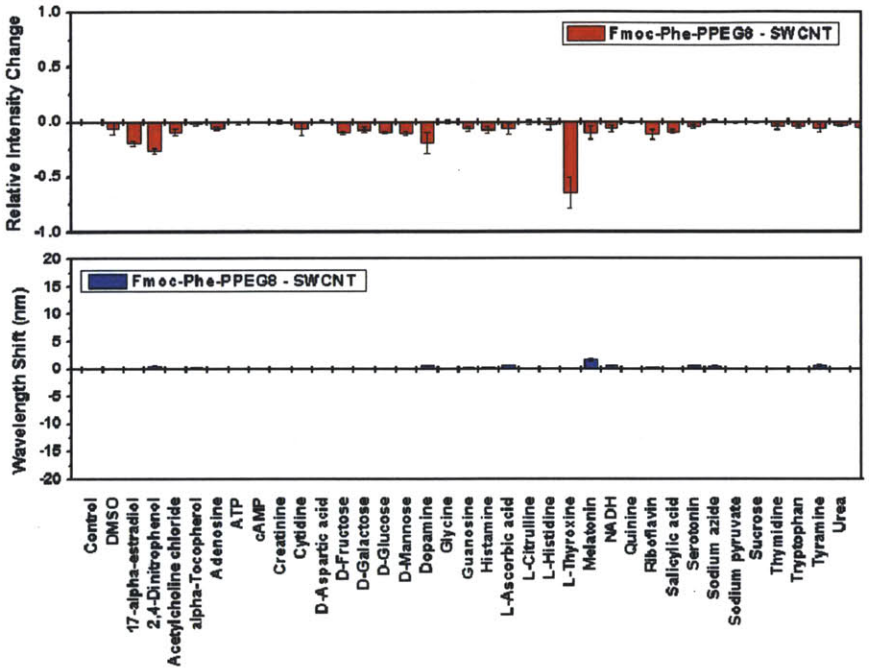

Figure 3.38 Fluorescence response of each nanotube species in Fmoc-Phe-PPEG8 – SWCNTs to 36 different analytes. Top panel: The relative fluorescence change compared to the control for Fmoc-Phe-PPEG8 – (7,5) SWCNT after being exposed to a panel of 36 analytes. Bottom panel: The shift in emission maximum of Fmoc-Phe-PPEG8 – (7,5) SWCNT after exposure to each analyte. For both modes of responses, reported response is an average of three separate measurements, and reported error bars are 2SD.

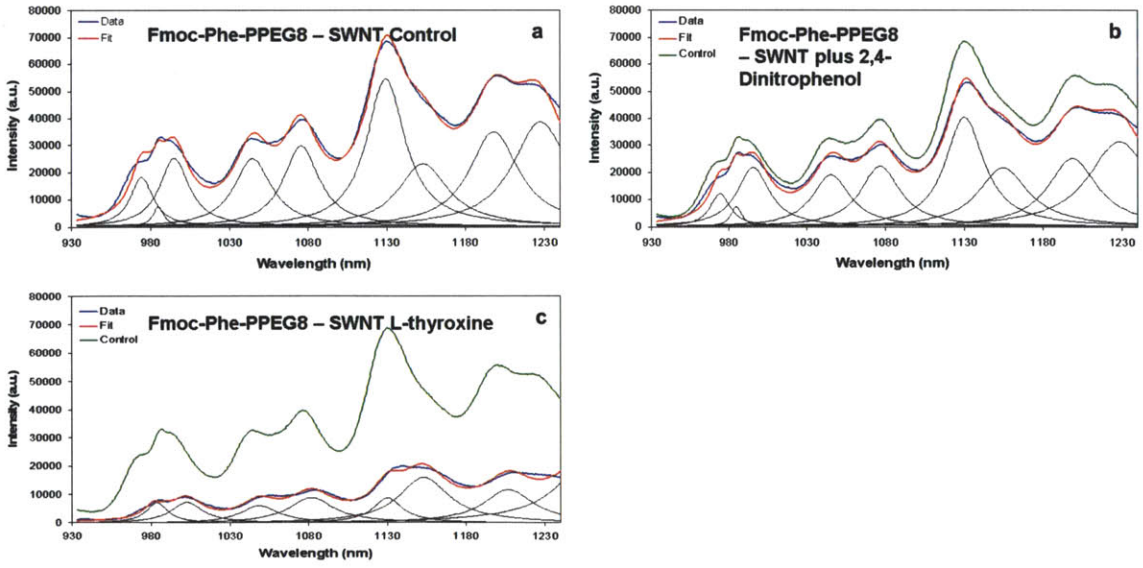

Figure 3.39 Deconvoluted spectra of fluorescence response of each nanotube species in Fmoc-Phe-PPEG8 – SWCNT to 36 different analytes. **a**, Fmoc-Phe-PPEG8 – SWCNT control deconvolution. Actual control data is shown in blue, the fitted spectrum is shown in red and the individual nanotube peaks are shown in black. **b-c**, Fmoc-Phe-PPEG8 – SWCNT fluorescence spectral response to 480 μM 2,4-dinitrophenol (**b**), 100 μM L-thyroxine (**c**). Actual response data is shown in blue, the fitted spectrum is shown in red, the control spectrum is shown in green and the individual nanotube peaks are shown in black.

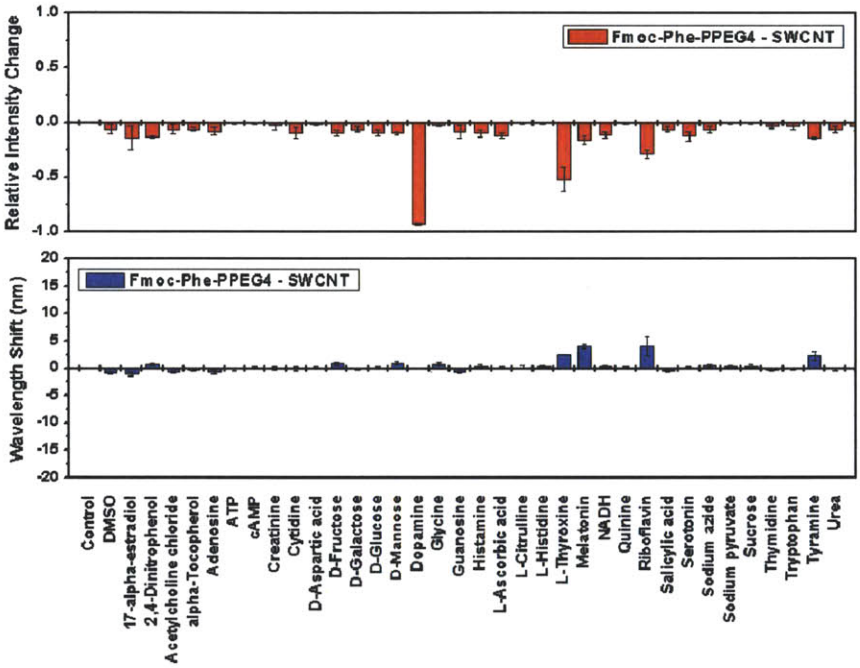

Figure 3.40 Fluorescence response of each nanotube species in Fmoc-Phe-PPEG4 – SWCNTs to 36 different analytes. Top panel: The relative fluorescence change compared to the control for Fmoc-Phe-PPEG4 – (7,5) SWCNT after being exposed to a panel of 36 analytes. Bottom panel: The shift in emission maximum of Fmoc-Phe-PPEG4 – (7,5) SWCNT after exposure to each analyte. For both modes of responses, reported response is an average of three separate measurements, and reported error bars are 2SD.

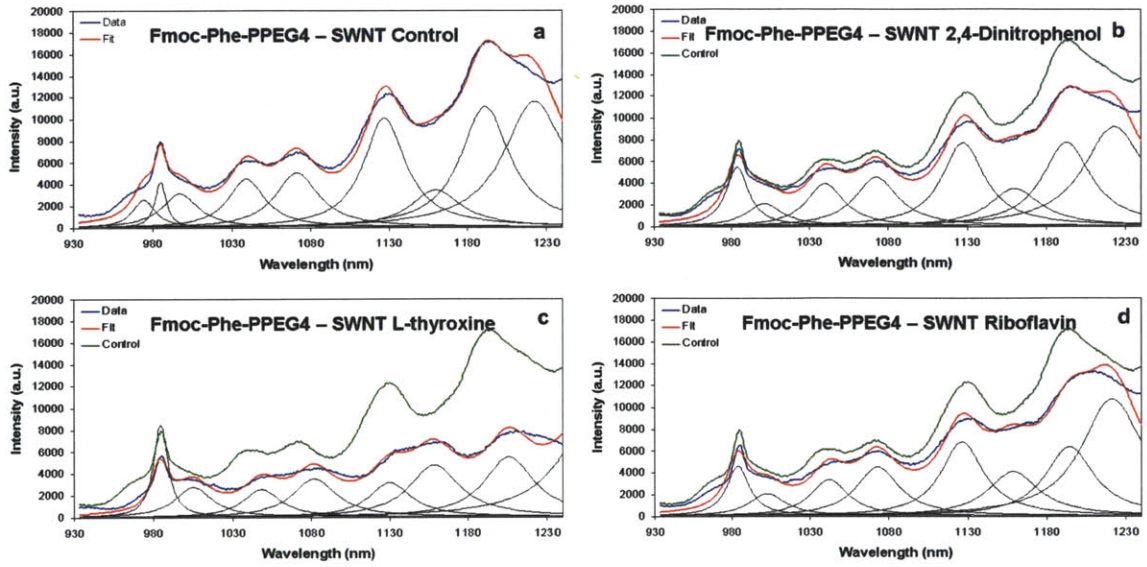

Figure 3.41 Deconvoluted spectra of fluorescence response of each nanotube species in Fmoc-Phe-PPEG4 – SWCNT to 36 different analytes. **a**, Fmoc-Phe-PPEG4 – SWCNT control deconvolution. Actual control data is shown in blue, the fitted spectrum is shown in red and the individual nanotube peaks are shown in black. **b-d**, Fmoc-Phe-PPEG4 – SWCNT fluorescence spectral response to 480 μM 2,4-dinitrophenol (**b**), 100 μM L-thyroxine (**c**), 100 μM riboflavin (**d**). Actual response data is shown in blue, the fitted spectrum is shown in red, the control spectrum is shown in green and the individual nanotube peaks are shown in black.

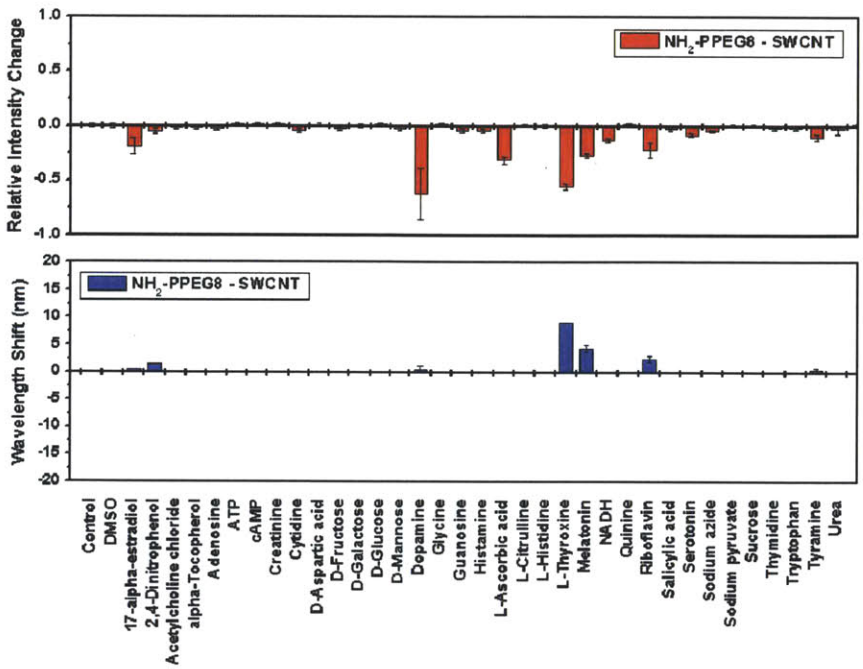

Figure 3.42 Fluorescence response of each nanotube species in NH_2-PPEG8 – SWCNTs to 36 different analytes. Top panel: The relative fluorescence change compared to the control for NH_2-PPEG8 – (7,5) SWCNT after being exposed to a panel of 36 analytes. Bottom panel: The shift in emission maximum of NH_2-PPEG8 – (7,5) SWCNT after exposure to each analyte. For both modes of responses, reported response is an average of three separate measurements, and reported error bars are 2SD.

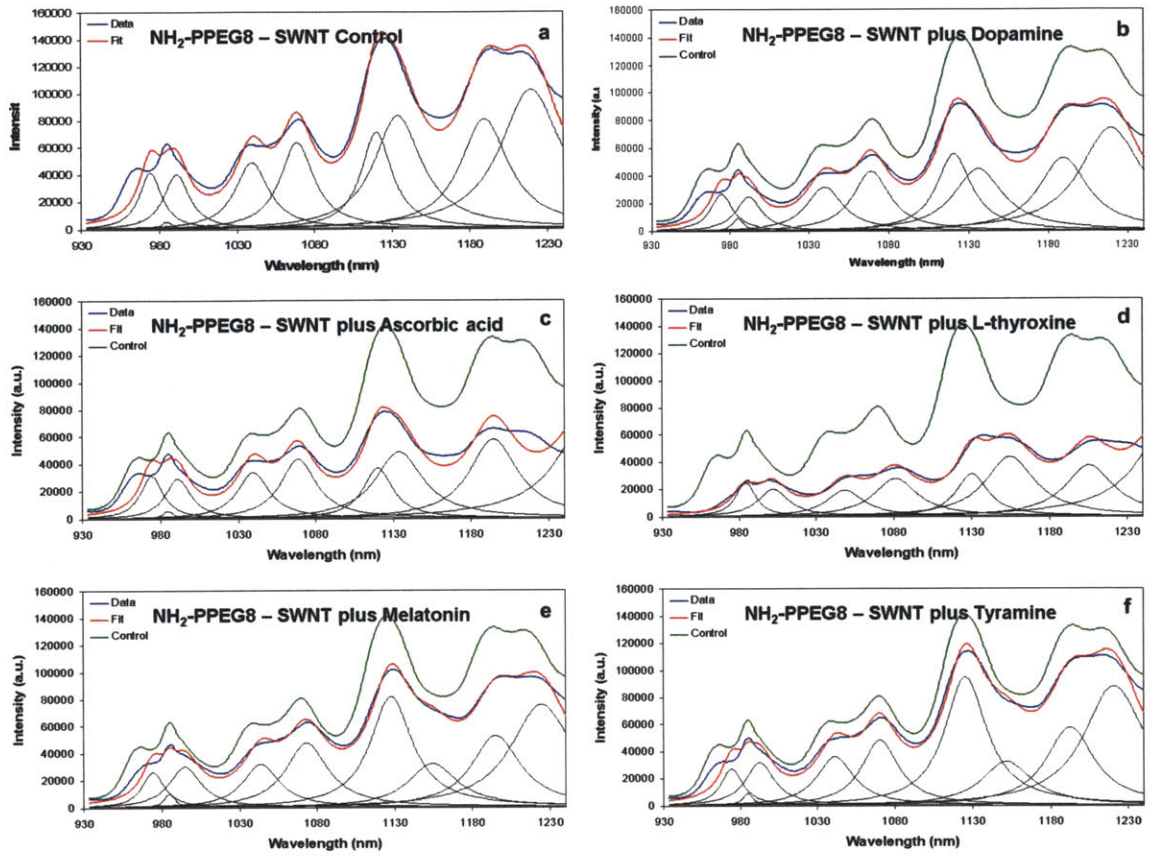

Figure 3.43 Deconvoluted spectra of fluorescence response of each nanotube species in NH_2-PPEG8 – SWCNT to 36 different analytes. **a**, NH_2-PPEG8 – SWCNT control deconvolution. Actual control data is shown in blue, the fitted spectrum is shown in red and the individual nanotube peaks are shown in black. **b-f**, NH_2-PPEG8 – SWCNT fluorescence spectral response to 490 μM dopamine (**b**), 500 μM L-ascorbic acid (**c**), 100 μM L-thyroxine (**d**), 490 μM melatonin (**e**), 490 μM tyramine (**f**). Actual response data is shown in blue, the fitted spectrum is shown in red, the control spectrum is shown in green and the individual nanotube peaks are shown in black.

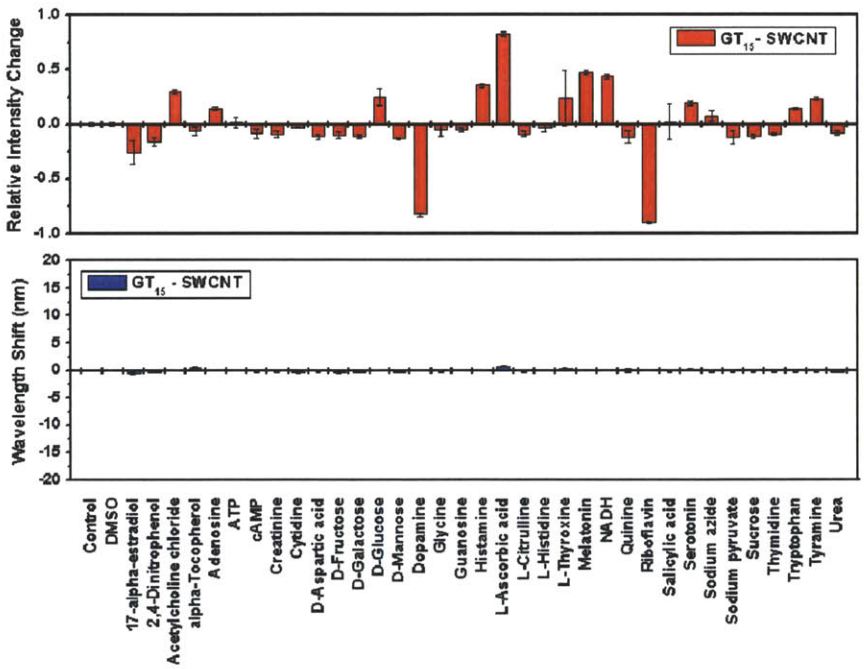

Figure 3.44 Fluorescence response of each nanotube species in GT_{15} – SWCNTs to 36 different analytes. Top panel: The relative fluorescence change compared to the control for GT_{15} – (7,5) SWCNT after being exposed to a panel of 36 analytes. Bottom panel: The shift in emission maximum of GT_{15} – (7,5) SWCNT after exposure to each analyte. For both modes of responses, reported response is an average of three separate measurements, and reported error bars are 2SD.

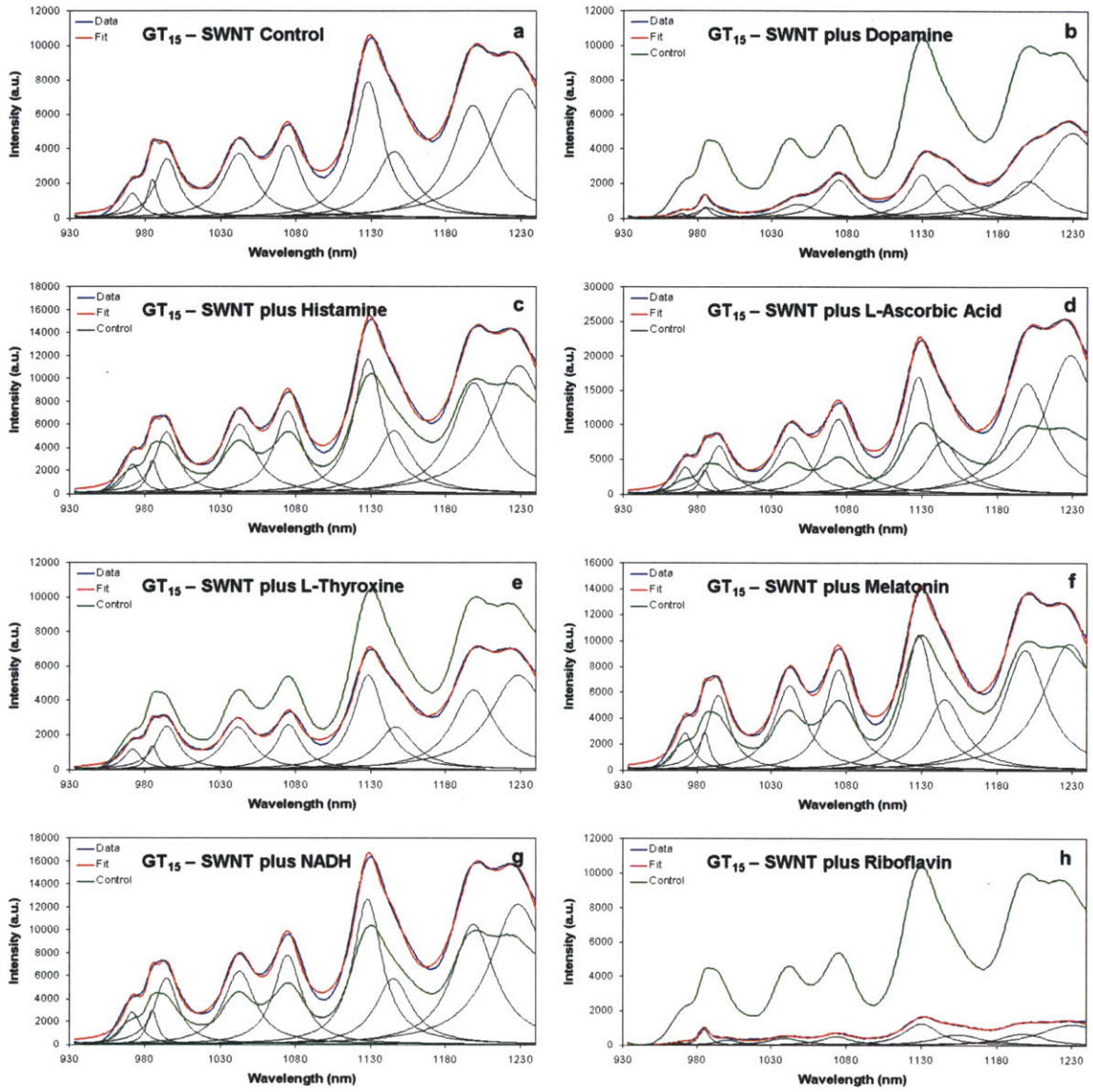

Figure 3.45 Deconvoluted spectra of fluorescence response of each nanotube species in GT_{15}– SWCNT to 36 different analytes. **a**, GT_{15} – SWCNT control deconvolution. Actual control data is shown in blue, the fitted spectrum is shown in red and the individual nanotube peaks are shown in black. **b-h**, GT_{15}– SWCNT fluorescence spectral response to 490 μM dopamine (**b**), 510 μM histamine (**c**), 500 μM L-ascorbic acid (**d**), 100 μM L-thyroxine (**e**), 490 μM melatonin (**f**), 510 μM NADH (**g**), 100 μM riboflavin (**h**). Actual response data is shown in blue, the fitted spectrum is shown in red, the control spectrum is shown in green and the individual nanotube peaks are shown in black.

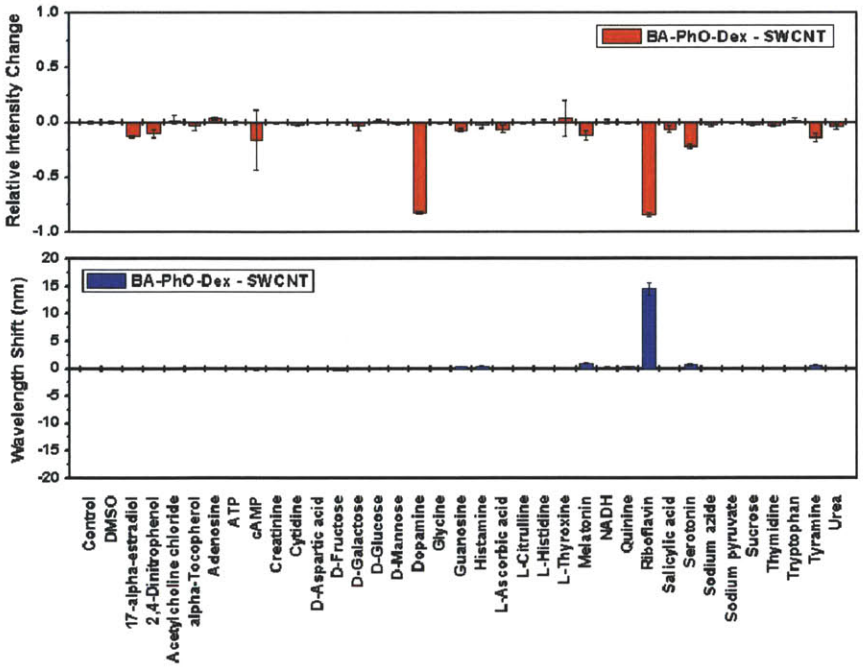

Figure 3.46 Fluorescence response of each nanotube species in BA-PhO-Dex – SWCNTs to 36 different analytes. Top panel: The relative fluorescence change compared to the control for BA-PhO-Dex – (7,5) SWCNT after being exposed to a panel of 36 analytes. Bottom panel: The shift in emission maximum of BA-PhO-Dex – (7,5) SWCNT after exposure to each analyte. For both modes of responses, reported response is an average of three separate measurements, and reported error bars are 2SD.

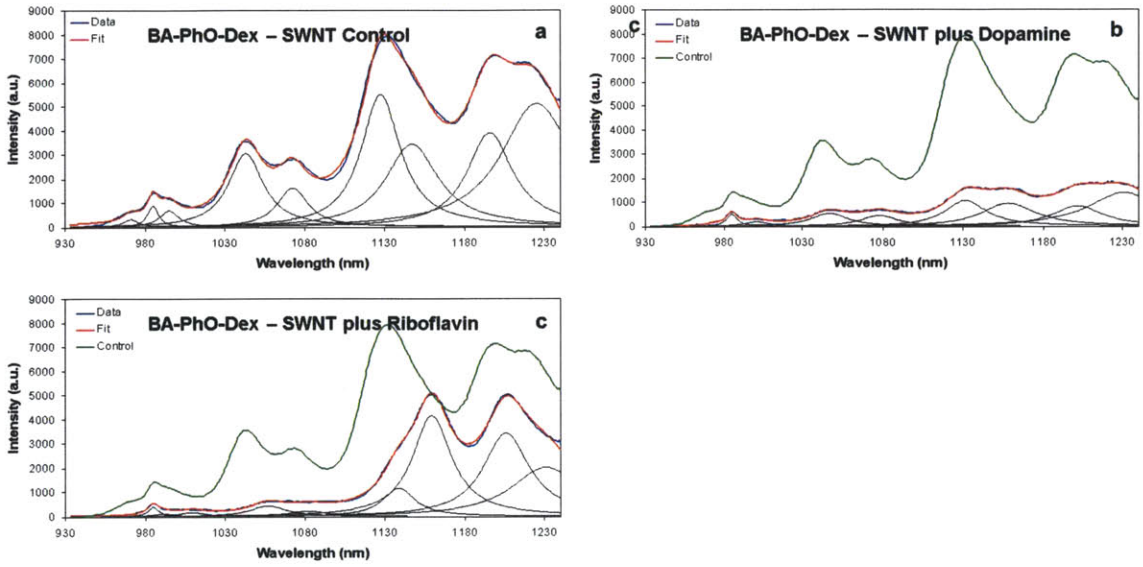

Figure 3.47 Deconvoluted spectra of fluorescence response of each nanotube species in BA-PhO-Dex – SWCNT to 36 different analytes. **a**, BA-PhO-Dex – SWCNT control deconvolution. Actual control data is shown in blue, the fitted spectrum is shown in red and the individual nanotube peaks are shown in black. **b-c**, BA-PhO-Dex – SWCNT fluorescence spectral response to 490 μM dopamine (**b**), 100 μM riboflavin (**c**). Actual response data is shown in blue, the fitted spectrum is shown in red, the control spectrum is shown in green and the individual nanotube peaks are shown in black.

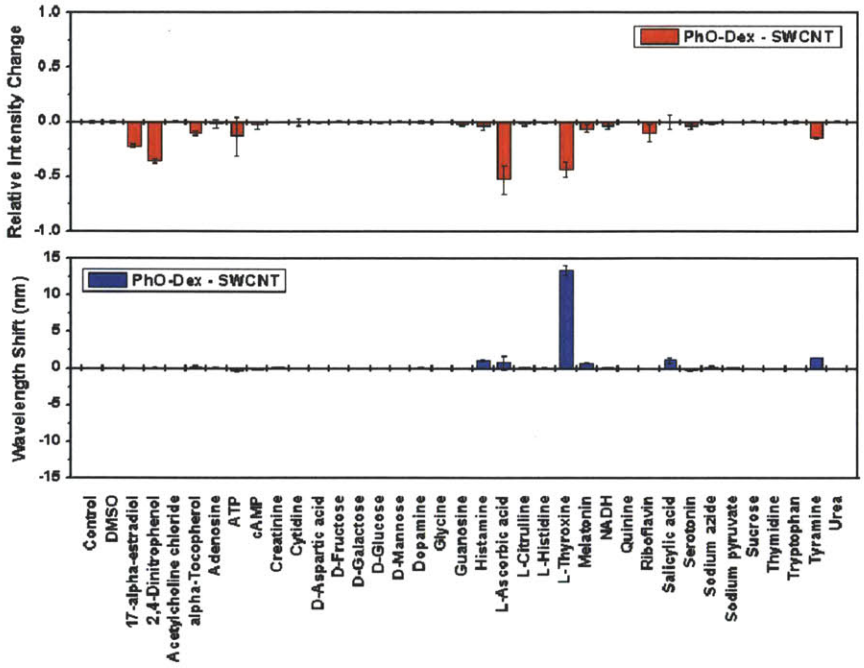

Figure 3.48 Fluorescence response of each nanotube species in PhO-Dex – SWCNTs to 36 different analytes. Top panel: The relative fluorescence change compared to the control for PhO-Dex – (7,5) SWCNT after being exposed to a panel of 36 analytes. Bottom panel: The shift in emission maximum of PhO-Dex – (7,5) SWCNT after exposure to each analyte. For both modes of responses, reported response is an average of three separate measurements, and reported error bars are 2SD.

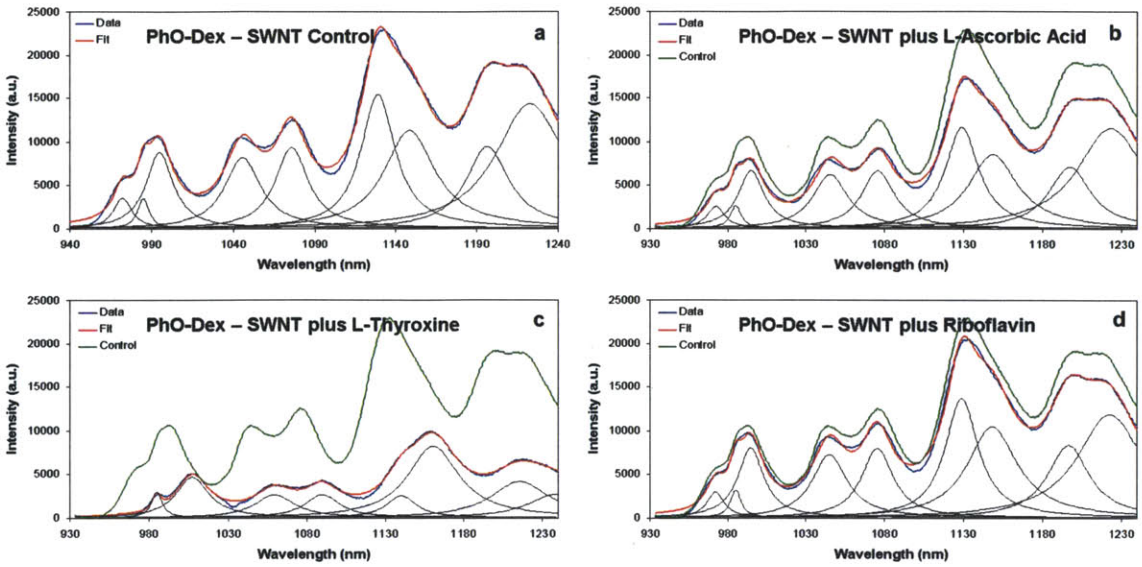

Figure 3.49 Deconvoluted spectra of fluorescence response of each nanotube species in PhO-Dex – SWCNT to 36 different analytes. **a**, PhO-Dex – SWCNT control deconvolution. Actual control data is shown in blue, the fitted spectrum is shown in red and the individual nanotube peaks are shown in black. **b-h**, PhO-Dex – SWCNT fluorescence spectral response to 500 μM L-ascorbic acid (**b**), 100 μM L-thyroxine (**c**), 100 μM riboflavin (**d**). Actual response data is shown in blue, the fitted spectrum is shown in red, the control spectrum is shown in green and the individual nanotube peaks are shown in black.

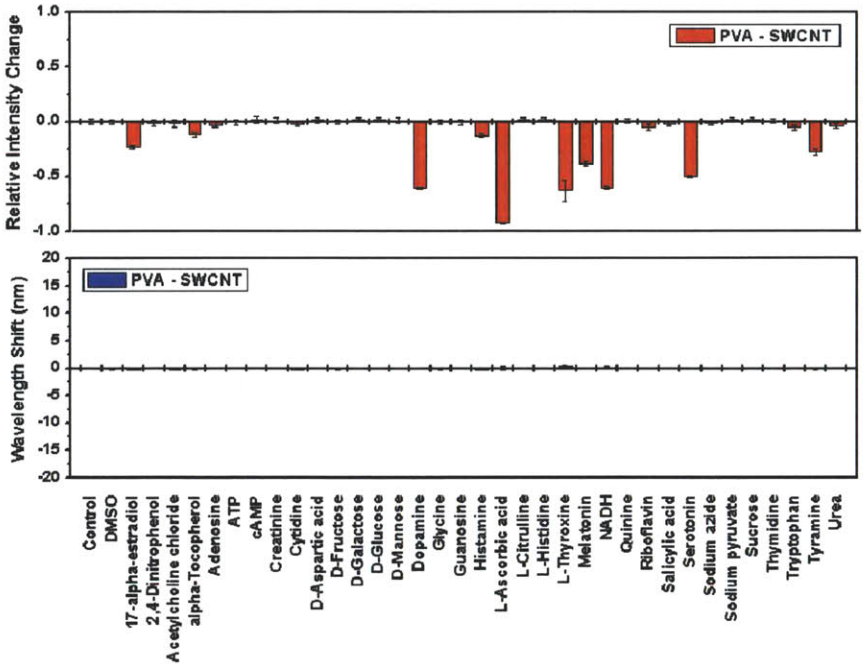

Figure 3.50 Fluorescence response of each nanotube species in PVA – SWCNTs to 36 different analytes. Top panel: The relative fluorescence change compared to the control for PVA – (7,5) SWCNT after being exposed to a panel of 36 analytes. Bottom panel: The shift in emission maximum of PVA – (7,5) SWCNT after exposure to each analyte. For both modes of responses, reported response is an average of three separate measurements, and reported error bars are 2SD.

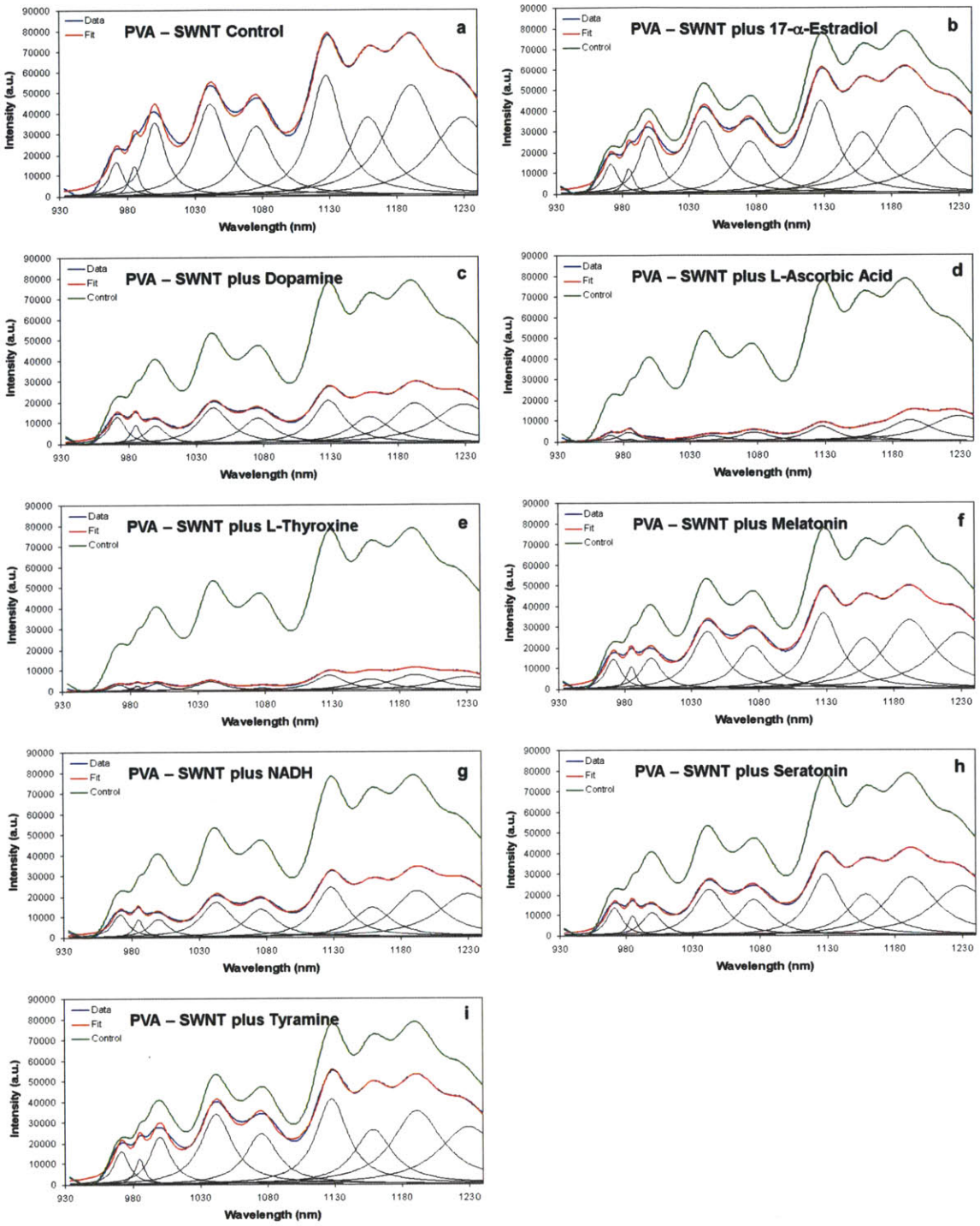

Figure 3.51 Deconvoluted spectra of fluorescence response of each nanotube species in PVA – SWCNT to 36 different analytes. **a**, PVA– SWCNT control deconvolution. Actual control data is shown in blue, the fitted spectrum is shown in red and the individual nanotube peaks are shown in black. **b-i**, PVA – SWCNT fluorescence spectral response to 100 μM 17-α-estradiol (**b**), 490 μM dopamine (**c**), 500 μM L-ascorbic acid (**d**), 100 μM L-thyroxine (**e**), 490 μM melatonin (**f**),

510 μM NADH (**g**), 100 μM seratonin (**h**), 490 μM tyramine (**i**). Actual response data is shown in blue, the fitted spectrum is shown in red, the control spectrum is shown in green and the individual nanotube peaks are shown in black.

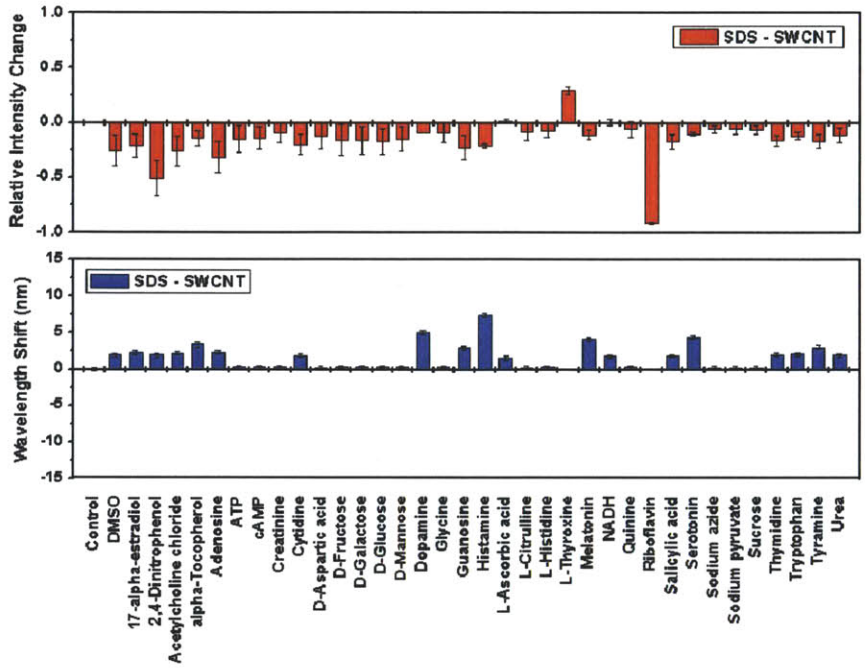

Figure 3.52 Fluorescence response of each nanotube species in SDS – SWCNTs to 36 different analytes. Top panel: The relative fluorescence change compared to the control for SDS – (7,5) SWCNT after being exposed to a panel of 36 analytes. Bottom panel: The shift in emission maximum of SDS – (7,5) SWCNT after exposure to each analyte. For both modes of responses, reported response is an average of three separate measurements, and reported error bars are 2SD.

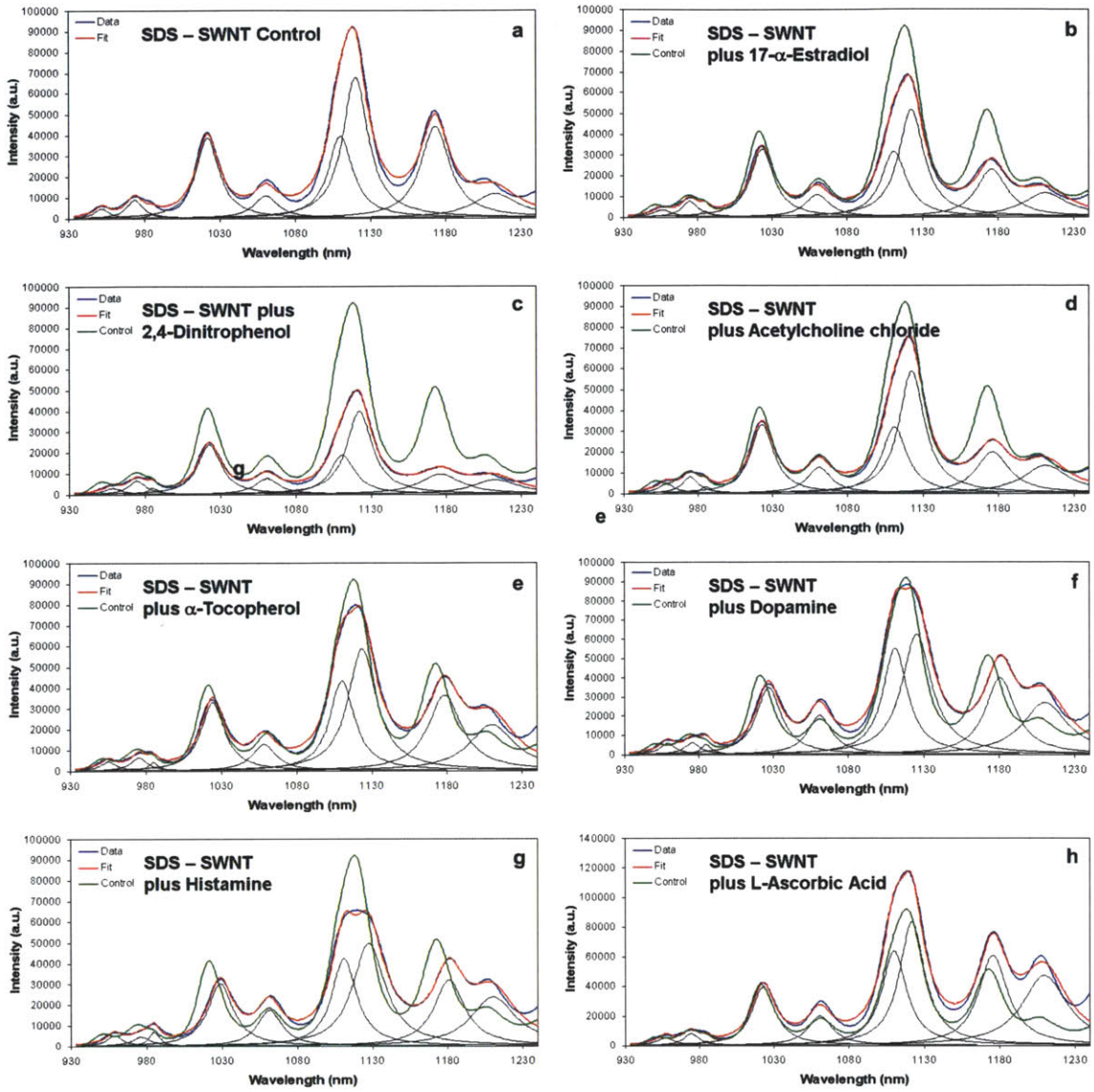
a
SDS – SWNT Control
b
SDS – SWNT
plus 17-α-Estradiol
c
SDS – SWNT plus
2,4-Dinitrophenol
d
SDS – SWNT
plus Acetylcholine chloride
e
SDS – SWNT
plus α-Tocopherol
f
SDS – SWNT
plus Dopamine
g
SDS – SWNT
plus Histamine
h
SDS – SWNT
plus L-Ascorbic Acid
Data
Fit
Control
Intensity (a.u.)
Wavelength (nm)

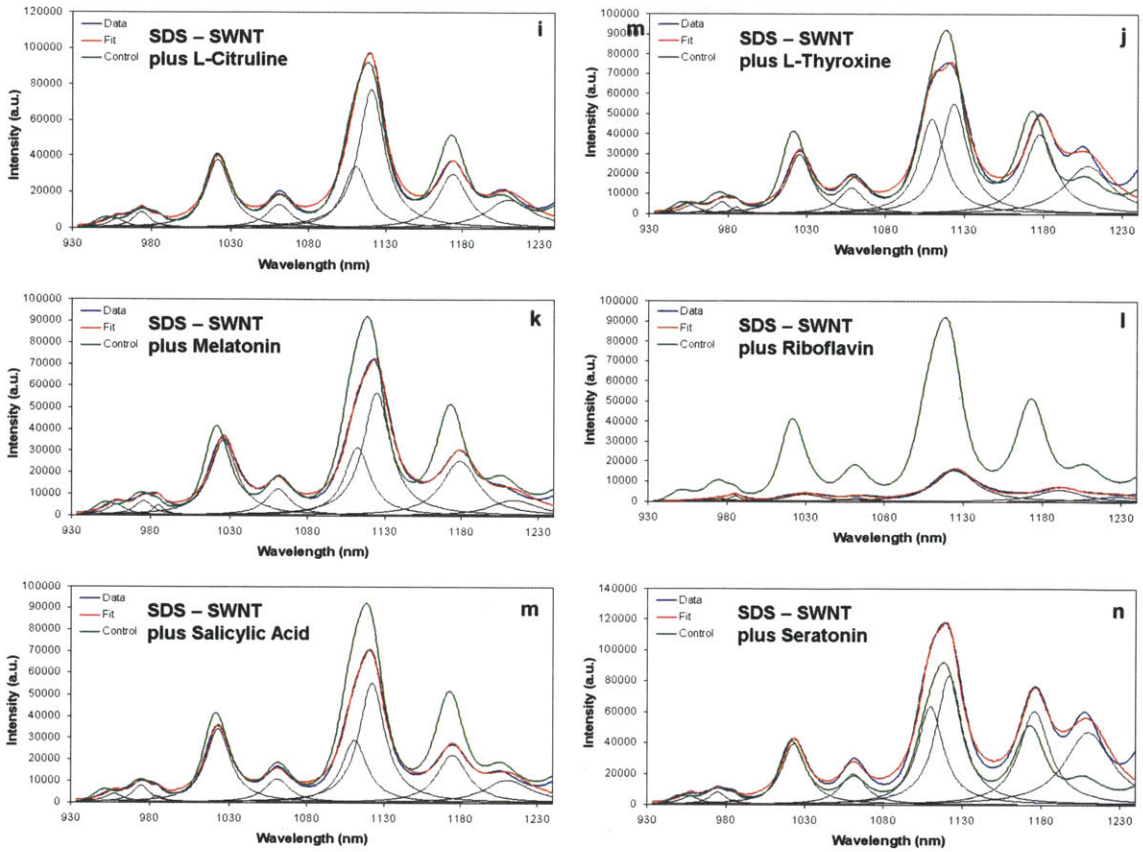

Figure 3.53 Deconvoluted spectra of fluorescence response of each nanotube species in SDS – SWCNT to 36 different analytes. **a**, SDS – SWCNT control deconvolution. Actual control data is shown in blue, the fitted spectrum is shown in red and the individual nanotube peaks are shown in black. **b-n,** SDS – SWCNT fluorescence spectral response to 100 μM 17-α-estradiol (**b**), 480 μM 2,4-dinitrophenol (**c**), 540 μM acetylcholine chloride (**d**), 510 μM α-tocopherol (**e**), 490 μM dopamine (**f**), 510 μM histamine (**g**), 500 μM L-ascorbic acid (**h**), 110 μM L-citruline (**i**), 100 μM L-thyroxine (**j**), 490 μM melatonin (**k**), 100 μM riboflavin (**l**), 490 μM salicylic acid (**m**), 100 μM serotonin (**n**). Actual response data is shown in blue, the fitted spectrum is shown in red, the control spectrum is shown in green and the individual nanotube peaks are shown in black.

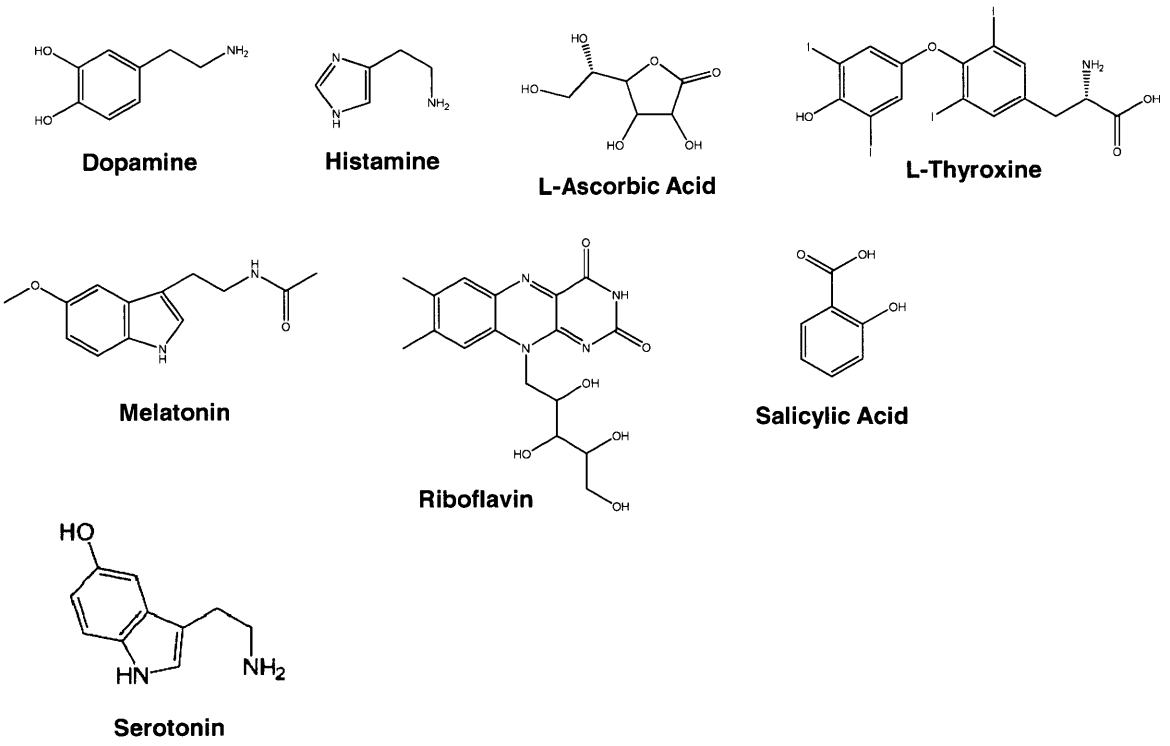

Figure 3.54 Molecular structures of analytes that generally result in a response in the SWCNT fluorescence assay.

4 2D Equation-of-state Model for Small-molecule Analyte Adsorbing onto the Single-walled Carbon Nanotube Surface

4.1 Overview

Single-walled carbon nanotube (SWCNT) fluorescence-based sensors are an emerging field of research. Recent experimental efforts have been focusing designing and synthesizing polymer wrapped carbon nanotubes that can detect molecules of interest. However, the challenge remains to engineer the nano-interface such that the detection is selective. Previous research has explored the concept of "molecular recognition" at this nano-interface where adsorbed phases created by different polymer-SWCNT complexes exhibit distinct fluorescence responses to various analyte molecules. A theoretical frame work that can provide insight into the mechanism for these responses and guide the design of future polymer synthesis is desirable, but so far unexplored. In this work, we modeled analyte molecules adsorbing onto the polymer-SWCNT surface using a modified thermodynamic model that was originally developed for describing competitive adsorption of surfactants at air-water interface, with model parameters determined with molecular simulations. The model provides physical insight into the key molecular parameters that govern the competitive adsorption between the analyte of interest and the hydrophobic segment of the polymer on the SWCNT surface. The resulting model is able to correctly predict 83% of the fluorescence responses from a recent experimental paper within 20% error of the experimental values.

4.2. Motivation

Single-walled carbon nanotubes (SWCNTs) are rolled graphene sheets that possess near-infrared (nIR) bandgap fluorescence. Since the discovery of its fluorescence in 2002[10], SWCNT fluorescence-based detection for analyte of interest has becoming an emerging field of research. SWCNT fluorescence based sensors have been developed for detecting various analytes, including β-D-glucose[24], DNA hybridization[49], divalent metal cations[22], assorted genotoxins[163], nitroaromatics[177], nitric oxide[25, 32], pH[26] and the protein avidin[153]. Many properties of SWCNTs enable them to be ideal sensing materials[18], especially for biological applications, and those properties include near-infrared fluorescence excitation and emission which do not overlap with the auto-fluorescence or absorption spectrum of the cell medium, blood or tissue; photo-stable emission of SWCNT; and single-molecule sensitivity to the analyte of interest[26-30, 32].

The main challenge in designing these sensors is determining how to engineer the nanotube interface such that it is selective for the analyte of interest. So far, most of the efforts have relied on suspending SWCNT in various polymer wrappings that have known interactions with the molecules of interest [24, 25, 49]. A new concept is to create polymer-SWCNT structures where the "adsorbed phase" can selectively recognize the molecules of interest through steric hindrance[32], Van de Waals interactions or electrostatic interactions[178]. Early work has explored this concept by screening fluorescence intensity change of various polymer-SWCNT complexes against a panel of molecules, thus providing the "fingerprint" of the polymer-SWCNT construct. Three examples were discussed in Section 3 (Figure 3.12, 3.17 and 3.18): a series of similar

polymers wrap around a SWCNT and the corresponding fluorescence response profiles show distinct 'fingerprints" to a panel of analytes. We do not intend to repeat ourselves; however, for the completeness of this chapter alone, the example shown in Figure 3.12 is revisited here in Figure 4.1. In this example, for instance, the first polymer-SWCNT, RITC-PEG-RITC-SWCNT (Figure 4.1a), shows selective response to estradiol, a hormone molecule in the human body; however, the other polymer-SWCNT complex, FITC-PEG-FITC-SWCNT (Figure 4.1b), does not show the same selectivity. Predicting the structure of the adsorbed polymer phase on nanoparticles is an unsolved problem in literature; and it is even more difficult to derive selectivity of polymer wrapped SWCNT towards analytes of interest. We thus aim to provide a simple but practical theoretical platform that is able to describe the adsorbed phase created by such polymer-SWCNT constructs, and provide insight to those distinct fluorescence responses.

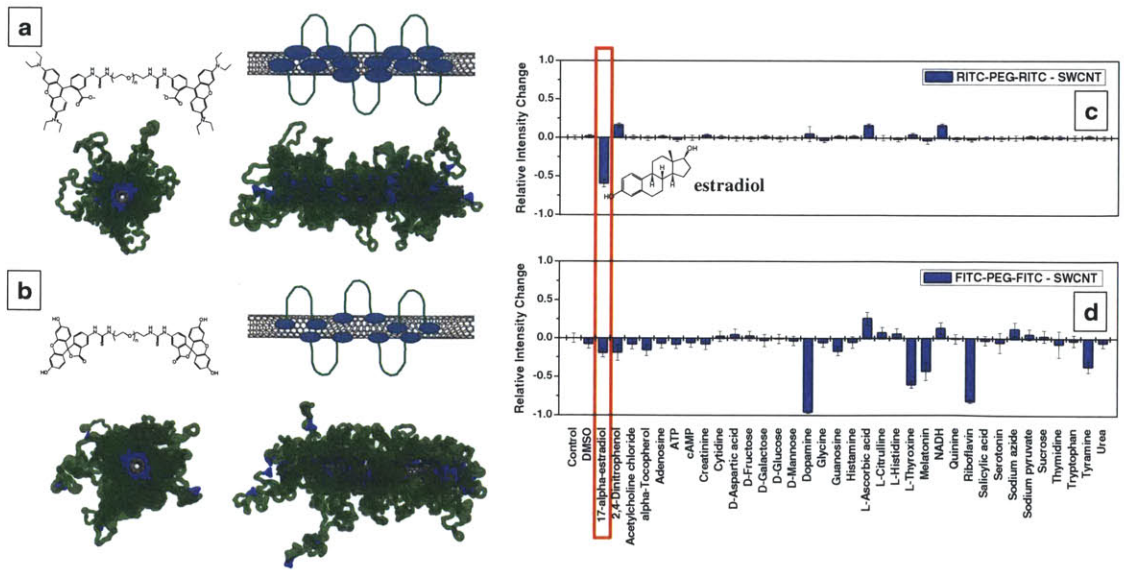

Figure 4.1 Structure and analyte-response profile of two polymer – SWCNT complexes. (a, b) Polymer structure, schematics of polymer-SWCNT complex, and front and side views calculated from MD simulation for RITC-PEG-RITC – SWCNT (a) and FITC-PEG-FITC (b).

The schematics are deduced from a combination of polymer molecular structure and fingerprinted response profile, supported by MD results. (c, d) Bar charts that show intensity change of RITC-PEG-RITC – SWCNT (c) and FITC-PEG-FITC – SWCNT (d) against a panel of 35 biological molecules. RITC-PEG-RITC – SWCNT show selective quenching response upon addition of 100 μM estradiol, but FITC-PEG-FITC – SWCNT show non-selective response profile.

4.3 2D EOS Model Formulation

We assume that the optical fluorescence modulation (intensity increase or decrease) of a SWCNT sensor shown in Figure 4.1 ($\Delta I / I_0$) is directly proportional to the analyte coverage on the SWCNT surface, θ,

$$\frac{\Delta I}{I_0} = \beta\theta, \quad (1)$$

where β is the coefficient that correlates the relative intensity change to the surface coverage of a specific analyte-polymer pair. Adsorption of certain analytes modulates the electronic structure of the SWCNT to a greater degree than others, leading to a more significant optical change and a larger value of β. Analytes modulate SWCNT fluorescence intensity via two major routes, either bleaching the valence-band electrons[16, 24] or quenching excited-state electrons[17]. Ideally, β can be estimated by calculating the overlap between the density of states of SWCNT and the unoccupied states of the electron-accepting molecules using Marcus theory [179-182]. The electronic states of those molecules can potentially be estimated from density functional theory. However, SWCNT are exitonic in nature. The actual calculation of β will in fact involve proper estimation or measurement for excited state lifetime, which are polymer-wrapping dependent. In addition, the polymer wrapping also modulates the redox level of the SWCNT, complicating the estimation of β. In reality, there is currently not a way to

readily estimate β with confidence. Therefore, we experimentally determine the value of β once assuming that β is unique to each analyte and is polymer-independent. Specifically, we chose two reference polymers, poly vinyl alcohol and FITC-PEG-FITC (Figure 4.1), the combination of which provide a relatively complete response profile for all the analytes in our library. We use a response-weighted estimate, $\overline{\beta} \equiv \frac{\beta_{PVA}(\Delta I / I_0)_{PVA} + \beta_{FITC-PEG-FITC}(\Delta I / I_0)_{FITC-PEG-FITC}}{(\Delta I / I_0)_{PVA} + (\Delta I / I_0)_{FITC-PEG-FITC}}$, since a large intensity response is a more reliable indicator of β. β is only computed once using the two reference polymers, and all other polymer-SWCNT construct predictions use this same estimated β.

The analyte surface area coverage θ is determined through a competitive adsorption process between the analyte and the polymer at the water-SWCNT interface. However, this would rely on an accurate prediction of the structure of the adsorbed polymers. Molecular dynamics simulation can provide such analysis but the large system sizes (>100,000 atoms) and time scales (microseconds) required to simulate the adsorption of the long (>5 kDalton) polymer chains used in this work makes such an approach currently computationally infeasible. Most literature efforts have instead focused on DNA adsorbed SWCNT [6, 108-111, 183-187], or the adsorption of small molecules like surfactants[165, 188-190], block copolymers[191, 192]. Even in these limited cases, it is difficult for these studies to reach the timescales necessary for complete adsorption equilibrium and instead make assumptions about the coverage of molecules on the surface. Other approaches have been attempted in literature to model polymer chains attached to various surfaces using statistical polymer theories[193-195], Monte Carlo

simulations[196, 197], but these do not provide the molecular description of the surface necessary to determine if analytes can adsorb.

For the polymers we have in the library, the hydrophobic "anchors" preferentially adsorb onto the SWCNT surface whereas the hydrophilic segments extend into aqueous phase. The unique properties of the polymers allowed us to further reduce the size of the problem by assuming that only the hydrophobic "anchors" compete with the analytes for the SWCNT surface, and that the contribution of the hydrophilic segment is negligible. This is a good assumption only if the polymer has only a few hydrophobic anchors such that those anchors behave independently of each other. Polymers PE-PEG, RITC-PEG-RITC, and FITC-PEG-FITC (in Figure 3.12) belong to this class of polymers, and are expected to be better represented by the model.

We modeled the competitive adsorption of polymer anchors or surfactant molecules, and analytes to the SWCNT surface using a thermodynamic model originally developed for modeling a layer of various surfactant molecules at an air-liquid interface[198]. The original model describes a thermodynamic equilibrium between surfactant molecules adsorbed at the interface and those present in the bulk aqueous solution. The same model is used here to describe the competitive adsorption of the polymer anchors and the analyte molecules on the SWCNT surface, illustrated in Figure 4.2. SWCNT is treated as a single layer of graphene, essentially neglecting the curvature effects to further simplify the problem. This is reasonable because for each polymer, all chiralities of SWCNTs show similar response, although the degree of responses may vary. We designate species 1 as the polymer "anchor" and species 2 as the analyte molecule. Adsorbing molecules are modeled as adsorbing hard discs with molecular radius r_i and area a_i, in equilibrium

with a bulk monomer with mole fraction x_{li}. The free energy difference between molecules on the surface and the bulk is affected by the standard state adsorption free energy, $\Delta\mu_i^0 = \mu_i^{\sigma,0} - \mu_i^{b,0}$, Van der Waals interactions between molecules on the surface (captured with the second-order virial coefficient B_{ik}) and hard-sphere repulsion. B_{11} and B_{22} describe self-interaction of the molecules, whereas B_{12} (and equivalently B_{21}) describe interactions between the analyte and polymer "anchors". The original model has also been extended to include electrostatic and double-layer effects from ionic molecules. However, in our case the assumption of a single double layer is complicated by the hydrophilic portion of polymer extending around the SWCNT. Since our analytes and polymers are mostly neutral we neglect these effects in this work.

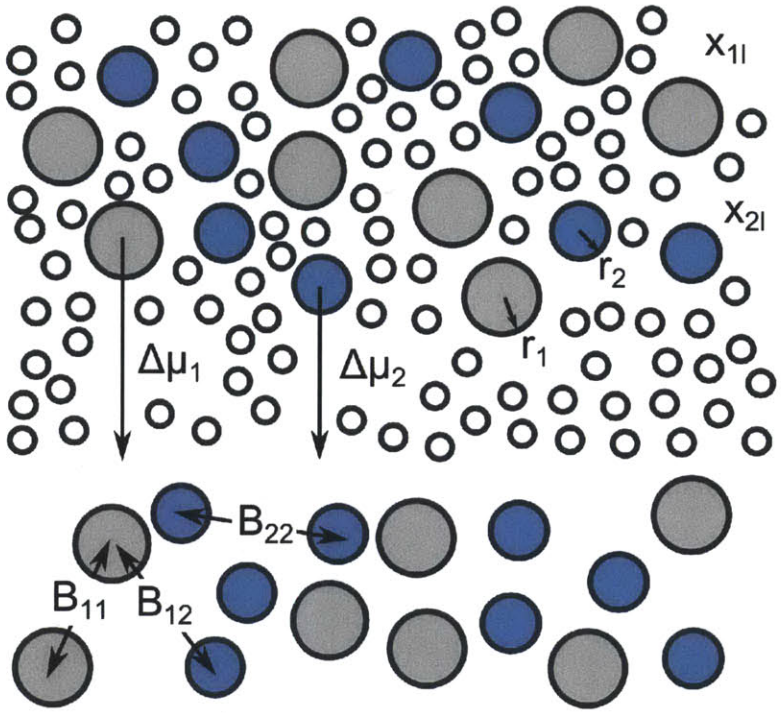

Figure 4.2 Equilibrium of polymer "anchors" (**1**) and the analyte molecules (**2**) adsorbing on the SWCNT surface. Each species on the surface is in thermodynamic equilibrium with the same species in the bulk solution.

The thermodynamic equilibrium between the analytes in the bulk solution and at the air-water interface is described by the equation of state shown in equation 2.

$$\ln(x_{li}) = \frac{\mu_i^{\sigma,0} - \mu_i^{b,0}}{k_B T} + \ln\left(\frac{x_i^s}{a - \sum_k x_k^s a_k}\right) + \frac{a_i + 2\pi r_i \sum_k x_k^s r_k}{a - \sum_k x_k^s a_k} + \frac{\pi a_i (\sum_k x_k^s r_k)^2}{(a - \sum_k x_k^s a_k)^2} + \frac{2}{a}\sum_k B_{ik} x_k^s \quad (2)$$

where x_i^s represents the molar fraction of species *i* on the surface. a is the area occupied per adsorbed surfactant molecule. $\Delta\mu_i^0 = \mu_i^{\sigma,0} - \mu_i^{b,0}$ defines the standard-state chemical potential difference of surfactant molecules of type *i* at the surface and in the bulk solution. It is important to note that units for the $\ln\left(\frac{x_i^s}{a - \sum_k x_k^s a_k}\right)$ term are accounted for with an adjustment of $\Delta\mu_i^0$ by approximately 6 kcal/mol, corresponding to the units of square angstroms for the molar surface area, a[44]. This system of equations leads to one equation for each species present - in our case, two species - with the additional constraint that all molar fractions must add to unity, $\sum_i x_i^s = 1$. Specifically, we have the following equations:

$$\ln(x_{l1}) = \frac{\Delta\mu_1^0}{k_B T} + \ln\left(\frac{x_1^s}{a - (x_1^s a_1 + x_2^s a_2)}\right) + \frac{a_1 + 2\pi r_1 (x_1^s r_1 + x_2^s r_2)}{a - (x_1^s a_1 + x_2^s a_2)} + \frac{\pi a_1 (x_1^s r_1 + x_2^s r_2)^2}{(a - (x_1^s a_1 + x_2^s a_2))^2} + \frac{2}{a}(B_{12} x_2^s + B_{11} x_1^s) \quad (3)$$

$$\ln(x_{l2}) = \frac{\Delta\mu_2^0}{k_B T} + \ln\left(\frac{x_2^s}{a - (x_1^s a_1 + x_2^s a_2)}\right) + \frac{a_2 + 2\pi r_2 (x_1^s r_1 + x_2^s r_2)}{a - (x_1^s a_1 + x_2^s a_2)} + \frac{\pi a_2 (x_1^s r_1 + x_2^s r_2)^2}{(a - (x_1^s a_1 + x_2^s a_2))^2} + \frac{2}{a}(B_{21} x_1^s + B_{22} x_2^s) \quad (4)$$

$$x_1^s + x_2^s = 1 \quad (5)$$

with three unknowns: the surface mole fractions x_1^s, x_2^s and the average area per molecule, a. The bulk mole fractions x_{l1}, x_{l2} are known from experimental preparation. For surfactants such as SDS and SC, bulk solutions were prepared with total surfactant concentrations above the critical micelle concentration (CMC), so the monomer

concentrations x_{li} were set to the CMC. Molecular volumes for each molecule are accessible using either experimentally determined parameters from the Van der Waal equation of state, or estimated from the molecular structure. r_i and a_i are computed with the molecular volume under the assumption that the molecules are spherical. B_{11}, B_{22}, B_{12}, and $\Delta\mu_1^0, \Delta\mu_2^0$ can be estimated with molecular simulations, and detailed discussions are in later sections. Thus, for each pair of various polymers and analytes, we can solve for (x_1^s, x_2^s, a) given the parameters $(r_1, r_2, a_1, a_2, B_{11}, B_{12}, B_{22}, \Delta\mu_1^0, \Delta\mu_2^0)$ by solving equations of (3) – (5). Once (x_1^s, x_2^s, a) are determined, the analyte surface coverage is calculated using

$$\theta_{cal} = \frac{a_2 x_2^s}{a} \quad (6)$$

To calculate the analyte surface area θ_{cal} it is necessary to estimate $\Delta\mu_1^0, \Delta\mu_2^0, B_{12}, B_{11}, B_{22}$. $\Delta\mu_1^0, \Delta\mu_2^0, B_{12}, B_{11}, B_{22}$, were computed using a series of all-atom molecular dynamics simulations. The MD simulations were performed by Zackary Ulissi, a graduate student in our research lab. The simulation was run in the software NAMD, with CharMM Force field parameters for the sp2-carbon atoms in nanotube/graphene were obtained from previous work[199] and parameters for the large variety of analyte and polymers were obtained automatically by the CGenFF force field and parameterization tool[200]. The tool compares the molecule of interest with existing molecules in the database, searching for the most accurate parameters for the simulation. However, CGenFF force field was unable to automatically type some of the molecules in this study, which include one analyte molecule, sodium azide, and two wrapping anchors,

boronic acid, and d(GT)15. Since sodium azide was not observed experimentally to influence the SWCNTs[178] so it is excluded from the results here. We also did not include $d(GT)_{15}$ in this model but it will be part of our future work. For boronic acid, we approximated the boron atom using nitrogen, and the resulting molecule was typable in CGenFF. In many cases the CGenFF analogy was poor, but the molecular parameters were used as a first approximation to avoid prohibitively expensive manual parameterization using quantum mechanical simulations. $\Delta\mu_i^0$ was computed using an adaptive biasing force simulation in NAMD. Specifically, the molecule of interest was placed in between two (3nm x 3nm) graphene sheets at a 6 nm separation, with periodic boundary conditions in all directions (Figure 4.3a). TIP3P water molecules then solvated the system, which was taken from an equilibrated water sample at room temperature and a pressure of 1 bar, and excess charge in the system was neutralized with counter-ions (Na^+ or Cl^-) depending on the simulation. The system was then equilibrated briefly under the NVT ensemble at room temperature for another 100 ps. The potential of mean force for the molecule of interest between the two graphene sheets was then computed using an adaptive biasing force (ABF)[201] simulation allowing the molecule to freely move. The potential of mean force was expected to converge as the potential of mean force became nearly symmetric (due to the symmetry of the system) and the energy minimum near the graphene surface was sufficiently resolved (Figure 4.3c). The calculated $\Delta\mu_i^0$ are summarized in Table 4.1.

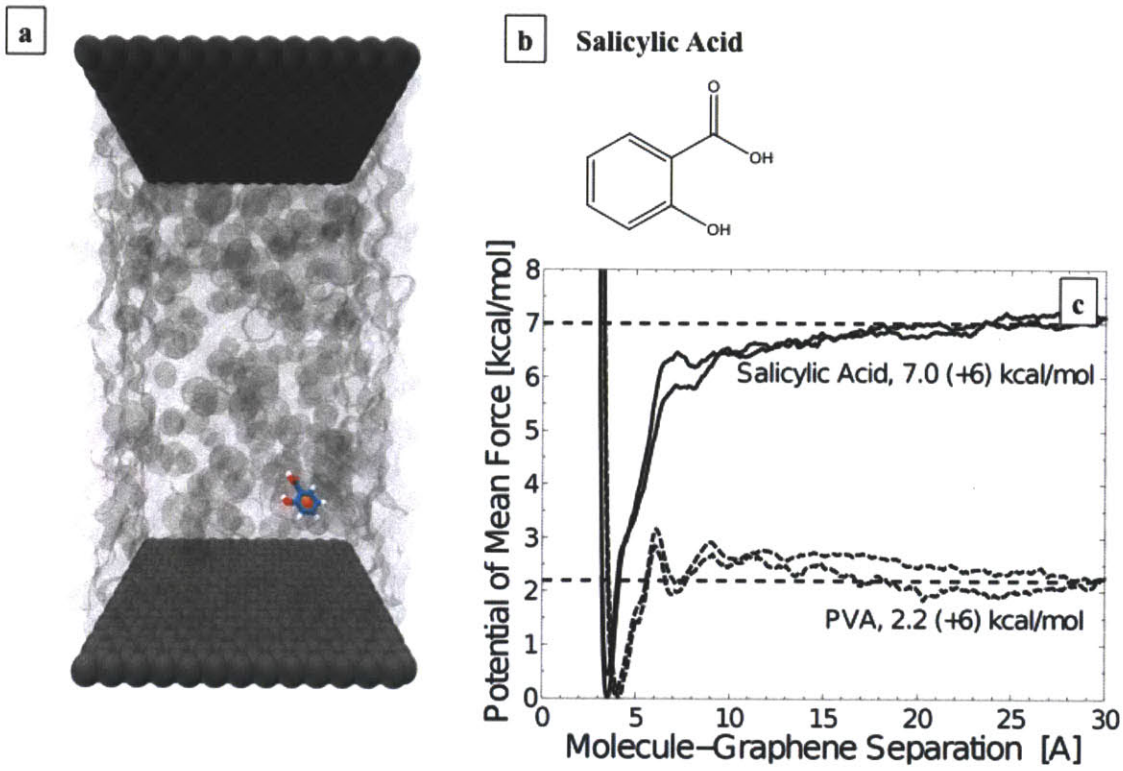

Figure 4.3 Molecular simulation of the molecules of interest. (a) Simulation cell of a salicylic acid molecule surrounded by water in between two graphene sheets. (b) The chemical structure of salicylic acid. (c) Two examples of $\Delta\mu_i^0$ calculation: $\Delta\mu_i^0$ calculated from the simulation as a function distance from the graphene surface for salicylic acid, and PVA.

B_{ik} captures the van der Waals interactions between molecule i and k, or self-interactions, and is defined as a correction to the hard-sphere model of intermolecular interactions. B_{ik} is defined as[202]

$$B_{ik} = 2\pi \int_{r_i+r_k}^{\infty} \left[1-\exp(-u_{ik}(r))/kT\right] r dr \quad (7)$$

where $u_{ik}(r)$ is the interaction energy between molecules i and k relative to infinite separation (no interaction) and r_i, r_k are the appropriate hard sphere radii from above. $u_{ik}(r)$ is affected by the environment in that the ensemble average of the potential at a

given distance depends on the local environment and water solvation (making certain molecule-molecule orientations more or less likely). However, as a first approximation to these parameters we calculated the energy between various molecules for distances ranging from 3Å to 100Å for a single set of molecular orientations using the same CHarMM/CGenFF force field parameters as above. The resulting B_{ik} parameters are summarized in Table 4.2. Future work is necessary to compare the potential curves measured in this way to ones obtained from solvated simulations. Parameters including r_i, a_i, B_{12} are provided in the supplementary materials (Table 4.3).

If one of the species adsorbs at the interface much more strongly than the other, computationally $(x_1^s \approx 1, x_2^s \approx 0)$ or $(x_1^s \approx 0, x_2^s \approx 1)$ results. The latter case indicates that it is possible that addition of analytes pushes the polymer anchors almost completely off the SWCNT surface, which was not observed experimentally. In our model, we treated polymer anchors as individual molecules, and as if they are not connected by the backbone of the polymer. Therefore, if adsorption of certain analytes is predicted to be much stronger than that of the polymer anchors, the model indicates that anchors are expected to be pushed off the SWCNT surface. However, in the actual experiments, since the anchors are inter-connected, only if all of anchors in the same polymer are off the SWCNT surface at the same time, the polymer is kinetically trapped onto the SWCNT surface. In other words, the model here does not account for this "kinetically trapping" effect of the polymer. In those special situations where either $(x_1^s \approx 1, x_2^s \approx 0)$ or $(x_1^s \approx 0, x_2^s \approx 1)$ is computed from the model, we compared values of $\frac{a_1}{a}$ of the polymer "foot" and the competing analyte assuming only one of them is present in the bulk, and

assign the one with the larger value to be the species present on the SWCNT surface. This criterion is consistent with the adsorption energy calculations shown in Figure 4.3. In other words, when the model predicts that the anchors of the polymers completely desorb from the surface as a result of strong analyte binding, we simply consider $(x_1^s = 1, x_2^s = 0)$ to avoid numerical problems in the calculation.

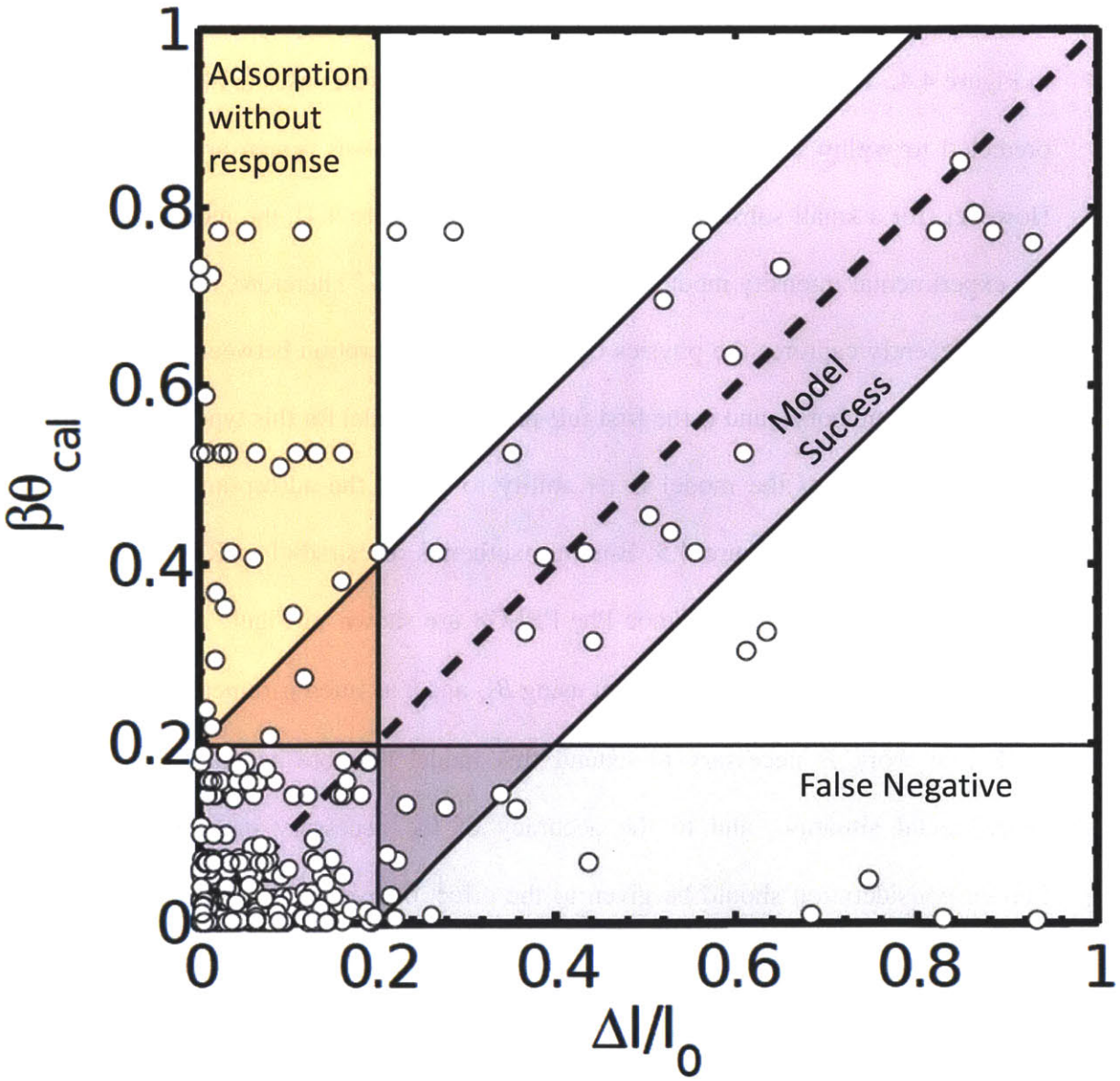

Figure 4.4 Calculated intensity response, $\beta\theta_{cal}$, as a function of experimental intensity modulation, $\Delta I / I_0$. Purple region indicates that modeled responses are within 20% error of the actual responses, which accounts for 83% of total amount of data. Orange is the "false positive" region (13.1%), where model overpredicts over 20%; and gray is the "false negative" region (3.7%) where model underpredicts the response more than 20%.

4.4 Conclusions

The accuracy of the model was tested by comparing the model response $\beta\theta_{cal}$ to experimental measurements for a library of analytes and SWCNT wrappings[178], shown in Figure 4.4. Using this model, 83% of the fluorescent responses (374 data points) were predicted to within 20% error of their experimental values (green area in Figure 4.4). However, for a small subset of cases (3.7%, red in Figure 4.4), the model underpredicts the experimental intensity modulation by more than 20%. Therefore, this 2D EOS based model decently captures the physics of competitive adsorption between the analytes and the polymer "anchors", and is the first full-predictive model for this type of problem.

A further test of the model is its ability to model the adsorption isotherm of the analyte, illustrated in Figure 4.5. Binding isotherms of estradiol to RITC-PEG-RITC – SWCNT and L-thyroxine to Fmoc-Phe-PPEG8 are shown in Figure 4.5; and we were able to fit the isotherm with our model using B_{12} and β as fitted parameters.

Future work is necessary to extend this model to more accurately resemble the experimental situation, and to the accuracy of the necessary molecular parameters. Further consideration should be given to the effect of hydrophilic connections between polymer "anchors", which inhibit the free adsorption of the anchors onto the SWCNT surface. In some cases the assumption of a molecular monolayer on the SWCNT surface may also be a poor one, especially if it is possible for the polymer chains to hinder

analyte access to the SWCNT surface. In addition, the force field parameters determined automatically need to be refined and verified. Finally, we anticipate that calculation of β from quantum mechanical calculations should be possible, and that doing so would allow the model to be fully predictive (no experimental determination for β even just on two cases).

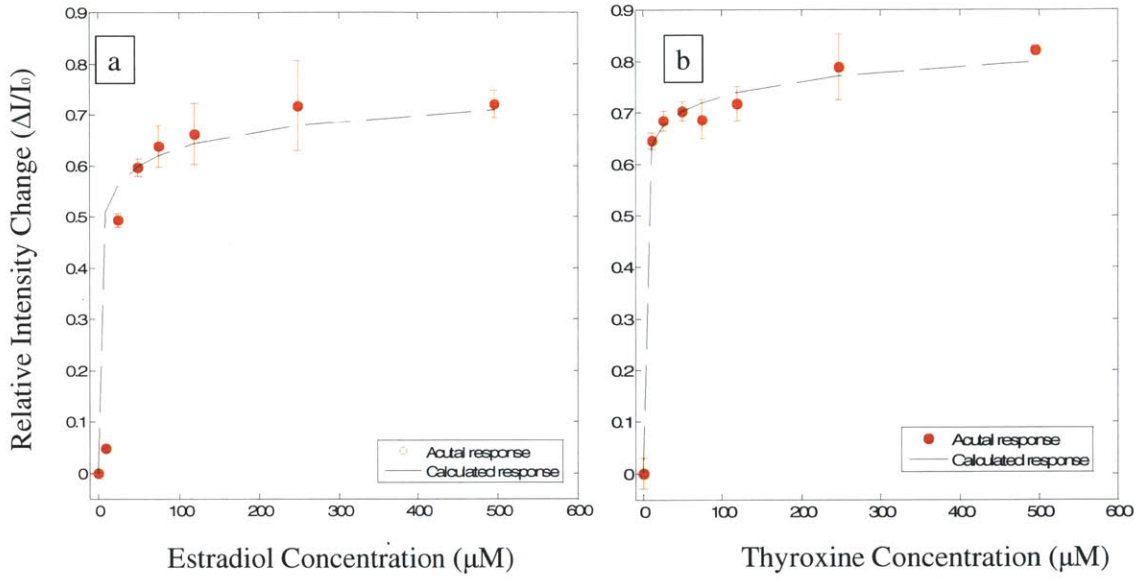

Figure 4.5 2D equation model describing analyte binding data. (a) Fluorescence quenching of (7,5) chirality of RITC-PEG-RITC – SWCNT as a function of estradiol concentration (red). Dashed black lines are fits of the data to the 2D EOS model with β of 1 and B_{12} of –400 Å^2. (b) Fluorescence quenching of (7,5) chirality of Fmoc-Phe-PPEG8 – SWCNT as a function of thyroxine concentration (red). Dashed black lines are fits of the data to the surface-adsorption model with β of 3.2 and B_{12} of –1150 Å^2. Data were taken with three replicates, and error bars are 2SD.

4.5 MD Calculated Parameters

Table 4.1 $\Delta\mu_i^0$ of the polymer "anchors" and analytes in the library (data highlighted in red is less accurate than the rest of the values due to convergence problems in the simulation)

$\Delta\mu_i^0 (kcal/mol)$			
17-alpha-estradiol	16.9	NADH	30.9
2,4-Dinitrophenol	15.0	Quinine	18.2
Acetylcholine chloride	11.5	Riboflavin	24.7
alpha-Tocopherol	25.9	Salicylic acid	13.0
Adenosine	15.5	Serotonin	14.0
ATP	22.7	Sodium pyruvate	9.0
cAMP	16.5	Sucrose	14.3
Creatinine	10.9	Thymidine	16.9
Cytidine	16.0	Tryptophan	16.2
D-Aspartic acid	9.6	Tyramine	11.6
D-Fructose	11.5	Urea	9.2
D-Galactose	10.7	BA-PhO-Dex	12.7
D-Glucose	11.7	PhO-Dex	11.6
D-Mannose	17.3	RITC-PEG-RITC	16.0
Dopamine	13.1	FITC-PEG-FITC	15.6
Glycine	8.5	PE-PEG	16.9
Guanosine	18.1	SC	16.5
Histamine	10.7	SDS	18.0
L-Ascorbic acid	13.2	PVA	8.8
L-Citrulline	10.5	Fmoc-Phe-PPEG8	15.3
L-Histidine	10.2	Fmoc-Phe-PPEG4	15.3
L-Thyroxine	15.4	NH2-PPEG8	8.1
Melatonin	20.3		

Table 4.2 B_{ij} values pairs of (analyte, and polymer anchor)

	BA-PhO-Dex	PhO-Dex	RITC-PEG-RITC	FITC-PEG-FITC	PE-PEG	SC	SDS	PVA	Fmoc-Phe-PPEG8	Fmoc-Phe-PPEG4	NH2-PPEG8
17-alpha-estradiol	54.1	43.2	400.0	73.5	42.5	164.5	41.6	42.9	121.6	121.6	22.7
2,4-Dinitrophenol	37.9	31.0	48.9	54.8	31.4	157.1	30.0	31.5	84.1	84.1	18.0
Acetylcholine chloride	30.6	26.1	40.2	46.1	27.3	107.9	23.7	26.1	66.8	66.8	14.4
alpha-Tocopherol	287.2	154.9	215.5	305.1	135.9	10755.5	111.5	162.5	769.1	769.1	93.4
Adenosine	81.9	69.1	88.6	114.9	56.9	1275.4	55.1	80.7	295.6	295.6	40.4
ATP	76.9	64.6	131.8	178.6	104.2	1102.3	61.9	60.6	194.6	194.6	33.3
cAMP	148.1	125.4	131.9	215.0	102.0	662.2	78.0	147.4	590.4	590.4	53.9
Creatinine	42.5	29.8	39.2	45.4	24.9	133.4	24.1	30.3	85.3	85.3	17.6
Cytidine	54.1	46.3	66.4	80.8	43.3	392.1	40.9	49.4	145.2	145.2	26.5
D-Aspartic acid	35.5	26.1	33.3	39.3	21.6	111.4	21.2	27.1	75.4	75.4	15.7
D-Fructose	54.3	42.2	52.8	63.3	33.6	222.3	35.2	45.9	144.4	144.4	26.4
D-Galactose	43.3	34.8	47.7	55.7	30.2	188.1	30.0	36.8	103.6	103.6	22.1
D-Glucose	71.0	47.5	55.5	71.5	36.6	385.8	35.3	51.8	244.8	244.8	33.7
D-Mannose	47.1	38.8	51.2	60.6	32.3	244.7	32.6	42.9	121.8	121.8	24.9
Dopamine	32.3	26.9	43.6	46.7	26.4	128.8	27.8	27.0	65.4	65.4	15.3
Glycine	21.8	18.2	23.0	27.6	15.4	80.7	15.1	19.8	52.6	52.6	12.0
Guanosine	190.6	154.7	132.8	243.1	96.0	1127.2	84.8	270.6	493.8	493.8	104.6
Histamine	29.7	22.7	33.9	38.8	20.7	96.6	21.5	23.2	59.3	59.3	13.6
L-Ascorbic acid	42.6	32.2	46.1	54.1	30.1	169.9	28.4	32.6	92.4	92.4	20.3
L-Citrulline	32.5	26.6	41.0	49.3	27.9	124.9	24.1	26.1	68.2	68.2	14.9
L-Histidine	70.7	41.5	50.9	61.0	30.4	182.0	33.2	42.9	137.9	137.9	26.6
L-Thyroxine	41.2	37.8	77.0	80.1	51.2	169.4	46.4	35.4	1150.0	1150.0	19.3
Melatonin	90.4	53.0	76.9	88.2	47.3	356.7	41.6	50.2	167.9	167.9	31.7
NADH	600.4	460.5	259.0	1788.5	890.3	75321.8	290.4	500.5	1019.6	1019.6	122.9
Quinine	783.2	664.6	239.1	773.2	190.9	1119.4	168.8	328.7	370.5	370.5	155.6
Riboflavin	500.0	450.0	189.5	414.4	150.6	1223.9	154.9	264.2	492.3	492.3	97.8
Salicylic acid	30.6	26.2	38.6	43.9	24.8	123.8	24.5	27.0	66.3	66.3	15.7
Serotonin	37.0	31.4	46.6	55.3	30.1	145.7	28.7	31.9	79.1	79.1	17.7
Sodium pyruvate	24.8	20.2	26.1	31.2	17.4	87.1	17.1	21.6	57.7	57.7	13.0
Sucrose	182.2	108.7	121.4	145.2	67.2	766.2	81.3	117.3	585.1	585.1	55.2
Thymidine	80.4	52.9	71.4	93.8	46.7	472.1	41.0	53.3	192.8	192.8	32.3
Tryptophan	37.5	31.0	48.4	55.3	30.6	131.3	28.7	31.1	74.7	74.7	17.1
Tyramine	28.4	24.9	40.0	42.9	24.5	114.6	24.5	24.9	56.2	56.2	13.4
Urea	25.0	20.1	22.4	28.7	14.9	85.5	15.1	22.7	65.1	65.1	12.7

(highlighted values are adjusted according to response isotherm)

Table 4.3 r_i *and* B_{ii} values of analyte molecules and polymer anchors

Chemical	r_i (Å)	B_{ii} (Å^2)	Chemical	r_i(Å)	B_{ii} (Å^2)
17-alpha-estradiol	4.55	-71.50	Melatonin	4.26	-92.20
2,4-Dinitrophenol	3.62	-42.80	NADH	4.95	-2715.10
Acetylcholine chloride	3.97	-32.20	Quinine	4.78	-327.90
alpha-Tocopherol	5.63	-103075.40	Riboflavin	4.84	-904.90
Adenosine	4.05	-1626.30	Salicylic acid	3.43	-34.60
ATP	4.66	-453.20	Serotonin	3.89	-42.70
cAMP	4.17	-520.30	Sodium pyruvate	2.94	-20.40
Creatinine	3.36	-38.90	Sucrose	4.35	-960.40
Cytidine	3.96	-139.00	Thymidine	3.99	-372.30
D-Aspartic acid	3.37	-41.40	Tryptophan	3.99	-47.60
D-Fructose	3.54	-125.70	Tyramine	3.67	-30.30
D-Galactose	3.54	-76.40	Urea	2.59	-21.00
D-Glucose	3.53	-326.30	BA-PhO-Dex	3.67	-29.02
D-Mannose	3.54	-137.60	PhO-Dex	3.59	-22.20
Dopamine	3.72	-33.80	RITC-PEG-RITC	5.52	-96.40
Glycine	2.93	-15.70	FITC-PEG-FITC	4.98	-98.70
Guanosine	4.42	-903.80	PE-PEG	4.72	-37.20
Histamine	3.31	-30.20	SC	4.81	-641.04
L-Ascorbic acid	3.44	-59.00	SDS	4.64	-32.29
L-Citrulline	3.78	-38.20	PVA	3.3	-22.80
L-Histidine	3.51	-70.80	Fmoc-Phe-PPEG8	4.07	-238.20
L-Thyroxine	4.84	-83.70	Fmoc-Phe-PPEG4	4.07	-238.20
			NH2-PPEG8	4.37	-8.20

5 A Rapid, Quantitative, and Label-Free Detection Platform for Cardiac Biomarker Troponin T

5.1 Nanosensor-based Direct and Label-free Detection for Protein Biomarkers; Engineering towards Point-of-care Diagnostics.

5.1.1 Advantage and Motivation of Using Direct and Label-free Method for Protein Bio-marker Detection

Biomarkers are proteins, microRNA, DNA or DNA fragments, either circulating in body fluid (blood, serum, urine) or presented on diseased cell surfaces, that are indicative of certain disease states. This section of the review focuses on protein biomarkers. Biomarker discovery and detection are two intermingled but parallel fields. The former focuses on the development of multiplexed, sensitive tools that can screen and compare body samples collected from large populations of healthy people and diseased patients, in order to identify new biomarkers. In this case, the body fluid samples can be pre-treated before analysis takes place (blood cell removal, serum protein removal, etc.); in addition, for screening such large sample populations, fast detection methods are desired, but not necessary. In contrast, biomarker detection focuses on rapid, sensitive detection of known biomarkers with minimal sample pre-processing, in order to diagnose certain diseases in a timely and accurate fashion. The two areas have different purposes and use different tools, but they also share some common problems and solutions. This section of the review will only focus on the area of biomarker detection and will not cover biomarker discovery techniques, but readers can refer to other review articles for the topic of biomarker discovery, specifically: (Ray, et al. *Proteomics*, 2011[203]) on label-

free methods, (Hua, et al. *Bioanalysis*, 2011[204]) on nano-LC-based methods, (Roy, et al. *Brief. Bioinform*, 2011 [205]) on mass spectroscopy data analysis, and (Larguinho, et al. *Journal of Proteomics*. 2012 [206]) on nanoparticle-based proteomics methods. There are also some recent advanced in technologies regarding biomarker discovery [207-209].

The biggest focus on bio-marker detection is point-of-care (POC) diagnostics. The global market for POC diagnostics, valued at $13.8 billion in 2011, is expected to grow to $16.5 billion in 2016, according to a new report on point-of-care diagnostics from BCC research (http://www.bccresearch.com/). The fastest growing segment, cardiac biomarker detection, is projected to increase at a CAGR (the five-year compound annual growth rate) of 14%, increasing from $1 billion in 2011 to $2 billion in 2016. The market grows at such a high rate simply because the detection of certain biomarkers, especially at low concentration, is the key to diagnosing the onset of some critical diseases, such as cancer, enabling the timely treatment of patients, and reducing medical costs.

Methods for biomarker detection can be divided into two separate categories, labeling methods, and label-free methods. Traditional POC protein biomarker detection techniques mostly rely on bench-top, commercialized, multistep antibody-based immuno-assays, such as ELISA (enzyme-linked immunosorbent assay), which is a labeling method. A typical sandwich ELISA involves the following steps: 1) application of the primary antibody; 2) application of the desired target protein, which binds to the primary antibody; 3) removal of the unbound target protein by washing; 4) application of labeled secondary antibody, which binds to the target protein at a different location from the primary antibody; 5) removal of the unbound secondary antibody. The process described here has not even accounted for necessary blocking steps to reduce non-specific binding.

In addition, each steps typically requires 20 – 30 minutes of incubation for the antibody-antigen binding to occur. Despite widespread-usage and recent advances, even in portable POC devices[210, 211], labeling assays have many limitations. The main problem is that the ELISA assay requires so many steps of sample application and washing, making it tedious, labor-intensive, and time consuming. The intermediate washing steps, designed to reduce non-specific signal, intrinsically restrict the usage of this technique to strong binding pairs.

There are also many other labeling methods being developed besides ELISA. However, in general, any assays that require fluorescently-labeled proteins face a variety of problems. Chemically labeling a protein can affect its native structure, reducing its binding affinity. Additionally, fluorescent labeling often occurs randomly on the protein surface, resulting in heterogeneous populations of proteins. Both factors can adversely affect test results[212]. Further, such assays require a pair of antibodies, with one antibody serving as the capture protein, while the other serves to label the target protein. The development of such antibody pairs, both of which have high specificity towards the targeted protein, is difficult and expensive, limiting the widespread applicability of label-based assays [213].

These limitations have motivated many research and commercial labs to develop novel detection tools that are direct and label-free, but still sensitive toward low-concentrations of protein biomarkers. This section of the review will present an overview of direct and label-free techniques for POC biomarker detection, as well their advantages, challenges, and potential solutions.

5.1.2 Overview of Nanosensor-based Label-free Techniques, Challenges and Innovative solutions.

Label-free technologies include (1) field-effect transistors[214, 215], (2) other electrical methods, including cyclic voltammetry[216] and impedimetric sensors[217, 218], and (3) spectroscopy or fluorescence-based methods[219-221]. In order to fit the overall content of this review, the focus will be on biomarker detection using nano-sensor devices. Within the field of nano-sensor biomarker detection, various nano-materials have been used, including (1) nanowires [214], (2) nanoparticles[219], (3) nanoclusters[222], (4) microspheres[223], (5) gold nanorods (see review *Xu, et al. 2011* [224] for reference), and (6) carbon nanotubes [218, 225].

Although label-free and direct detection methods are more desirable for the reasons mentioned above, these techniques have only been developed fairly recently and also face many challenges. One of the main problems associated with any label-free method is the elimination of non-specific adsorption. Unlike a sandwich ELISA assay where many washing steps are involved to remove non-specifically bound proteins or secondary antibodies, many label-free methods only involve one step of sample application, and no washing is required. This is advantageous, because the overall assaying process is much simpler, and therefore, much less time consuming; however, this also requires that the assay technique be intrinsically resistant to non-specific adsorption from undesired proteins. The ultimate goal of this type of detection is to be able to detect low-concentration biomarkers in human serum or whole blood directly, with minimal sample pre-treatment at POC. To date, many researchers have come up with innovative methods to reduce or even eliminate non-specific adsorption. In particular, coating the sensor

surface with passivating agents, including PEG molecules[226-228], certain surfactants[215], or zwitterionic molecules[229, 230] is the most commonly used method to resist non-specific protein adsorption. Second, microfluid channels can be engineered to remove blood cells or certain proteins existing in whole blood samples [210]. Third, smart hydrogels, or membranes with particular pore-sizes, can be synthesized such that they exclude large and abundant proteins such as human serum albumin (HSA), increasing their sensitivity toward low molecular weight biomarkers [231, 232].

In addition to the common problem of non-specific adsorption, each technology also has its own challenges. This review will discuss each technology, its own challenge and potential solutions, with a summary and side-by-side comparison provided in Table 5.1.

5.1.3 Different Nano-sensor Based Label-free Techniques and Comparisons

5.1.3.1 Field-effective transistors (FETs)

Silicon nanowire FETs (SiNW) have recently attracted tremendous attention as a potentially useful tool for biomarker detection. Chen et. al. recently published a comprehensive review on this topic**[233]**. In this section of the review, we do not intend to re-write a new review on this topic, but would like to mention a few examples which address two of the common problems in the SiNW or NW field, including non-specific adsorption and low sensitivity towards specific biomarkers at high ionic strength (physiologically relevant).

The Zhou group at UCLA has demonstrated a very promising FET consisting of In_2O_3-nanowires[214]. The scheme of the device is shown in Figure 5.1a. In this scheme, specific antibodies are reacted with carboxylic acid groups on the In_2O_3 nanowire, and the nanowire is then treated with 50 ug/ml Tween 20 for 1 hour, prior to addition of target

proteins. The sensor is only sensitive at an ionic strength equivalent of 1.5 mM phosphate buffer saline (PBS). Therefore, for target protein detection, the authors have to either dilute, or desalt the serum in order to match the ionic strength. Figure 5.1b shows the sensor response to an epithelial ovarian cancer biomarker, CA-125 in 100x diluted serum with detection limit of 0.1 U/ml (0.5 pM). Figure 5.1c shows the sensor response to another epithelial ovarian cancer biomarker, IGF-II after the serum has been desalted, and the detection limit is reported to be 8 ng/ml. Note that technically this technique cannot be directly used for either serum or whole blood, due to the low ionic strength requirement. However, the sensitivity of detection is rather low if the ionic strength of serum can be adjusted, and therefore, this technique can still find utility for real sensing applications. A comparison between the sensor's detection limit and the physiologically relevant concentration of those biomarkers is summarized in Table 5.1. In addition, it was also reported that without Tween 20 treatment, the FET device shows non-specific response to serum, and is unable to detect CA-125 (Figure 5.1d-2). However, after Tween-20 treatment, the non-specific response is eliminated, and the sensor is able to respond to CA-125 in 100x diluted serum (Figure 5.1d-3), with a similar response to that obtained in buffer (Figure 5.1d-1).

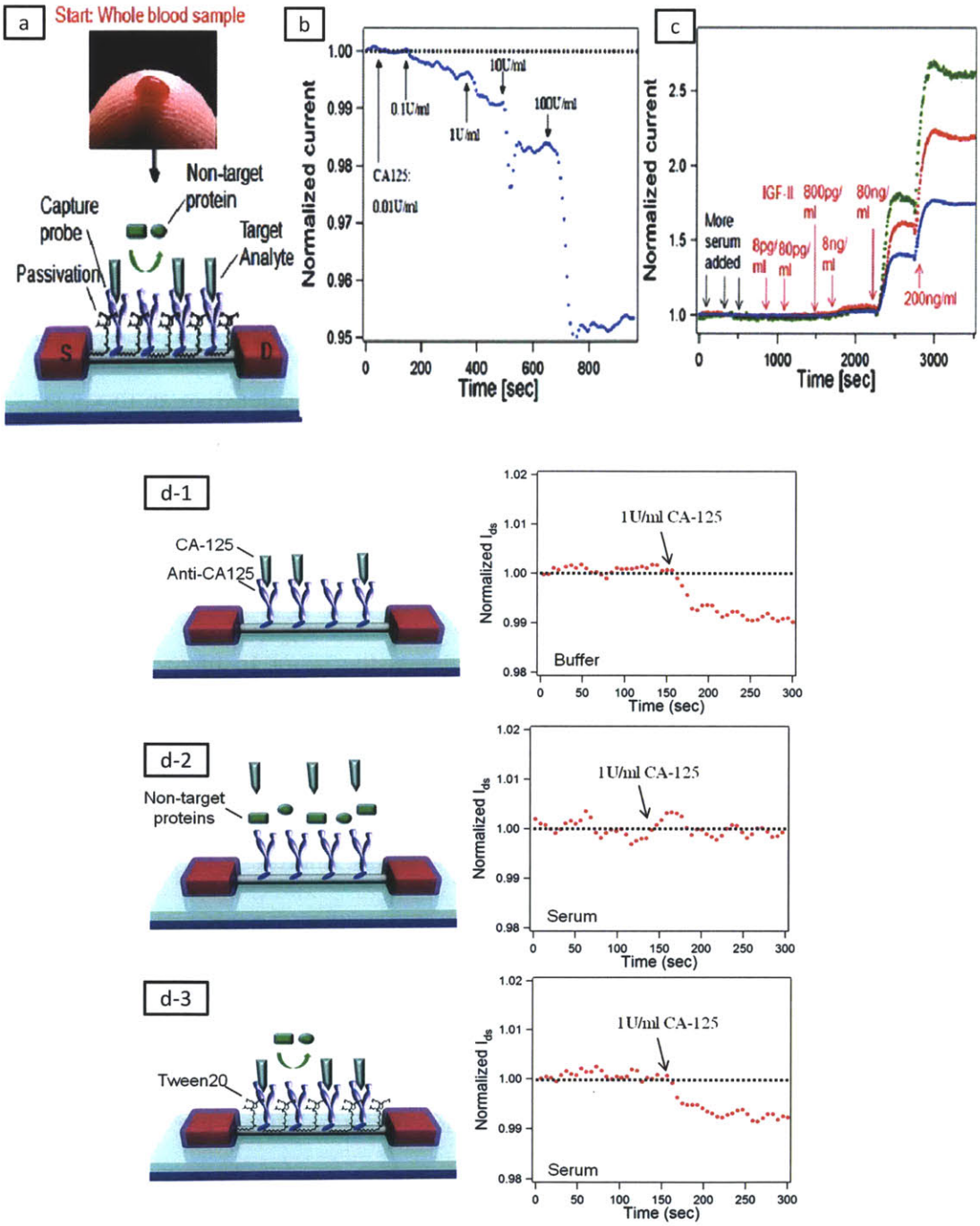

Figure 5.1 Sensor scheme and detection process. (a) Schematic of system configuration. (b) CA-125 detection in 100x diluted human serum, with detection limit of 0.1 u/ml (0.5 pM). (c) IGF-II detection in desalted serum, with detection limit of 8 ng/ml. (d) Device configuration and real-time sensing response for (d-1) unpassivated CA-125 nanosensor in buffer, (d-2) unpassivated CA-125 nanosensor in serum, and (d-3) Tween 20-passivated nanosensor in serum (inset: structure of Tween 20). (Figure adopted with permission from reference[214]. Copyright 2011 American Chemical Society)

As we can see from this previous work, one of the major challenges of FET sensors is the low ionic strength operating requirement (usually < 1 mM). However, physiologically relevant salt concentrations are much higher, at approximately 150 mM. This difficulty results from the fact that as the concentration of the salt increases, the Debye length decreases. Immunoglobulin G (IgG) antibodies are estimated to have a height of approximately 14 nm, a width of 8.5 nm, and thickness of 4.0 nm[234-236]. Once the Debye length decreased to the extent that it is much smaller than antibody size, the FET can no longer detect the changes in the local charge environment which result from a binding of the target molecule. Although researchers can either dilute the blood or serum sample, or use desalting methods to decrease the ionic strength of the sample, there are a few drawbacks: (1) Diluting the sample requires the senor to have a very good detection limit, which could be difficult to attain in some instances; (2) dilution may affect the pH and salt concentration, resulting in undesired signal; and (3) some of the target biomarker may be lost during the desalting procedure. Therefore, a FET sensor that can operate at physiologically relevant salt concentrations is desirable.

Identifying this problem, the Sung group developed a new type of processing scheme to allow the FET to operate at physiologically relevant ionic strengths[215]. The scheme is shown in Figure 5.2a and 5.2b. After the antibodies are immobilized, a reference buffer that is at low ionic strength is injected into the Si-FET (step I); then human serum containing the target antigen flows through the FET sensor to promote target protein binding (Step II); finally, the original reference buffer is flowed through FET to exchange the serum (step III). If the target antigen is still bound to the immobilized antibody, the conductance level will differ from the original level, and the difference can be measured.

With this method, a detection limit of 0.2 ng/ml was attained, with quantitative detection of the biomarker between 0.2 to 114 ng/ml for carcinoembryonic antigen (CEA).

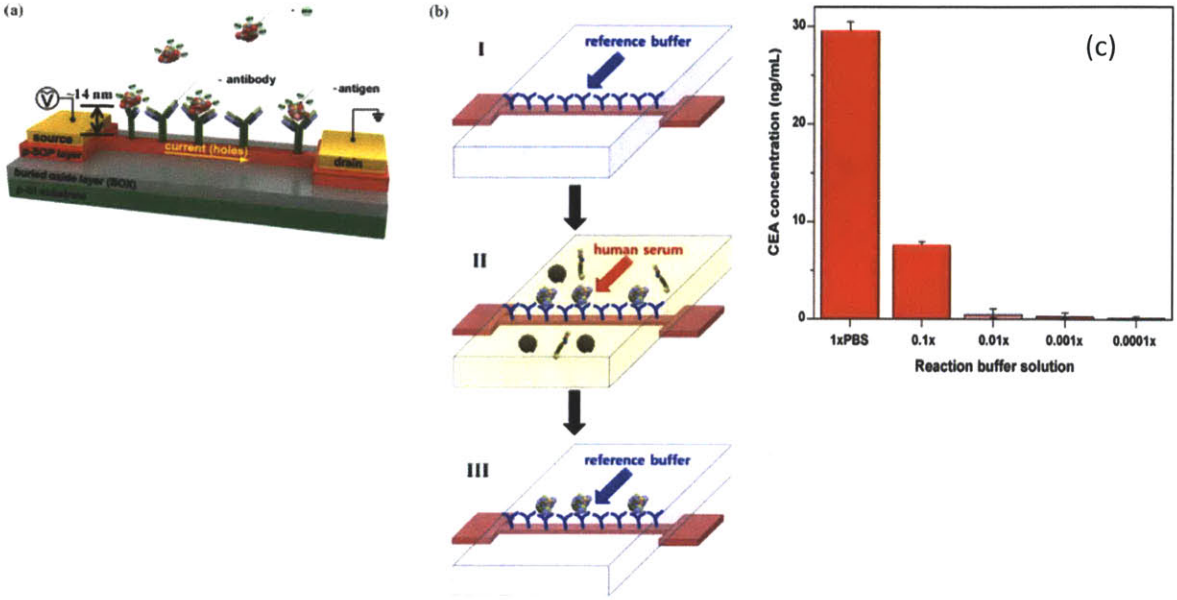

Figure 5.2 FET-based sensor structure and detection. (a) FET-based sensor structure immobilized with antibodies and detection of negatively charged antigen and (b) schematic illustration of novel immunodetection using the FET-based sensor in serum. (c) The dependence of antigen-antibody affinity on the ionic concentration of the reaction buffer tested by using sandwich ELISA. Calibrated CEA concentration plot for reaction buffers with various ionic concentrations demonstrated by using the ELISA. (Reprinted from reference [215] (2010), with permission from Elsevier.)

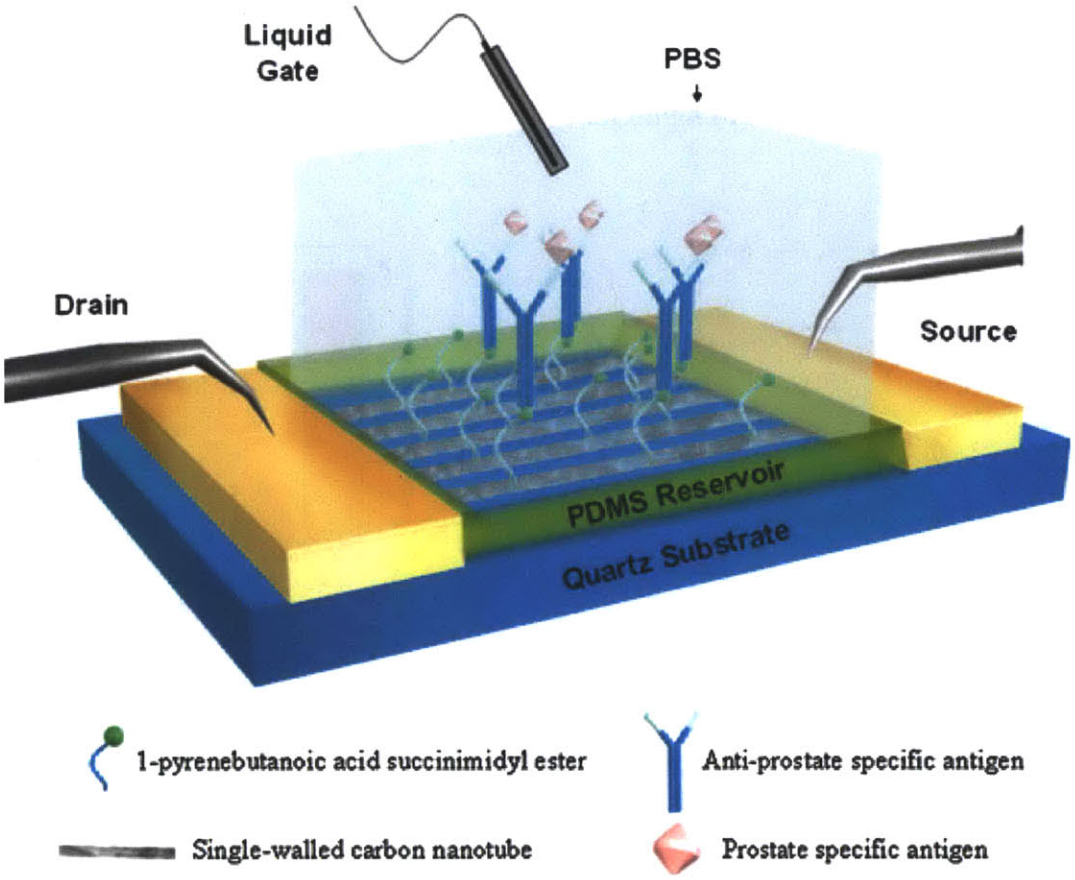

Figure 5.3 Schematic of SWCNT sensor on quartz substrate for real time electronic detection of biomolecules; transistor electrodes are fabricated perpendicular to the growth direction and the quartz substrate is directly used as biosensors by adopting liquid gating configuration. (Reprinted from reference [225] (2010), with permission from Elsevier.)

To explore novel materials, the Mhaisalkar group developed an aligned carbon nanotube FET device which is schematically depicted in Figure 5.3[225]. Theoretically, the alignment minimizes the tube-to-tube contact resistance, thereby improving the conductance, and ultimately the overall performance of the device. Using this device geometry, they were able to achieve a detection limit of 100 pM of PSA in PBS buffer.

5.1.3.2 Other electrical measurements

The Merkoçi group developed a novel nanochannel-based detection method, shown in Figure 5.4[232]. The formation of the immunocomplexes, inside the pores, produces a

partial blockage of the ionic species passing through the nanochannel, resulting in a decrease in the current signal. The voltammetric behavior can be monitored by cyclic voltammetry or differential pulse voltammetry (DPV). This method was originally designed to be label-free, however, with a label-free approach, the detection limit was found to be only 500 μg mL^{-1} of human IgG using 200nm-pore membranes. Therefore, the authors used gold nanoparticle tags to further block the signal, resulting in increased sensitivity. The optimized detection limit toward IgG was 50 ng/ml.

The authors further applied this technique to detect cancer biomarker CA15-3, with a detection limit of 52 Ug/ml in whole blood. One benefit of this method is that it does not require any pre-sample preparation, since the membrane pores are able to effectively block blood cells from passing through, thereby eliminating interference effects.

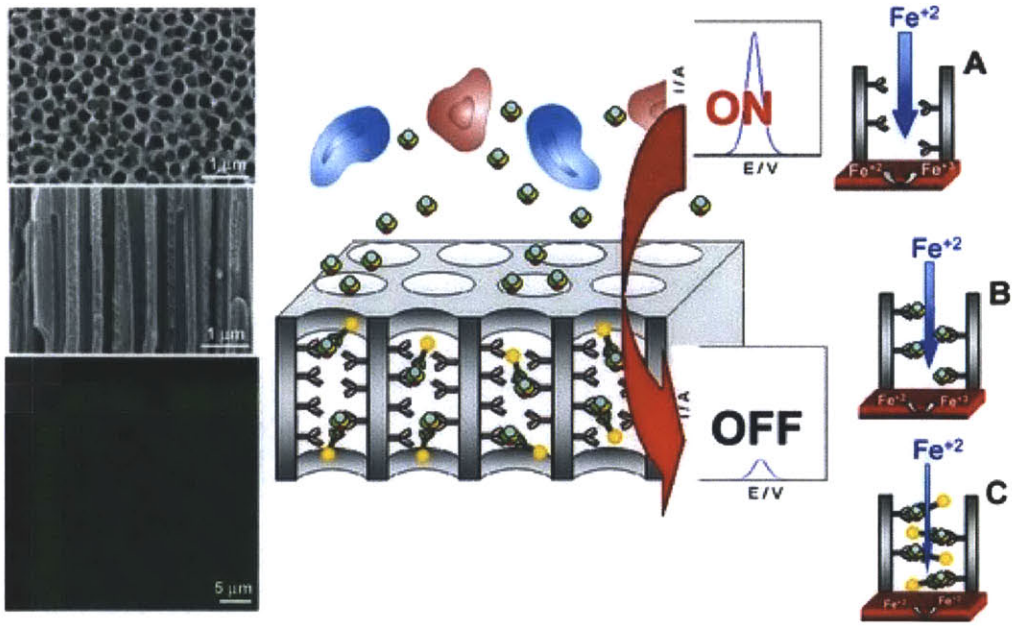

Figure 5.4 Protein sensing scheme from Merkoci group. Center: Protein sensing technology using an AAO nanoporous membrane. The cells in the sample remain outside the pores and the proteins enter inside and are recognized by specific antibodies. Right: Sensing principle in the absence (A) and presence (B) of the specific protein in the sample and in the case of the sandwich assay using AuNP tags (C). Left: SEM images of a top view and cross-sectional view of the AAO nanoporous membrane containing 200-nm pores, and confocal microscopy image of a top and

cross-sectional view 5 μm in depth from both sides of the membrane. (Reprinted from reference [232] (2011), with permission from John Wiley and Sons.)

The Iqbal group has [237] developed a gold break-junction that, after attachment of anti-EGFR aptamers, can be used to detect EGFR at a detection limit of 50 ug/ml (see Figure 5.5). However, physiologically relevant EGFR concentrations in cancer patients are typically 45–78 ng/ml [237], and can be as low as 200 fmol/ml (27 ng/ml)[238]. Therefore, with the current sensitivity, this method is not yet suitable for biological applications. In addition, non-specific background binding is fairly significant, even with blocking reagent.

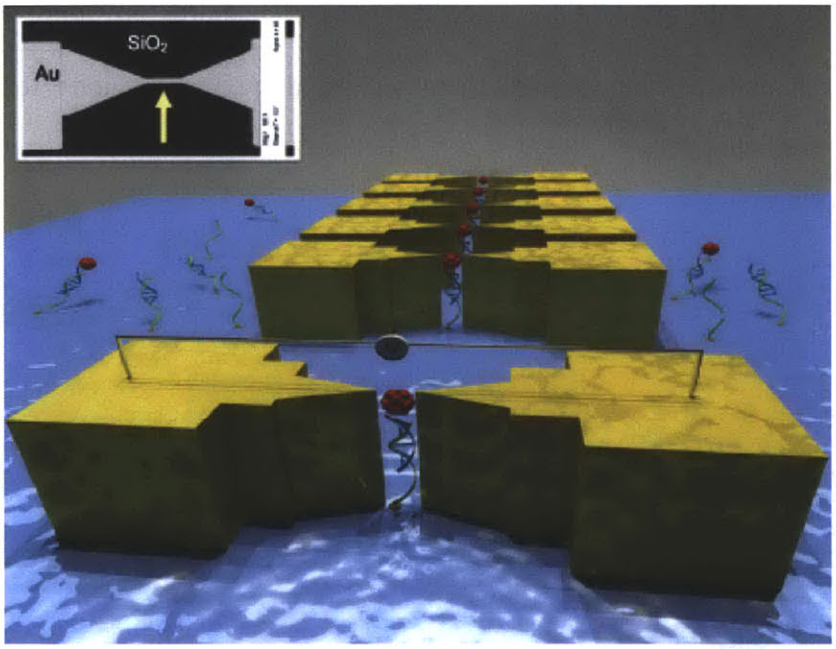

Figure 5.5 A 3D sketch of the device that demonstrates the mechanism of the electronic detection (not to scale). The inset shows an SEM micrograph of the thin Au line on the SiO_2 chip. Arrow in the inset shows where the scratch is made with FIB. (Figure reprinted from reference [237] with permission from IOPP Publishing 2012).

5.1.3.3. Impedimetric based methods:

The Mayer group reported a label-free impedimetric aptasensor for lysozyme detection based on carbon nanotube-modified, screen-printed electrodes**[218]**. The detection scheme is shown in Figure 5.6. In this case, electrodes are modified with carbon nanotubes, taking advantage of the high surface area and electron-acceptor properties of the carbon nanotubes. The limit of detection was calculated to be 12.09 μg/ml (equal to 862 nM).

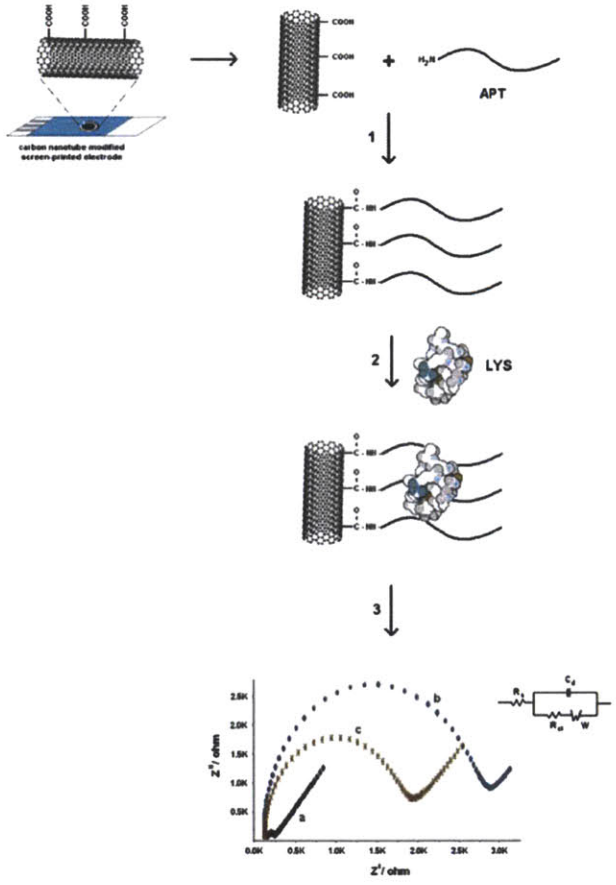

Figure 5.6 Impedimetric based device sensing scheme. Before (1) and after (2) immobilization of amino-linked DNA aptamer onto the surface of MWCNT–SPEs and (3) the interaction of LYS with APT and by using EIS measurement. Representative Nyquist diagrams show the EIS measurements for (a) bare (unmodified) electrode, (b) APT-modified electrode, and (c) APT+LYS-modified MWCNT–SPEs. (Reprinted from reference [218] (2012), with permission from Elsevier.)

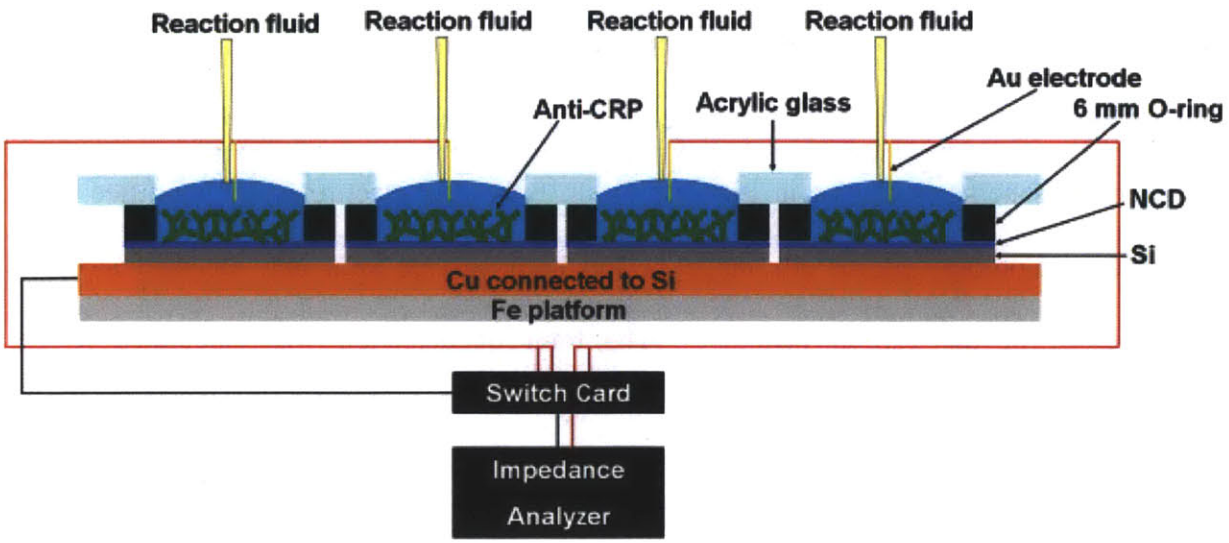

Figure 5.7 Schematic diagram of the immunosensor setup used in the experiments. The sensor houses four anti-CRP-functionalized NCD samples, allowing the simultaneous measurement of four conditions. (Reprinted from reference [239] (2011), with permission from Elsevier.)

The Michiels group developed an Impedimetric, diamond-based immmunosensor for the detection of C-reactive protein (CRP) [239]. The sensor setup is displayed in Figure 5.7. Nanocrystalline diamond (NCD) is coated with anti-CRP antibodies, functioning as working electrodes, and are mounted on a copper back contact using silver paste. The device is connected with an impedance analyzer to monitor frequency change upon binding of CRP onto the sensor surface. The sensor has a detection limit of 10 nM, below the physically relevant value of 25 nM; however, the authors have only tried to run one test (500 nM) in serum, so the sensitivity limit under these conditions is unknown.

5.1.3.4. Spectroscopy or Fluorescence-based methods

The Ren group reported a one-step immunoassay for cancer biomarker detection using resonance light scattering correlation spectroscopy (RLSCS)[219] . Technically, this technique does require labeling, however it avoids washing steps that are needed in many traditional labeling immunoassay, and therefore, we included this work in the review. GNP–Ab1 and GNP–Ab2 express the bioconjugates of antibody-1 and antibody-2 with GNPs. The immunocomplex expresses a sandwich immunocomplex with GNP–Ab1 and GNP–Ab2. The diffusion time of gold nanoparticles (GNP) increases upon binding of the antigen, and the change in diffusion time can be captured and analyzed by RLSCS. The detection method is very sensitive, with linear range from 1 pM to 1 nM in serum. However, the instrumentation is fairly complicated. In addition, the linear range only applies at low concentration, and therefore, the authors need to dilute healthy samples by 400x, and diseased patient samples by 4,000x, in order to work within the linear range.

The Suri Group[220] developed a Zeta potential-based colorimetric immunoassay for the direct detection of diabetic marker HbA1c using gold nanoprobes. Without target protein present, the aggregating capability of antibody functionalized GNPs increase as salt concentration increases. Addition of the target protein (HbA1c) prevents the aggregation. Because GNP solutions change color from red to blue upon aggregation, this color change can be used to indicate the presence of the target protein. The detection shows a dynamic response range from 0.001–0.004 mg/ml for glycosylated hemoglobin HbA1c with a detection limit of 0.0015 mg/ml.

www

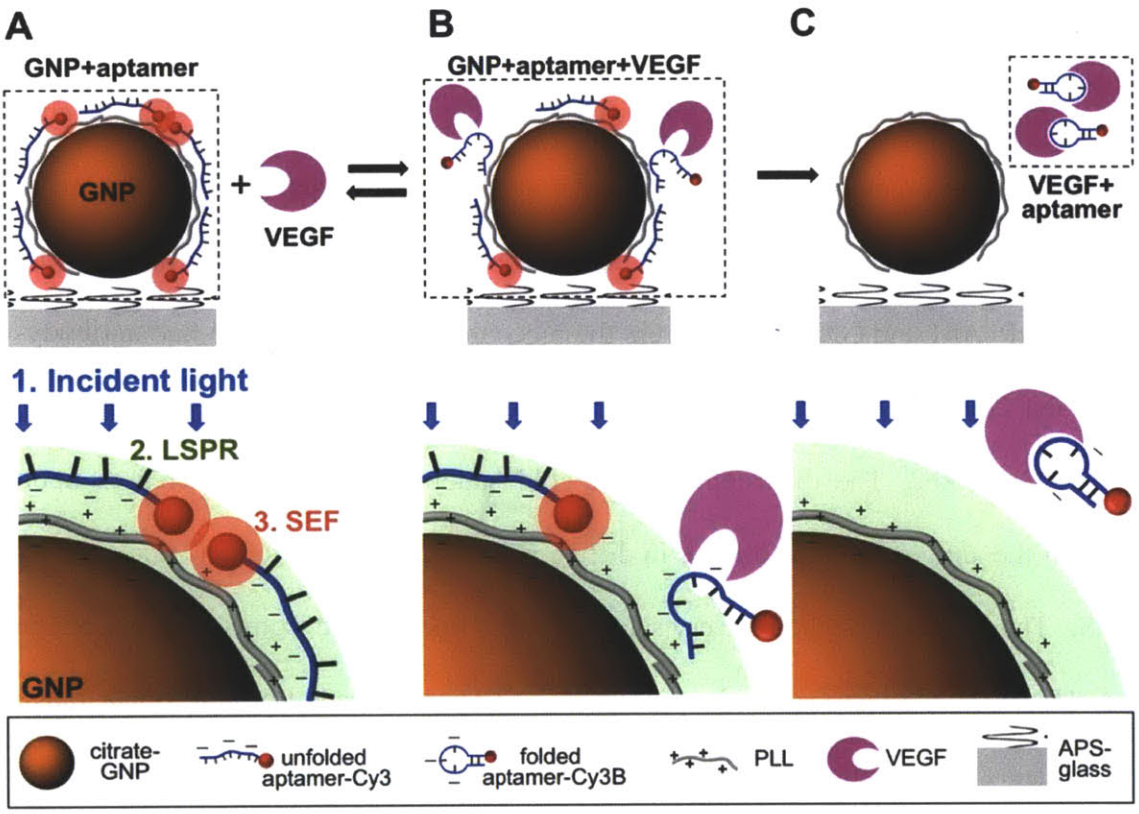

Figure 5.8 Schematic representations of detection mechanism of the aptasensor for $VEGF_{165}$. (A) In the absence of target molecules, $VEGF_{165}$, unfolded $VEGF_{165}$ aptamer is electrostatically bound to a positively charged PLL-coated gold nanoparticle (GNP) surface and surface-enhanced fluorescence (SEF) of Cy3B conjugated with the $VEGF_{165}$ aptamer is created by both a metal interaction increasing the radiative fluorescent decay rate of Cy3B and the local surface plasmon resonance (LSPR) enhancing the intensity of an incident light. (B) The interaction of the $VEGF_{165}$ aptamer to its target induces the reversible conformation change of the aptamer and, consequently, the decreased electrostatic binding force. (C) As a result, the target-binding interaction of the aptamer causes the irreversible detachment of the aptamer from the GNP surface and avoids the SEF effect of Cy3B. (Figure reprinted with permission from reference [221]. Copyright 2012 American Chemical Society)

The Lee group devised a detection scheme for vascular endothelial growth factor-165 ($VEGF_{165}$), a predominant biomarker of cancer angiogenesis, by taking advantage of surface plasmon enhancement[221]. The scheme is shown in Figure 5.8. In the absence of VEGF, unfolded VEGF aptamer is electrostatically bound to a positively charged PLL-coated GNP surface; because the aptamer is labeled with Cy3B, adhering it close to the

surface creates surface-enhanced fluorescence. Addition of VEGF pulls the specific aptamer off the gold surface, and the previously enhanced fluorescence disappears. The sensor has a high selectivity towards VEGF with linear detection from 25 pg/mL to 25 μg/mL (=from 1.25 pM to 1.25 μM) in buffer. However, the sensor shows weak interaction towards human serum albumin (HSA). Specifically, at physiologically relevant concentrations, VEGF (2.5 ng/ml) and HSA (40 mg/mL) show similar signals.

Finally, the advantages, disadvantages, sensitivities and applications of different techniques are summarized in Table 5.1.

Table 5.1 Summary of advantage, disadvantage, sensitivity and application of different techniques.

Detection Method	Sample pre-processing?	Advantages	Disadvantages	Detected Biomarker	Detection Limit	Physiological Concentration in Diseased Patients	Reference
In2O3 nanowires, electrical measurements	Yes. Filter off blood cells	Very high sensitivity	1) Works in 1.5 mM ionic strength; 2) serum needs to be diluted or desalted into buffer; 3) and each device has a different calibration curve	CA-125, an epithelial ovarian cancer biomarker	0.5 pM in 100x diluted serum	100-275 U/mL, or 0.5 - 1.375 nM	[214]
				IGF-II, an epithelial ovarian cancer biomarker	8 ng/ml (1.5 mM buffer)	800 ng/ml	
Si-FET, reference buffer method	No.	Can work with serum directly		cancer marker, carcinoembryonic antigen (CEA)	0.2 -114 ng/ml (in serum)	0-2.5 ng/ml healthy people; cancer patients significantly vary[240]	[215]
Aligned carbon nanotube on quartz FET	Unclear, only demonstrated in buffer		Currently only demonstrated in buffer.	PSA	100 pM (buffer)	Further screening for cancer may be required for elevated PSA levels in serum in the order of >~4 ng/ml (>~150 pM).	[225]
impedimetric apatasensor	Unclear, only demonstrated in buffer	Cheap	detection limit is in ug/ml range; response is not linear	lysozyme	12.09 µg/ml (equal to 862 nM) in buffer		[218]
Nanochannel/Nanoparticle-Based Filtering and Sensing	No. Size-exclusion effect removes blood cells		Still needs AuNP label to enhance sensitivity; label-free method has lower sensitivity.	CA-153	52 U mL–1 (in blood)	< 30 U ml-1 in normal person, but levels as high as 100 U mL – 1 can sometimes be seen in women who do not have cancer	[232]
				IgG	50 ng/ml (in buffer)	< 30 U ml-1 in normal person	
Break-Junction	Only tested in buffer		1) Seem to be complicated to make; 2) Control samples also show some binding	EGFR	50 ug/ml (in buffer)	45–78 ng/ml, or 200 fmol/ml - 27 ng/ml[238]	[237]
Impedimetric, diamond-based immmunosensor	No.	Seem to be sensitive; linear response	Data are difficult to analyze	C-reactive protein, cardiovascular diseases biomarker	10 nM	>25 nM are indicative of cardiovascular disease	[239]
resonance light scattering correlation spectroscopy (RLSCS)	No.	High sensitivity	Require diluting the sample quite a bit to obtain meaningful results; and the setup is complicated	liver cancer biomarker alpha-fetoprotein (AFP)	linear 1 pM to 1 nM (in buffer); tested patients in 400 x - 4000 x diluted serum)		[157]
Zeta potential based colorimetric immunoassay	Only tested in buffer		Has only been tested in buffer.	Glycosylated hemoglobin (HbA1c)	1.5 ug/ml (in buffer)	5.5% of the total hemoglobin content	[220]
Surface-enhanced fluorescence with Cy3-labeled VEGF-aptamer	Tested in buffer, has high response to physiological concentration of human serum albumin	Very simple, cheap, one-step.	Has relatively high response towards human serum albumin	vascular endothelial growth factor-165 ($VEGF_{165}$), a predominant biomarker of cancer angiogenesis	25 pg/mL to 25 µg/mL (=from 1.25 pM to 1.25 µM) in buffer	500 pg/mL to 8 ng/mL	[221]

5.2 Introduction for Troponin T Detection

Every year, about 935,000 Americans have an acute myocardial infarction (AMI, or heart attack)[241]. As a result, cardiovascular disease has been ranked the No. 1 cause of death for both men and women for more than a decade, with 600,000 death every year[242]. Each minute that heart tissue is deprived of oxygen during AMI, cell death rate increases, and cardiac function is permanently lost. A rapid, reliable and cost-effective diagnostic tool for point-of-care (POC) AMI detection is very imperative.

Human cardiac troponin I and T (cTnT and cTnI) are the international standard protein biomarkers used to diagnose AMI[9]. cTnT is released from contractile apparatus via proteolytic degradation into the blood during AMI. cTnT's half-life is thought be 120 minutes in patient samples[243], and appears to be stable at room temperature and 4°C, even after many freezing-thawing cycles. A conventional troponin assay requires the patient sample to be sent to an in-house laboratory, and assay requires many sample loading and washing steps, taking more than 2 hours to complete[244]. State of the art troponin detection technologies have been extended to operate at the POC to shorten the otherwise lengthy time lag. To date, troponin assays are mainly pioneered by large diagnostic companies including Alere, Abbott, Roche, and Siemens, and a list of techniques they have developed are summarized and compared in a review published earlier this year [9]. Most of those assays are fairly sensitive with detection limit ranging from 0.01 to 0.9 ng/ml. These techniques fundamentally all rely on integrated microfluidic or capillary devices to separate blood cells and perform many cycles of sample loading and washing, are complicated and expensive to manufacture and maintain. In addition, an intravenous blood draw is necessary to be able to supply enough sample

volume for each test, and therefore a certified physician or professional must be on site, which is expensive, but also limits the access of the device from many other health care settings besides hospital. Therefore, there is still an increasing need in developing a much simpler but still rapid POC assay that only requires a minimal sample volume, such as a finger-pricked blood drop. This will potentially better enable prompt and accurate diagnoses for AMI.

With the recent advances in nanotechnology, many research labs have developed novel assays that take advantages of useful properties of nano-materials[245-263]. The Dong lab, for instance, developed an gold nanoparticle based fluorescence anisotropy assay to measure cTnT and cTnI in 10% plasma, with a detection limit of 15 pM (~60 pg/ml for cTnT). The primary antibody recognizes a peptide that has been fluorescently labeled, and the secondary antibody is labeled with gold nanoparticles. Troponin competes with the peptide to the primary antibody binding site, resulting in a decrease in fluorescence anisotropy[262]. The Aslan lab developed an microwave accelerated metal-enhanced fluorescence assay to detect cTnI from whole blood with a detection limit of 0.05 ng/ml, and the assay is completely within 1 min [257]. The Shankar group developed an fluorescent immunoassay based TiO_2 nanotubes with the detection limit of 0.1 pg/ml for cTnI in buffer [263]. These are pioneering research efforts, performed by research labs, on cTnT or cTnI detections that have demonstrated high sensitivity and selectivity. Although most of them are still at early-stage, those novel assays provide promises for potential POC detection for AMI.

In this work, we have demonstrated a novel near-infrared fluorescent assay specific for cTnT detection, using single-walled carbon nanotubes (SWCNT). SWCNTs are rolled

grapheme cylinders with nanometer-sized diameters. They fluoresce in the near-infrared (nIR), where blood and tissue are most transparent and there is minimal auto-fluorescence[37] and exhibit no reported photobleaching threshold[19-21]. Moreover, the one-dimensional electronic structure of SWCNTs imparts a greater sensitivity to adsorbates than other, higher dimensional structures. Electron-donating or -accepting groups can increase or decrease emission[24, 25, 153] with single molecule sensitivity[26, 32, 264]. These properties make SWCNTs particularly advantageous as sensors in biological media (reviewed in [18], such as whole blood, making them suitable for the potential usage in a POC setting. Previously, our laboratory, as well as others, have used SWCNT as nIR fluorescent sensors for D-glucose[24], divalent metal cations[22], assorted genotoxins[163], nitric oxide[25, 32], pH[26], DNA hybridization[49], protein avidin[153], and protein-protein interactions[265]. In the current work, we developed a rapid, label-free and quantitative SWCNT sensor array that specifically detects cTnT. Comparing with traditional ELISA assay and other labeling methods, this method is simple, and does not require a secondary antibody. Fluorescent SWCNT itself transduces signal, providing a sensing readout. In this work, we also developed two new chemical characterization assays that allow us to quantify amine and carboxylic acids in a soft gel, providing a useful assay tool for characterizing the mostly widely used chemical groups in soft gels, which other researchers working with soft gels or hydrogels may find interest in.

5.3 Experimental Section

5.3.1 Materials

Anti-cTnT antibody and cTnT were purchased from AbCAM. S-4FB and His6 Tag-HyNic (Cat. No. SP-E001-010) were purchased from Solulink. Printer tips (ceramic, 190 μm orifice, 0.75 inch long, catalog number 6002-0365) were purchased from BioDot. PTFE printed slides with poly-l-lysine adhesive surface (24 well/3 mm, slide ID: 24-30) were purchased from Tekdon. TNBSA (2,4,6-trinitrobenzene sulfonic acid) was ordered from Thermo Scientific. Acetic acid, chitosan, succinic anhydride, N-(3-dimethylaminopropyl)-N′-ethylcarbo diimide hydrochloride (EDC·HCl), N-hydroxysuccinimide (NHS), Na,Na-bis(carboxymethyl)-L-lysine (NTA) and nickel (II) sulfate were purchased from Sigma-Aldrich. SWCNT was purchased from Unidym (unpurified), and purified through hexane/water extraction, and dried overnight before usage. The human blood sample was provided courtesy of MGH, Blood Donor Center through Dr. Christopher Stowell, and received as a gift from Tatyana Shatova. The sample was collected with an acid-citrose-dextrose anticoagulant.

5.3.2 Chitosan-SWCNT Suspension

Chitosan (l5kDa MW) was first dissolved at 0.25 wt% in 1 wt% acetic acid. 12 mg Unidym SWCNT was mixed with 40 ml of the chitosan/acetic acid solution and tip-sonicated with a 6 mm sonication tip (*Cole-Parmer*) at 48% amplitude for 45 min, in an ice bath. The sample was centrifuged at 16,100 RCF for 180 minutes (*Eppendorf Centrifuge 5415D*). Afterwards, the supernatant was collected and the pellet discarded. UV absorption at 632 nm was used to estimate the concentration of the SWCNT with ε_{632}

= 0.036 $(mg/l)^{-1}cm^{-1}$. A typical SWCNT concentration was between 23-37 mg/l (Figure 5.9a).

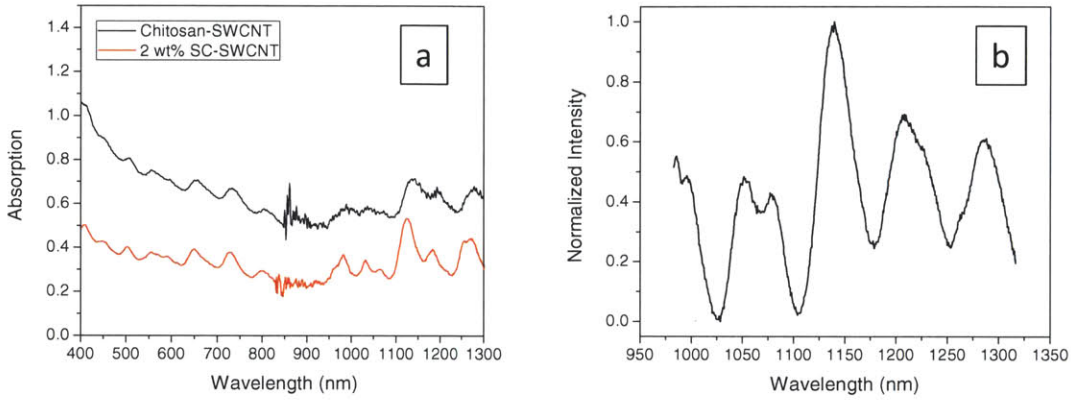

Figure 5.9 Typical absorption spectrum of a chitosan-SWCNT suspension (2 times diluted, black) in comparison with a 2 wt% sodium cholate suspended SWCNT solution (red) (a) and the corresponding SWCNT fluorescence of the Ni/NTA/chitosan-SWCNT sensor array (b).

5.3.3 Chemistry and printing of chitosan-SWCNT sensor array.

To explore reaction conditions, chitosan-SWCNT solution and glutaraldehyde/H_2O solution at various concentrations (0.25v/v%, 0.025v/v%, 0.0075v/v%, 0.00375v/v%) were prepared in two separate wells in a 24 wellplate, and transferred to the microarray printer (DigiLab MicroSys). Relative humidity was set to be 80%. The robotic head of the printer was programmed to alternate between dispensing the SWCNT solution and glutaraldehyde through two separate printing tips, 0.125 μl at a time, and 8 layers total per spot (2 μl per spot). The amine groups on the chitosan-SWCNT will crosslink themselves inside the gel, as well as with the lysine on the glass surface. After immobilizing the chitosan-SWCNT for 7 or 14 hours, the glass slides were washed with 0.01 M NaOH and H_2O alternatingly three times to remove unreacted glutaraldehyde and acetic acid. The slides were then immersed into a 45 ml solution of succinic anhydride

(450 mg/45 ml, or 0.1M) in phosphate buffer (500 mM, pH = 8) for another 12 hours. After washing four times with H_2O (5 min each), the glass slides were activated with a mixture of EDC (863 mg, 0.1M) and NHS (575 mg, 0.11M) in 45 ml MES buffer (0.1 M, pH = 4.7) for 2 more hours. After washing with H_2O, each well on the glass slide was exposed to 20 μl of NTA (0.1 M) dissolved in water or phosphate buffer (500 mM, pH = 8) for 4, 8 or 20 hours. After washing with water for four times, the glass slides were ready for experiments. All the chemistry steps were performed at room temperature.

For the optimized chip, 0.00375v/v% glutaraldehyde was chosen to react with the chitosan-SWCNT for 7 hours, followed by 12 hour of succinic anhydride reaction, 2 hour of EDC/NHS activation, and 20 hour of NTA reaction (0.1 M, phosphate buffer (500 mM, pH = 8)).

5.3.4 6xHis-tag conjugation of antibodies and characterization.

Anti-cTnT antibody was exchanged to *modification buffer* (100 mM total phosphate, 150 mM sodium chloride, pH 7.4) using Zeba spin columns (Pierce Biotechnology, Cat. No. 89889). A stock solution of S-4FB/DMSO at 18 mg/ml was pre-made and stored in a desiccator until being used. 5 molar equivalents of S-4FB was added to the Anti-cTnT antibody, and allowed to react for 2 hours at RT. The reaction mixture was then exchanged to *conjugation buffer* (100 mM total sodium phosphate concentration, 150 mM sodium chloride, pH 6.0). His6 Tag-HyNic was dissolved in *conjugation buffer* at a concentration of 10 mg/ml. 10 equivalents of the peptide (to the original protein molar equivalent) were added to the antibody solution followed by addition of TurboLink catalyst (1/10th of the protein volume). The reaction was allowed to proceed for 2 hours at RT. The 6xHis-Anti-cTnT antibody was purified by another Zeba spin column,

exchanging it to standard PBS 1x buffer (pH = 7.2). The protein/PBS solution was aliquoted into multiple Eppendorf tubes, and stored at -20°C before usage. The conjugation was quantified by UV absorption at 354 nm following the protocol provided by Solulink (Figure 5.10).

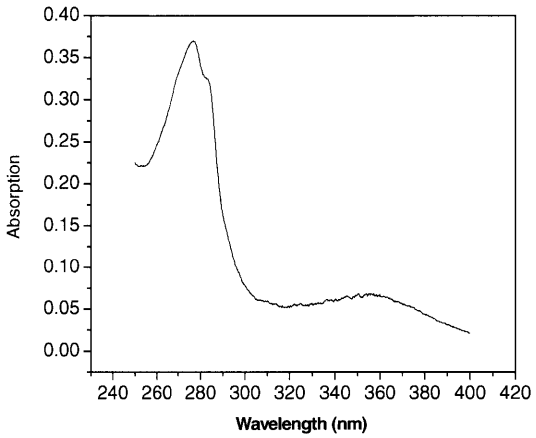

Figure 5.10 Typical absorption spectrum of 6xHis-Anti-Trop antibody in PBS. Protein concentration was determined by λ_{280} = 1.4 $(mg/ml)^{-1} cm^{-1}$, and degree of His-tag conjugation was quantified by ε_{354} = 29,000 $M^{-1} cm^{-1}$.

5.3.5 High-throughput Screening of Chitosan-SWCNT Against a Panel of Proteins.

The chitosan-SWCNT solution was diluted using phosphate buffer (50 mM, pH = 7.4) to a final SWCNT concentration of 2 mg/l. A panel of proteins that were recombinantly expressed in *E. coli* in house were added to the SWCNT solution in a 96-well format, such that the final concentration was 10 μg/ml, and the mixture was incubated for 1 hour at room temperature. The resultant fluorescence of the SWCNT was measure using a home-built near-infrared microscope with an automated stage control that is compatible with a 96-well plate. The details of the spectroscopy setup is similar to that is previously

published in literature [32, 265]. Briefly, a Zeiss AxioVision inverted microscope was coupled to a Princeton Instruments InGaAs OMA V 1-D array detector through a PI Acton SP2500 spectrometer. The sample was excited using a 50x objective by a 785 nm laser with 150 mW power at the sample. The relative intensity change is defined as the relative difference of fluorescence intensity of the SWCNT incubated with the protein and with just the phosphate buffer, $(I_{protein} - I_{buffer})/I_{buffer}$.

5.3.6 Optical microscopy and atomic force microscopy.

Optical images were taken using Zeiss inverted microscope coupled with AxioCam ERc 5s detector with a 10x objective. The images were processed with software Zen, provided by Zeiss.

AFM images were taken using Asylum MFP-3D model in AC mode with Asylum Tapping/AC mode soft tips (AC240TS). Typical scan size was 5 μm or 10 μm; and scan rate was in between 1- 1.5 Hz, adjusted based on the image quality, and the scan angle was always set to be 0.0°. AFM images were analyzed using Gwyddion software, and 0-degree flatting was applied in the images shown in Figure 5.13f.

5.3.7 Primary Amine Characterization

TNBSA solution (original is 5%) was dissolved to 0.01% in phosphate buffer (pH = 8, 500 mM). This step has to be done immediately before the assay. Apply 20 μl of the 0.01% TNBSA solution to each well that needs to assayed, and then incubate the glass slide in a wetbox at 37 °C. After 2 hours, the top liquid on each well is immediately removed, and washed at least three times with the phosphate buffer. After complete removal of liquid

on the well, absorption spectrum of each well was taken, from 260 – 600 nm with 200 msecond exposure time, using a plate reader (Varioskan Flask, Thermo Scientific). Two wells that have SWCNT printed but have not been subjected to TNBSA were used as blanks.

A stand series was generated as follows: 50 µl of chitosan solutions at various concentrations (0%, 0.005w/v%, 0.01w/v%, 0.025w/v%, 0.05w/v%, 0.25w/v%) in 1% acetic acid was mixed with 5 µl TNBSA at 5 v/v% and 200 µl phosphate buffer (200 mM, pH = 8). After incubating for 2 hours at 37 °C, absorption spectra were immediately measured at 260 – 600 nm. Peak value at 350 nm was used to obtain a calibration curve (Figure 5.11).

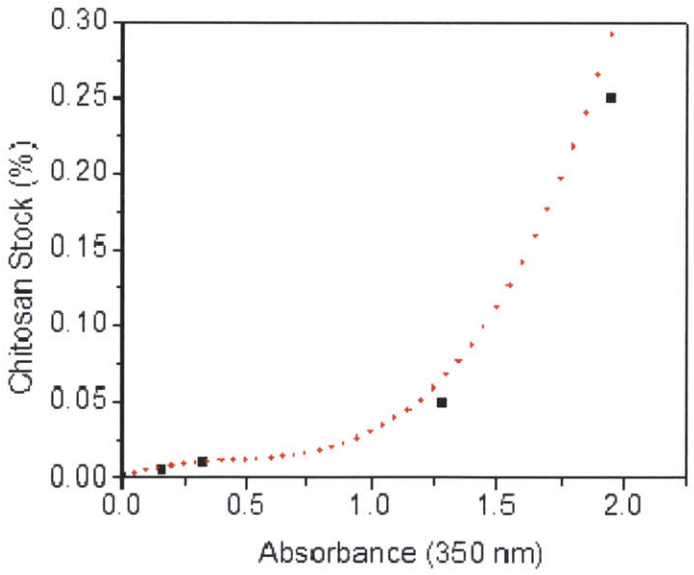

Figure 5.11 Calibration of chitosan-amines. w/v% chitosan as a function of A_{350} after the amine assay.

5.3.8 Carboxylic Acid Characterization

Bromocresol green solution was prepared by dissolving 40 mg bromocresol green in 100 ml DMSO, which shows a yellow color. A solution of NaOH (0.1 M in water) was added drop-wise until a light blue color just appeared in solution. Although normally bromocresol solution is prepared in ethanol, we have to use DMSO because otherwise ethanol would wet the PTFE surface and solution from different wells on the same glass chip would be mixed.

50% acetic acid was spotted on each well for 5 minutes to protonate the carboxylic acid groups. The slides were then thoroughly rinsed with water to remove excess carboxylic acid. After a quick arir-dry, 2.5 μl of the bromocresol green/DMSO solution was spotted onto each well, and the absorption spectra were monitored using a plate reader (Varioskan Flask, Thermo Scientific), scanning from 300 – 800 nm. A_{412}/A_{622} indicates the COOH content in the gel.

5.3.9 Electron-dispersive X-ray Spectroscopy (EDX)

Chips used in Figure 15.5 were prepared using the following reaction condition: different spots in the same chip were printed with various glutaraldehyde concentration (0.25 v/v%, 0.025 v/v%, 0.0075 v/v%, 0.00375 v/v%), and incubated in the printer with humidity of 80% for 7 hours, followed by 24 hr succinic anhydride (450 mg/ml) in phosphate buffer (500 mM, pH = 8), and 2 hour EDC/NHS (0.1M/0.11 M, in 0.1M MES) and then 8 hour of NTA (0.1 M) in phosphate buffer (500 mM, pH = 8). The entire chip was soaked in $NiSO_4$ for 20 min, and rinsed with H_2O 5 times to remove excess Ni^{2+}. The chip was dried using nitrogen before EDX measurement.

EDS was used to characterize relative amounts of nickel in the samples. Samples were imaged in a JEOL 6700 scanning electron microscope, and EDS measurements were taken with a Noran System SIX. The same acquisition parameters were maintained across all characterized samples: 5 kV accelerating voltage, 10.0 uA beam current, 1000 s acquisition time, 15 mm working distance, and 0.56 mm^2 sample area. The built-in quantitative analysis program was used to assess the relative amounts of elements among the samples. The highest Si content across all the samples is 1.5% at the current experimental condition, meaning little signal was collected from the glass underneath the sample, and most of the signal is from the gel that is on top of the glass.

5.3.10 Fluorescence monitoring of the sensor.

To test the sensor response to cTnT, the chitosan-SWCNT construct was incubated with 6xHis-Anti-cTnT antibody (40 μg/ml, 2.5 μl) for 30 min in PBS (1x, pH = 7.2) and washed with PBS three times to remove un-bound antibodies. After antibody conjugation, the glass chip was placed on the inverted microscope described in Section 2.5, and each sensor spot was incubated in 20 μl of PBS (1x, pH = 7.2). Under laser illumination, the fluorescence of each spot was recorded at a frame rate of 10 sec/frame. We usually observe a sharp intensity decrease at the beginning, presumably due to laser heating. Each sensor spot was equilibrated for 10 min under laser illumination to obtain a stable baseline, and cTnT diluted in PBS (1x, pH = 7.2) at various concentrations were added. For cTnT test in plasma (Figure 5.17d). We diluted plasma in PBS (1x, pH = 7.2) at indicated concentrations, and then mixed with troponin to obtain the desired final concentration.

5.4 Results and Discussions

5.4.1 Chitosan-SWCNT Sensing Scheme

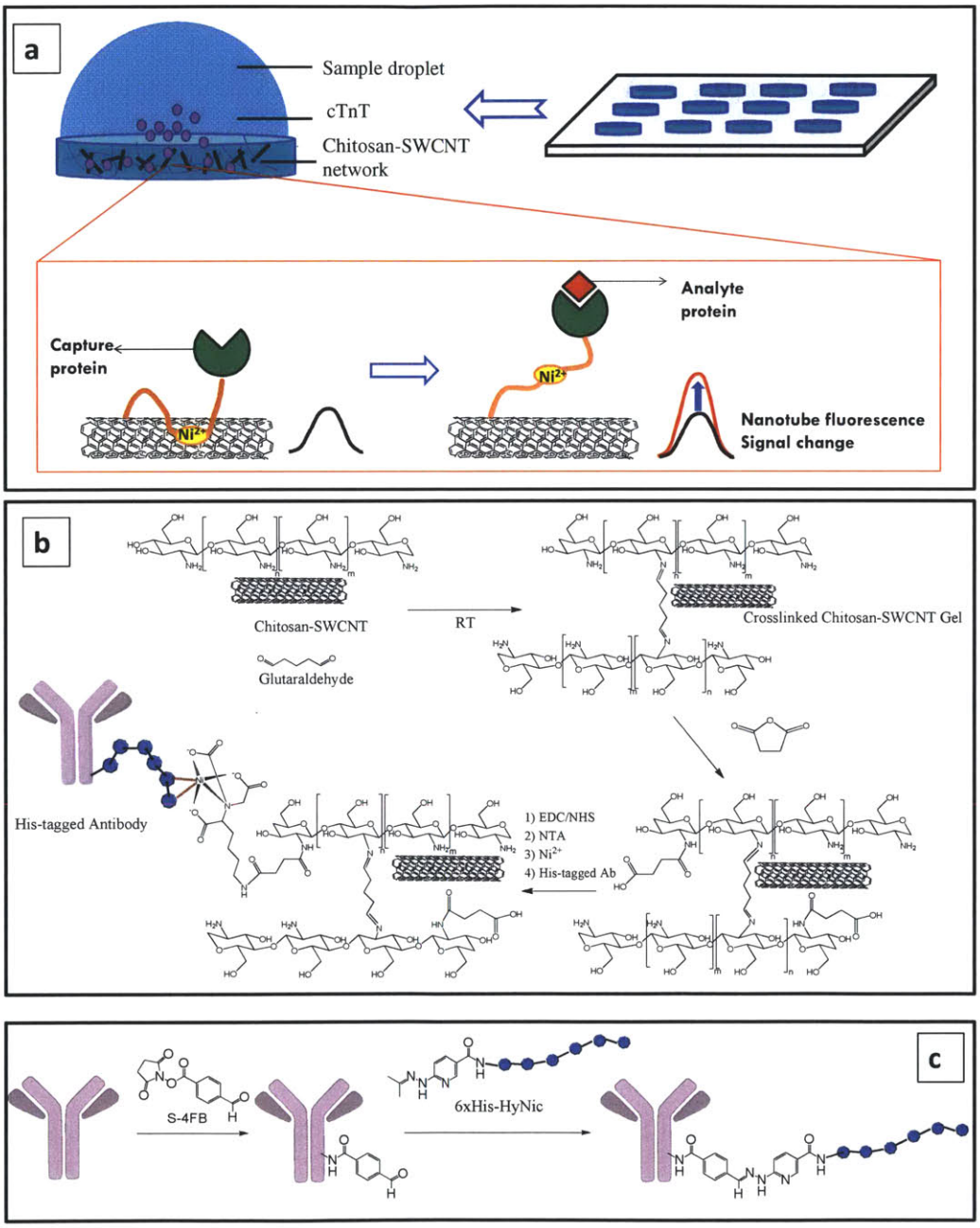

Figure 5.12 Scheme and chemistry of troponin detection using the SWCNT sensor. (**a**) Scheme of the sensor operation. An array of fluorescent SWCNT sensors with each spot fabricated for detecting one specific protein. This multiplexed format is chosen such that the platform can be extended to other protein biomarkers. Each spot consists a derivatized gel network encapsulating chitosan-wrapped SWCNT (gray) that has further conjugated on a NTA-

Ni^{2+} complex (yellow). Upon binding of the troponin to the Anti-troponin antibody, the local environment of the SWCNT alters, causing an increase in the SWCNT fluorescence signal[265]. (**b**) Chemistry of the SWCNT sensor array and creation of His-tagged antibody. Chitosan suspended SWCNT is printed with glutaraldehyde (at different concentrations) together on poly-l-lysine modified glass surface, using a micro-array printer at 2 ul per spot (3 mm in diameter). Chitosan is crosslinked by glutaraldehyde, forming a SWCNT containing network. The unreacted amine functional groups on chitosan is converted to COOH using succinic anhydride, and followed by EDC/NHS to conjugate NTA. Upon Ni^{2+} binding, NTA forms NTA/Ni^{2+} complex that can bind to 6xHis-tagged antibodies. (**c**) Schematic of the conjugation of the 6xHis-tagged protein. S-4FB was attached to the target antibody through COOH/NHS chemistry to create S-4FB/protein, which is further reacted with 6xHis-HyNic to create 6xHis-protein (following Solulink protocol).

Figure 5.12 illustrates the sensor operation with the sensing scheme shown in Figure 5.12a, and detailed chemistry in Figure 5.12b, 5.12c. The chitosan-SWCNT sensor is fabricated by creating a derivatized gel network that enables antibody immobilization with optical micrographs shown in Figure 5.13a. Specifically, Individual SWCNTs are initially suspended in the biopolymer chitosan (Figure 5.9), and crosslinked using glutaraldehyde onto an poly-l-lysine functionalized glass slide. A microarray printer (see Experimental Section) was used to ensure consistency across each of the 24 wells, with a robotic head dispensing 1 μl glutaraldehyde solution (various concentration)/1 μl SWCNT solution in each well. The unreacted amines on chitosan are further converted to carboxylic acid by reacting with succinic anhydride, followed by EDC/NHS activation and conjugation with lysine-NTA. Ni^{2+} forms a coordinated metal complex with NTA that can bind to 6xHis-tagged proteins including antibodies[265-267]. Any 6xHis-tagged antibodies specific for proteins of interest can be captured by the Ni-NTA functional group, and binding of the target protein changes the local environment of the SWCNT sensor, leading to an optical response in fluorescence[265]. This scheme presumably can be applied for detection of any proteins of interest. In this work, we are focusing only on

the detection of the cardiac biomarker, cTnT. Binding of the cTnT to the 6xHis-Anti-cTnT antibody changes the local environment of the SWCNT, and modulates the fluorescence signal of the SWCNT gel, providing a readout for sensing, similar to a previous scheme[265].

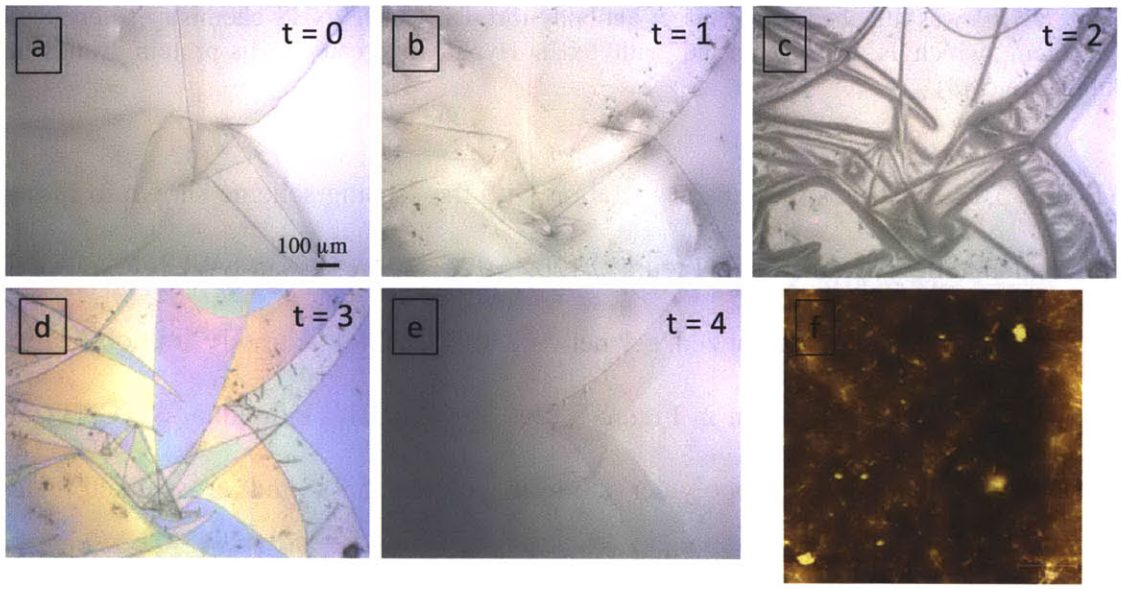

Figure 5.13 Physical characterization of the gel. (**a-e**) Optical microscopy images of a chemistry completely chitosan-gel experiencing drying (**a**, completely wet; **b**, slightly dry; **c**, more dry; **d**, completely dry) and rehydration (**e**). (**f**) Atomic force microscopy image of a dried sensor with synthesized with optimized chemistry conditions (scale bar, 1 µm).

We chose to use chitosan as the SWCNT polymer wrapping for three reasons. First, chitosan is highly biocompatible, having been used extensively in gene delivery [268]. Second, the primary amines on the chitosan can easily be used to introduce chemical groups allowing for easy modification of the sensor. Third, previous studies have shown that chitosan shows minimal non-specific protein adsorption at physiological pH (pH = 7.4)[269]. We tested non-specific adsorption experimentally by screening chitosan-SWCNT against 33 proteins (Figure 5.14a) of varying size (Figure 5.14b) and isoelectric

point (Figure 5.14c) and found that the native chitosan-SWCNT exhibited little to no non-specific protein adsorption.

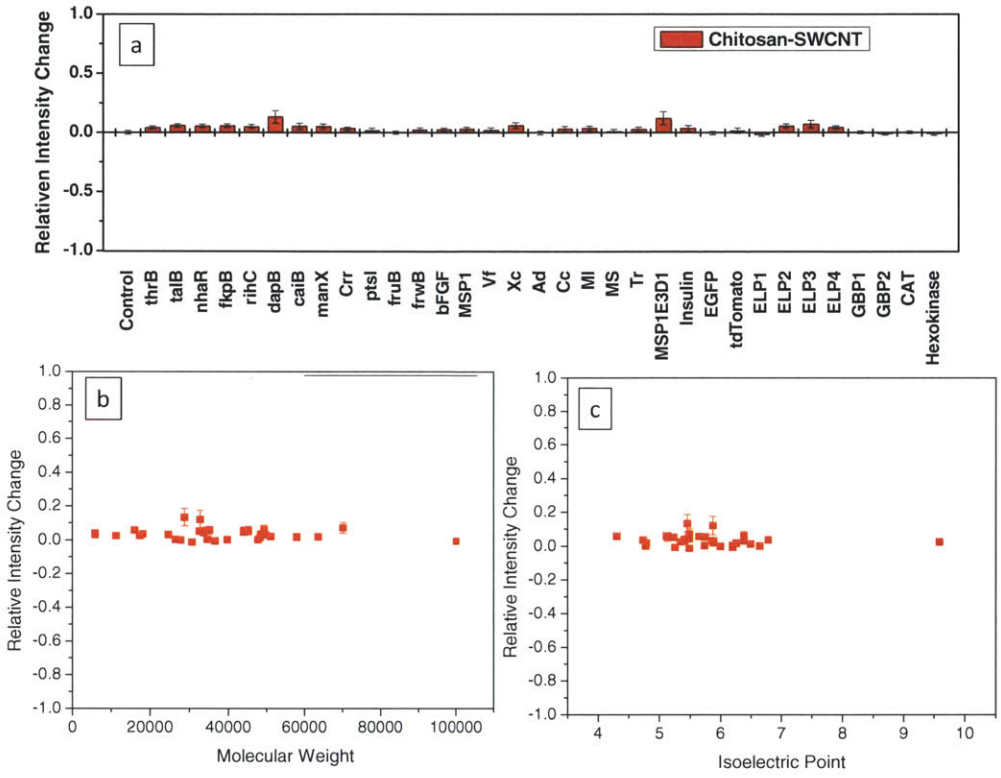

Figure 5.14 Chitosan-SWCNT low nonspecific adsorption profile. **(a)** Fluorescence response of chitosan-SWCNT (2 mg/l) to 33 proteins (10 µg/ml each). Fluorescence ($I_{protein}$) was recorded after incubating the chitosan-SWCNT for 1-hour with the proteins, with I_{buffer} being the SWCNT fluorescence in the absence of the proteins. Relative intensity change are defined as ($I_{protein}$ – I_{buffer})/ I_{buffer}. Reported data points are averages of three separate measurements and reported error bars are 2SD. MW of those proteins range from 10 to 100 kDa (**b**), isoelectric point values range from 4 to 10 (**c**). When a protein adsorbs to the chitosan-SWCNT there is a change in the fluorescence. The lack of response from all proteins tested is indicative of low non-specific protein adsorption.

Schematic of the conjugation of the His-tagging protein is shown in Figure 5.12c. S-4FB was attached to the target antibody through COOH/NHS chemistry to create S-4FB/protein, which is further reacted with 6xHis-HyNic to create 6xHis-protein. The conjugation ratio, or number of 6x-His per protein is quantified by UV absorption at 354 nm. This particular His-tag conjugation scheme is very simple, and can be completely

within 5 hours with only 1 hour of processing time, and we are able control the conjugation ratio fairly well. However, currently it is impossible to control the exact location of the 6xHis tag on the antibody. We are considering using new conjugation methods in the future. For instance, the Sokolov group has published a protocol that only modifies the glycosylated Fc region of an antibody such that the binding affinity of the Fab region of the antibody will remain unaltered[270]. We will explore similar chemistry in the future to ensure a more robust antibody conjugation scheme.

5.4.2 Chitosan Gel Chemical Characterization and Optimization

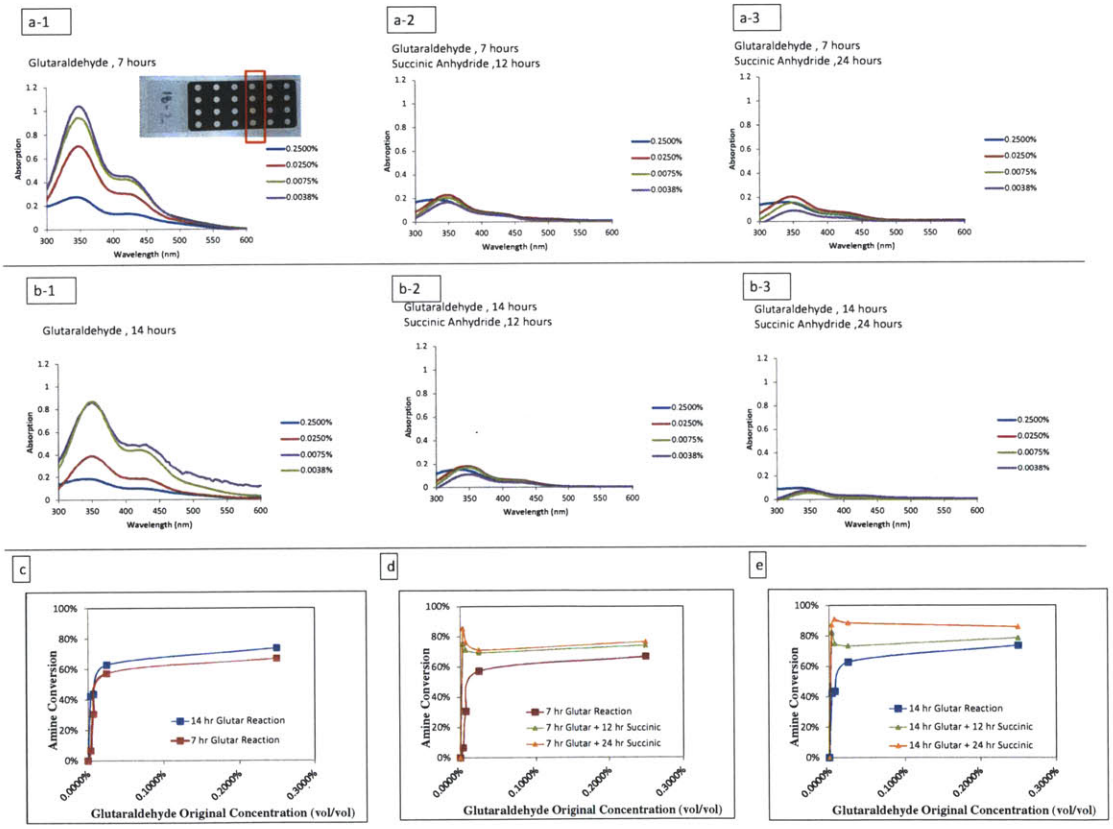

Figure 3- Glutaraldehyde Crosslinking Reaction and Succinic Anhydride Reaction

Figure 5.15 Amine group characterization. (**a-b**) Amine assays performed with TNBSA probe: after the glass chips were exposed to TNBSA probe for 2 hours at 37 °C, absorption from 200 nm to 600 nm for each reaction conditions were measured (7 hour of glutaraldehyde reaction, **a-1**; 7 hour of glutaraldehyde reaction followed by 12 hour of succinic anhydride, **a-2,** 7 hour of

glutaraldehyde reaction followed by 24 hour of succinic anhydride, **a-3**, 14 hour of glutaraldehyde reaction, **b-1**; 14 hour of glutaraldehyde reaction followed by 12 hour of succinic anhydride, **b-2,** 14 hour of glutaraldehyde reaction followed by 24 hour of succinic anhydride, **b-3**). The color change from yellow (more amines) to clear (less amines) are shown in the pictures, with red boxes highlighting the spots that have been assayed. Glutaraldehyde content is indicated in the legend. (**c**) Amine conversion calculated using A_{350} after first reaction (glutaraldehyde crosslinking reaction) as a function of glutaraldehyde content, and reaction time. **(d)** Amine conversion calculated using A_{350} for wells that have been reacted for 7 hours in glutaraldehyde (red), 7 hours of glutaraldehyde followed by 12 (green) or 24 (orange) hours of succinic anhydride reaction. (**e**) Amine conversion calculated using A_{350} for wells that have been reacted for 14 hours in glutaraldehyde (blue), 14 hours of glutaraldehyde followed by 12 (green) or 24 (orange) hours of succinic anhydride reaction.

Since cTnT binding events occur at those Ni-NTA sites, the amount of which is therefore expected to be directly linked to the sensitivity of the detection. The network has been optimized such that the number of functional Ni-NTA groups in the gel is maximized. Close examination in the reaction scheme (Figure 5.12a) reveals that by reacting more amines in the crosslinking process, the amount of unreacted amines for the further reactions are limited. Thus, using as few amines as possible is desired in the crosslinking step while still allowing for the formation of a gel. To explore different conditions, we crosslinked the chitosan-SWCNT (0.25% wt% chitosan, 1% acetic acid) with glutaraldehyde at 0.25 v/v%, 0.025 v/v%, 0.0075 v/v%, 0.00375 v/v%, allowing for two different reaction times, 7 hours and 14 hours, at each condition. Quantification of unreacted amines directly in a thin gel on a glass substrate is difficult; analytical techniques such as NMR are typically applied for characterizing solution phase samples. We attempted to perform FTIR, however, with our thin gel, it is impossible to deconvolute the gel FTIR signal from a strong glass background signal. TNBSA probe, however, has been widely used to quantify protein amine content[271], which presents a yellow color and absorbs strongly at 350 nm after reacting with amines. We used this technique in order to quantify primary amines in the chitosan-gel. Gels synthesized at

different crosslinking conditions were then exposed to TNBSA dye, and rinsed thoroughly with water to remove unreacted TNBSA molecule, and absorption (200 – 600 nm) was measured. Figure 5.15a-1 (7 hour reaction) and 5.15b-1 (14 hour reaction) present the raw absorption spectra for each crosslinking condition, and the percentage of amine conversion at each condition is summarized in Figure 5.15c. As expected, increasing the amount of glutaraldehyde in the original reaction mixture significantly reduces the absorption at 350 nm, indicating more amines are reacted in the first step to form crosslinkers. Conversions with 7 hour of reaction and 14 hour of reaction show similar trend, and after 7 hours, prolonging the reaction does little to help the reaction proceed further. Therefore, we choose to use 0.00375% glutaraldehyde and 7 hour of reaction time for the crosslinking step.

The optimization of the second reaction focuses on converting all of the unreacted primary amines left from the crosslinking step into carboxylic acids. In order to keep the primary amines deprotonated throughout the course of the reaction, the gel was immersed in succinic anhydride in a high ionic strength phosphate buffer (500 mM) at pH of 8, and the reaction was allowed for 12 and 24 hours each. The same amine-quantification assay was used for this step, and it is expected that if the reaction goes to completion, there would be little to no absorption at 350 nm since majority of the amines would have been reacted. Our data show that for the gel synthesized with optimized crosslinking reaction, more than 75% of the total amines are converted after 12 hour of succinic anhydride reaction, and extending the reaction from 12 hour to 24 hours only converts 10% more of the total amines (Figure 5.15d, e). Therefore, to shorten the entire gel synthesis time, we choose to use 12 hours for this reaction step.

Different reaction conditions to conjugate Lysine-NTA to the gel were explored. Each NTA has effectively three carboxylic acids; therefore, after the reaction, the overall carboxylic acid content of the gel would increase by three times in theory. Bromocresol green assay is widely used for visualizing carboxylic acid derivatization in thin layer chromatography, and we adopted it here to quantify carboxylic acid by monitoring the absorption ratio of A_{412}/A_{622} after exposing the gel to the bromocresol green. We find that the reaction does not proceed in water (light green and blue in Figure 5.16a), but completes within 4 hours in a phosphate buffer at pH of 8 (red and black in Figure 5.16a). Increasing the NTA concentration from 0.01 M (black) to 0.1 M (red) increases the relative change of A_{412}/A_{622} from 1.19 to 1.44, corresponding to a conversion from 5.5% to 22%. This particular reaction, even at the optimal reaction condition, does not appear very efficient, and is presumably due to that the complex gel matrix sterically hinders the access of the reacting molecules before the NHS ester becomes unstable.

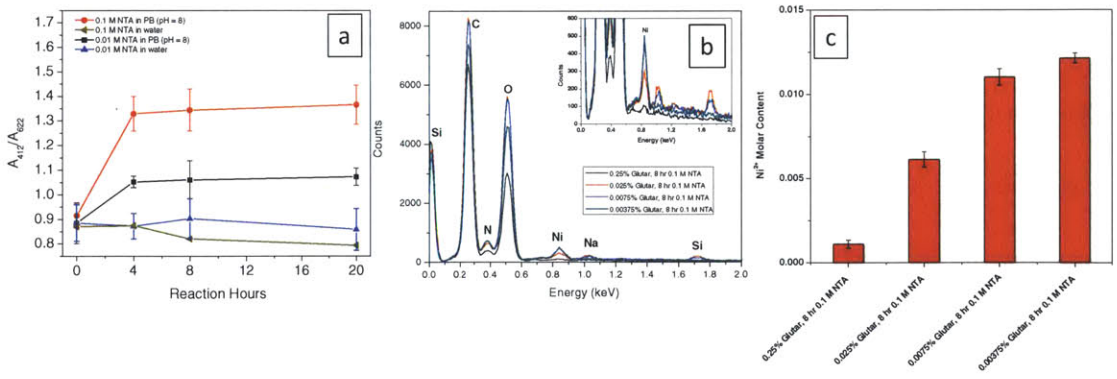

Figure 5.16 NTA moiety and Ni^{2+} quantification. **(a)** Chips prepared with various NTA reaction conditions were exposed to 2.5 µl of the bromocresol green solution and the absorption spectra were monitored using plate reader (Varioskan Flask, Thermo Scientific), scanning from 300 – 800 nm. A_{412}/A_{622} indicates the converted carboxylic acid content in the gel. **(b,c)** EDX spectra **(b)** and calculated molar content of Ni atoms in the gel **(c)** as a function of gels with various starting glutaraldehyde concentration.

Electron dispersive X-ray was applied to confirm that Ni^{2+} coordination is indeed related with the amount of NTA moiety in the gel. We tested gels reacted with the four different glutaraldehyde concentrations studied and followed by the same reaction conditions in succinic anhydride and NTA steps. As expected, amount of Ni^{2+} coordinated in the gel increases as the glutaraldehyde concentration decreases, or NTA content increases, confirming that residual Ni^{2+} in the gel is indeed a function of NTA content (Figure 5.16b, 5.16c).

5.4.3 Chitosan Gel Physical Characterization

The morphology of the gel is monitored under optical microscope as the gel experiences drying (Figure 5.13a-d) and rehydration, and we find that the morphology is strongly dependent upon processing history. Those optical images indicate that although those gels are thin, they remain three-dimensional when hydrated (Figure 5.13a); drying gradually reduces the dimensionality until the entire gel becomes practically flat and forms interference patterns that are presumably due to ordered crystalline phases of chitosan polymer (Figure 5.13d)[272]. In addition, rehydrating the (Figure 5.13e) gel does not restore the original structure, therefore the deformation caused by drying is irreversible, and should be avoided upon storage. Atomic force microscopy image shows that SWCNTs are uniformed distributed inside the gel, forming a sensor network (Figure 5.13f).

5.4.4 cTnT Detection in buffer and in human serum

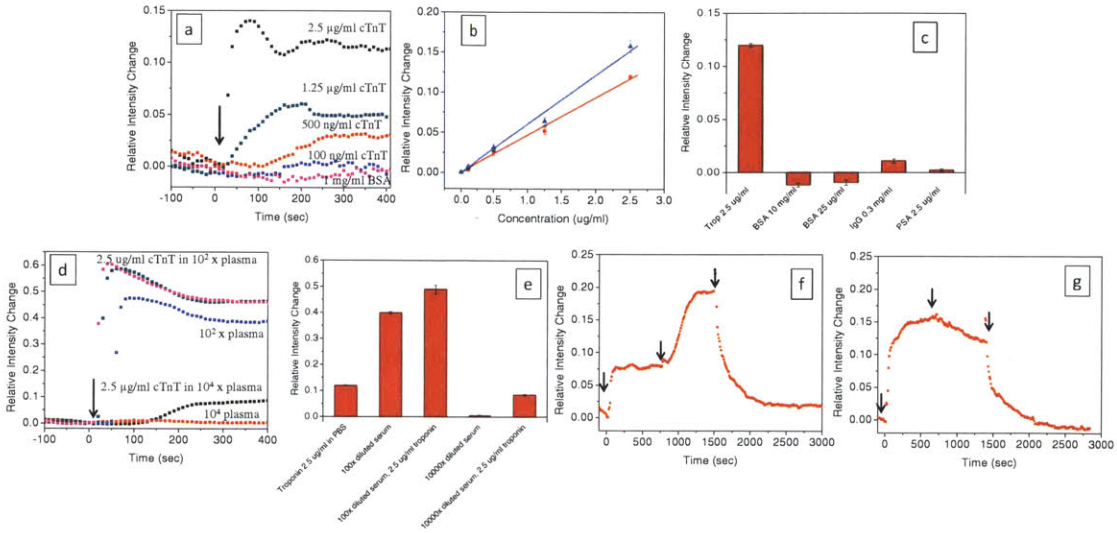

Figure 5.17 Fluorescence response of 6xHis-Anti-Trop/Ni/NTA/Chitosan-SWCNT sensor to troponin. (**a**) 6xHis-Anti-cTnT/Ni/NTA/Chitosan-SWCNT fluorescence signal increases upon addition of cTnT at various concentrations (black, 2.5 μg/ml; green, 1.25 μg/ml; red, 500 ng/ml; blue, 100 ng/ml) and BSA at 10 mg/ml (pink). Each response completes within 3 minutes. The sensor response appears linear with experimental detection limit of 100 ng/ml to cTnT. (**b**) Sensor Calibration performed by two batches of sensors (slope = 0.47, red; slope = 0.61, blue). (**c**) Cross-reactivity is tested with proteins that exist abundantly in the blood, such as BSA (10 mg/ml), immunoglobulin G (0.3 mg/ml) and another cancer biomarker prostate specific andtigen (2.5 μg/ml), and minimal responses were observed from those proteins compared with cTnT (2.5 μg/ml), showing the high selectivity of the sensor towards cTnT. Reported data points are averaged from transient data points from t = 250 sec to t = 300 sec, and reported error bars are 2SD. (**d**) The sensor response from 10,000x diluted plasma solution (red), 2.5 μg/ml cTnT in the 10,000x diluted plasma (black), 100x diluted plasma (blue), 1.25 μg/ml cTnT in 100x diluted plasma (green) and 2.5 μg/ml cTnT in 100x diluted plasma (pink). (**e**) Relative intensity change as the sensor is exposed to various media. Reported data points are averaged from transient data points from t = 250 sec to t = 300 sec, and reported error bars are 2SD. (**f**) Relative fluorescence change of a 6xHis-Anti-cTnT/Ni/NTA/Chitosan-SWCNT sensor upon addition of 10% glycerol (viscosity of 1.38 mPa·s, first arrow), followed by another addition of cTnT (2.5 μg/ml, second arrow), and a washing with PBS (third arrow). (**g**) Relative fluorescence change of a 6xHis-Anti-cTnT/Ni/NTA/Chitosan-SWCNT sensor upon addition of 20% glycerol (first arrow), followed by a quick dilution of glycerol to 10% (second arrow), and a complete washing with PBS (third arrow). This demonstrates that the viscosity effect is reversible.

To test the sensor response to cTnT, the chitosan-SWCNT construct was incubated with 6xHis-Anti-Trop antibody for 30 min in PBS (1x, pH = 7.2) and washed with PBS

three times to remove unbound antibodies. And the sensor array exhibits bright near-infrared (1000 – 1400 nm) fluorescence (Figure 5.9) under laser illumination (785 nm), which was recorded in real-time by a near-infrared one-dimensional array detector at a frame rate of 10 s/frame. Addition of cTnT result in a fluorescent increase (Figure 5.17a), and the relative fluorescence change increases linearly as cTnT concentration increases (Figure 5.17b), with the experimental detection limit of 100 ng/ml (2.5 nM). Two different batches of sensor present calibration curves deviated by 20% in slope, and this type of batch-to-batch variation may be overcome by more rigorous controlling of gel reaction time and conditions in the future. Cross-reactivity is tested with proteins that exist abundantly in the blood, including bovine serum albumin (BSA, 1mg/ml), immunoglobulin G (IgG, 0.3 mg/ml) and another cancer biomarker PSA (2.5 μg/ml), and minimal responses were observed from those proteins compared with cTnT (2.5 μg/ml), showing the high selectivity of the sensor.

We attempted to apply the sensor to detect cTnT in human plasma. Plasma is prepared by spinning human blood at 3400 RPM (1000 g) for 20 min followed by removal of the cell pellets. Human serum contains approximately 70 mg/ml total proteins[273]. Diluting full serum by 10,000 times results in a solution with ~ 7 μg/ml proteins. The sensor is able to completely suppress the response from a 10,000x diluted plasma solution (red, Figure 5.17d) and still responds to cTnT (2.5 μg/ml) in the diluted plasma without being affected (black, Figure 5.17d). However, increasing the plasma concentration to 100x diluted (700 μg/ml proteins) results in a strong fluorescence signal (Figure 5.17d, blue), affecting the sensor response. In this 100x diluted plasma environment, cTnT tested at two different concentrations (1.25 μg/ml, blue; and 2.5

μg/ml, pink, Figure 5.17d) can no longer be distinguished. One hypothesis is that non-specific adsorption from other proteins in the sensor prevents the cTnT detection. However, non-specific adsorption, if occurs, is expected to have already caused significant intensity change even at a much lower concentration than 700 ug/ml proteins. In addition, the sensor shows little response to 10 mg/ml BSA (Figure 5.17a,c), so we do not expect the large response introduced by 100x diluted plasma is caused by non-specific adsorption. The same data are also presented as bar chart in Figure 5.17e. We do notice that the plasma solution has a much higher viscosity (1.38 mPa·s)[274] than PB buffer (1.0 mPa·s) due to the presence of fibrinogen and many other proteins. One hypothesis is that the sensor array is affected by sudden viscosity change upon addition of the plasma-containing solution, resulting in fluorescence modulation. To test this, we added 10% glycerol (1.31 mPa·s)[275] to the sensor and observed a 7.5% increase in fluorescence intensity (first arrow Figure 5.17f). Further addition of cTnT at 2.5 μg/ml troponin (second arrow, Figure 5.17f) on the gel still leads to 12.5% response, which is comparable with the response observed in the experiment without glycerol. Glycerol is expected to be inert to the sensor, but it significantly increases the viscosity around the SWCNT. This observation supports the hypothesis that viscosity change does impose an optical effect in the detection. However, the optical effect caused by viscosity is reversible, as exchanging the glycerol with PBS completely removes the artifact (Figure 5.17g). In an experiment where 100x diluted plasma was added, although apparent viscosity in the solution is not as high as in complete plasma, local viscosity inside the gel can be appreciable. Moreover, a small viscosity change in the nanoscale, surrounding the SWCNT, may significantly alter the mean-distance between the quencher molecule

and the SWCNT via slowing down molecule vibration speed, thus affecting the fluorescence intensity. Future work will involve further engineering of the gel matrix to eliminate the undesired optical artifact. We notice that the current gel is very thin, and any optical artifact due to the addition of the plasma will be translated into the detection; one idea is to increase the gel thickness, which can potentially eliminate the artifact without influencing the sensing capability.

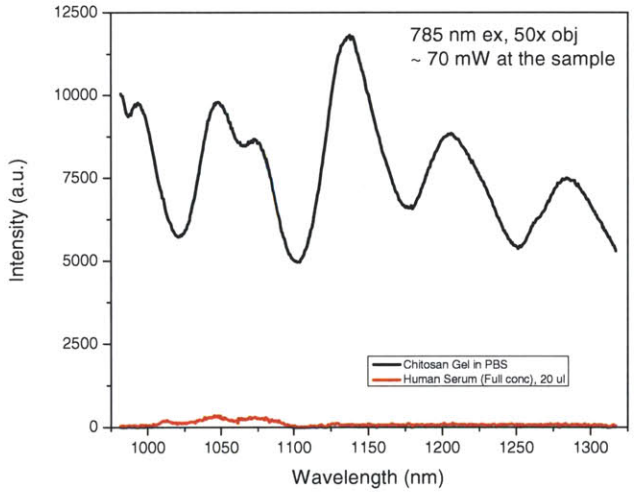

Figure 5.18 20 μl human full serum fluorescence compared with a chemistry completed chitosan-gel incubated in 20 μl PBS, under 785 nm laser illumination.

5.4 Conclusions

In summary, we have developed the first near-infrared single-walled carbon nanotube sensor array for selective cardiac troponin T, cTnT, detection. Detection can be completed within 3 minutes, and the sensor responds linearly to the cTnT concentrations, with the experimental detection limit of 100 ng/ml (2.5 nM). The sensor arrays shows little to no response to proteins that present abundantly in the blood at a much higher

concentration than troponin, including serum proteins (10 mg/ml), and immunoglobulin proteins (0.3 mg/ml). The sensor currently is unable to quantitatively detect cTnT in full plasma; however it can easily distinguish cTnT signal from background plasma proteins if plasma are diluted to a similar level of concentrations as cTnT. The sensor gel was optimized in such a way that the number of NTA-groups on the SWNT-wrapping is maximized to enhance the sensor sensitivity. NTA groups served as a site-directed anchor point for His-tagged antibodies. Therefore this approach can be easily adapted to detect other proteins of interest by using specific antibodies for those proteins. Moreover, the work presented two useful means of characterizing and quantifying two commonly used functional groups, amines and carboxylic acids in the soft gels, and this will be very useful for other researchers studying hydrogel chemistry. In conclusion, this work demonstrated the first SWCNT fluorescence-based sensor for detecting cardiac biomarker troponin, providing the basis of developing novel tools for POC AMI detection using fluorescent SWCNTs. Future work involves improving the sensitivity of the sensor array and extending the detection in full serum or full blood.

6 Divalent Metal Ions Modulate Fluorescence of Single-walled Carbon Nanotubes in an Ionic Hydrogel

6.1 Introduction

Single-walled carbon nanotubes (SWCNTs) are rolled graphene sheets that possess near-infrared (nIR) bandgap fluorescence. Since the discovery of its fluorescence in 2002[10], SWCNT fluorescence-based detection has become an emergent field of research. Many sensors have been developed for various analytes, including β-D-glucose[24], DNA hybridization[49], assorted genotoxins[163], nitroaromatics[177], nitric oxide[25, 32], pH[26], and even proteins[153, 265].

From the standpoint of both photophysics and sensing applications, it is interesting to study the fluorescence response of SWCNTs to metal ions, including group 2 and group 12 ions [276], and transition metal ions[22, 277]. Our group previously discovered that transition metal ion Hg^{2+} quenches DNA wrapped SWCNT[22]; In addition, the Barron group [276, 277] studied a series of group 2, 12 and transition metal ions, concluding that the quenching mechanisms for group 2 and 12 ions are due to electron transfer, and that quenching due to transition metal ions results from surfactant molecules interacting with transition metal ions. However, these results were complicated by the fact that the SDBS surfactant strongly interacts with the metal ions that were studied. Precipitation or ion crowding effects were observed in their experiments, making data interpretation difficult. In addition, many research efforts have taken advantage of the fact that certain ions can modulate SWCNT fluorescence, and have developed sensors that indirectly utilized those ions as fluorescence modulators. For instance, early work from our laboratory reported an

Fe^{3+}-incorporated, glucose oxidase-based SWCNT sensor for glucose detection, where addition of glucose results in the production of H_2O_2, which partially raises the Fermi level of SWCNT, increasing the nanotube fluorescence[24]. A second example probes protein-protein interaction using a chitosan-wrapped SWCNT hydrogel. In this study, Nα,Nα-bis(carboxymethyl)-L-lysine (NTA) is grafted to chitosan, and further chelated with Ni^{2+}. It was proposed in this work that Ni^{2+} acts as a quenching molecule to SWCNT; addition of His-tagged protein affects the distance of Ni^{2+} to the SWCNT surface, modulating the SWCNT fluorescence signal. Although those metal ions have been extensively used as modulators for SWCNT fluorescence, the fluorescence quenching mechanism remains an active area of research.

In this study, we were interested in further exploring the mechanism of fluorescence modulation in a series of gel systems similar to the system used in the previous, protein detection work. In doing so, we synthesized and characterized chitosan-gels, embedding SWCNTs both with and without NTA groups, and compared fluorescence responses upon addition of four different ions, including Ni^{2+}, Co^{2+}, Mg^{2+}, and Mn^{2+}. We hypothesized that the addition of metal ions to NTA-modified chitosan gel causes de-swelling of the gel, resulting in an increase of the local concentration of the SWCNTs, and thereby leading to a fluorescence increase. We then mathematically modeled the de-swelling and subsequent fluorescence change, based on the Flory-Huggins theory. The model well describes the data, suggesting that upon addition of $NiSO_4$, the difference in the ionic concentration inside and outside the gel decreases, and the gel requires less water content in order to balance the chemical potentials of the gel and solution. As a

result, water diffuses out of the gel, causing de-swelling of the gel and a fluorescence increase.

6.2 Experimental Section

6.2.1 Materials

Printer tips (ceramic texture, 190 μm orifice, 0.75 inch long, catalog number 6002-0365) were purchased from BioDot. PTFE printed slides with poly-L-lysine adhesive surface (24 well/3 mm, slide ID: 24-30) were purchased from Tekdon. Acetic acid, chitosan, succinic anhydride, N-(3-dimethylaminopropyl)-N′-ethylcarbo diimide hydrochloride (EDC·HCl), N-hydroxysuccinimide (NHS), Na,Na-bis(carboxymethyl)-L-lysine (NTA) and nickel (II) sulfate were purchased from Sigma-Aldrich and all reagents were used directly without any further purification. SWCNT was purchased from Unidym (unpurified), and purified through hexane/water extraction following the protocol offered by Unidym, and dried overnight before usage.

6.2.2 Chitosan-SWCNT Suspension

To avoid notation confusion, we define *chitosan-SWCNT* being SWCNT that is suspended in chitosan solution, *c-chitosan-SWCNT* sensor array being chitosan suspended SWCNT that is crosslinked on glass substrate through glutaraldehyde chemistry, and *c-NTA-chitosan-SWCNT* being crosslinked chitosan-SWCNT that is further reacted to graft on NTA groups.

For chitosan-SWCNT suspension, chitosan (15kDa MW) was first dissolved at 0.25 wt% in 1 v/v% acetic acid. 12 mg Unidym SWCNT was mixed with 40 ml of the chitosan/acetic acid solution and probe-tip sonicated with a 6 mm sonication tip (*Cole-*

Parmer) at 48% amplitude for 45 min, in an ice bath. The sample was centrifuged at 16,100 RCF for 90 minutes (*Eppendorf Centrifuge 5415D*) for twice. Afterwards, the supernatant was collected and the pellet discarded. UV absorption at 632 nm was used to estimate the concentration of the SWCNT with ε_{632} = 0.036 $(mg/l)^{-1}cm^{-1}$. A typical SWCNT concentration was between 23-37 mg/l.

6.2.3 Chemistry of Chitosan-SWCNT Sensor Array With and Without NTA

c-chitosan-SWCNT sensor array: SWCNT containing chitosan-gel were synthesized using an automatic printer. Chitosan-SWCNT solution and glutaraldehyde/H2O solution (0.00375v/v%) were prepared in two separate wells in a 24 wellplate, and transferred to the microarray printer (DigiLab MicroSys). Relative humidity was set at 80%. The robotic head of the printer was programmed such that two printing tips alternate between dispensing the SWCNT solution and glutaraldehyde, 0.125 μl at a time, and 8 layers were printed for each reagent per spot (totaling 2 μl per spot). The amine moieties on the chitosan polymers crosslink with themselves inside the gel, and also crosslink with the lysine groups on the glass surface. After immobilizing the chitosan-SWCNT for 8 hours, the glass slides were washed with 0.01 M NaOH and H_2O alternatingly three times to remove unreacted glutaraldehyde and acetic acid. Those chips were ready for experiments.

c-NTA-chitosan-SWCNT sensor array: In order to conjugate NTA groups onto the chitosan, the slides were further immersed into a 45 ml solution of succinic anhydride (450 mg/45 ml, or 0.1M) in phosphate buffer (500 mM, pH = 8) for another 12 hours. After washing four times with H_2O (5 min each), the glass slides were activated with a mixture of EDC (863 mg, 0.1M) and NHS (575 mg, 0.11M) in 45 ml MES buffer (0.1 M,

pH = 4.7) for 2 more hours. After washing with H_2O, each well on the glass slide was exposed to 20 μl of NTA (0.1 M) dissolved in water or phosphate buffer (500 mM, pH = 8) for 20 hours. After washing with water for four times, the glass slides were ready for experiments. All the chemistry steps were performed at room temperature.

6.2.4 Amine, and Carboxylic Acid Quantification inside the Gel

The chemical quantification of the gel is similar to reported previously (chapter 5). Briefly, 20 μl TNBSA solution at 0.01% in phosphate buffer (pH = 8, 500 mM) was prepared and spotted on an air-dried gel, and then incubated in a wetbox at 37 °C for 2 hours. After removing the top liquid and rinsing with water for a few times, the spot was scanned using a plate reader (Varioskan Flask, Thermo Scientific) at 260 – 600 nm. The standard was prepared using chitosan solution with various concentrations. Peak value at 350 nm was used to quantify amine content in the gel by comparing with the standard. This assay was used to quantify the yield of the first crosslinking reaction as well as the succinic anhydride reaction.

For carboxylic acid quantification, bromocresol green solution was prepared by dissolving 40 mg bromocresol green in 100 ml DMSO, and adjusted to a light blue color using droplets of NaOH (0.1 M in water). After spotting the gel with 50% acetic acid for 5 min and washing the gels with water, the prepared bromocresol green was dropped on the gel at 2 μl per spot, and absorption spectra were monitored, scanned from 300 – 800 nm. A_{412}/A_{622} indicates the COOH content in the gel. Since we have already quantified the amount of COOH after succinic anhydride reaction through the amine assay, the change of A_{412}/A_{622} before NTA and after NTA reaction allows us to estimate the yield of

NTA reaction. It turns out 22% of the original COOH was converted to NTA, with 78% unreacted.

6.2.5 Fluorescence Response of the Chitosan-SWCNT Suspension upon Ion Addition

The spectroscopy setup is similar to previous work [32, 265]. Specifically, a Zeiss AxioVision inverted microscope was coupled to a Princeton Instruments InGaAs OMA V 1-D array detector through a PI Acton SP2500 spectrometer. The sample was excited using a 50x objective by a 785 nm laser with 150 mW power at the sample. The focus at the sample was adjusted through maximizing the signal.

The tests were performed in a 96 well plate. Each well consists of 8.3 uL of SWCNT stock solution in a total volume of 250 μl HEPES (500 mM, pH = 7.2), with a final ion concentration of 33mM. The SWNCT: ion ratio tested in this procedure is the same as in an ion assay in a c-chitosan-SWCNT gel (Figure 6.3). The experiment is performed in triplicate, with controls containing 8.3 uL of SWCNT stock solution in a total volume of 250 μl HEPES without ions.

6.2.6 Fluorescence Monitoring of C-Chitosan-SWCNT and C-NTA-Chitosan-SWCNT

Transient measurements: To test the sensor response (for both c-chitosan-SWCNT and c-NTA-chitosan-SWCNT) to ions, the glass chips were placed on the inverted microscope described in Section 2.5, and each sensor spot was incubated in 20 μl of HEPES buffer (4-(2-hydroxyethyl)-1-piperazineethanesulfonic acid, adjusted with 0.1 M NaOH, 500 mM, pH = 7.2, without NaCl). Under laser illumination, the fluorescence of each spot was recorded at a frame rate of 10 sec/frame. We usually observe a sharp

intensity decrease at the beginning, presumably due to laser heating. Each sensor spot was equilibrated for about 1000 seconds under laser illumination to obtain a stable baseline, and various ion solutions (in 500 mM HEPES buffer) were added to reach a final concentration of 33 mM. The normalized intensity is defined by $I_t/I_{t=0}$ where $I_{t=0}$ defines the starting intensity of the gel.

6.2.7 UV Absorption of the Chitosan-SWCNT Suspension

Each testing solution consists of 41.5 μl of SWCNT stock solution in a total volume of 250 μl HEPES (500 mM, pH = 7.2), with a final ion concentration of 33 mM. The SWNCT: ion ratio tested here is the 5 times higher than the assay tested in a c-chitosan-SWCNT gel, in order to obtain sensitive measurements using UV-Vis spectrometer. The baseline is taken using 41.5 μl of 1 v/v% acetic acid with a total volume of 250 μl HEPES (500 mM, pH = 7.2), and is subtracted from each spectrum. In figure 6.2, those are the terms we use for this paper: "Ion only" consists of 41.5 μl 1 v/v acetic acid mixed with ion containing HEPES to reach a final volume of 250 μl ion solution at 33 mM final concentration. "chitosan-SWCNT" consists of 41.5 μl 1 v/v chitosan-SWCNT suspension in 1 v/v% acetic acid mixed with HEPES to reach a final volume of 250 μl. "chitosan-SWCNT w/ion" consists of 41.5 μl 1 v/v chitosan-SWCNT suspension in 1 v/v% acetic acid mixed with ion containing HEPES to reach a final volume of 250 μl ion solution at 33 mM final concentration. "chitosan-SWCNT plus ion" are the numerical addition of "Ion only" and "chitosan-SWCNT" spectra, in order to compare with the "chitosan-SWCNT w/ion" spectrum.

6.3 Flory-Huggins Polymer Theory Based Gel De-swelling Model

6.3.1 Hypothesis: C-NTA-chitosan Gel De-swells, Resulting in fluorescence increase

We use Ni^{2+} as a model ion to investigate the fluorescence change for the c-NTA-chitosan gels (Figure 6.4). Initially, the outside solution only contains Na^{+}, HEPES buffer. The high influx of Na^{+} diffuses into the gel, electrostatically balancing the negatively charged NTA^{3-} and COO^{-} sites on the gel. This results in a large mobile ion concentration difference inside and outside the gel, generating high imbalance of ionic chemical potential, μ_{ionic}. In order to balance this large μ_{ionic}, water diffuses into the gel, forming a swollen gel. As we added Ni^{2+} to the gel, Ni^{2+} ions diffuse into the gel, many of which are chelated onto the gel matrix and are no longer mobile. Electroneutrality was ensured through a combination of mobile (Na^{2+}, Ni^{2+}) and immobile ions (Ni^{2+}). As a result, the large initial deviation between the mobile ion concentration inside and outside the gel decreases, resulting in a reduction of the μ_{ionic} term. The gel therefore re-equilibrates to a less-swollen state, resulting in an increase in local SWCNT concentration within the excitation focal volume, and consequently, an increase in florescence signal.

6.3.2 Flory-Huggins Thermodynamic Equilibrium

At steady-state, chemical equilibrium is reached, or,

$$\mu_{ionic} = \mu_{mix} + \mu_{eleastic} \quad [1]$$

we redefine a new variable, $\mu = \mu / RT$ as a dimensionless chemical potential just to simply the equations and derivations.

Using Flory-Huggins theory, we have:

$$\mu_{ionic} = (-\ln x_{water,in} + \ln x_{water,out}) \quad [2\text{-}1]$$

$$\mu_{mix} = [\ln(1-\phi) + \phi + \chi_1\phi^2] \quad [2\text{-}2]$$

$$\mu_{elastic} = \mathrm{v}_1(v_e / V_0)(\phi^{1/3} - \phi/2) \quad [2\text{-}3]$$

$$(-\ln x_{water,in} + \ln x_{water,out}) = [\ln(1-\phi) + \phi + \chi_1\phi^2] + \mathrm{v}_1(v_e / V_0)(\phi^{1/3} - \phi/2) \quad [3]$$

where $x_{water,in}$ is the molar fraction of the solvent in the gel, and $x_{water} = 1 - \sum_i x_i$, and when $\sum_i x_i \square 1$, we will have $\ln x_{water} = \ln(1 - \sum_i x_i) \square -\sum_i x_i$. v_1 is the molar volume of the solvent, or $1.8\text{x}10^{-2}$ l/mol. ϕ is the equilibrium state volume of unswollen gel/ volume of swollen gel, or, $\frac{1}{1+H}$, where H describes the hydration state of the gel. V_0 is the volume of the unswollen gel, and we will estimate this a little bit later. v_e is the total number of crosslinkers in the gel, and χ_1 is the Flory interaction parameter between the gel and the water (or electrolyte).

Before we added $NiSO_4$, we have HEPES buffer in both the external and internal solution. HEPES buffer has the three following ionic forms, and it undergoes transformation at different pH, and pKa of the first pair (L-/HL) is 7.55, and pKa of the second pair (HL/H_2L+) is 3[278]. Since we adjusted the pH of the buffer to 7.26, H_2L^+ only accounts for a very small concentration of the ionic forms, and therefore can be neglected.

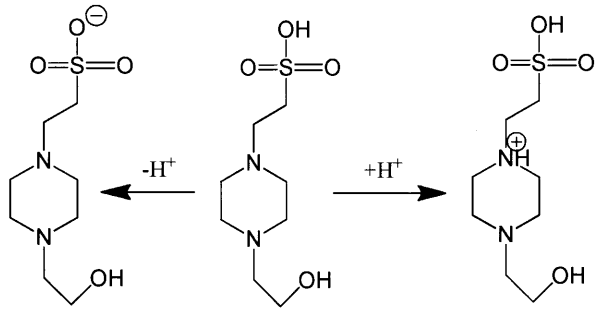

Therefore it can be assumed that before NiSO4 was added, HL, L^- as well as Na^+ were present in the solution. In reality, Na^+ was introduced through the addition of NaOH to adjust pH of the HEPES buffer.

In summary, we have the following:

	Inside the gel	Outside the gel
Before addition of $NiSO_4$	COO- (immobile), NTA^{3-} (immobile), H^+, HL, L^-, Na^+ (mobile)	H^+, HL, L^-, Na^+ (mobile)
After addition of $NiSO_4$	COO- (immobile), NTA^{3-} (immobile), Ni^{2+} (bound to NTA) H^+, HL, L^-, Na^+, Ni^{2+}, SO_4^{2-} (mobile)	H^+, HL, L^-, Na^+, Ni^{2+}, SO_4^{2-} (mobile)

Here we assume that all NTA^{3-} and COO- groups are deprotonated. This is actually a safe assumption to make because dissociation constant of those two groups are very large. Subscript of "bound" and "immobile" indicate that those ions are either bound to the gel electrostatically or are immobilized chemical groups in the gel. All the concentrations indicated here refer to mobile ions unless specified otherwise. In addition, subscript "in" means inside the gel and "out" means outside the gel.

So equation [2] becomes,

$$(C_{Na^+,in} + C_{Ni^{2+},in} + C_{H^+,in} + C_{L^-,in} + C_{SO_4^{2-},in} + C_{HL,in}) - (C_{Na^+,out} + C_{Ni^{2+},out} + C_{H^+,out} + C_{L^-,out} + C_{SO_4^{2-},out} + C_{HL,out}))/C_{water}$$
$$= [\ln(1-\phi) + \phi + \chi_1\phi^2] + v_1(v_e/V_0)(\phi^{1/3} - \phi/2)$$

[4]

We have the following unknowns, $C_{Na^+,in}, C_{H^+,in}, C_{Ni^{2+},in}, C_{L^-,in}, C_{SO_4^{2-},in} C_{HL,in}$ and ϕ.

This equation is also consistent with equation (22) in paper [279] with a different notation.

6.3.3 Chemical Equilibrium for Individual Ion Species

At steady-state, each mobile ionic species is also in chemical potential equilibrium. In other words,

$$\mu_{i,in} = \mu_{i,out} \quad [5]$$

If we expand the chemical potential terms on both sides, we will have,

$$\mu^0_{i,in} + RT\ln a_{i,in} + zFV_{in} = \mu^0_{i,out} + RT\ln a_{i,out} + zFV_{out} \quad [6]$$

Because the definition of standard potential asserts that $\mu^0_{i,in} = \mu^0_{i,out}$, automatically, we have,

$$\ln\frac{a_{i,in}}{a_{i,out}} = \frac{zF}{RT}(V_{out} - V_{in}) \quad [7]$$

where $a_{i,in}, a_{i,out}$ are defined as activities of ion species, *i*, inside and outside of the gel.

We know that z(Na^+) = +1, z(L^-) = -1, z(HL) = 0, z(Ni^{2+}) = +2, z(SO_4^{2-}) = -2. So the equations below follow:

$$a_{Na^+,in}a_{L^-,in} = a_{Na^+,out}a_{L^-,out} \quad [8\text{-}1]$$

$$a_{Ni^{2+},in}a_{SO_4^{2-},in} = a_{Ni^{2+},out}a_{SO_4^{2-},out} \quad [8\text{-}2]$$

$$a_{Ni^{2+},in}/(a_{Na^+,in})^2 = a_{Ni^{2+},out}/(a_{Na^+,out})^2 \quad [8\text{-}3]$$

$a_{Na^+,in} / a_{H^+,in} = a_{Na^+,out} / a_{H^+,out}$ [8-4]

$a_{HL,in} = a_{HL,out}$ [8-5]

$a = c\gamma$, where γ is the activity coefficient, and we assumed that to be 1 for all monovalent ions, but used tabulated values in reference [280] for Ni^{2+} and SO_4^{2-}. Since the gel is very thin, ions being taken up by the gel are not expected to alter the concentrations of those species outside the gel, so the values of the right-hand side of the equations are all known.

6.3.4 Electroneutrality

The gel will also be under electroneutrality at equilibrium, which means

$$C_{Na^+,in} + 2C_{Ni^{2+},in} + 2C_{Ni^{2+},bound} + 2C_{H^+,in} - (C_{L^-,in} + 2C_{SO_4^{2-},in} + C_{COO^-,immobilized} + 3C_{NTA^{3-},immobilized}) = 0$$ [9]

Notice that $C_{COO^-,immobilized} = C_{COO^-,immobilized,0}\phi$ and $C_{NTA^{3-},immobilized} = C_{NTA^{3-},immobilized,0}\phi$, where $C_{COO^-,immobilized,0}$ and $C_{NTA^{3-},immobilized,0}$ are defined as immobilized COO^- and NTA^{3-} when the gel was still unswollen, or at a dried state. Because we have fully characterized our gel, we have a good estimate of the initial immobilized COO^- and NTA^{3-} concentrations on the gel.

In addition, the amount of $C_{Ni^{2+},bound}$ is a function of the $C_{Ni^{2+},in}$ inside the gel. We know that Ni^{2+} binds to NTA strongly, and establishes an equilibrium, $[Ni-NTA]^- \square \quad Ni^{2+} + NTA^{3-}$. The dissociation constant, K_{Ni-NTA}, is defined as

$$K_{Ni-NTA} = \frac{C_{Ni^{2+},in}(C_{NTA^{3-},immobolized} - C_{Ni-NTA})}{C_{Ni-NTA}} = \frac{C_{Ni^{2+},in}(C_{NTA^{3-},immobolized} - C_{Ni^{2+},bound})}{C_{Ni^{2+},bound}}$$ [10]

Re-arrange this equation gives,

$$C_{Ni^{2+},bound} = C_{NTA^{3-},immobilized,0}\phi\frac{C_{Ni^{2+},in}}{C_{Ni^{2+},in}+K_{Ni-NTA}} \quad [11]$$

Now we have 7 equations, including equation [4], [8-1]-[8-5] and equation [9], and 7 unknowns. We can solve for $C_{Na^+,in}, C_{H^+,in}, C_{Ni^{2+},in}, C_{L^-,in}, C_{SO_4^{2-},in} C_{HL,in}$ and ϕ. As the gel de-swells, the local concentration of the SWCNT increases, resulting in a fluorescence increase, or, mathematically, we have:

$$\frac{I}{I_0}-1=(\frac{H_0+1}{H+1})-1=\frac{\phi}{\phi_0}-1 \quad [12]$$

6.3.5 Parameters in the Model

χ_1 is measured to be -0.01 both in the absence and in the presence of salt[281].

$\rho_0 = \nu_e / V_0$ defines the density of crosslinkers in units of moles/liter. We know ν through chemistry characterization, and for the lowest crosslinking gel we are studying, there are 4.61x10^{-7} mmol/mm^2 crosslinkers, and the gel is 3 mm in diameter. We estimated a dried gel to be 0.5 μn in thickness, and therefore we have the following:

$$\rho_0 = \nu_e / V_0 = \frac{9.23/2\times10^{-10} mol/mm^2 \times Area}{0.5\times10^{-6} m \times Area} = 923 mol/m^3 = 0..923 mol/l$$

$$C_{NTA^{3-},immobolized} = \frac{8.78\times10^{-10} mol/mm^2 \times Area * 0.22}{0.5\times10^{-6} m \times Area} = 386 mol/m^3 = 0.386 mol/l$$

$$C_{COO^-,immobolized} = \frac{8.78\times10^{-10} mol/mm^2 \times Area * 0.78}{0.5\times10^{-6} m \times Area} = 1368 mol/m^3 = 1.368 mol/l$$

6.4 Results and Discussions

Solution phase fluorescence results indicate that the chitosan-SWCNT suspension is quenched upon addition of the transition metal ions Ni^{2+}, Co^{2+}, and Mn^{2+} (33 mM), but does not respond to Mg^{2+} (Figure 6.1). While Mg^{2+} is on the same row as those

transitional metal ions in the periodic table, it is categorizes as a Group 2 metal ion. In addition, Ni2+ causes the largest quenching, followed by Co^{2+}, and then Mn^{2+}. Specifically, ranked from largest-to-smallest fluorescence modulation, the divalent cations are: $Ni^{2+} > Co^{2+} > Mn^{2+} > Mg^{2+}$. The Barron group[276, 277] has previously reported that some divalent ions cause the quenching of SDBS surfactant suspended SWCNTs. Their findings also suggested that $MgSO_4$ quenches SWCNT to the least extent, with quenching constant of 36 for (7,6) chirality at 785 nm excitation. Although $CoSO_4$ and $NiSO_4$ both lead to greater quenching than MgSO4, their findings suggested that $CoSO_4$ (quenching constant of 548 for (7,6) at 785 nm excitation) quenches more than $NiSO_4$ (quenching constant of 109 for (7,6) at 785 nm excitation), differing from what we observed experimentally.

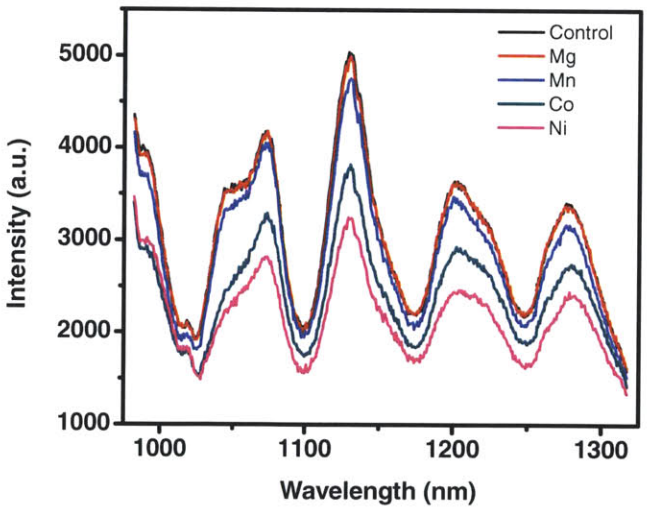

Figure 6.1 Fluorescence of chitosan-SWCNT in modulation upon addition of divalent metal ions, $MgSO_4$ (red), $MnSO_4$ (blue), $CoSO_4$ (green), and $NiSO_4$ (purple) at 33 mM each. The solution was excited by 785 nm laser at 150 mW power at the sample.

Fluorescence quenching can be caused by a number of possible mechanisms, including acid induced fluorescence quenching, absorption bleaching[16], and exciton

quenching[17]. Even bundling of SWCNTs can cause fluorescence decrease, resulting from exciton energy transfer from semiconducting SWCNTs to metal SWCNTs, or between semiconducting species. We first looked into the possibility of absorption bleaching by comparing UV-Vis spectra of chitosan-SWCNT both with and without the metal ions present (Figure 6.2). MgSO4 and MnSO4 do not absorb between 200 – 1400 nm; moreover, the presence of MgSO4 and MnSO4 do not influence the chitosan-SWCNT absorption. Although CoSO4 and NiSO4 absorb between 200 – 600 nm, the presence of those metal ions do not bleach the SWCNT absorption (Figure 6.2c, d). Therefore, the SWCNT quenching is therefore concluded not to be related to absorption bleaching. Barron's group proposed that the enhanced quenching was due to the strong interaction between metal^{2+} ··· SDBS on the surfactant micelle surface, resulting in a higher effective ion concentration in the vicinity of the SWCNT than in the bulk solution. Although in our system, we use chitosan instead of SDBS surfactant, similar effects can also cause fluorescence quenching. In fact, transition metal ions tend to chelate on the chitosan polymer through the amine lone pair electrons, as reported previously[282]. Presumably, the strong interaction between the metal ions and the polymer induces a higher concentration of ions near the SWCNT surface than in the bulk, causing the stronger quenching.

To further explore the fluorescence modulation caused by transition metal ions, we synthesized chitosan-based gels that have SWCNTs embedded inside (Figure 6.3). This approach will allow us to eliminate any potential artifact that could be associated with any solution-based suspension, such as SWCNT aggregation, since the SWCNTs were already immobilized within the gel. We find that in this cationic c-chitosan-SWCNT gel,

we observed much larger quenching from both Ni^{2+} and Co^{2+} than Mg^{2+}, and we observed a fluorescence increase response from Mn^{2+} (Figure 6.3 e-f). We have not yet been able to identify the reason for the increase caused by Mn^{2+}. However, the decrease in the fluorescence of SWCNT in the presence of Ni^{2+} and Co^{2+}, in both the solution and gel form, indicates that the quenching is mostly likely due to the strong interaction between the metal ion and the polymer, further supporting the previous finding.

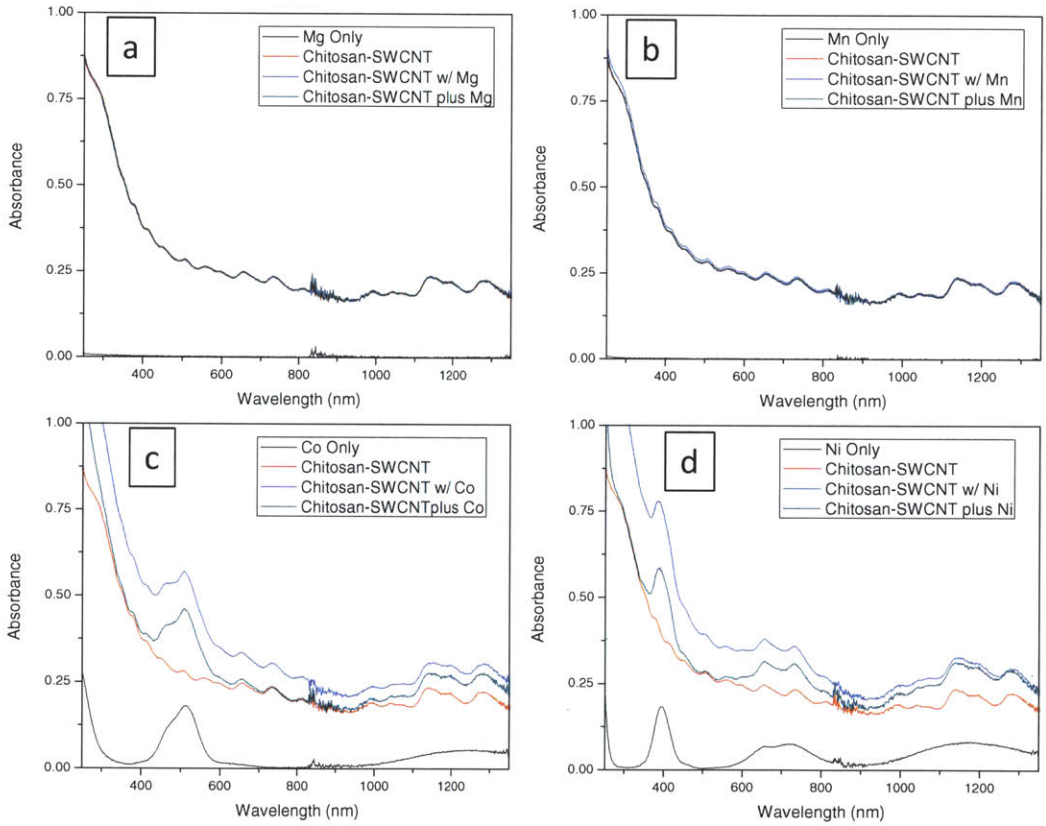

Figure 6.2 Absorption of chitosan-SWCNT solution upon addition of $MgSO_4$ (a), $MnSO_4$ (b), $CoSO_4$ (c), and $NiSO_4$ (d), at 33 mM each. Each testing solution consists of 41.5 µl of 1 v/v% acetic acid with or without SWCNT, ion sufate at a final ion concentration of 33 mM, in a total volume of 250 µl HEPES (500 mM, pH = 7.2). The baseline of the spectrum was taken using 41.5 µl of 1 v/v% acetic acid with a total volume of 250 µl HEPES (500 mM, pH = 7.2), and was subtracted from each spectrum. Black spectrum consists of 41.5 µl 1 v/v acetic acid mixed with ion containing HEPES to reach a final volume of 250 µl ion solution at 33 mM final concentration. Red spectrum consists of 41.5 µl 1 v/v chitosan-SWCNT suspension in 1 v/v% acetic acid mixed with HEPES to reach a final volume of 250 µl. Blue spectrum consists of 41.5

μl 1 v/v chitosan-SWCNT suspension in 1 v/v% acetic acid mixed with ion containing HEPES to reach a final volume of 250 μl ion solution at 33 mM final concentration. Green spectrum is the numerical addition of red and black spectra, in order to compare with the blue spectrum.

We also further investigated chitosan-SWCNT gels that had been NTA groups grafted on (the chemistry is described in Section 6.2). In the c-NTA-chitosan-SWCN gel, which is anionic, addition of all the metal ions universally cause a fluorescence increase (Figure 6.3a-d) although to a different degree, which is opposite from the trend observed in the SWCNT suspension or in the c-chitosan-SWCNT gel. Mn2+ causes the largest fluorescence change, followed by Co2+, and then Ni^{2+}. Mg^{2+} induces a very small change (Figure 6.3 e-f). All the intensity modulations appear reversible, and can be repeated through at least two cycles of addition and washing. Some of the washing processes introduce a delayed fluorescence recovery (Figure 6.3b, 6.3d, 6.3h), which seems to suggest that some metal ions may initially bind to the gel, and gradually leak out of the gel after washing. Currently, we do not have a model which describes all of the phenomena we observe during transient measurements, however, we will further explore this in the future.

The intensity change in the anionic c-NTA-chitosan-SWCNT gel is very interesting to us. Ni^2+-NTA is a widely used chelator for HexaHistidine-conjugated proteins (His-tag protein). It was discovered by our own group that once a His-tagged protein is bound to the Ni-NTA-chitosan gel, binding of a second protein onto this His-tagged protein would cause a fluorescence modulation[265]. It is important to explore this intensity modulation mechanism such that the sensing scheme can be further engineered and improved.

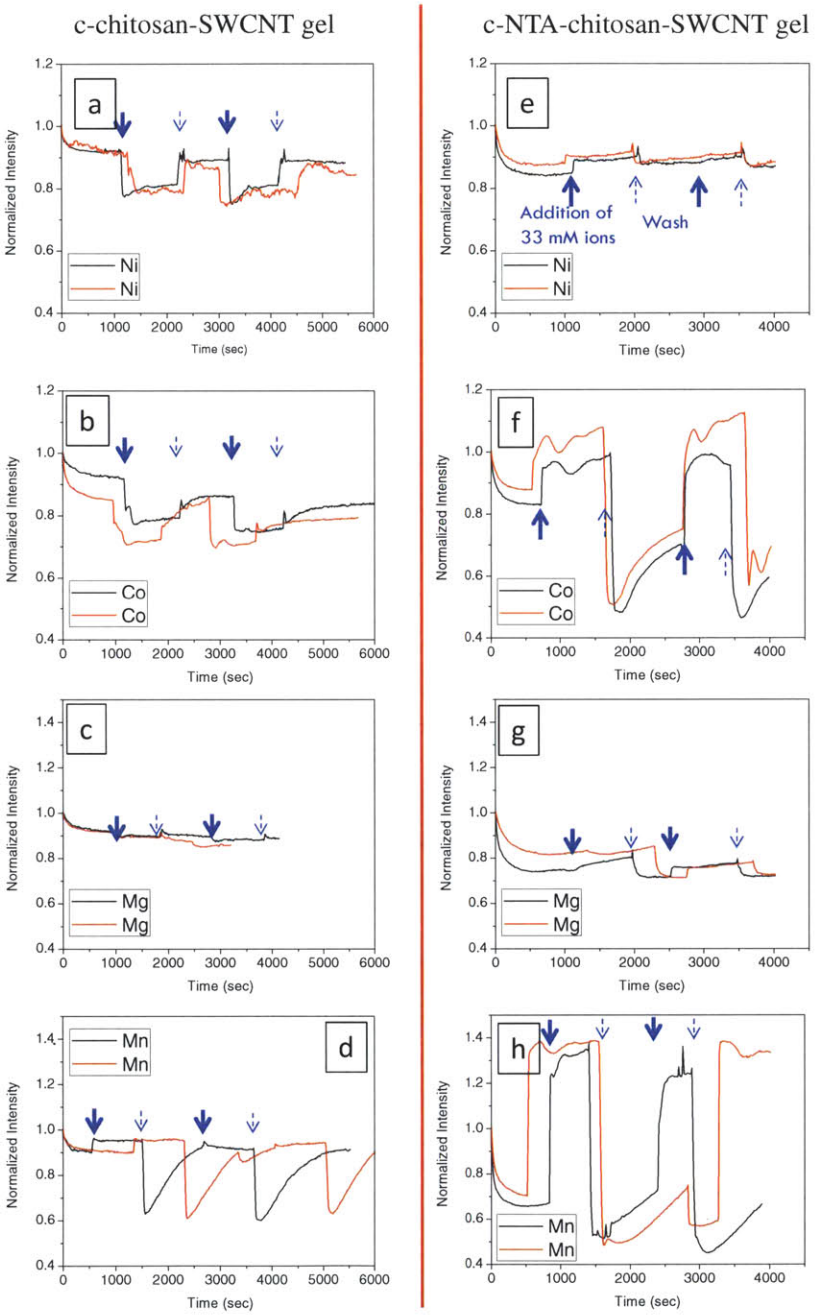

Figure 6.3 Intensity, normalized to the starting intensity, of c-chitosan-SWCNT (a-d) and c-NTA-chitosan-SWCNT (e-h) monitored overtime under a fluorescence microscope (excited at 785 nm, 150 mW at the sample), upon 2 cycles of addition of ions and washing processes. SWCNT gels were incubated in 20 µl HEPES (500 mM, pH = 7.2) and were exposed to subsequent ion addition (indicated by thick arrows, 33 mM in 500 mM HEPES), and washing with HEPES buffer (thin arrows). The arrows only indicate the addition and washing events for the black curve; however, addition and washing time points for the experiments indicated in the red curve are similar to the experiments with the black curve.

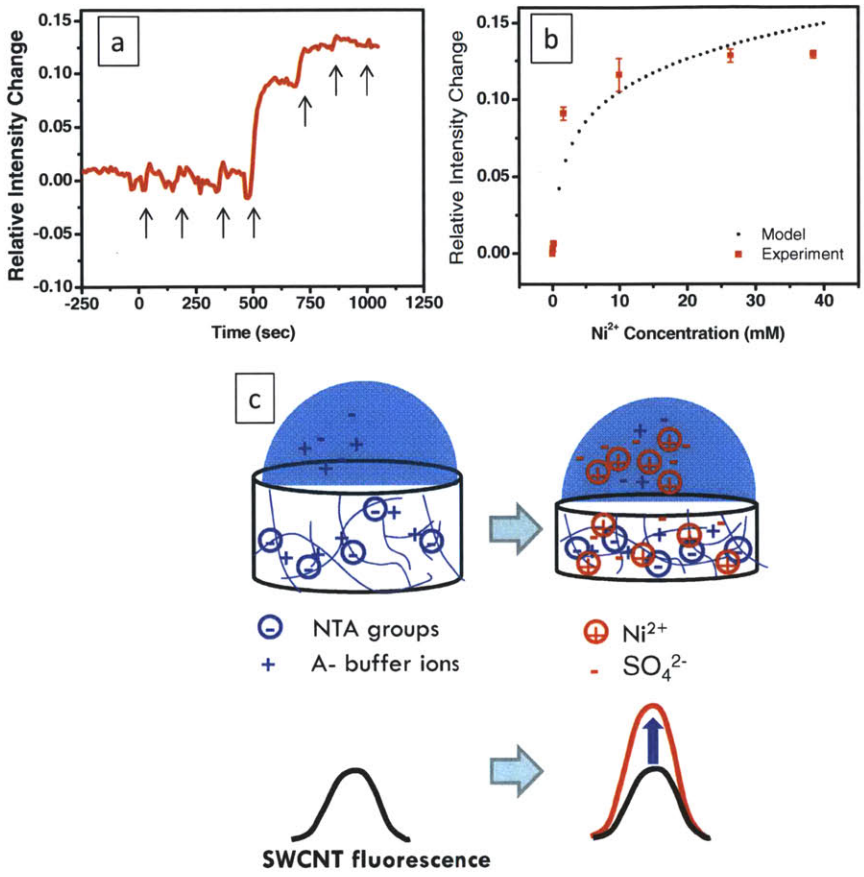

Figure 6.4 Schematic, experimental, and modeling results of the c-NTA-chitosan-SWCNT de-swelling upon addition of NiSO4, upon addition of NiSO4. (a) Relative intensity change of c-NTA-chitosan-SWCNT incubated in 20 μl of HEPES (50 mM, pH = 7.2) upon a series addition of NiSO4 at various concentrations (0, 0.042, 0.167, 1.67, 10, 26.4, 38.5 mM in HEPES, each addition is indicated by an arrow). (b) Relative SWCNT fluorescence change as a function of $NiSO_4$ concentration (red, experimental data; black, model). (a) Schematic of c-NTA-chitosan-SWCNT de-swells upon addition of NiSO4. The gel was under chemical equilibrium initially; the large ionic strength difference inside and outside of the gel is balance by large influx of water into the gel, resulting in a swollen gel. Upon addition of $NiSO_4$, Ni^{2+} ions are chelated onto the NTA, decreasing the number of mobile ions in the gel. As a result, the difference in ionic concentration inside and outside the gel decreases, and the gel requires much less water inside to keep the chemical potential balance, causing the gel to de-swell. Consequently, the local concentration of SWCNT increases, resulting in a fluorescence increase.

We further looked into the relative fluorescence change as a function of Ni^2+ concentration. The c-NTA-chitosan was initially equilibrated with HEPES buffer, and was exposed to a series of buffer solution containing $NiSO_4$ at various time points

indicated by the arrows in the figure 6.4b (0, 0.042, 0.167, 1.67, 10, 26.4, 38.5 mM). Plotting relative intensity change as a function Ni2+ concentration reveals an equilibrium binding curve (Figure 6.4c).

We proposed a gel de-swelling model, derived from Flory-Huggins polymer theory to describe the experimental observation. We hypothesized that the relative intensity change of the gel is inversely proportional to the decrease of the hydration, or $\frac{I}{I_0} = \frac{H_0 + 1}{H + 1} = \frac{\phi}{\phi_0}$.

ϕ is the equilibrium state volume of unswollen gel/ volume of swollen gel, or, $\frac{1}{1+H}$, where H describes the hydration state of the gel. Therefore the goal of this model is to solve for $\frac{\phi}{\phi_0}$.

Before Ni^2+ was added, a swollen gel was formed, and the three chemical potential terms, μ_{ionic}, μ_{mix}, and $\mu_{elastic}$ are in balance, or $\mu_{ionic} = \mu_{mix} + \mu_{elastic}$. Specifically, those three terms can be expressed by the following, according to the Flory-Huggins polymer theory.

$$\mu_{ionic} = (-\ln x_{water,in} + \ln x_{water,out})$$

$$\mu_{mix} = [\ln(1-\phi) + \phi + \chi_1 \phi^2]$$

$$\mu_{elastic} = \mathrm{v}_1 (v_e / V_0)(\phi^{1/3} - \phi/2)$$

where $x_{water,in}$ is the molar fraction of the solvent in the gel, and $x_{water} = 1 - \sum_i x_i$, and when $\sum_i x_i \square 1$, we will have $\ln x_{water} = \ln(1 - \sum_i x_i) \square -\sum_i x_i$. v_1 is the molar volume of

the solvent, or 1.8x10-2 l/mol. V_0 is the volume of the unswollen gel, and v_e is number of crosslinkers. χ_1 is the Flory interaction parameter between the gel and the water (or electrolyte). Here, both μ_{ionic} and $\mu_{elastic}$ have positive values, but μ_{mix} is negative.

We hypothesize that upon Ni2+ addition, the established chemical potential equilibrium is shifted such that water diffuses out of the gel, resulting in de-swelling and a SWCNT concentration increase within the gel, and thus giving a fluorescence increase (Figure 6.4c). Specifically, before Ni^2+ was added, the gel was heavily charged due to the presence of COO- groups from the NTA moieties. Local electroneutrality inside the hydrogel ensures that those negative charges are compensated by mobile Na^+ ions. As a result, there are more mobile ions inside than outside the gel, resulting in a chemical potential imbalance. In order to equilibrate the chemical potentials, water diffuses into the gel, expanding the gel matrix. The elastic force, induced by the crosslinked network, counteracts this expansion. When Ni^2+ is then added, there is an immediate rise in the ionic concentration outside of the gel. However, in this case, the chemical imbalance is opposite to the initial case, and draws water from the gel into the bulk solution. Therefore, the gel de-swells, resulting in an increase in the local concentration of the SWCNTs inside gel, as well as an increase in the fluorescence. Mathematically, we need to solve for all the ion species present inside the gel, $C_{Na^+,in}, C_{H^+,in}, C_{Ni^{2+},in}, C_{L^-,in}, C_{SO_4^{2-},in} C_{HL,in}$ as well as ϕ as a function of $C_{Ni^{2+},out}$ by using chemical potential balance, or $\mu_{ionic} = \mu_{mix} + \mu_{elastic}$, as well as the electroneutrality equation.

We find as Ni^{2+} increases, $\frac{I}{I_0} = \frac{H_0 + 1}{H + 1} = \frac{\phi}{\phi_0}$ indeed increases, and the modeled curve (black, Figure 6.4b) indeed describes the trend of the data (red, Figure 6.4b). The detailed model derivation and solving procedure can be found in Section 6.3. The small deviation is expected to stem from two sources: (1) the estimate on the height of the gel might not be accurate. We attempted with some measurements to probe the thickness of the gel; however, the gel was not formed completely uniform across the sample, making the measurement rather difficult. In addition, we also attempted to directly monitor the de-swelling of the gel, but with little success due to the very thin nature of the gel; (2) we used Flory-Huggins theory to describe our gel network, which may not fully describe the actual system. Some other work has proposed that polysaccharide gel resembles a network of stiff rods[283], however no quantitative theory has been proposed for polysaccharide network yet. Developing a new theory is beyond the scope of this work, but will be explored in the future.

Further, the model provides insights on the mechanism of the fluorescence response. Before Ni^{2+} was added, negatively charged NTA^{3-} and COO^- sites on the gel were electrostatically balanced by mobile Na^+ (Figure 6.5e), resulting in a large mobile ion concentration difference inside and outside the gel. As Ni^{2+} concentration increases, many Ni2+ ions diffuse into the gel, many of which are chelated onto the gel matrix and no longer mobile. As a result, the large difference between the mobile ion concentration inside and outside the gel decreases, and reduces μ_{ionic} term (Figure 6.5a), and thus resulting in an increase in absolute values of μ_{mix} and $\mu_{elastic}$, indicating that the gel de-swells (Figure 6.5b, and Figure 6.5c). The relative change of the chemical potentials,

$\mu - \mu_{Ni^{2}+=0}$, are plotted on Figure 5d. The model also predicted other relevant ion concentrations as shown in Figure 6.5e-i.

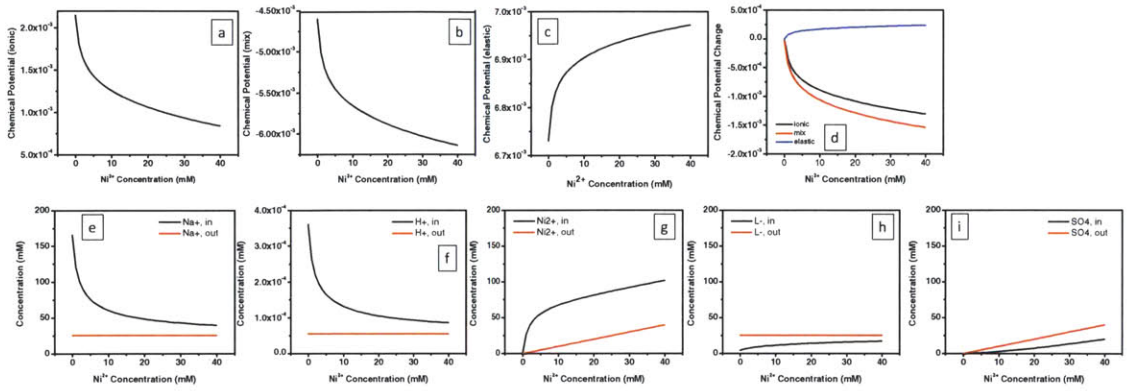

Figure 6.5 Model-calculated chemical potentials and ionic concentrations inside and outside the c-NTA-chitosan gel. (a-c) Chemical potential of ionic (a), mixing (b), and elastic (c) components of the chemical potential as a function of Ni^{2+} concentrations. (d) Relative change of the chemical potential, or $\mu - \mu_{Ni^{2+}=0}$, as a function of Ni^{2+} concentrations. (e-i) Ion (Na^{+}, e; H^{+}, f; Ni^{2+}, g; L-, h; SO_4^{2-}, i) concentrations inside and outside the c-NTA-chitosan as a function Ni^{2+} concentrations.

6.5 Conclusions

In summary, we explored mechanisms of transition-metal ion-induced fluorescence modulation in chitosan suspended SWCNT, in both a solution and gel form. We discovered that Ni^{2+} and Co^{2+} both cause fluorescence quenching for crosslinked chitosan gel (c-chitosan-SWCNT) as well as chitosan suspended SWCNT solution (chitosan-SWCNT). We conclude that this type of quenching is largely due to the strong interaction between the chitosan polymer and the ion, leading to a higher concentration of those transition metal ions near the SWCNT surface than in the bulk. Further, addition of Ni^{2+}, Co^{2+}, Mg^{2+}, and Mn^{2+} universally cause SWCNT fluorescence increase in a crosslinked chitosan gel that has been conjugated with NTA groups (c-NTA-chitosan-SWCNT). We used Ni^{2+} as a model ion to study this observation, and proposed a model that based

Flory-Huggins' theory to describe this experimental observation. We concluded that the strong binding of Ni^{2+} onto NTA groups reduces the number of mobile ions in the gel, resulting in a decrease in ionic chemical potential inside the gel. As a result, water diffuses out of the gel, causing de-swelling of the gel and a local SWCNT concentration increase, thereby increasing the SWCNT fluorescence signal.

7 Conclusions and Future Applications

The central focus of my thesis was to engineer molecular recognition sites using polymer-SWCNT complexes for detection of small molecules and proteins, including reactive oxygen and nitrogen species (chapter 2), important biological small molecules (chapters 3 and 4) as well as proteins/biomarkers (chapters 5 and 6). We began the thesis with a very empirical approach where polymer-SWCNT complexes were designed and synthesized, and then screened against a panel of molecules, to search and identify selective recognition events, through SWCNT optical modulation. We identified that a specific DNA sequence of $d(AT)_{15}$ oligonucleotides wrapped SWCNT selectively recognize nitric oxide, and then we identified three novel polymer-SWCNT complexes that are able to respond to estradiol, L-thyroxine and riboflavin respectively. A mathematical model was derived based on the 2D equation of state theory not only to understand the experimental results but also to provide guidance in future polymer design. Finally, we explored engineering SWCNT sensors toward protein detection by using SWCNT embedding hydrogels. A model that was derived from Flory-Huggins polymer theory was developed to elucidate the sensing mechanism.

In the first chapter, I described the SWCNT fluorescence as well as the optical sensing mechanism. I also described the advantage of using SWCNT for optical sensing especially in biological systems.

In the second chapter, we reported the selective detection of single nitric oxide (NO) molecules using a specific DNA sequence of $d(AT)_{15}$ oligonucleotides, adsorbed to an array of near infrared fluorescent semiconducting single-walled carbon nanotubes (AT_{15}-SWNT). This $d(AT)_{15}$ sequence imparts SWCNT with a distinct selectivity toward NO,

while SWCNT suspended with eight other variant DNA sequences show fluorescence quenching or enhancement from analytes. After tethering the AT_{15}-SWNT onto a APTES modified glass slide, a stepwise fluorescence decrease is observed when the nanotubes are exposed to NO, reporting the dynamics of single-molecule NO adsorption via SWNT exciton quenching. A *birth-and-death* Markov model was developed to describe the experimental observation, and the maximum likelihood estimator of adsorption and desorption rates of NO is derived. Applying the method to Kinetic Monte Carlo (KMC) simulated traces indicates that the resulting error in estimation is less than 5% under our experimental conditions, allowing for calibration using a series of NO concentrations. As expected, the adsorption rate is found to be linearly proportional to NO concentration, and the intrinsic single-SWNT-site NO adsorption rate constant is 0.001 s^{-1} μM NO^{-1}. The ability to detect nitric oxide quantitatively at the single-molecule level may find applications in new cellular assays for the study of nitric oxide carcinogenesis and chemical signaling, as well as medical diagnostics for inflammation. In addition, other students in the lab have continued with this effort by further investigating the sensitivity of the sensor [284], and studying releasing kinetics of NO-releasing drug (unpublished).

In the third chapter, I introduced the concept of "molecular recognition" by using polymer – SWCNT complexes, synthetic polymers that create unique and highly selective molecular recognition sites once adsorbed onto a SWCNT surface. I overviewed three distinct examples we explored that show selective response toward three important biological molecules: a rhodamine isothiocyanate-difunctionalized poly(ethylene glycol) – SWCNT complex, or RITC-PEG-RITC – SWCNT, responding to estradiol; Fmoc L-phenylalanine conjugated PEG brush – SWCNT selectively responding to L-thyroxine;

and boronic acid conjugated phenoxy-dextran – SWCNT specifically responding to riboflavin. We also discovered that the affinity of this type of recognition can be tuned by changing both the composition of the polymer and SWCNT parameters such as the diameter. We also confirmed the binding of the analyte to the polymer-SWCNT complexes via radiolabeling assays. Finally, we studied riboflavin update by macrophage cells by using a dual channel microscope taking advantage of the selective sensing rendered by the boronic acid conjugated phenoxy-dextran – SWCNT complex.

In the fourth chapter, we developed a theoretical frame work that can provide insight into the mechanism for these "molecular recognition" responses and guide the design of future polymer synthesis, which is desirable but so far unexplored. We modeled analyte molecules adsorbing onto the polymer-SWCNT surface using a modified thermodynamic model that was originally developed for describing competitive adsorption of surfactants at air-water interface, with model parameters determined with molecular simulations. The model provides physical insight into the key molecular parameters that govern the competitive adsorption between the analyte of interest and the hydrophobic segment of the polymer on the SWCNT surface. The resulting model is able to correctly predict 83% of the fluorescence responses from a recent experimental paper within 20% error of the experimental values.

In the fifth chapter, I first reviewed recent advances, challenges and potential solutions of using direct and label-free method for protein bio-marker detection. Then I introduced the importance of detection for cardiac troponin T (potentially in a point-of-care setting). In this part of the thesis work, we have demonstrated a novel, rapid and label-free near-infrared fluorescent assay specific for cTnT detection, using single-walled

carbon nanotubes (SWCNT). Comparing with traditional ELISA assay and other labeling methods, this method is simple, and does not require a secondary antibody. Fluorescent SWCNT itself transduces signal, providing a sensing readout. In addition, we developed two new chemical characterization assays that allow us to quantify amine and carboxylic acids in a soft gel, providing a useful assay tool for characterizing the mostly widely used chemical groups in soft gels, which other researchers working with soft gels or hydrogels may find interest in.

In the sixth chapter, we were interested in further exploring the mechanism of fluorescence modulation in a series of gel systems similar to the system used in the previous protein detection work. In doing so, we synthesized and characterized chitosan-gels, embedding SWCNTs both with and without NTA groups, and compared fluorescence responses upon addition of four different ions, including Ni^{2+}, Co^{2+}, Mg^{2+}, and Mn^{2+} in both a SWCNT-embedded gel and in a SWCNT solution. We hypothesized that the addition of metal ions to NTA-modified chitosan gel causes de-swelling of the gel, resulting in an increase of the local concentration of the SWCNTs, and thereby leading to a fluorescence increase. We then mathematically modeled the de-swelling and subsequent fluorescence change, based on the Flory-Huggins theory. The model well describes the data, suggesting that upon addition of $NiSO_4$, the difference in the ionic concentration inside and outside the gel decreases, and the gel requires less water content in order to balance the chemical potentials of the gel and solution. As a result, water diffuses out of the gel, causing de-swelling of the gel and a fluorescence increase. This effort contributes to the basis of a theoretical framework that describes SWCNT optical sensing in the context of a hydrogel.

Overall, this thesis opens up many interesting areas of research that will be worth exploring further. In the "molecular recognition" work, in particular, model-guided polymer synthesis can be performed, and the experimental results will further assist to elucidate the recognition mechanism. On the protein-recognition work, hydrogels can be further engineered to completely remove non-specific adsorption or other effects from blood or other proteins.

8 Bibliography

1. Scanlan, C., et al., *Exploiting the defensive sugars of HIV-1 for drug and vaccine design.* Nature, 2007. **446**(7139): p. 1038-1045.
2. Ellington, A.D. and J.W. Szostak, *In vitro selection of RNA molecules that bind specific ligands.* Nature, 1990. **346**(6287): p. 818-822.
3. Cho, E.J., J.W. Lee, and A.D. Ellington, *Applications of Aptamers as Sensors.* Annual Review of Analytical Chemistry, 2009. **2**: p. 241-264.
4. Nish, A., et al., *Highly selective dispersion of single-walled carbon nanotubes using aromatic polymers.* Nature Nanotechnology, 2007. **2**(10): p. 640-646.
5. Tsyboulski, D., et al., *Self-Assembling Peptide Coatings Designed for Highly Luminescent Suspension of Single-Walled Carbon Nanotubes.* J. Am. Chem. Soc, 2008. **130**(50): p. 17134-17140.
6. Zheng, M., et al., *DNA-assisted dispersion and separation of carbon nanotubes.* Nature Materials, 2003. **2**(5): p. 338-342.
7. Tu, X., et al., *DNA sequence motifs for structure-specific recognition and separation of carbon nanotubes.* Nature, 2009. **460**(7252): p. 250-253.
8. Bhuiya, F.A., S.R. Pitts, and L.F. McCaig, *Emergency Department Visits for Chest Pain and Abdominal Pain: United States, 1999–2008.* 2010.
9. Apple, F.S., P.O. Collinson, and f.t.I.T.F.o.C.A.o.C. Biomarkers, *Analytical Characteristics of High-Sensitivity Cardiac Troponin Assays.* Clinical Chemistry, 2012. **58**(1): p. 54-61.
10. Bachilo, S.M., et al., *Structure-assigned optical spectra of single-walled carbon nanotubes.* Science, 2002. **298**(5602): p. 2361-2366.
11. Walsh, A.G., et al., *Screening of excitons in single, suspended carbon nanotubes.* Nano Lett, 2007. **7**(6): p. 1485-1488.
12. Wang, F., et al., *The optical resonances in carbon nanotubes arise from excitons.* Science, 2005. **308**(5723): p. 838-841.
13. Maultzsch, J., et al., *Exciton binding energies in carbon nanotubes from two-photon photoluminescence (vol 72, art. no. 241402(R), 2005).* Physical Review B, 2006. **74**(16).
14. Dresselhaus, M.S., et al., *Exciton Photophysics of Carbon Nanotubes.* Annual Review of Physical Chemistry, 2007. **58**(1): p. 719-747.
15. Kane, C.L. and E.J. Mele, *Electron interactions and scaling relations for optical excitations in carbon nanotubes.* Physical Review Letters, 2004. **93**(19).
16. O'Connell, M., E. Eibergen, and S. Doorn, *Chiral selectivity in the charge-transfer bleaching of single-walled carbon-nanotube spectra.* Nature Materials, 2005. **4**(5): p. 412-418.
17. Satishkumar, B.C., et al., *Reversible fluorescence quenching in carbon nanotubes for biomolecular sensing.* Nat Nano, 2007. **2**(9): p. 560-564.
18. Boghossian□, A.A., et al., *Near-Infrared Fluorescent Sensors based on Single-Walled Carbon Nanotubes for Life Sciences Applications.* ChemSusChem, 2011. **4**(7): p. 848-863.
19. O'Connell, M.J., et al., *Band gap fluorescence from individual single-walled carbon nanotubes.* Science, 2002. **297**(5581): p. 593-596.
20. Saito, R., M.S. Dresselhaus, and G. Dresselhaus, *Physical Properties of Carbon Nanotubes.* 1998, London: Imperial College Press.

21. Heller, D.A., et al., *Single-walled carbon nanotube spectroscopy in live cells: Towards long-term labels and optical sensors.* Advanced Materials, 2005. **17**(23): p. 2793-2798.
22. Heller, D.A., et al., *Optical detection of DNA conformational polymorphism on single-walled carbon nanotubes.* Science, 2006. **311**(5760): p. 508.
23. Barone, P.W., R.S. Parker, and M.S. Strano, *In vivo fluorescence detection of glucose using a single-walled carbon nanotube optical sensor: Design, fluorophore properties, advantages, and disadvantages.* Anal. Chem, 2005. **77**(23): p. 7556-7562.
24. Barone, P.W., et al., *Near-infrared optical sensors based on single-walled carbon nanotubes.* Nature Materials, 2005. **4**(1): p. 86-92.
25. Kim, J., et al., *The rational design of nitric oxide selectivity in single-walled carbon nanotube near-infrared fluorescence sensors for biological detection.* Nature Chemistry, 2009. **1**(6): p. 473-481.
26. Cognet, L., et al., *Stepwise quenching of exciton fluorescence in carbon nanotubes by single-molecule reactions.* Science, 2007. **316**(5830): p. 1465.
27. Siitonen, A.J., et al., *Surfactant-dependent exciton mobility in single-walled carbon nanotubes studied by single-molecule reactions.* Nano Letters, 2010. **10**(5): p. 1595-1599.
28. Siitonen, A.J., et al., *Dependence of exciton mobility on structure in single-walled carbon nanotubes.* The Journal of Physical Chemistry Letters, 2010. **1**(14): p. 2189-2192.
29. Jin, H., et al., *Stochastic analysis of stepwise fluorescence quenching reactions on single-walled carbon nanotubes: single molecule sensors.* Nano letters, 2008. **8**(12): p. 4299-4304.
30. Jin, H., et al., *Detection of single-molecule H2O2 signalling from epidermal growth factor receptor using fluorescent single-walled carbon nanotubes.* Nat Nano, 2010. **5**(4): p. 302-309.
31. Keiding, N., *Maximum likelihood estimation in birth-and-death process.* Annals of Statistics, 1975. **3**(2): p. 363-372.
32. Zhang, J., et al., *Single Molecule Detection of Nitric Oxide Enabled by d(AT)15 DNA Adsorbed to Near Infrared Fluorescent Single-Walled Carbon Nanotubes.* Journal of the American Chemical Society, 2010. **133**(3): p. 567-581.
33. Mujumdar, R., et al., *Cyanine dye labeling reagents: sulfoindocyanine succinimidyl esters.* Bioconj Chem, 1993. **4**: p. 105-111.
34. Benson, R. and H. Kues, *Fluorescence Properties of Indocyanine Green as Related to Angiography.* Phys. Med. Biol., 1978. **23**(1): p. 159-163.
35. Lakowicz, J., *Principles of Fluorescence Spectroscopy.* 2nd Ed. ed. 1999, New York, Moscow, Dordecht: Academic/Plenum Publishers.
36. Magde, D., G. Rojas, and P. Seybold, *Solvent Dependence of the Fluorescence Lifetimes of Xanthene Dyes.* Photochem. Photobiol., 1999. **70**: p. 737.
37. Wray, S., et al., *Characterization of the near infrared absorption spectra of cytochrome aa3 and haemoglobin for the non-invasive monitoring of cerebral oxygenation.* Biochimica et Biophsica Acta, 1988. **933**: p. 184-192.
38. Saxena, V., M. Sadoqi, and J. Shao, *Degradation Kinetics of Indocyanine Green in Aqueous Solution.* J. of Pharm. Sci., 2003. **92**(10): p. 2090-2097.
39. Kim, S., et al., *Near-infrared fluorescent type II quantum dots for sentinel lymph node mapping.* Nature Biotechnology, 2004. **22**(1): p. 93-97.

40. McCartney, L.J., et al., *Near-infrared fluorescence lifetime assay for serum glucose based on allophycocyanin-labeled concanavalin A.* Analytical Biochemistry, 2001. **292**(2): p. 216-221.
41. Klonis, N., et al., *Characterization of a series of far-red-absorbing thiobarbituric acid oxonol derivatives as fluorescent probes for biological applications.* Analytical Biochemistry, 2003. **317**(1): p. 47-58.
42. Liu, Z., et al., *In vivo biodistribution and highly efficient tumour targeting of carbon nanotubes in mice.* Nat Nano, 2007. **2**(1): p. 47-52.
43. Liu, Z., et al., *Drug delivery with carbon nanotubes for in vivo cancer treatment.* Cancer Research, 2008. **68**(16): p. 6652-6660.
44. Cui, D.X., et al., *Effect of single wall carbon nanotubes on human HEK293 cells.* Toxicology Letters, 2005. **155**(1): p. 73-85.
45. Sayes, C.M., et al., *Functionalization density dependence of single-walled carbon nanotubes cytotoxicity in vitro.* Toxicology Letters, 2006. **161**(2): p. 135-142.
46. Singh, R., et al., *Tissue biodistribution and blood clearance rates of intravenously administered carbon nanotube radiotracers.* Proceedings of the National Academy of Sciences of the United States of America, 2006. **103**(9): p. 3357-3362.
47. Dumortier, H., et al., *Functionalized carbon nanotubes are non-cytotoxic and preserve the functionality of primary immune cells.* Nano Letters, 2006. **6**(7): p. 1522-1528.
48. Heller, D.A., et al., *Multimodal optical sensing and analyte specificity using single-walled carbon nanotubes.* Nature Nanotechnology, 2009. **4**: p. 114-120.
49. Jeng, E.S., et al., *Detection of DNA hybridization using the near-infrared band-gap fluorescence of single-walled carbon nanotubes.* Nano Letters, 2006. **6**(3): p. 371-375.
50. Jeng, E.S., et al., *Detection of a Single Nucleotide Polymorphism Using Single-Walled Carbon-Nanotube Near-Infrared Fluorescence13.* Small, 2010. **6**(1): p. 40-43.
51. Pender, M.J., et al., *Peptide-mediated formation of single-wall carbon nanotube composites.* Nano Lett, 2006. **6**(1): p. 40-44.
52. Witus, L.S., et al., *Peptides that non-covalently functionalize single-walled carbon nanotubes to give controlled solubility characteristics.* Journal of Materials Chemistry, 2007. **17**(19): p. 1909-1915.
53. Kim, J.H., et al., *The rational design of nitric oxide selectivity in single-walled carbon nanotube near-infrared fluorescence sensors for biological detection.* Nature Chemistry, 2009. **1**(6): p. 473-481.
54. Moncada, S., R.M. Palmer, and E.A. Higgs, *Nitric oxide: physiology, pathophysiology, and pharmacology.* Pharmacological Reviews, 1991. **43**(2): p. 109-142.
55. Garthwaite, J. and C.L. Boulton, *Nitric-oxide signaling in the central-nervous-system.* Annual Review of Physiology, 1995. **57**: p. 683-706.
56. Steinert, J.R., T. Chernova, and I.D. Forsythe, *Nitric oxide signaling in brain function, dysfunction, and dementia.* Neuroscientist, 2010. **16**(4): p. 435-452.
57. Liu, V.W.T. and P.L. Huang, *Cardiovascular roles of nitric oxide: A review of insights from nitric oxide synthase gene disrupted mice.* Cardiovascular Research, 2008. **77**(1): p. 19-29.
58. Cai, H. and D.G. Harrison, *Endothelial dysfunction in cardiovascular diseases - The role of oxidant stress.* Circulation Research, 2000. **87**(10): p. 840-844.

59. Gimbrone, M.A., et al., *Endothelial dysfunction, hemodynamic forces, and atherogenesis*, in *Atherosclerosis V: The Fifth Saratoga Conference*, F. Numano and M.A. Gimbrone, Editors. 2000. p. 230-240.
60. Grange, R.W., et al., *Nitric oxide contributes to vascular smooth muscle relaxation in contracting fast-twitch muscles.* Physiological Genomics, 2001. **5**(1): p. 35-44.
61. Tripathi, P., L. Kashyap, and V. Singh, *The role of nitric oxide in inflammatory reactions.* Fems Immunology and Medical Microbiology, 2007. **51**(3): p. 443-452.
62. Wink, D.A. and J.B. Mitchell, *Nitric oxide and cancer: An introduction.* Free Radical Biology and Medicine, 2003. **34**(8): p. 951-954.
63. Wink, D.A., et al., *The multifaceted roles of nitric oxide in cancer.* Carcinogenesis, 1998. **19**(5): p. 711.
64. Lancaster, J.R. and K.P. Xie, *Tumors face NO problems?* Cancer Research, 2006. **66**(13): p. 6459-6462.
65. Hofseth, L.J., et al., *Nitric oxide in cancer and chemoprevention.* Free Radical Biology and Medicine, 2003. **34**(8): p. 955-968.
66. Hofseth, L.J., *Nitric oxide as a target of complementary and alternative medicines to prevent and treat inflammation and cancer.* Cancer Letters, 2008. **268**(1): p. 10-30.
67. Rivot, J.P., et al., *Nitric oxide (NO): in vivo electrochemical monitoring in the dorsal horn of the spinal cord of the rat.* Brain research, 1997. **773**(1-2): p. 66-75.
68. Wink, D.A. and J.B. Mitchell, *Chemical biology of nitric oxide: Insights into regulatory, cytotoxic, and cytoprotective mechanisms of nitric oxide.* Free Radical Biology and Medicine, 1998. **25**(4-5): p. 434-456.
69. Yao, D., A.G. Vlessidis, and N.P. Evmiridis, *Determination of nitric oxide in biological samples.* Microchimica Acta, 2004. **147**(1): p. 1-20.
70. Hetrick, E.M. and M.H. Schoenfisch, *Analytical Chemistry of Nitric Oxide.* Annual Review of Analytical Chemistry, 2009. **2**: p. 409-433.
71. Williams, R.J.P., *Nitric oxide in biology: Its role as a ligand.* Chemical Society Reviews, 1996. **25**(2): p. 77-&.
72. Moller, M.N., et al., *Acceleration of nitric oxide autoxidation and nitrosation by membranes.* Iubmb Life, 2007. **59**(4-5): p. 243-248.
73. Girard, P. and P. Potier, *NO, thiols and disulfides.* Febs Letters, 1993. **320**(1): p. 7-8.
74. Thomas, D.D., et al., *Superoxide fluxes limit nitric oxide-induced signaling.* Journal of Biological Chemistry, 2006. **281**(36): p. 25984-25993.
75. Gomes, A., E. Fernandes, and J. Lima, *Use of fluorescence probes for detection of reactive nitrogen species: A review.* Journal of Fluorescence, 2006. **16**(1): p. 119-139.
76. Nagano, T. and T. Yoshimura, *Bioimaging of nitric oxide.* Chemical Reviews, 2002. **102**(4): p. 1235-1270.
77. Miller, E.W. and C.J. Chang, *Fluorescent probes for nitric oxide and hydrogen peroxide in cell signaling.* Current Opinion in Chemical Biology, 2007. **11**(6): p. 620-625.
78. Nagano, T., *Practical methods for detection of nitric oxide.* Luminescence, 1999. **14**(6): p. 283-290.
79. Tarpey, M.M., D.A. Wink, and M.B. Grisham, *Methods for detection of reactive metabolites of oxygen and nitrogen: in vitro and in vivo considerations.* American Journal of Physiology-Regulatory Integrative and Comparative Physiology, 2004. **286**(3): p. R431-R444.

80. Kojima, H., et al., *Development of a fluorescent indicator for nitric oxide based on the fluorescein chromophore.* Chemical & Pharmaceutical Bulletin, 1998. **46**(2): p. 373-375.
81. Kojima, H., et al., *Detection and imaging of nitric oxide with novel fluorescent indicators:□ diaminofluoresceins.* Analytical Chemistry, 1998. **70**(13): p. 2446-2453.
82. Kojima, H., et al., *Fluorescent indicators for imaging nitric oxide production.* Angewandte Chemie International Edition, 1999. **38**(21): p. 3209-3212.
83. Sasaki, E., et al., *Highly sensitive near-infrared fluorescent probes for nitric oxide and their application to isolated organs.* Journal of the American Chemical Society, 2005. **127**(11): p. 3684-3685.
84. Yang, Y., et al., *A highly selective low-background fluorescent imaging agent for nitric oxide.* Journal of the American Chemical Society, 2010. **132**(38): p. 13114–13116.
85. Meineke, P., et al., *Cheletropic traps for the fluorescence spectroscopic detection of nitric oxide (nitrogen monoxide) in biological systems.* Chemistry – A European Journal, 1999. **5**(6): p. 1738-1747.
86. Meineke, P., et al., *Nitric oxide detection and visualization in biological systems. Applications of the FNOCT method.* Biological Chemistry, 2000. **381**(7): p. 575-582.
87. Smith, R.C., et al., *Conjugated polymer-based fluorescence turn-on sensor for nitric oxide.* Organic Letters, 2005. **7**(16): p. 3573-3575.
88. Smith, R.C., A.G. Tennyson, and S.J. Lippard, *Polymer-bound dirhodium tetracarboxylate films for fluorescent detection of nitric oxide.* Inorganic Chemistry, 2006. **45**(16): p. 6222-6226.
89. Lim, M.H. and S.J. Lippard, *Copper complexes for fluorescence-based NO detection in aqueous solution.* Journal of the American Chemical Society, 2005. **127**(35): p. 12170-12171.
90. Lim, M.H. and S.J. Lippard, *Fluorescent nitric oxide detection by copper complexes bearing anthracenyl and dansyl fluorophore ligands.* Inorganic Chemistry, 2006. **45**(22): p. 8980-8989.
91. Lim, M.H., et al., *Direct nitric oxide detection in aqueous solution by copper(II) fluorescein complexes.* Journal of the American Chemical Society, 2006. **128**(44): p. 14364-14373.
92. Lim, M.H., D. Xu, and S.J. Lippard, *Visualization of nitric oxide in living cells by a copper-based fluorescent probe.* Nature Chemical Biology, 2006. **2**(7): p. 375-380.
93. Lim, M.H. and S.J. Lippard, *Metal-based turn-on fluorescent probes for sensing nitric oxide.* Accounts of Chemical Research, 2007. **40**(1): p. 41-51.
94. McQuade, L.E., M.D. Pluth, and S.J. Lippard, *Mechanism of nitric oxide reactivity and fluorescence enhancement of the NO-specific probe CuFL1.* Inorganic Chemistry, 2010. **49**(17): p. 8025-8033.
95. McQuade, L.E., et al., *Visualization of nitric oxide production in the mouse main olfactory bulb by a cell-trappable copper(II) fluorescent probe.* Proceedings of the National Academy of Sciences of the United States of America, 2010. **107**(19): p. 8525-8530.
96. McQuade, L.E. and S.J. Lippard, *Fluorescence-based nitric oxide sensing by Cu(II) complexes that can be trapped in living cells.* Inorganic Chemistry, 2010. **49**(16): p. 7464-7471.

97. Pluth, M.D., L.E. McQuade, and S.J. Lippard, *Cell-trappable fluorescent probes for nitric oxide visualization in living cells.* Organic Letters, 2010. **12**(10): p. 2318-2321.
98. Wang, S.H., M.Y. Han, and D.J. Huang, *Nitric oxide switches on the photoluminescence of molecularly engineered quantum dots.* Journal of the American Chemical Society, 2009. **131**(33): p. 11692-+.
99. Yan, X.Q., et al., *Fluorescence sensing of nitric oxide in aqueous solution by triethanolamine-modified CdSe quantum dots.* Luminescence, 2009. **24**(4): p. 255-259.
100. Barone, P.W. and M.S. Strano, *Reversible control of carbon nanotube aggregation for a glucose affinity sensor.* ANGEWANDTE CHEMIE, 2006. **118**(48): p. 8318.
101. Kikuchi, K., T. Nagano, and M. Hirobe, *Novel detection method of nitric oxide using horseradish peroxidase.* Biological & Pharmaceutical Bulletin, 1996. **19**(4): p. 649-651.
102. Inoue, T., et al., *Diameter dependence of exciton-phonon interaction in individual single-walled carbon nanotubes studied by microphotoluminescence spectroscopy.* Physical Review B, 2006. **73**(23): p. 233401.
103. Reiter, C.D., R.-J. Teng, and J.S. Beckman, *Superoxide Reacts with Nitric Oxide to Nitrate Tyrosine at Physiological pH via Peroxynitrite.* Journal of Biological Chemistry, 2000. **275**(42): p. 32460-32466.
104. Mizukawa, H. and E. Okabe, *Inhibition by singlet molecular oxygen of the vascular reactivity in rabbit mesenteric artery.* British Journal of Pharmacology, 1997. **121**(1): p. 63-70.
105. Zheng, M., et al., *Structure-based carbon nanotube sorting by sequence-dependent DNA assembly.* Science, 2003. **302**(5650): p. 1545-1548.
106. Jin, H., et al., *Divalent Ion and thermally induced DNA conformational polymorphism on single-walled carbon nanotubes.* Macromolecules, 2007. **40**(18): p. 6731-6739.
107. Hughes, M.E., E. Brandin, and J.A. Golovchenko, *Optical absorption of DNA–carbon nanotube structures.* Nano Letters, 2007. **7**(5): p. 1191-1194.
108. Meng, S., et al., *DNA nucleoside interaction and identification with carbon nanotubes.* Nano Letters, 2006. **7**(1): p. 45-50.
109. Manohar, S., T. Tang, and A. Jagota, *Structure of homopolymer DNA–CNT hybrids.* The Journal of Physical Chemistry C, 2007. **111**(48): p. 17835-17845.
110. Johnson, R.R., A.T.C. Johnson, and M.L. Klein, *Probing the structure of DNA–carbon nanotube hybrids with molecular dynamics.* Nano Letters, 2008. **8**(1): p. 69-75.
111. Johnson, R.R., et al., *Free energy landscape of a DNA–carbon nanotube hybrid using replica exchange molecular dynamics.* Nano Letters, 2009. **9**(2): p. 537-541.
112. Khamis, S.M., et al., *Homo-DNA functionalized carbon nanotube chemical sensors.* Journal of Physics and Chemistry of Solids, 2010. **71**(4): p. 476-479.
113. Johnson, A.T.C., et al., *DNA-Coated nanosensors for breath analysis.* Ieee Sensors Journal, 2010. **10**(1): p. 159-166.
114. Johnson, A.T.C., et al., *DNA-decorated carbon nanotubes for chemical sensing.* Semiconductor Science and Technology, 2006. **21**(11): p. S17-S21.
115. Bartberger, M.D., et al., *The reduction potential of nitric oxide (NO) and its importance to NO biochemistry.* Proceedings of the National Academy of Sciences of the United States of America, 2002. **99**(17): p. 10958-10963.

116. Anderson, R.F., *Energetics of the one-electron reduction steps of riboflavin, FMN and FAD to their fully reduced forms.* Biochimica et Biophysica Acta (BBA) - Bioenergetics, 1983. **722**(1): p. 158-162.
117. References for potential levels in this work are with respect to normal hydrogen electrode (NHE).
118. Shoda, M., et al., *Probing Interaction between ssDNA and Carbon Nanotubes by Raman Scattering and Electron Microscopy.* The Journal of Physical Chemistry C, 2009. **113**(15): p. 6033-6036.
119. Tanaka, Y., et al., *Determination of electronic states of individually dissolved (n,m) single-walled carbon nanotubes in solution.* Chemical Physics Letters, 2009. **482**(1-3): p. 114-117.
120. Wang, F., et al., *Observation of rapid Auger recombination in optically excited semiconducting carbon nanotubes.* Physical Review B, 2004. **70**(24): p. 241403.
121. Dukovic, G., et al., *Reversible surface oxidation and efficient luminescence quenching in semiconductor single-wall carbon nanotubes.* Journal of the American Chemical Society, 2004. **126**(46): p. 15269-15276.
122. Anderson, R.F., *Energetics of the one-electron steps in the NAD+-NADH redox couple* Biochimica Et Biophysica Acta, 1980. **590**(2): p. 277-281.
123. Mahal, H.S., H.S. Sharma, and T. Mukherjee, *Antioxidant properties of melatonin: A pulse radiolysis study.* Free Radical Biology and Medicine, 1999. **26**(5-6): p. 557-565.
124. Turyan, Y.I. and R. Kohen, *Formal redox potentials of the dehydro-L-ascorbic acid L-ascorbic-acid system.* Journal of Electroanalytical Chemistry, 1995. **380**(1-2): p. 273-277.
125. Tanaka, Y., et al., *Experimentally determined redox potentials of individual (n,m) single-walled carbon nanotubes.* Angewandte Chemie-International Edition, 2009. **48**(41): p. 7655-7659.
126. Zheng, M. and B.A. Diner, *Solution redox chemistry of carbon nanotubes.* Journal of the American Chemical Society, 2004. **126**(47): p. 15490-4.
127. Wang, F., et al., *Time-resolved fluorescence of carbon nanotubes and its implication for radiative lifetimes.* Physical Review Letters, 2004. **92**(17): p. 177401.
128. Tarte, P., *Rotational isomerism as a general property of alkyl nitrites.* Journal of Chemical Physics, 1952. **20**(10): p. 1570-1575.
129. Bates, J.N., *The study of biological nitric oxide.* Neuroprotocols, 1992. **1**(2): p. 99-107.
130. Kelm, M., *Nitric oxide metabolism and breakdown.* BBA-Bioenergetics, 1999. **1411**(2-3): p. 273-289.
131. Clancy, R.M., Y. Miyazaki, and P.J. Cannon, *Use of thionitrobenzoic acid to characterize the stability of nitric oxide in aqueous solutions and in porcine aortic endothelial cell suspensions.* Analytical Biochemistry, 1990. **191**(1): p. 138-143.
132. Wink, D.A., et al., *Reactions of the bioregulatory agent nitric oxide in oxygenated aqueous media: Determination of the kinetics for oxidation and nitrosation by intermediates generated in the nitric oxide/oxygen reaction.* Chemical Research in Toxicology, 1993. **6**(1): p. 23-27.
133. Lindig, B.A., M.A.J. Rodgers, and A.P. Schaap, *Determination of the lifetime of singlet oxygen in water-d2 using 9,10-anthracenedipropionic acid, a water-soluble probe.* Journal of the American Chemical Society, 1980. **102**(17): p. 5590-5593.

134. Egorov, S.Y., et al., *Rise and decay kinetics of photosensitized singlet oxygen luminescence in water. Measurements with nanosecond time-correlated single photon counting technique.* Chemical Physics Letters, 1989. **163**(4-5): p. 421-424.
135. Rodgers, M.A.J. and P.T. Snowden, *Lifetime of oxygen (O2(1.DELTA.g)) in liquid water as determined by time-resolved infrared luminescence measurements.* Journal of the American Chemical Society, 1982. **104**(20): p. 5541-5543.
136. Beckman, J.S., et al., *Apparent hydroxyl radical production by peroxynitrite: implications for endothelial injury from nitric oxide and superoxide.* Proceedings of the National Academy of Sciences of the United States of America, 1990. **87**(4): p. 1620-1624.
137. Radi, R., *Peroxynitrite Reactions and Diffusion in Biology.* Chemical Research in Toxicology, 1998. **11**(7): p. 720-721.
138. Romero, N., et al., *Diffusion of Peroxynitrite in the Presence of Carbon Dioxide.* Archives of Biochemistry and Biophysics, 1999. **368**(1): p. 23-30.
139. McKinney, S.A., C. Joo, and T. Ha, *Analysis of single-molecule FRET trajectories using hidden Markov modeling.* Biophysical journal, 2006. **91**(5): p. 1941-1951.
140. Feigin, P.D., *Maximum likelihood estimation for continuous-time stochastic-process.* Advances in Applied Probability, 1976. **8**(4): p. 712-736.
141. Kerssemakers, J.W.J., et al., *Assembly dynamics of microtubules at molecular resolution.* Nature, 2006. **442**(7103): p. 709-712.
142. Both algorithms fail when applied to control data in which there are no actual transitions, fitting steps within the noise (Figure S9). We attempted to subject each trace to a noise reduction program based on reference 94. Chung, S.H. and R.A. Kennedy, Forward-backward non-linear filtering technique for extracting small biological signals from noise. Journal of Neuroscience Methods, 1991. 40(1): p. 71-86. before applying HMM or error-minimizing step-finding algorithms, but the over-fitting of noise on control data persisted (Figure S9). We therefore concluded that these algorithms cannot be utilized on traces containing no authentic transitions. To resolve this issue, we first determine which traces contain actual transitions in fluorescence intensity and perform the analysis only on these data sets. The relatively high signal-to-noise ratio in the data aids in this, and bias is minimized through randomizing all traces prior to analysis (Figure S10). And the step-fitting algorithm is applied thereafter only to traces that contain transitions, and zero-transitions are assigned to the remainder.
143. Gillespie, D.T., *Exact stochastic simulation of coupled chemical reactions.* J. Phys. Chem, 1977. **81**(25): p. 2340-2361.
144. Saerens, D., et al., *Antibody Fragments as Probe in Biosensor Development.* Sensors, 2008. **8**: p. 4669-4686.
145. Byrne, B., et al., *Antibody-Based Sensors: Principles, Problems and Potential for Detection of Pathogens and Associated Toxins.* Sensors, 2009. **9**: p. 4407-4445.
146. de Koning-Ward, T.F., et al., *A newly discovered protein export machine in malaria parasites.* Nature, 2009. **459**(7249): p. 945-949.
147. Skottrup, P.D., M. Nicolaisen, and A.F. Justesen, *Towards on-site pathogen detection using antibody-based sensors.* Biosensors and Bioelectronics, 2008.
148. Peluso, P., et al., *Optimizing antibody immobilization strategies for the construction of protein microarrays.* Analytical biochemistry, 2003. **312**(2): p. 113-124.
149. Turner, A.P.F. and S. Piletsky, *Biosensors and Biomimetic Sensors for the Detection of Drugs, Toxins and Biological Agents.* Nato Security Through Science Series B Physics and Biophysics, 2005. **1**: p. 261.

150. Forster, T., *Zwischenmolekulare energiewanderung und fluoreszenz.* Ann. Phys, 1948. **2**(2): p. 55.
151. Frommer, W.B., M.W. Davidson, and R.E. Campbell, *Genetically encoded biosensors based on engineered fluorescent proteins.* Chemical Society Reviews, 2009. **38**(10): p. 2833-2841.
152. Miyawaki, A., et al., *Fluorescent indicators for Ca^{2+} based on green fluorescent proteins and calmodulin.* Nature, 1997. **388**: p. 883.
153. Satishkumar, B.C., et al., *Reversible fluorescence quenching in carbon nanotubes for biomolecular sensing.* Nature Nanotechnology, 2007. **2**(9): p. 560-564.
154. Fournier, C., et al., *EPR spectroscopy analysis of hydrophobically modified dextran-coated polystyrene.* Journal of Colloid and Interface Science, 1998. **198**(1): p. 27-33.
155. Merrifield, R.B., *Solid Phase Peptide Synthesis. I. The Synthesis of a Tetrapeptide.* Journal of the American Chemical Society, 1963. **85**(14): p. 2149-2154.
156. Hermkens, P.H.H., H.C.J. Ottenheijm, and D.C. Rees, *Solid-phase organic reactions II: A review of the literature Nov 95-Nov 96.* Tetrahedron, 1997. **53**(16): p. 5643-5678.
157. Jin, H., D.A. Heller, and M.S. Strano, *Single-Particle Tracking of Endocytosis and Exocytosis of Single-Walled Carbon Nanotubes in NIH-3T3 Cells.* Nano Letters, 2008. **8**(6): p. 1577-1585.
158. Jin, H., et al., *Size-Dependent Cellular Uptake and Expulsion of Single-Walled Carbon Nanotubes: Single Particle Tracking and a Generic Uptake Model for Nanoparticles.* Acs Nano, 2009. **3**(1): p. 149-158.
159. Tsyboulski, D.A., et al., *Translational and Rotational Dynamics of Individual Single-Walled Carbon Nanotubes in Aqueous Suspension.* Acs Nano, 2008. **2**(9): p. 1770-1776.
160. van Bruggen, M.P.B., H.N.W. Lekkerkerker, and J.K.G. Dhont, *Long-time translational self-diffusion in isotropic dispersions of colloidal rods.* Physical Review E, 1997. **56**(4): p. 4394.
161. Boghossian, A.A., et al., *Dynamic and Reversible Self-Assembly of Photoelectrochemical Complexes Based on Lipid Bilayer Disks, Photosynthetic Reaction Centers, and Single-Walled Carbon Nanotubes.* Langmuir, 2011. **27**(5): p. 1599-1609.
162. Usrey, M.L., et al., *Controlling the Electrophoretic Mobility of Single-Walled Carbon Nanotubes: A Comparison of Theory and Experiment.* Langmuir, 2007. **23**(14): p. 7768-7776.
163. Heller, D.A., et al., *Multimodal optical sensing and analyte specificity using single-walled carbon nanotubes.* Nature Nanotechnology, 2008.
164. Gruber, K., et al., *Cantilever Array Sensors Detect Specific Carbohydrate–Protein Interactions with Picomolar Sensitivity.* Acs Nano, 2011. **5**(5): p. 3670-3678.
165. Lin, S. and D. Blankschtein, *Role of the Bile Salt Surfactant Sodium Cholate in Enhancing the Aqueous Dispersion Stability of Single-Walled Carbon Nanotubes: A Molecular Dynamics Simulation Study.* The Journal of Physical Chemistry B, 2010. **114**(47): p. 15616-15625.
166. Choi, J.H. and M.S. Strano, *Solvatochromism in single-walled carbon nanotubes.* Applied Physics Letters, 2007. **90**(22): p. 223114-223114-3.

167. Tummala, N.R. and A. Striolo, *SDS Surfactants on Carbon Nanotubes: Aggregate Morphology.* Acs Nano, 2009. **3**(3): p. 595-602.
168. Xu, Z., X. Yang, and Z. Yang, *A Molecular Simulation Probing of Structure and Interaction for Supramolecular Sodium Dodecyl Sulfate/Single-Wall Carbon Nanotube Assemblies.* Nano Letters, 2010. **10**(3): p. 985-991.
169. Zorbas, V., et al., *Preparation and characterization of individual peptide-wrapped single-walled carbon nanotubes.* J. Am. Chem. Soc, 2004. **126**(23): p. 7222-7227.
170. Scrutton, N.S., A. Berry, and R.N. Perham, *Redesign of the Coenzyme Specificity of a Dehydrogenase by Protein Engineering.* Nature, 1990. **343**(6253): p. 38-43.
171. Lindberg, R.L.P. and M. Negishi, *Alteration of Mouse Cytochrome P450coh Substrate Specificity by Mutation of a Single Amino-acid Residue.* Nature, 1989. **339**(6226): p. 632-634.
172. Ge, X., L. Tolosa, and G. Rao, *Dual-labeled glucose binding protein for ratiometric measurements of glucose.* Anal. Chem, 2004. **76**(5): p. 1403-1410.
173. Mason, C.W., et al., *Recognition, Cointernalization, and Recycling of an Avian Riboflavin Carrier Protein in Human Placental Trophoblasts.* Journal of Pharmacology and Experimental Therapeutics, 2006. **317**(2): p. 465.
174. Rao, P.N., et al., *Elevation of serum riboflavin carrier protein in breast cancer.* Cancer Epidemiology Biomarkers & Prevention, 1999. **8**(11): p. 985.
175. Andersson, B. and R. Hoechl, *Autofluorescence of living cells.* Journal of microscopy, 2002. **191**(1): p. 1-7.
176. Huang, S., M. Phelps, and P. Swaan, *Involvement of endocytic organelles in the subcellular trafficking and localization of riboflavin.* Journal of Pharmacology and Experimental Therapeutics, 2003. **306**(2): p. 681.
177. Heller, D.A., et al., *Peptide secondary structure modulates single-walled carbon nanotube fluorescence as a chaperone sensor for nitroaromatics.* Proceedings of the National Academy of Sciences, 2011.
178. Zhang, J., et al., *Molecular Recognition Using Nanotube-Adsorbed Polymer Assemblies.* **(Submitted)**.
179. Marcus, R.A., *On the Theory of Oxidation-Reduction Reactions Involving Electron Transfer. I.* The Journal of Chemical Physics, 1956. **24**(5): p. 966-978.
180. Marcus, R.A., *Electrostatic Free Energy and Other Properties of States Having Nonequilibrium Polarization. I.* The Journal of Chemical Physics, 1956. **24**(5): p. 979-989.
181. Nair, N., et al., *A Structure–Reactivity Relationship for Single Walled Carbon Nanotubes Reacting with 4-Hydroxybenzene Diazonium Salt.* Journal of the American Chemical Society, 2007. **129**(13): p. 3946-3954.
182. Hilmer, A.J., N. Nair, and M.S. Strano, *A kinetic Monte Carlo analysis for the production of singularly tethered carbon nanotubes.* Nanotechnology, 2010. **21**: p. 495703.
183. Johnson, R.R., A.T.C. Johnson, and M.L. Klein, *The Nature of DNA-Base–Carbon-Nanotube Interactions.* Small, 2010. **6**(1): p. 31-34.
184. Roxbury, D., A. Jagota, and J. Mittal, *Sequence-Specific Self-Stitching Motif of Short Single-Stranded DNA on a Single-Walled Carbon Nanotube.* Journal of the American Chemical Society, 2011. **133**(34): p. 13545-13550.
185. Roxbury, D., S. Manohar, and A. Jagota, *Molecular Simulation of DNA β-Sheet and β-Barrel Structures on Graphite and Carbon Nanotubes.* The Journal of Physical Chemistry C, 2010. **114**(31): p. 13267-13276.

186. Roxbury, D., J. Mittal, and A. Jagota, *Molecular-Basis of Single-Walled Carbon Nanotube Recognition by Single-Stranded DNA.* Nano Letters, 2012. **12**(3): p. 1464-1469.
187. Xiao, Z., et al., *Base- and Structure-Dependent DNA Dinucleotide–Carbon Nanotube Interactions: Molecular Dynamics Simulations and Thermodynamic Analysis.* The Journal of Physical Chemistry C, 2011. **115**(44): p. 21546-21558.
188. Lin, S., et al., *Molecular Insights into the Surface Morphology, Layering Structure, and Aggregation Kinetics of Surfactant-Stabilized Graphene Dispersions.* Journal of the American Chemical Society, 2011. **133**(32): p. 12810-12823.
189. Angelikopoulos, P. and H. Bock, *The Differences in Surfactant Adsorption on Carbon Nanotubes and Their Bundles.* Langmuir, 2009. **26**(2): p. 899-907.
190. Wallace, E.J. and M.S.P. Sansom, *Carbon Nanotube/Detergent Interactions via Coarse-Grained Molecular Dynamics.* Nano Letters, 2007. **7**(7): p. 1923-1928.
191. Shvartzman-Cohen, R., et al., *Aggregation and Self-Assembly of Amphiphilic Block Copolymers in Aqueous Dispersions of Carbon Nanotubes.* Langmuir, 2008. **24**(9): p. 4625-4632.
192. Nativ-Roth, E., et al., *Physical Adsorption of Block Copolymers to SWNT and MWNT: A Nonwrapping Mechanism.* Macromolecules, 2007. **40**(10): p. 3676-3685.
193. Eisenriegler, E., A. Hanke, and S. Dietrich, *Polymers interacting with spherical and rodlike particles.* Physical Review E, 1996. **54**(2): p. 1134-1152.
194. Mondescu, R.P. and M. Muthukumar, *Brownian motion and polymer statistics on certain curved manifolds.* Physical Review E, 1998. **57**(4): p. 4411-4419.
195. Piculell, L., C. Viebke, and P. Linse, *Adsorption of a Flexible Polymer onto a Rigid Rod. A Model Study.* The Journal of Physical Chemistry, 1995. **99**(48): p. 17423-17430.
196. Gurevitch, I. and S. Srebnik, *Monte Carlo simulation of polymer wrapping of nanotubes.* Chemical Physics Letters, 2007. **444**(1–3): p. 96-100.
197. Gurevitch, I. and S. Srebnik, *Conformational behavior of polymers adsorbed on nanotubes.* The Journal of Chemical Physics, 2008. **128**(14): p. 144901-8.
198. Mulqueen, M. and D. Blankschtein, *Prediction of Equilibrium Surface Tension and Surface Adsorption of Aqueous Surfactant Mixtures Containing Ionic Surfactants.* Langmuir, 1999. **15**(26): p. 8832-8848.
199. Werder, T., et al., *On the Water–Carbon Interaction for Use in Molecular Dynamics Simulations of Graphite and Carbon Nanotubes.* The Journal of Physical Chemistry B, 2003. **107**(6): p. 1345-1352.
200. Vanommeslaeghe, K., et al., *CHARMM general force field: A force field for drug-like molecules compatible with the CHARMM all-atom additive biological force fields.* Journal of Computational Chemistry, 2010. **31**(4): p. 671-690.
201. Darve, E., D. Rodriguez-Gomez, and A. Pohorille, *Adaptive biasing force method for scalar and vector free energy calculations.* The Journal of Chemical Physics, 2008. **128**(14): p. 144120-13.
202. Nikas, Y.J., S. Puvvada, and D. Blankschtein, *Surface tensions of aqueous nonionic surfactant mixtures.* Langmuir, 1992. **8**(11): p. 2680-2689.
203. Ray, S., G. Mehta, and S. Srivastava, *Label-free detection techniques for protein microarrays: Prospects, merits and challenges.* PROTEOMICS, 2010. **10**(4): p. 731-748.
204. Hua, S., C. Lebrilla, and H.J. An, *Application of nano-LC-based glycomics towards biomarker discovery.* Bioanalysis, 2011. **3**(22): p. 2573-2585.

205. Roy, P., et al., *Protein mass spectra data analysis for clinical biomarker discovery: a global review.* Briefings in Bioinformatics, 2011. **12**(2): p. 176-186.
206. Larguinho, M. and P.V. Baptista, *Gold and silver nanoparticles for clinical diagnostics — From genomics to proteomics.* Journal of Proteomics, 2012. **75**(10): p. 2811-2823.
207. Hughes, A.J., et al., *Microfluidic integration for automated targeted proteomic assays.* Proceedings of the National Academy of Sciences, 2012. **109**(16): p. 5972-5977.
208. Lundberg, M., et al., *Multiplexed Homogeneous Proximity Ligation Assays for High-throughput Protein Biomarker Research in Serological Material.* Molecular & Cellular Proteomics, 2011. **10**(4).
209. Halfinger, B., et al., *Unmasking low-abundance peptides from human blood plasma and serum samples by a simple and robust two-step precipitation/immunoaffinity enrichment method.* Electrophoresis, 2011. **32**(13): p. 1706-1714.
210. Raamanathan, A., et al., *Programmable Bio-Nano-Chip Systems for Serum CA125 Quantification: Toward Ovarian Cancer Diagnostics at the Point-of-Care.* Cancer Prevention Research, 2012. **5**(5): p. 706-716.
211. Jokerst, J.V., et al., *Location of Biomarkers and Reagents within Agarose Beads of a Programmable Bio-nano-chip.* Small, 2011. **7**(5): p. 613-624.
212. Thomas, D.D., et al., *The biological lifetime of nitric oxide: Implications for the perivascular dynamics of NO and O2.* Proceedings of the National Academy of Sciences of the United States of America, 2001. **98**(1): p. 355-360.
213. Yu, X., D. Xu, and Q. Cheng, *Label-free detection methods for protein microarrays.* PROTEOMICS, 2006. **6**(20): p. 5493-5503.
214. Chang, H.-K., et al., *Rapid, Label-Free, Electrical Whole Blood Bioassay Based on Nanobiosensor Systems.* Acs Nano, 2011. **5**(12): p. 9883-9891.
215. Kim, A., et al., *Direct label-free electrical immunodetection in human serum using a flow-through-apparatus approach with integrated field-effect transistors.* Biosensors and Bioelectronics, 2010. **25**(7): p. 1767-1773.
216. Islam, K., et al., *Microfluidic Biosensor for beta-Amyloid(1-42) Detection Using Cyclic Voltammetry.* Journal of Nanoscience and Nanotechnology, 2011. **11**(7): p. 5657-5662.
217. Loaiza, O.A., et al., *Nanostructured Disposable Impedimetric Sensors as Tools for Specific Biomolecular Interactions: Sensitive Recognition of Concanavalin A.* Analytical Chemistry, 2011. **83**(8): p. 2987-2995.
218. Rohrbach, F., et al., *Label-free impedimetric aptasensor for lysozyme detection based on carbon nanotube-modified screen-printed electrodes.* Analytical Biochemistry, 2012. **421**(2): p. 454-459.
219. Lan, T., et al., *Single particle technique for one-step homogeneous detection of cancer marker using gold nanoparticle probes.* Analyst, 2011. **136**(20): p. 4247-4253.
220. Wangoo, N., et al., *Zeta potential based colorimetric immunoassay for the direct detection of diabetic marker HbA1c using gold nanoprobes.* Chemical Communications, 2010. **46**(31): p. 5755-5757.
221. Cho, H., et al., *Single-Step Nanoplasmonic VEGF165 Aptasensor for Early Cancer Diagnosis.* Acs Nano, 2012. **6**(9): p. 7607-7614.
222. Peng, J., et al., *Calcium Carbonate-Gold Nanocluster Hybrid Spheres: Synthesis and Versatile Application in Immunoassays.* Chemistry-a European Journal, 2012. **18**(17): p. 5261-5268.

223. Peng, J., et al., *Multifunctional Manganese Carbonate Microspheres with Superparamagnetic and Fluorescent Properties: Synthesis and Biological Application.* Chemistry-a European Journal, 2011. **17**(39): p. 10916-10923.
224. Xu, L., et al., *Gold nanorod ensembles as artificial molecules for applications in sensors.* Journal of Materials Chemistry, 2011. **21**(42): p. 16759-16782.
225. Palaniappan, A., et al., *Aligned carbon nanotubes on quartz substrate for liquid gated biosensing.* Biosensors and Bioelectronics, 2010. **25**(8): p. 1989-1993.
226. Star, A., et al., *Electronic Detection of Specific Protein Binding Using Nanotube FET Devices.* Nano Letters, 2003. **3**(4): p. 459-463.
227. Shim, M., et al., *Functionalization of Carbon Nanotubes for Biocompatibility and Biomolecular Recognition.* Nano Letters, 2002. **2**(4): p. 285-288.
228. Chen, R.J., et al., *Noncovalent functionalization of carbon nanotubes for highly specific electronic biosensors.* Proceedings of the National Academy of Sciences, 2003. **100**(9): p. 4984-4989.
229. Vaisocherová, H., et al., *Ultralow Fouling and Functionalizable Surface Chemistry Based on a Zwitterionic Polymer Enabling Sensitive and Specific Protein Detection in Undiluted Blood Plasma.* Analytical Chemistry, 2008. **80**(20): p. 7894-7901.
230. Brault, N.D., et al., *Ultra-low fouling and functionalizable zwitterionic coatings grafted onto SiO2 via a biomimetic adhesive group for sensing and detection in complex media.* Biosensors and Bioelectronics, 2010. **25**(10): p. 2276-2282.
231. Luchini, A., et al., *Smart Hydrogel Particles: Biomarker Harvesting: One-Step Affinity Purification, Size Exclusion, and Protection against Degradation.* Nano Letters, 2007. **8**(1): p. 350-361.
232. de la Escosura-Muñiz, A. and A. Merkoçi, *A Nanochannel/Nanoparticle-Based Filtering and Sensing Platform for Direct Detection of a Cancer Biomarker in Blood.* Small, 2011. **7**(5): p. 675-682.
233. Chen, K.-I., B.-R. Li, and Y.-T. Chen, *Silicon nanowire field-effect transistor-based biosensors for biomedical diagnosis and cellular recording investigation.* Nano Today, 2011. **6**(2): p. 131-154.
234. Silverton, E.W., M.A. Navia, and D.R. Davies, *Three-dimensional structure of an intact human immunoglobulin.* Proceedings of the National Academy of Sciences, 1977. **74**(11): p. 5140-5144.
235. Schoning, M.J. and A. Poghossian, *Recent advances in biologically sensitive field-effect transistors (BioFETs).* Analyst, 2002. **127**(9): p. 1137-1151.
236. Lee, K.-B., et al., *Protein Nanoarrays Generated By Dip-Pen Nanolithography.* Science, 2002. **295**(5560): p. 1702-1705.
237. Ilyas, A., et al., *Electrical detection of cancer biomarker using aptamers with nanogap break-junctions.* Nanotechnology, 2012. **23**(27).
238. Gokhale, A.S., et al., *Serum concentrations of interleukin-8, vascular endothelial growth factor, and epidermal growth factor receptor in patients with squamous cell cancer of the head and neck.* Oral Oncology, 2005. **41**(1): p. 70-76.
239. Vermeeren, V., et al., *Impedimetric, diamond-based immmunosensor for the detection of C-reactive protein.* Sensors and Actuators B: Chemical, 2011. **157**(1): p. 130-138.
240. Moertel Cg, F.T.R.M.J.S.H.D.G.L.J.A.T.C., *AN evaluation of the carcinoembryonic antigen (cea) test for monitoring patients with resected colon cancer.* JAMA: The Journal of the American Medical Association, 1993. **270**(8): p. 943-947.

241. *Centers for Disease Control and Prevention.* Available from: http://www.cdc.gov/heartdisease/facts.htm.
242. Miniño, A.M., *Death in the United States, 2009.* 2011.
243. Katus, H.A., et al., *Intracellular compartmentation of cardiac troponin T and its release kinetics in patients with reperfused and nonreperfused myocardial infarction.* The American Journal of Cardiology, 1991. **67**(16): p. 1360-1367.
244. Apple, F.S., et al., *National Academy of Clinical Biochemistry and IFCC Committee for Standardization of Markers of Cardiac Damage Laboratory Medicine Practice Guidelines: Analytical Issues for Biochemical Markers of Acute Coronary Syndromes.* Clinical Chemistry, 2007. **53**(4): p. 547-551.
245. Kong, T., et al., *CMOS-compatible, label-free silicon-nanowire biosensors to detect cardiac troponin I for acute myocardial infarction diagnosis.* Biosensors & Bioelectronics, 2012. **34**(1): p. 267-272.
246. Billah, M.M., et al., *Directed immobilization of reduced antibody fragments onto a novel SAM on gold for myoglobin impedance immunosensing.* Bioelectrochemistry, 2010. **80**(1): p. 49-54.
247. Choi, D.H., et al., *A dual gold nanoparticle conjugate-based lateral flow assay (LFA) method for the analysis of troponin I.* Biosensors & Bioelectronics, 2010. **25**(8): p. 1999-2002.
248. Ahammad, A.J.S., et al., *Electrochemical Detection of Cardiac Biomarker Troponin I at Gold Nanoparticle-Modified ITO Electrode by Using Open Circuit Potential.* International Journal of Electrochemical Science, 2011. **6**(6): p. 1906-1916.
249. Zhou, F., et al., *Electrochemical Immunosensor for Simultaneous Detection of Dual Cardiac Markers Based on a Poly(Dimethylsiloxane)-Gold Nanoparticles Composite Microfluidic Chip: A Proof of Principle.* Clinical Chemistry, 2010. **56**(11): p. 1701-1707.
250. Qiao, Y., et al., *Enhanced Fluorescence Anisotropy Assay for Human Cardiac Troponin I and T Detection.* Journal of Fluorescence, 2011. **21**(6): p. 2101-2110.
251. Song, S.Y., et al., *A fluoro-microbead guiding chip for simple and quantifiable immunoassay of cardiac troponin I (cTnI).* Biosensors & Bioelectronics, 2011. **26**(9): p. 3818-3824.
252. Bhalla, V., et al., *Gold nanoparticles mediated label-free capacitance detection of cardiac troponin I.* Sensors and Actuators B-Chemical, 2012. **161**(1): p. 761-768.
253. Ren, J., et al., *Increased detection of human cardiac troponin I by a decrease of nonspecific adsorption in diluted self-assembled monolayers.* Applied Surface Science, 2012. **258**(13): p. 5230-5237.
254. Zhang, G.-J., et al., *An integrated chip for rapid, sensitive, and multiplexed detection of cardiac biomarkers from fingerprick blood.* Biosensors & Bioelectronics, 2011. **28**(1): p. 459-463.
255. Shen, W., et al., *Nanoparticle-based electrochemiluminescence immunosensor with enhanced sensitivity for cardiac troponin I using N-(aminobutyl)-N-(ethylisoluminol)-functionalized gold nanoparticles as labels.* Biosensors & Bioelectronics, 2011. **27**(1): p. 18-24.
256. Yeom, S.-H., et al., *Nanoporous aluminum anodic oxide-based optical biosensor for real-time detection of Troponin T.* 2011 Ieee Sensors. 2011. 288-291.
257. Aslan, K. and T.A.J. Grell, *Rapid and Sensitive Detection of Troponin I in Human Whole Blood Samples by Using Silver Nanoparticle Films and Microwave Heating.* Clinical Chemistry, 2011. **57**(5): p. 746-752.

258. Bruls, D.M., et al., *Rapid integrated biosensor for multiplexed immunoassays based on actuated magnetic nanoparticles.* Lab on a Chip, 2009. **9**(24): p. 3504-3510.
259. Dittmer, W.U., et al., *Rapid, high sensitivity, point-of-care test for cardiac troponin based on optomagnetic biosensor.* Clinica Chimica Acta, 2010. **411**(11-12): p. 868-873.
260. Lee, J., et al., *Sensitive and Simultaneous Detection of Cardiac Markers in Human Serum Using Surface Acoustic Wave Immunosensor.* Analytical Chemistry, 2011. **83**(22): p. 8629-8635.
261. Feng, L.-N., et al., *Ultrasensitive multianalyte electrochemical immunoassay based on metal ion functionalized titanium phosphate nanospheres.* Analytical Chemistry, 2012. **84**(18): p. 7810-5.
262. Qiao, Y., et al., *Enhanced Fluorescence Anisotropy Assay for Human Cardiac Troponin I and T Detection.* Journal of Fluorescence, 2011. **21**(6): p. 2101-2110.
263. Kar, P., et al., *Ultrahigh sensitivity assays for human cardiac troponin I using TiO2 nanotube arrays.* Lab on a Chip, 2012. **12**(4).
264. Jin, H., et al., *Stochastic analysis of stepwise fluorescence quenching reactions on single-walled carbon nanotubes: single molecule sensors.* Nano letters, 2008. **8**(12): p. 4299-4304.
265. Ahn, J.-H., et al., *Label-Free, Single Protein Detection on a Near-Infrared Fluorescent Single-Walled Carbon Nanotube/Protein Microarray Fabricated by Cell-Free Synthesis.* Nano Letters, 2011. **11**(7): p. 2743-2752.
266. Hochuli, E., et al., *Genetic Approach to Facilitate Purification of Recombinant Proteins with a Novel Metal Chelate Adsorbent.* Nat Biotech, 1988. **6**(11): p. 1321-1325.
267. Paul N, H., *Purification of His-Tag fusion proteins from Escherichia coli.* Trends in Biochemical Sciences, 1995. **20**(7): p. 285-286.
268. Mao, S.R., W. Sun, and T. Kissel, *Chitosan-based formulations for delivery of DNA and siRNA.* Advanced Drug Delivery Reviews, 2010. **62**(1): p. 12-27.
269. Orelma, H., et al., *Modification of Cellulose Films by Adsorption of CMC and Chitosan for Controlled Attachment of Biomolecules.* Biomacromolecules, 2011. **12**(12): p. 4311-4318.
270. Kumar, S., J. Aaron, and K. Sokolov, *Directional conjugation of antibodies to nanoparticles for synthesis of multiplexed optical contrast agents with both delivery and targeting moieties.* Nat. Protocols, 2008. **3**(2): p. 314-320.
271. Cayot, P. and G. Tainturier, *The Quantification of Protein Amino Groups by the Trinitrobenzenesulfonic Acid Method: A Reexamination.* Analytical Biochemistry, 1997. **249**(2): p. 184-200.
272. Urbanczyk, G.W. and B. Lipp-Symonowicz, *The influence of processing terms of chitosan membranes made of differently deacetylated chitin on the crystalline structure of membranes.* Journal of Applied Polymer Science, 1994. **51**(13): p. 2191-2194.
273. Schwellnus, M.P., et al., *Serum electrolyte concentrations and hydration status are not associated with exercise associated muscle cramping (EAMC) in distance runners.* British Journal of Sports Medicine, 2004. **38**(4): p. 488-492.
274. Lowe, G., et al., *Relation between extent of coronary artery disease and blood viscosity.* British Medical Journal, 1980. **280**(6215): p. 673-674.
275. Gregory, S., *Physical properties of glycerine.* 1991: Marcel Dekker: New York.
276. Brege, J.J., C. Gallaway, and A.R. Barron, *Fluorescence Quenching of Single-Walled Carbon Nanotubes in SDBS Surfactant Suspension by Metal Ions:*

Quenching Efficiency as a Function of Metal and Nanotube Identity†. The Journal of Physical Chemistry C, 2007. **111**(48): p. 17812-17820.

277. Brege, J.J., C. Gallaway, and A.R. Barron, *Fluorescence Quenching of Single-Walled Carbon Nanotubes with Transition-Metal Ions.* The Journal of Physical Chemistry C, 2009. **113**(11): p. 4270-4276.
278. Long, R.D., et al., *Comparison of zwitterionic N-alkylaminomethanesulfonic acids to related compounds in the Good buffer series.* Beilstein journal of organic chemistry, 2010. **6**.
279. Chu, Y., et al., *pH-induced swelling kinetics of polyelectrolyte hydrogels.* Journal of Applied Polymer Science, 1995. **58**(12): p. 2161-2176.
280. Kielland, J., *Individual Activity Coefficients of Ions in Aqueous Solutions.* Journal of the American Chemical Society, 1937. **59**(9): p. 1675-1678.
281. Safronov, A.P. and A.Y. Zubarev, *Flory–Huggins parameter of interaction in polyelectrolyle solutions of chitosan and its alkylated derivative.* Polymer, 2002. **43**(3): p. 743-748.
282. Huai-min, G. and C. Xian-su, *Study of cobalt(II)-chitosan coordination polymer and its catalytic activity and selectivity for vinyl monomer polymerization.* Polymers for Advanced Technologies, 2004. **15**(1-2): p. 89-92.
283. Davidovich-Pinhas, M. and H. Bianco-Peled, *A quantitative analysis of alginate swelling.* Carbohydrate Polymers, 2010. **79**(4): p. 1020-1027.
284. Sen, F., et al., *Observation of Oscillatory Surface Reactions of Riboflavin, Trolox and Singlet Oxygen using Single Carbon Nanotube Fluorescence Spectroscopy.* Acs Nano, 2012.
285. ANA2, *American Cancer Society. Cancer Facts & Figures; http://www.cancer.org/downloads/STT/2008CAFFfinalsecured.pdf.*
286. Vestergaard, M., et al., *An Overview of Label-free Electrochemical Protein Sensors.* Sensors, 2007. **7**(12): p. 3442-3458.

Appendix A: Comparison between Effectiveness of Step-finding Algorithm on both the Control Trace and the Trace That is Subjected to NO

Both algorithms (HMM-based and Chi-squared error-minimizing methods) fail when applied to control data in which there are no actual transitions, fitting steps within the noise (Figure Appendix A). We attempted to subject each trace to a noise reduction program based on reference[108] before applying HMM or error-minimizing step-finding algorithms, but the over-fitting of noise on control data persisted (Figure Appendix A). We therefore concluded that these algorithms cannot be utilized on traces containing no authentic transitions. To resolve this issue, we first determine which traces contain actual transitions in fluorescence intensity and perform the analysis only on these data sets. The relatively high signal-to-noise ratio in the data aids in this, and bias is minimized through randomizing all traces prior to analysis (Figure Appendix B). And the step-fitting algorithm is applied thereafter only to traces that contain transitions`, and zero-transitions are assigned to the remainder.

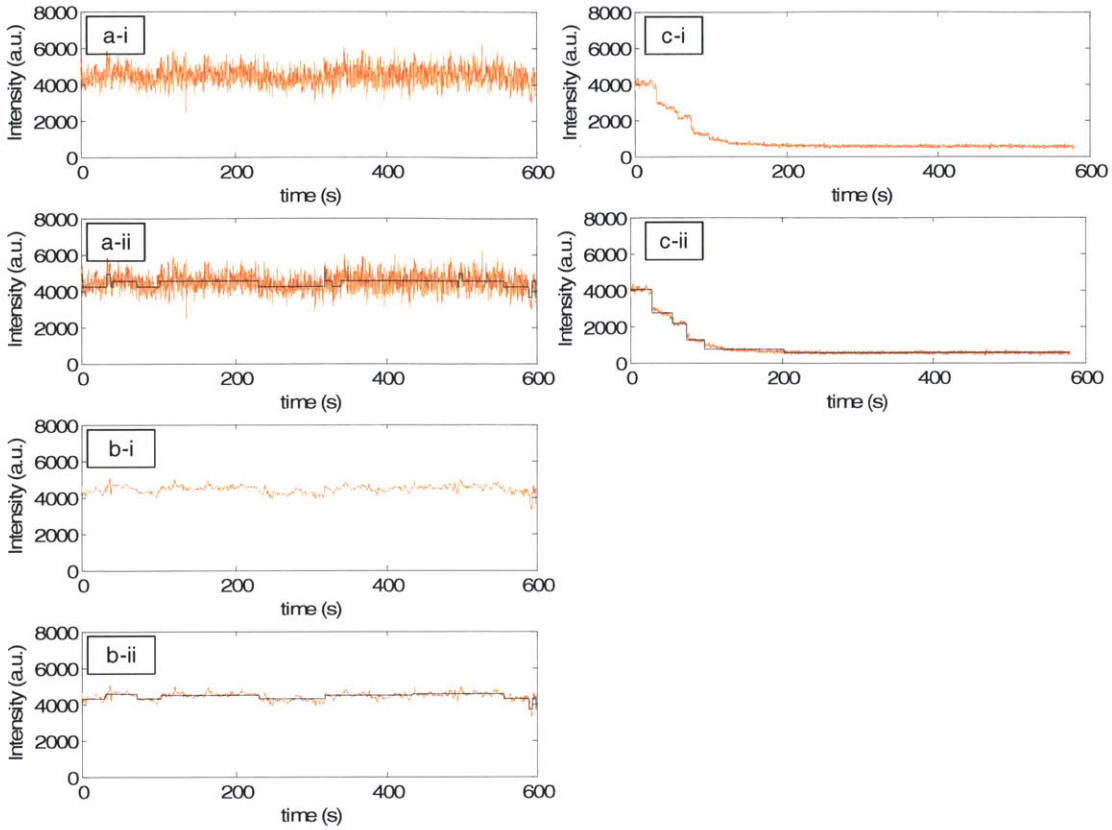

Figure Appendix A Comparison between the effectiveness of applying the Chi-squared error-minimizing step-finding algorithm on the control data and the data where NO is added. (**a**) Time-trace of a diffraction limited spot (2x2 pixel) in a control experiment where no analytes are added (red) and fitted trace (Chi-squared error-minimizing step-finding algorithm, black). Over-fitting on noise is observed. (**b**) Time-trace after applying noise-reduction algorithm on the time-trace in (**a**) (red), and fitted steps on the noise-reduced trace (black). Over-fitting on noise is observed. (**c**) Time-trace of a diffraction limited spot (2x2 pixel) in an experiment where 25 μM NO is added (red) and fitted trace (Chi-squared error-minimizing step-finding algorithm, black) without applying the noise-reduction method. It appears that the intensity fluctuation is more obvious in the control dataset compared to the dataset of which the array is exposed to NO even for the same starting SWNT intensity. We are still investigating the source of this fluctuation.

Appendix B: Intensity Time-traces of 50 Brightest SWNT Upon Exposure to Different Concentrations of NO Ranging from 0 to 20 μM.

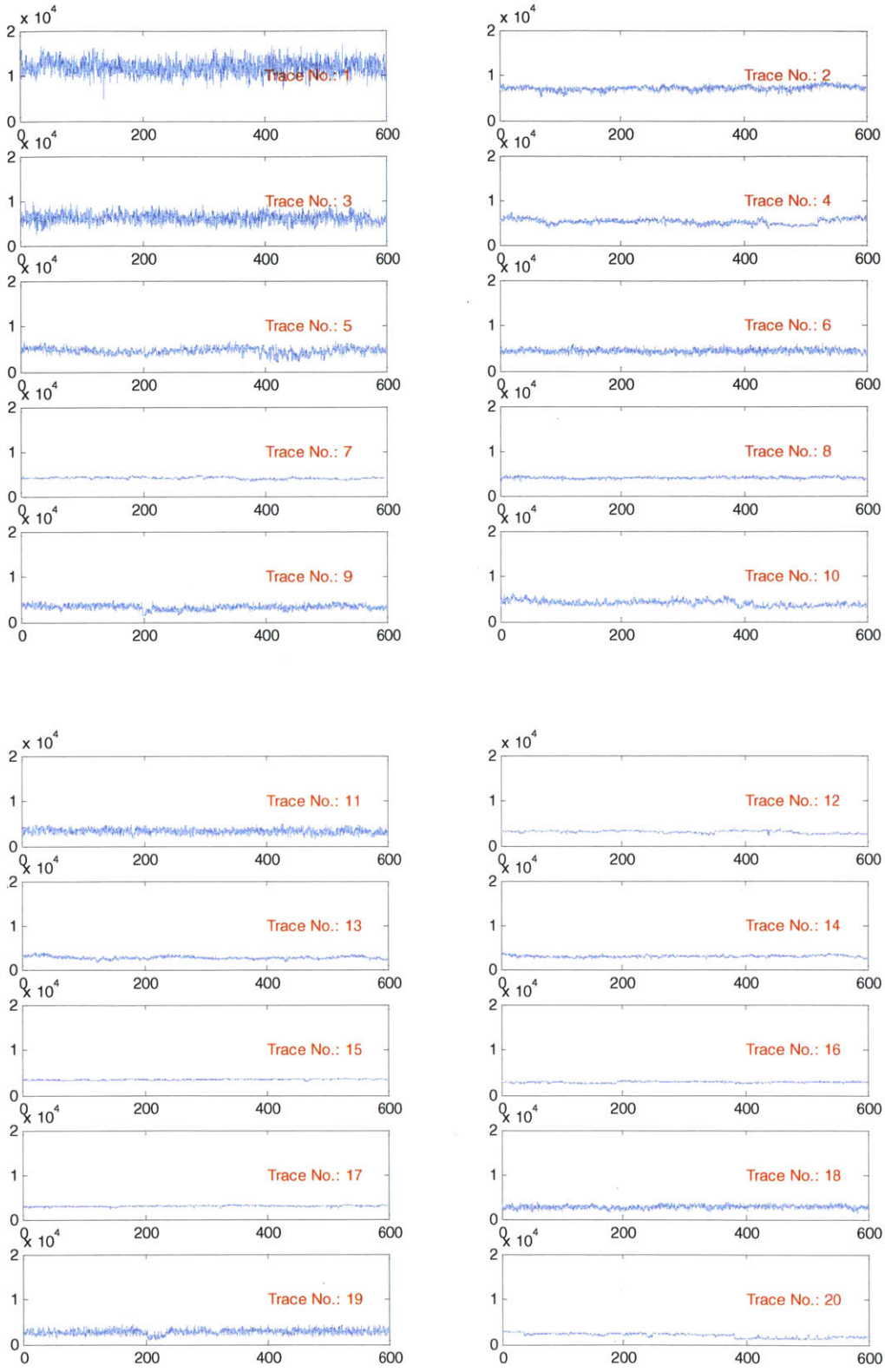
x 10^4
Trace No.: 1
Trace No.: 2
Trace No.: 3
Trace No.: 4
Trace No.: 5
Trace No.: 6
Trace No.: 7
Trace No.: 8
Trace No.: 9
Trace No.: 10
Trace No.: 11
Trace No.: 12
Trace No.: 13
Trace No.: 14
Trace No.: 15
Trace No.: 16
Trace No.: 17
Trace No.: 18
Trace No.: 19
Trace No.: 20
0
200
400
600
1
2


x 10^4
Trace No.: 21
Trace No.: 22
Trace No.: 23
Trace No.: 24
Trace No.: 25
Trace No.: 26
Trace No.: 27
Trace No.: 28
Trace No.: 29
Trace No.: 30
Trace No.: 31
Trace No.: 32
Trace No.: 33
Trace No.: 34
Trace No.: 35
Trace No.: 36
Trace No.: 37
Trace No.: 38
Trace No.: 39
Trace No.: 40
0
200
400
600
1
2

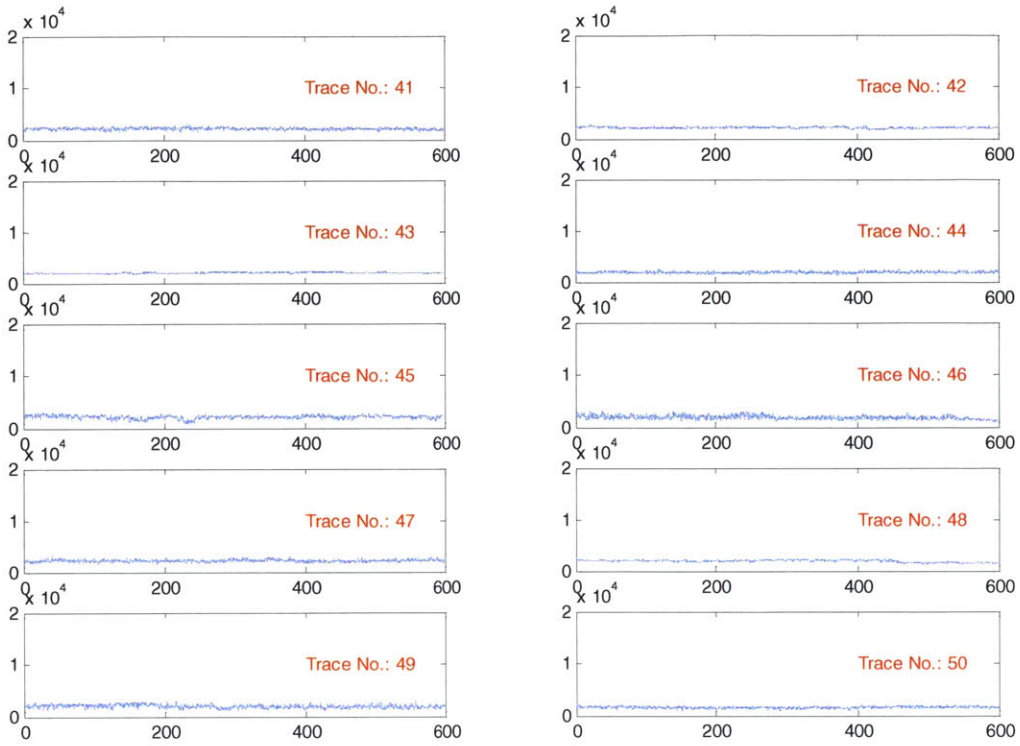

Figure Appendix B1 Fluorescence time traces of the 50 brightest diffraction limited spots (2x2 pixels) in a control experiment in which no NO is added. The trace images are displayed in a descending order of the starting fluorescence intensity. Traces of number 1,2,3,4,5,6,7,8,10,11,13,14,15,16,17,18,22,23,26,27,28,29,30,31,32,33,34,35,36,37,38,39, 40,41,42,43,44,46,47,48,49,50 are identified as zero-transitions.


x 10^4
Trace No.: 1
Trace No.: 2
Trace No.: 3
Trace No.: 4
Trace No.: 5
Trace No.: 6
Trace No.: 7
Trace No.: 8
Trace No.: 9
Trace No.: 10
Trace No.: 11
Trace No.: 12
Trace No.: 13
Trace No.: 14
Trace No.: 15
Trace No.: 16
Trace No.: 17
Trace No.: 18
Trace No.: 19
Trace No.: 20
0
200
400
600
1
2


x 10^4
Trace No.: 21
Trace No.: 22
Trace No.: 23
Trace No.: 24
Trace No.: 25
Trace No.: 26
Trace No.: 27
Trace No.: 28
Trace No.: 29
Trace No.: 30
Trace No.: 31
Trace No.: 32
Trace No.: 33
Trace No.: 34
Trace No.: 35
Trace No.: 36
Trace No.: 37
Trace No.: 38
Trace No.: 39
Trace No.: 40
0
200
400
600
1
2

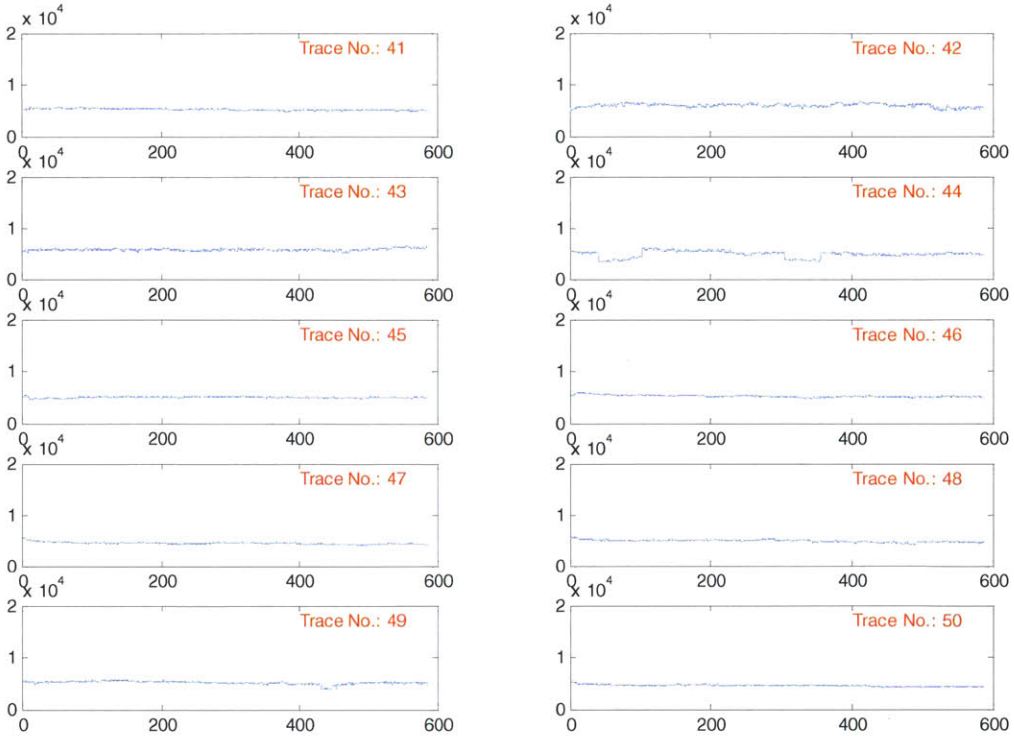

Figure Appendix B2 Fluorescence time traces of the 50 brightest diffraction limited spots (2x2 pixels) upon exposure to NO solution (0.16 μM, 1x PBS) at t = 0 s. The trace images are displayed in a descending order of the starting fluorescence intensity. Traces of number 4,5,7,10,11,12,17,18,21,25,27,29,30,32,33,34,35,36,37,41,42,43,46,47,48,50 are identified as zero-transitions.

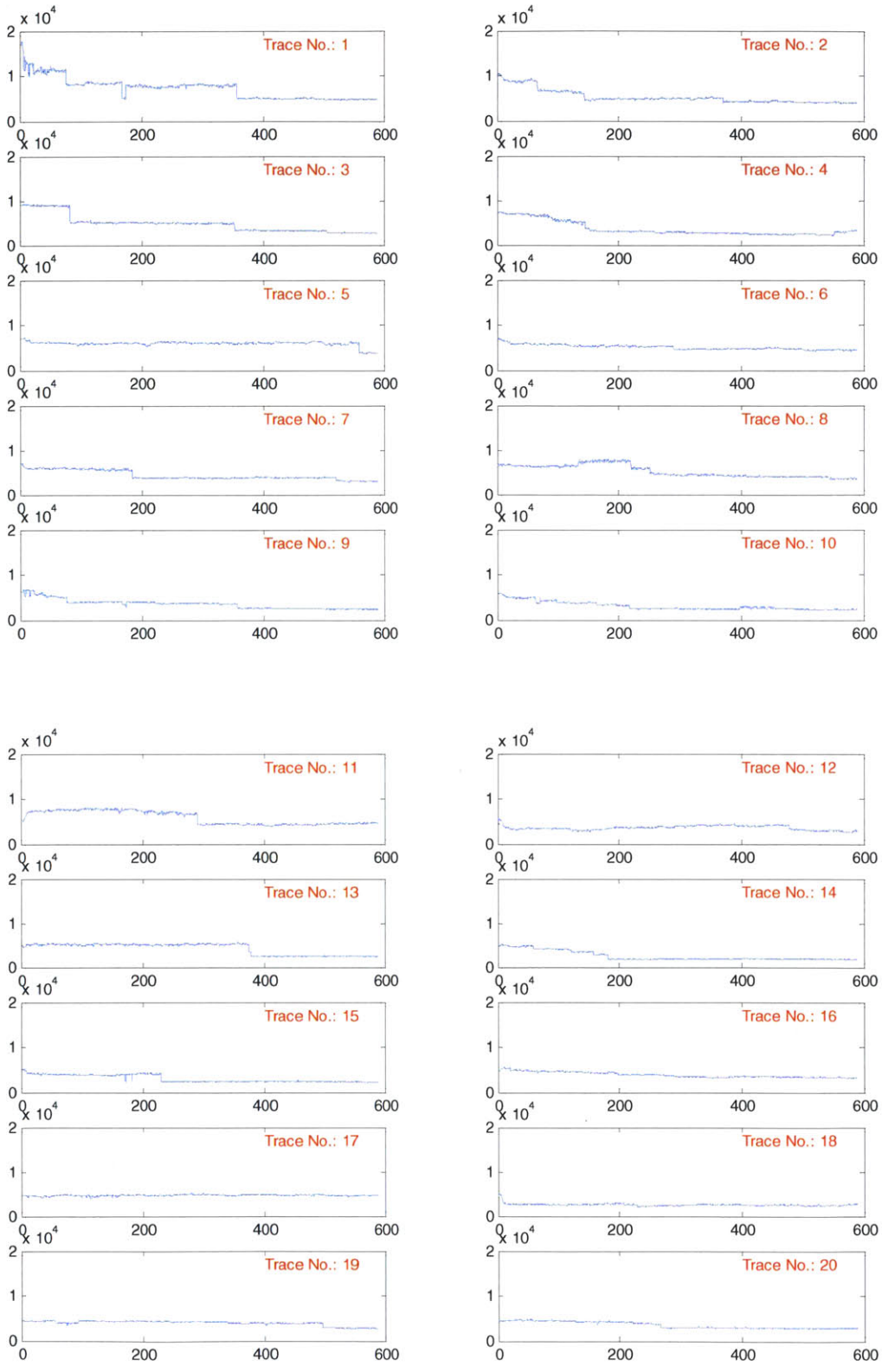
x 10^4
Trace No.: 1
Trace No.: 2
Trace No.: 3
Trace No.: 4
Trace No.: 5
Trace No.: 6
Trace No.: 7
Trace No.: 8
Trace No.: 9
Trace No.: 10
Trace No.: 11
Trace No.: 12
Trace No.: 13
Trace No.: 14
Trace No.: 15
Trace No.: 16
Trace No.: 17
Trace No.: 18
Trace No.: 19
Trace No.: 20
0
200
400
600
1
2

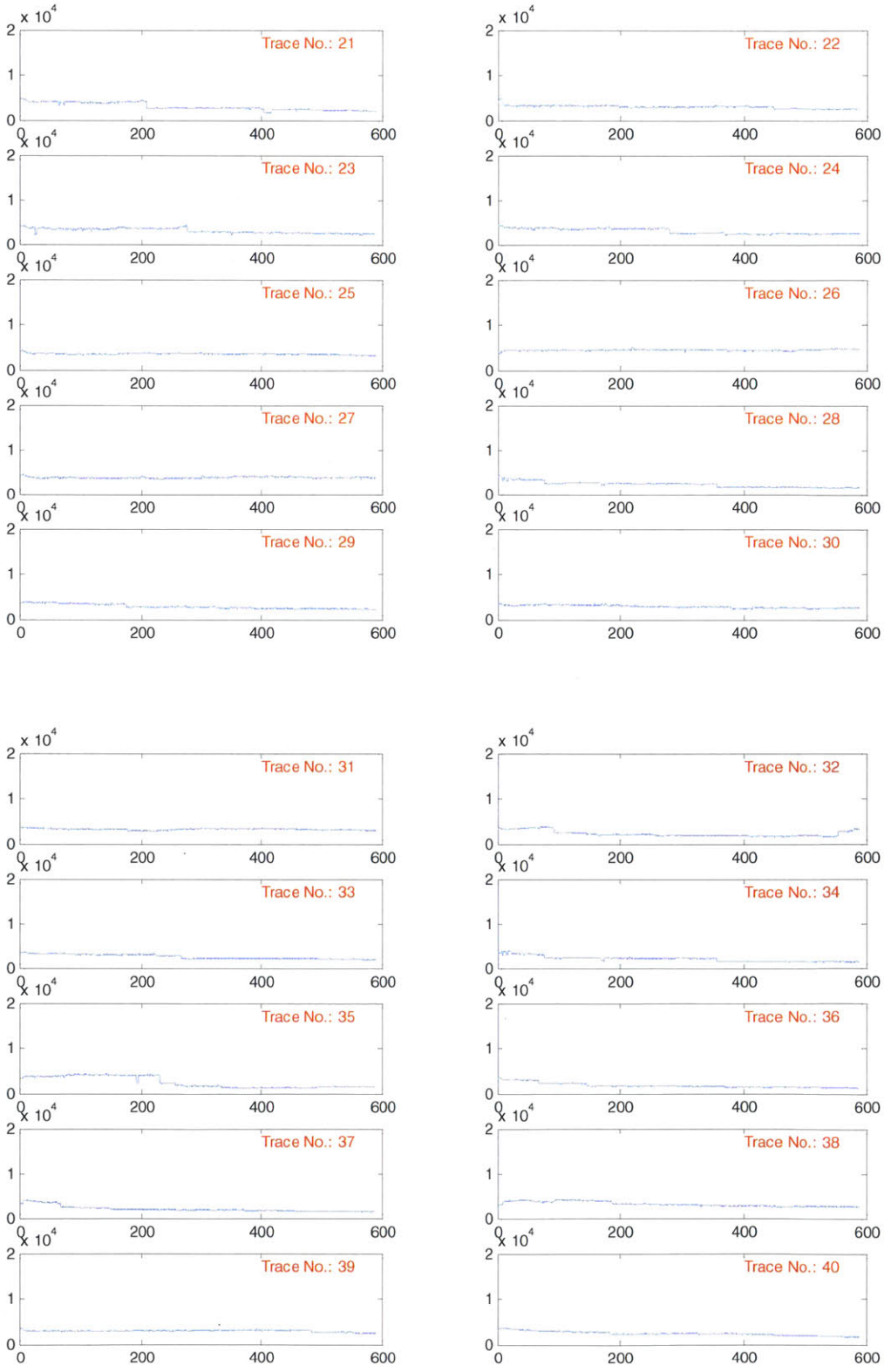
x 10^4
Trace No.: 21
Trace No.: 22
Trace No.: 23
Trace No.: 24
Trace No.: 25
Trace No.: 26
Trace No.: 27
Trace No.: 28
Trace No.: 29
Trace No.: 30
Trace No.: 31
Trace No.: 32
Trace No.: 33
Trace No.: 34
Trace No.: 35
Trace No.: 36
Trace No.: 37
Trace No.: 38
Trace No.: 39
Trace No.: 40
0
1
2
200
400
600

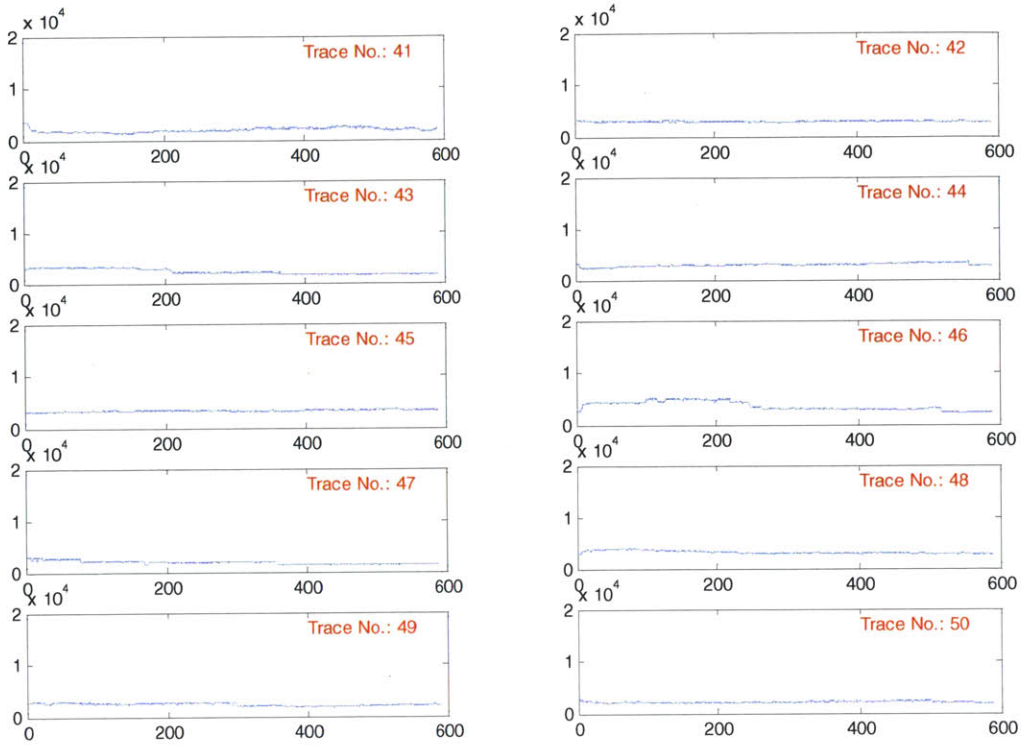

Figure Appendix B3 Fluorescence time traces of the 50 brightest diffraction limited spots (2x2 pixels) upon exposure to NO solution (0.78 μM, 1x PBS) at t = 0 s. The trace images are displayed in a descending order of the starting fluorescence intensity. Traces of number of 17, 25,26,27,31,42,45,48,50 are identified as zero-transitions.

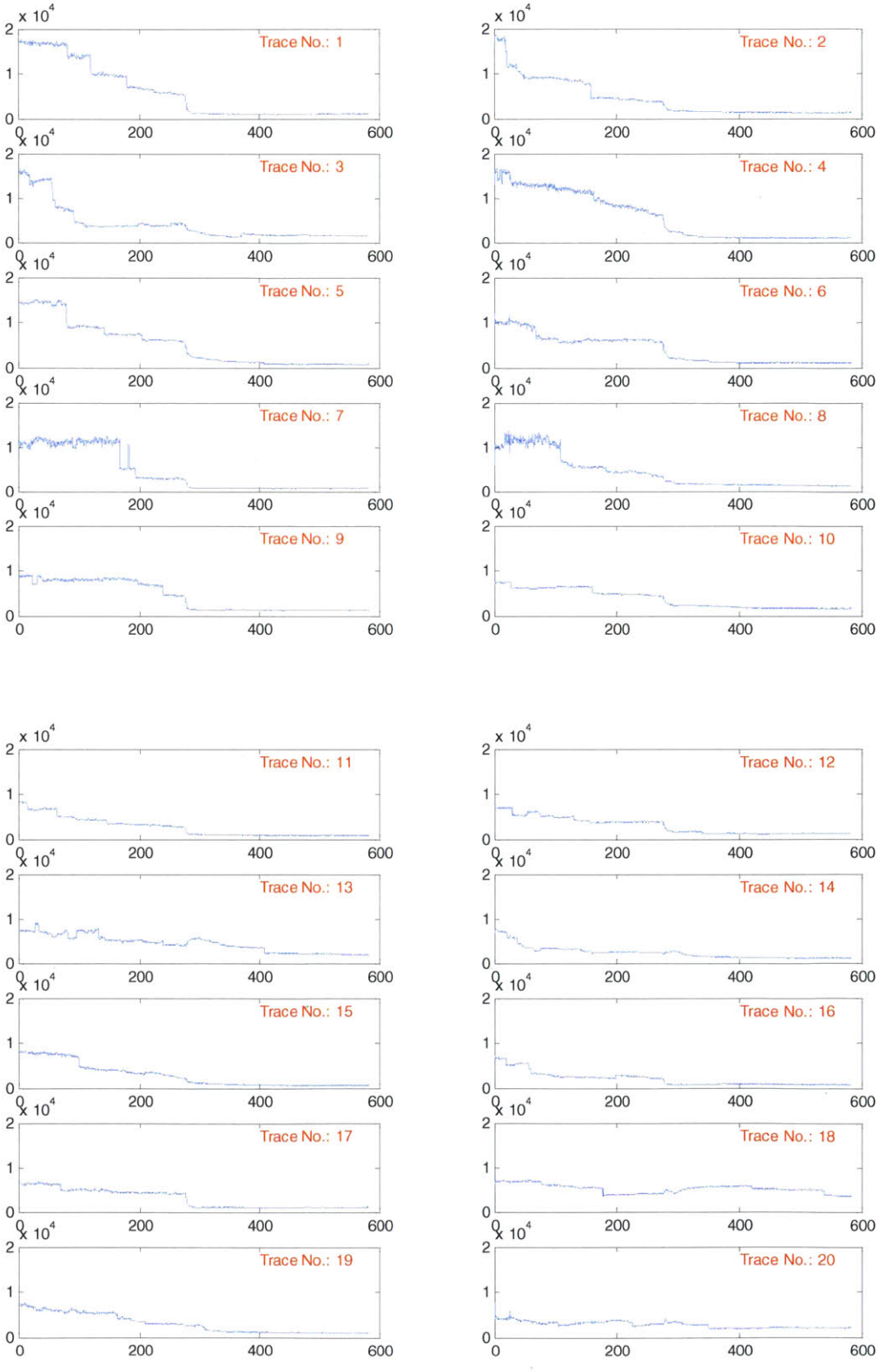
x 10^4
Trace No.: 1
Trace No.: 2
Trace No.: 3
Trace No.: 4
Trace No.: 5
Trace No.: 6
Trace No.: 7
Trace No.: 8
Trace No.: 9
Trace No.: 10
Trace No.: 11
Trace No.: 12
Trace No.: 13
Trace No.: 14
Trace No.: 15
Trace No.: 16
Trace No.: 17
Trace No.: 18
Trace No.: 19
Trace No.: 20
0
1
2
200
400
600

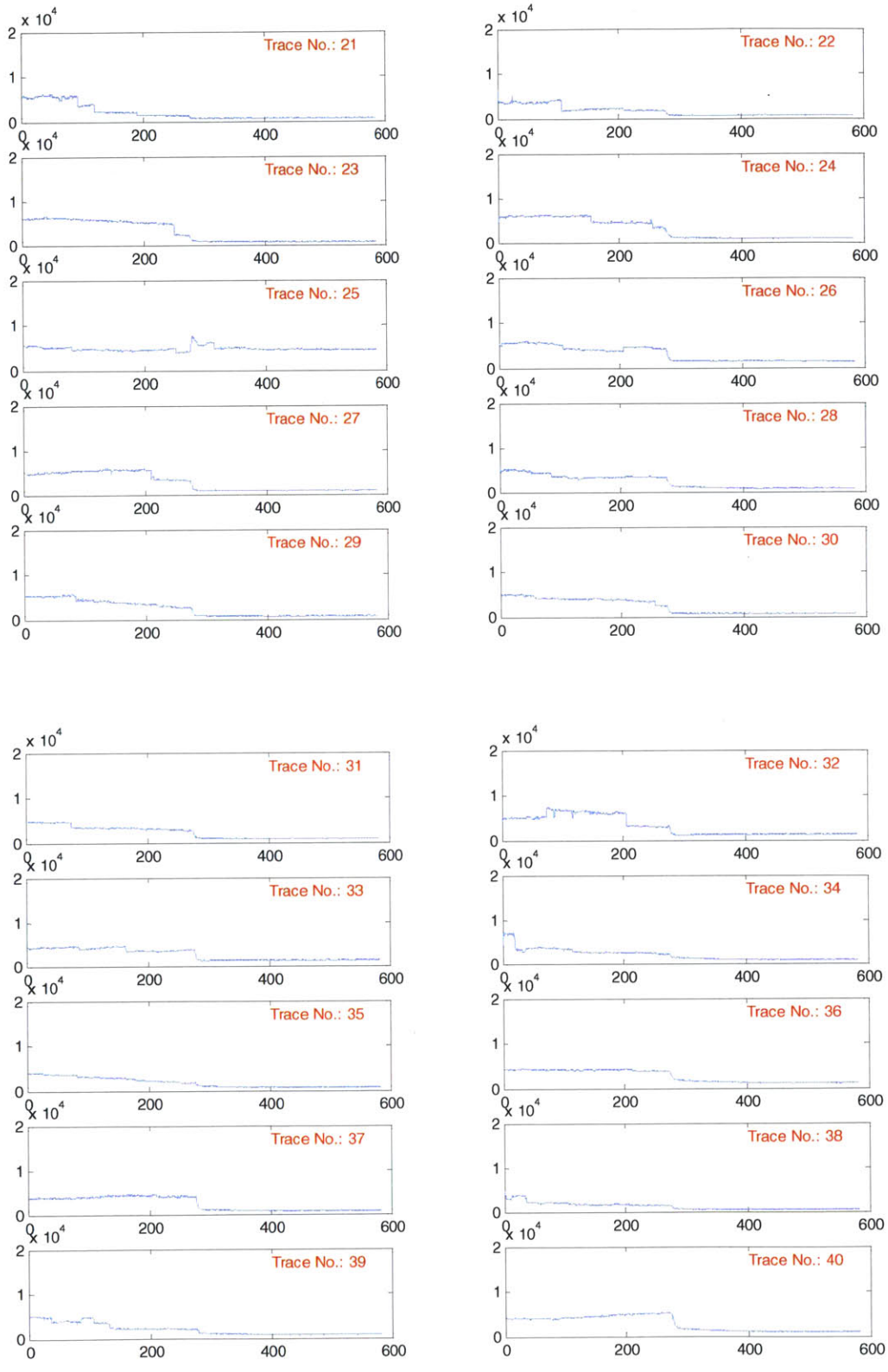
x 10^4
Trace No.: 21
Trace No.: 22
Trace No.: 23
Trace No.: 24
Trace No.: 25
Trace No.: 26
Trace No.: 27
Trace No.: 28
Trace No.: 29
Trace No.: 30
Trace No.: 31
Trace No.: 32
Trace No.: 33
Trace No.: 34
Trace No.: 35
Trace No.: 36
Trace No.: 37
Trace No.: 38
Trace No.: 39
Trace No.: 40
0
200
400
600
1
2

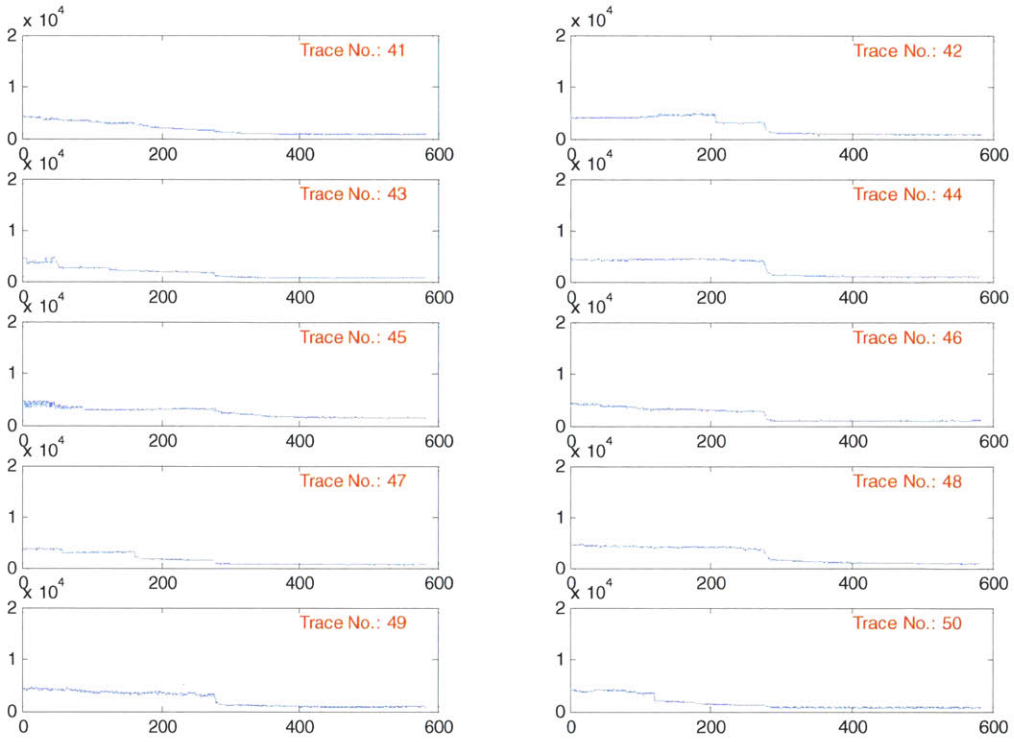

Figure Appendix B4 Fluorescence time traces of the 50 brightest diffraction limited spots (2x2 pixels) upon exposure to NO solution (3.9 μM, 1x PBS) at t = 0 s. The trace images are displayed in a descending order of the starting fluorescence intensity. Each trace contains at least one transition.


x 10^4
Trace No.: 1
Trace No.: 2
Trace No.: 3
Trace No.: 4
Trace No.: 5
Trace No.: 6
Trace No.: 7
Trace No.: 8
Trace No.: 9
Trace No.: 10
Trace No.: 11
Trace No.: 12
Trace No.: 13
Trace No.: 14
Trace No.: 15
Trace No.: 16
Trace No.: 17
Trace No.: 18
Trace No.: 19
Trace No.: 20
0
200
400
600
1
2


x 10^4
Trace No.: 21
Trace No.: 22
Trace No.: 23
Trace No.: 24
Trace No.: 25
Trace No.: 26
Trace No.: 27
Trace No.: 28
Trace No.: 29
Trace No.: 30
Trace No.: 31
Trace No.: 32
Trace No.: 33
Trace No.: 34
Trace No.: 35
Trace No.: 36
Trace No.: 37
Trace No.: 38
Trace No.: 39
Trace No.: 40
0
200
400
600
1
2

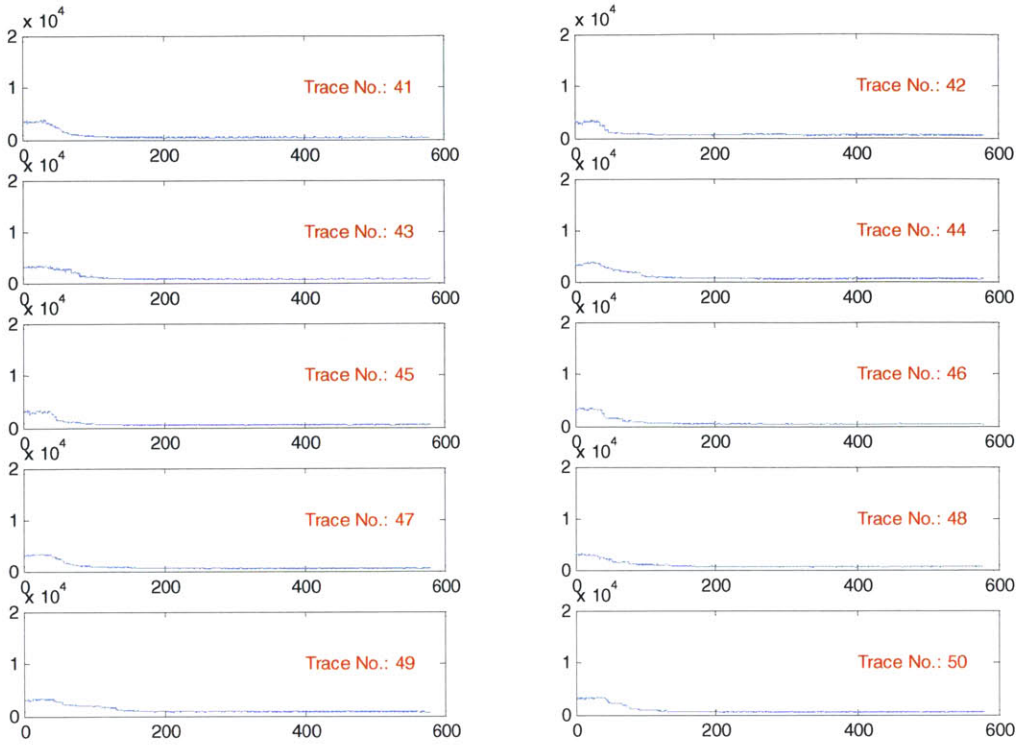

Figure Appendix B5 Fluorescence time traces of the 50 brightest diffraction limited spots (2x2 pixels) upon exposure to NO solution (19.4 μM, 1x PBS) at t = 0 s. The trace images are displayed in a descending order of the starting fluorescence intensity. Each trace contains at least one transition.

Appendix C: Birth-and-death Markov Model

```
% If the input is empty, Prompt user to select col_SWNT.xls;
% Otherwise, input can be provided by another program which calls this
% program.
Program_PathName = pwd;  %Program directory

if isempty(varargin)

    [FileName, PathName] = uigetfile('*.txt', 'Select
SWNTcoordinates.txt from Step 1 (SWNTImages folder)');
    cd(PathName);
    SWNTcoordinates = load([PathName FileName]);
    col_SWNT = SWNTcoordinates(2,:);
    row_SWNT = SWNTcoordinates(1,:);

    %Prompt user to select folder containing corresponding *.dat files
    [FileName, PathName_dat] = uigetfile('*.dat', 'Select any of the
original *.dat files (from Step 1)');
    cd(PathName_dat);

    %Prompt user to select folder containing dwell files to convert to
rate constants
    [FileName, PathName] = uigetfile('*dwell.dat', 'Select any
*dwell.dat file in the directory of interest');
    cd(PathName_dat);

    %Prompt user to find the number of states for eacht trace
%     [FileName_states, PathName_states] = uigetfile('*.txt', 'Select
NumofStates.txt from Step 2');
%     NumofStates = load([PathName_states FileName_states]);
%     cd(PathName_dat);

    % observation time
    a = textread(fullfile(PathName_dat,'1.dat'));
    [m,n] = size(a);
    exposure = a(2,1) - a(1,1);
    varargin1 = m*exposure;

else

    %Read in input filenames/directories
    FileName = varargin[32];
    PathName_coordinate = varargin[285];
    SWNTcoordinates = load(fullfile(PathName_coordinate,FileName));
    col_SWNT = SWNTcoordinates(2,:);
    row_SWNT = SWNTcoordinates(1,:);
    PathName_dat  = varargin[286];
    PathName      = varargin{4};
    varargin1 = varargin{5}; % observation time
    % NumofStates = [];  % We dont work with # of states in this case.
```

```
end

%Calculate rate constants using the *dwell.dat files in selected
directory
calculateRate(PathName, row_SWNT, col_SWNT, PathName_dat, varargin1);

return;

%% ------------------------ CALCULATE RATE ---------------------------
----
function [] = calculateRate(PathName, row_SWNT, col_SWNT, PathName_dat,
varargin)

%This function calculates the rate constant for each SWNT trace and
plots
%it on the image map

%Calculate rate constants from *log.dat files
Output = Cal_BDMarkov(PathName,PathName_dat, varargin);


%Save rate constant results as text file
f1 = fopen([PathName 'BirthDeath_RateandStates_SepTrace.txt'], 'w+');
fprintf(f1, '%s        %s        %s\r\n', 'State', 'ForwardRate',
'ReverseRate');
fprintf(f1, '%f     %e     %e\r\n', Output');
fclose(f1);

%For each trace number, summarize number of states and rate constants
summary1 = zeros(length(row_SWNT),6);
for i =1:1:length(row_SWNT)

    %Find indices of corresponding SWNT
    row_index = row_SWNT(i);
    col_index = col_SWNT(i);

    %Summarize Output for method 1
    summary1(i,1) = i;
    summary1(i,2) = col_index;
    summary1(i,3) = row_index;
    summary1(i,4) = Output(i,1);  % state number
    summary1(i,5) = Output(i,2);  % forward rate
    summary1(i,6) = Output(i,3);  % reverse rate

end

if ~isempty(varargin)
    f1 =
fopen(fullfile(PathName,['BirthDeath_ResultsSummary_SepTrace_',num2str(
varargin{1}),'s.txt']), 'w+');
else
    f1 = fopen([PathName 'BirthDeath_ResultsSummary_SepTrace.txt'],
'w+');
```

```
end
fprintf(f1, '%s  %s  %s  %s  %s  %s\r\n', 'TraceNumber', 'x(column)
Coordinate', 'y(row) Coordinate', 'NumberofStates', 'ForwardRate',
'ReverseRate');
fprintf(f1, '%f     %f     %f     %f     %e     %e\r\n', summary1');
fclose(f1);

return;

%% ---------------------- CALCULATE rf, rr from BIRTHDEATH PROCESS ----
----------------------
function Output = Cal_BDMarkov(PathName,PathName_dat, varargin)

% Obtain names of the dwell files under the folder.
locate_dwell_orig = dir(fullfile(PathName,'*dwell.dat'));
dwelldirs = {locate_dwell_orig.name}';
nofiles = size(dwelldirs, 1);
Output = zeros(nofiles,3);

for mm = 1: nofiles
    dwell = textread([PathName num2str(mm) 'dwell.dat']);
    dat = textread([PathName_dat num2str(mm) '.dat']);
    exposure = dat(2,1) - dat(1,1);
    fitdata = convert_dwelldata_to_fitdata(dwell,dat); % Obtain fitted
data from dwell files.
    time = dat(:,1);
    [rf,rr,state] = BirthDeathEstimate(dwell, fitdata, time, dat,
exposure,  varargin);
    Output(mm,:) = [state,rf,rr];
end

Output;
a = 1


function [rf,rr,state] = BirthDeathEstimate(dwell, fitdata, time, dat,
exposure, varargin)
% varargin{1}: obs_time, which is the observation time, different from
% simulation time.
Xnt = fitdata;

% If remove datapints from the end of the traces ----------
if ~isempty(varargin)
    temp = varargin{1};
    obs_time = temp{1}{1};
    temp2 = Xnt(1:round(obs_time/exposure));
    Xnt = temp2;
    temp3 = time(1:round(obs_time/exposure));
    time = temp3;
    clear temp temp2 temp3
end
% If ends ------------------------------------------------

tau = time(2) - time(1);
```

```
std_est = std(dat(1:50,3))/1000; % estimate the first 300 frames' std
std_est = 0;

method = 2;

if method == 1

    if ~isempty(find(Xnt ==0))
        ind1 = find(Xnt==0);  % find Xnt = 0
        ind2 = find(Xnt(ind1-1)~=0);  % among the Xnt =0 ,find the
Xnt(index-1) isnt 0.
        ind3 = ind1(ind2);
        if ind3(end) ~= length(Xnt)
            offspring_0 = Xnt(ind3);  % these should be zeros and the
number before those zeros should be non-zero.
            Ct = numel(ind3);
        else
            Ct = max(numel(ind3)-1,1); % eliminate C_tau, but Ct has to
be greater than 1.
        end
    else
        Ct = 1;
    end

    SumXnt = sum(Xnt(1:1:end-1));
    alpha = Ct/SumXnt;
    beta = (Xnt(end) - Xnt(1) + Ct)/sum(Xnt(2:1:end));
    mu = log((alpha-1)/(beta-1))/tau/(beta/alpha-1);
    lamda = beta/alpha * mu;

elseif method == 2

    [num_rows1, num_cols1] = size(dwell);
    Bt = 0;
    Dt = 0;
    for k = 1:1:num_rows1
        temp = cumsum(dwell(1:k,3));
        if temp(end) <= length(Xnt);
            if abs(dwell(k,1) - dwell(k,2)) > 1.5*std_est
                if dwell(k,1)< dwell(k,2)
                    Bt = Bt + dwell(k,2) - dwell(k,1);  % if it is a
birth
                else
                    Dt = Dt + dwell(k,1) - dwell(k,2);  % if it is a
birth
                end
            end
        end
    end
    St = trapz(time,Xnt');
    tN = time(end)* max(Xnt);
    lamda = Bt/(tN - St);
    mu = Dt/St;
```

```
else
    error('no method exists!');
end

rf = mu;
rr = lamda;
state = 1;  % arbitrary for now



function fitdata = convert_dwelldata_to_fitdata(fulldata1,fulldata2)

%This sub-function reads the data from the *dwell.dat file and returns
the
%corresponding best fit trace based on that file

[num_rows1, num_cols1] = size(fulldata1);
[num_rows2, num_cols2] = size(fulldata2);
if num_rows1 == 0
    fitdata(1:num_rows2) = ones(1, num_rows2) .*
mean(fulldata2(:,3)./1000);
else
    fitdata = zeros(num_rows2,1)' ;
    timepoint = 0;
    for k = 1 : num_rows1
        start = fulldata1(k,1);
        residence = fulldata1(k,3);
        fitdata(timepoint+1:timepoint+residence) =
start*ones(residence,1);
        timepoint = timepoint + residence;
    end
    fitdata(timepoint+1:num_rows2) = fulldata1(k,2)*ones((num_rows2-
timepoint), 1);
end

return;
```